Chemistry and Properties of Nanocrystals of Different Shapes

Clemens Burda,*[,†,‡] Xiaobo Chen,[†] Radha Narayanan,[§] and Mostafa A. El-Sayed*[,§]

Center for Chemical Dynamics and Nanomaterials Research, Department of Chemistry, Case Western Reserve University—Millis 2258, Cleveland, Ohio 44106, and Laser Dynamics Laboratory, School of Chemistry and Biochemistry, Georgia Institute of Technology, Atlanta, Georgia 30332-0400

Received July 22, 2004

Contents

1. General Introduction and Comments 1025
2. Preparation of Nanostructures of Different Shapes 1027
   2.1. Introduction: Nucleation and Particle Growth 1027
   2.2. Preparation Methods 1028
      2.2.1. Sol Process 1028
      2.2.2. Micelles 1031
      2.2.3. Sol–Gel Process 1034
      2.2.4. Chemical Precipitation 1034
      2.2.5. Hydrothermal Synthesis 1036
      2.2.6. Pyrolysis 1036
      2.2.7. Vapor Deposition 1038
   2.3. Growth Mechanism of Nanostructures of Different Shapes 1040
      2.3.1. Effect of Monomer Concentration on the Shape of the Semiconductor QDs 1040
      2.3.2. Vapor–Liquid–Solid Growth for Nanowire by CVD and PVD Methods 1041
      2.3.3. Light-Induced Shape Change Mechanism of Metal Nanorods 1042
3. Surface Chemical Modification of Nanoparticles 1042
4. Assembly of Nanoparticles 1042
5. Optical, Thermal, and Electrical Properties of Particles of Different Sizes and Shapes 1047
   5.1. Semiconductor Nanoparticles 1047
      5.1.1. Discrete Electronic Structure 1047
      5.1.2. Optical Transitions in Nanostructures of Different Shapes 1048
   5.2. Metallic Nanoparticles 1057
   5.3. High Surface-to-Volume Ratio 1059
   5.4. Melting Point 1060
   5.5. Conductivity and Coulomb Blockade 1061
6. Nonradiative Relaxation of Nanoparticles of Different Shapes 1063
   6.1. Nonradiative Relaxation in Metal Nanostructured Systems 1063
      6.1.1. Background 1063
      6.1.2. Theoretical Modeling of the Transient Optical Response 1063
      6.1.3. Electron–Electron Thermalization in Gold Nanoparticles 1063
      6.1.4. Electron–Phonon Relaxation in Gold Nanoparticles 1064
      6.1.5. Shape and Size Dependence on the Electron–Phonon Relaxation Rate 1065
      6.1.6. Pump Power Dependence of the Electron–Phonon Relaxation Rate 1066
   6.2. Nonradiative Relaxation in Semiconductor Nanostructured Systems 1066
      6.2.1. II–VI Semiconductor Systems 1067
      6.2.2. I–VII Semiconductor Systems 1074
      6.2.3. III–V Semiconductor Systems 1074
      6.2.4. Group IV Semiconductor Systems 1074
      6.2.5. Metal Oxides Systems 1075
      6.2.6. Other Systems 1075
   6.3. Hot Electrons and Lattice Temperatures in Nanoparticles 1076
   6.4. Phonon Bottleneck 1078
   6.5. Quantized Auger Rates 1079
   6.6. Trapping Dynamics 1079
7. Nanocatalysis 1081
   7.1. Introduction 1081
   7.2. Homogeneous Catalysis 1081
      7.2.1. Chemical Reactions Catalyzed Using Colloidal Transition Metal Nanocatalysts 1083
   7.3. Heterogeneous Catalysis on Support 1086
      7.3.1. Lithographically Fabricated Supported Transition Metal Nanocatalysts 1087
      7.3.2. Chemical Reactions Catalyzed Using Supported Transition Metal Nanocatalysts 1087
8. Summary 1090
   8.1. Reviews 1090
      8.1.1. Synthesis 1090
      8.1.2. Properties 1090
      8.1.3. General 1091
   8.2. Books 1091
      8.2.1. Metal Nanoparticles 1091
      8.2.2. Semiconductor Nanoparticles 1091
      8.2.3. Carbon Nanotubes and Nanoparticles 1091
      8.2.4. Nanoparticles in General 1092
9. Acknowledgment 1092
10. References 1092

* To whom correspondence should be addressed. Phone, 404-894-0292; fax, 404-894-0294; e-mail, mostafa.el-sayed@chemistry.gatech.edu.
† Case Western Reserve University—Millis 2258.
‡ Phone, 216-368-5918; fax, 216-368-3006; e-mail, burda@case.edu.
§ Georgia Institute of Technology.

1. General Introduction and Comments

The interest in nanoscale materials stems from the fact that new properties are acquired at this length scale and, equally important, that these properties

10.1021/cr030063a CCC: $53.50
Published on Web 03/18/2005

Prof. Clemens Burda is the Director of the Center for Chemical Dynamics and Nanomaterials Research in the Chemistry Department at Case Western Reserve University. He is appointed as Professor of Physical Chemistry specializing in Nanoscience and technology. His research evolves around optically useful nanocrystals, applied toward diverse areas such as photovoltaics, photocatalysis, photobiology, and biomedical applications, including bioimaging, therapy, and tissue targeting for drug delivery. Prof. Burda received his chemistry education in Basel, Switzerland, and graduated as a doctor of philosophy and science with honors in 1997 from the Jakob Wirz group at the University of Basel. Prof. Burda was a postdoctoral research fellow with Prof. Mostafa El-Sayed before assuming his current position at Case. Dr. Burda is a reviewer for several nanoscience journals, an editorial board member for the *International Journal of Nanotechnology*, and an organizer of the Nanomaterials Conference at the 50th annual SPIE meeting in 2005.

Xiaobo Chen did his undergraduate research at Peking University and did his Master's research on inorganic membranes at Dalian Institute of Chemical Physics (Chinese Academy of Sciences). His current research interest as a Ph.D. candidate on Prof. Burda's research team is focused on the development of photocatalytic nanomaterials. In his spare time Xiaobo is an excellent cook and ping-pong player.

change with their size or shape. The change in the properties at this length scale is not a result of scaling factors. It results from different causes in different materials. In semiconductors, it results from the further confinement of the electronic motion to a length scale that is comparable to or smaller than the length scale characterizing the electronic motion in bulk semiconducting material (called the electron Bohr radius, which is usually a few nanometers). As noble metals are reduced in size to tens of nanometers, a new very strong absorption is observed resulting from the collective oscillation of the electrons in the conduction band from one surface of the particle to the other. This oscillation has a frequency that absorbs the visible light. This is called the

Radha Narayanan was born in Savannah, GA. She got her B.S. in Chemistry from Armstrong Atlantic State University. She is currently a Ph.D. Candidate in chemistry under the direction of Professor Mostafa A. El-Sayed at Georgia Institute of Technology. She will be graduating with a Ph.D. in May 2005. Her Ph.D. research involves investigating the stability and recycling potential of differently shaped colloidal transition metal nanoparticles during their catalytic function. She has compared the stability and catalytic activity of tetrahedral, cubic, and spherical platinum nanoparticles during the catalytic process. Her other research interests include the rational design of nanoparticles for various applications such as sensing, molecular transport, and so forth.

Professor Mostafa A. El-Sayed was born in Zifta, Egypt. He obtained his B.S. degree in chemistry from Ain Shams University at Cairo, Egypt. He got his Ph.D. degree in Chemistry from Florida State University. During his Ph.D. studies, he worked with Professor Michael Kasha, Professor Ray Sheline, and Professor R. Wolfgang. He was a research associate at Harvard, Yale, and California Institute of Technology. In 1961, he was appointed to the faculty of University of California, Los Angeles. In 1994, he became the Julius Brown Chair in the School of Chemistry and Biochemistry at Georgia Institute of Technology. He is also the Regents' Professor and Director of the Laser Dynamics Laboratory at Georgia Tech. He has served as the Editor-in-Chief of *The Journal of Physical Chemistry* from 1980 to 2004. He has received numerous fellowships such as Alfred P. Sloan Fellow, John Simon Guggenheim Fellow, Sherman Fairchild Distinguished Scholar, and Senior Alexander von Humboldt Fellow. He was elected to the National Academy of Sciences and the Third World Academy of Science. He became an elected fellow of the American Academy of Arts and Sciences, the American Physical Society, and the American Association for the Advancement of Science. He has also received numerous national awards such as the Fresenius Award, the McCoy Award, the Harris Award, and the Irving Langmuir ACS National Award as well as regional ACS awards from the California, Southern California, Florida, Eastern Tennessee, and Northeastern sections. He has also received the King Faisel International Award in Science. His research interests include understanding the optical properties and ultrafast dynamics of metal and semiconductor nanoparticles and the catalytic properties of transition metal nanoparticles of different shapes. His other research interests include the study of the primary processes involved in the photoisomerization and the proton pump in bacteriorhodopsin photosynthesis.

surface plasmon absorption. This strong absorption, giving rise to vivid characteristic color, has been observed and used, but not understood, since the 17th century. The gold particles, giving rise to a brilliant rose color, have been used throughout Europe in stained glass windows of cathedrals and by the Chinese in coloring vases and other ornaments. In transition metal nanoparticles, the decrease in the particle size to the nanometer length scale increases the surface-to-volume ratio. This, together with our ability to make them in different sizes and shapes, makes them potentially useful in the field of catalysis.

The past couple of decades have witnessed an exponential growth of activities in this field worldwide, driven both by the excitement of understanding new science and by the potential hope for applications and economic impacts. The largest activity in this field at this time has been in the synthesis of new nanoparticles of different sizes and new shapes. The unraveling of the physics of these particles and the application of computation methods to understand their behavior is being investigated. Self-assembly of these nanoparticles by different techniques, either from the bottom-up techniques (assembling particles synthesized in solution) or from the top-down techniques (different lithographic methods), is being pursued. Although many future applications will make use of the properties of the individual nanoparticles (sensors, medical diagnostics, homogeneous catalysis, etc.), there are other important applications that would require self-assembled nanoparticles (nanoelectronics, optoelectronics, photonics, heterogeneous catalysis, etc).

Besides giving us new properties, creating novel nanostructures requires new understanding of the properties of their surfaces. In most of their potential applications, the quality and the structure of the surface of nanoparticles will undoubtedly play the pivotal role in determining their functions. Being small could make the surface of a nanoparticle unstable due to the high surface energy and the large surface curvature. Thus, the properties change as these particles are used. Not only could the surface structure and shape change, but the chemical nature of their surface could be altered, too. In addition, for device applications, these nanoparticles need to be connected to our macroscopic world. The perturbation at interconnects could have larger effects on the properties of nanoparticles than quantum confinement or other physical forces involved within the nanoparticle space. Thus, it is clear that using these nanoparticles fully and effectively will depend on our understanding of their general properties and also of their surface properties and stability.

It is hoped that before we move quickly into producing large-scale "dream devices" in nanotechnology, the nanoscience is carried out. Not only should we be able to make any nanostructure of any shape and in any assembled form, we should also know a great deal about the properties of the individual nanoparticles as well as their assembled structures.

In this review, we discuss the synthesis and properties of individual nanoparticles. We start with a discussion of the different bottom-up methods of the synthesis of the nanoparticles. Techniques using electron, ion, or photon beams in lithography to make nanostructures are not discussed. Due to the explosion of publications in this field, we do not claim that this dominantly wet-chemistry review includes all of the published work, but rather an exposure of the methods. We apologize to the authors of the excellent work that due to the large activity in this area, we have unintentionally left out.

In the property sections, we tried very hard to give a reasonable account of the science and the important fundamental work carried out in this area. The details were given intentionally because the concepts involved in this field are rather new to many chemists who are not directly involved in it.

2. Preparation of Nanostructures of Different Shapes

2.1. Introduction: Nucleation and Particle Growth

The chemical growth of bulk or nanometer-sized materials inevitably involves the process of precipitation of a solid phase from solution. A good understanding of the process and parameters controlling the precipitation helps to improve the engineering of the growth of nanoparticles to the desired size and shape. For a particular solvent, there is a certain solubility for a solute, whereby addition of any excess solute will result in precipitation and formation of nanocrystals. Thus, in the case of nanoparticle formation, for nucleation to occur, the solution must be supersaturated either by directly dissolving the solute at higher temperature and then cooling to low temperatures or by adding the necessary reactants to produce a supersaturated solution during the reaction.[1,2] The precipitation process then basically consists of a nucleation step followed by particle growth stages.[3,4]

Generally, there are three kinds of nucleation processes: homogeneous nucleation, heterogeneous nucleation, and secondary nucleation. Homogeneous nucleation occurs in the absence of a solid interface by combining solute molecules to produce nuclei. Homogeneous nucleation happens due to the driving force of the thermodynamics because the supersaturated solution is not stable in energy. The overall free energy change, ΔG, is the sum of the free energy due to the formation of a new volume and the free energy due to the new surface created. For spherical particles

$$\Delta G = -\frac{4}{V}\pi r^3 k_B T \ln(S) + 4\pi r^2 \gamma \qquad (1)$$

where V is the molecular volume of the precipitated species, r is the radius of the nuclei, k_B is the Boltzmann constant, S is the saturation ratio, and γ is the surface free energy per unit surface area. When $S > 1$, ΔG has a positive maximum at a critical size, r^* (see Figure 1). This maximum free energy is the activation energy for nucleation. Nuclei larger than

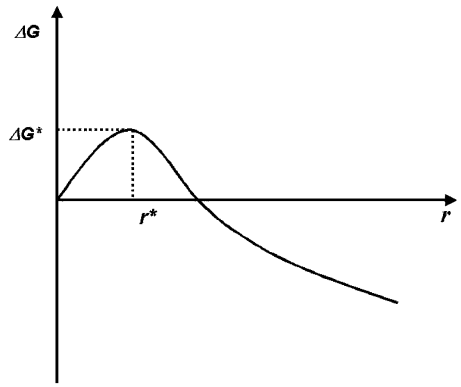

Figure 1. Illustration of the overall free energy ΔG as a function of the growth particle size r.

the critical size will further decrease their free energy for growth and form stable nuclei that grow to form particles. The critical nuclei size r^* can be obtained by setting $d\Delta G/dr = 0$.

$$r^* = \frac{2V\gamma}{3k_B T \ln(S)} \quad (2)$$

For a given value of S, all particles with $r > r^*$ will grow and all particles with $r < r^*$ will dissolve. From the above equation, it follows that the higher the saturation ratio S, the smaller the critical nuclei size r^* is.

After the nuclei are formed from the solution, they grow via molecular addition, which relives the supersaturated step. When the concentration drops below the critical level, nucleation stops and the particles continue to grow by molecular addition until the equilibrium concentration of the precipitated species is reached. Uniformity of the size distribution is achieved through a short nucleation period that generates all of the particles obtained at the end of the reaction followed by a self-sharpening growth process. At this stage, the smaller particles grow more rapidly than the larger ones because the free energy driving force is larger for smaller particles than for larger ones if the particles are slightly larger than the critical size. At this stage, focusing in size occurs.[1] Nearly monodisperse size distribution can be obtained at this stage by either stopping the reaction (nucleation and growth) quickly or by supplying reactant source to keep a saturated condition during the course of the reaction.

On the other hand, when the reactants are depleted due to particle growth, Ostwald ripening or defocusing will occur, where the larger particles continue to grow, and the smaller ones get smaller and finally dissolve. Because the saturation ratio (S) decreases now and the corresponding critical nuclei size (r^*) increases according to eq 2, any particles smaller than this new critical size will dissolve. If the reaction is quickly stopped at this stage, the particles will have a broad size distribution, which is featured by a distribution centering two size regimes, a bigger one and a smaller one, and the critical size now at this saturation is in between. Once the reaction (mainly the growth of the particles) goes into this stage, it is difficult to get monodisperse particles unless the reaction is extended to long enough times to completely deplete the supersaturation and the smaller nuclei. In the latter case, the size of the particles gets relatively large and can extend into the micrometer size regime. During an actual experiment, when there is no continuous supply of the reactants, the saturation ratio continues to decrease and the critical nuclei size continues to increase. To get a short burst of nucleation, a high saturation ratio (S) is suitable.

In addition to the growth by molecular addition where soluble species deposit on the solid surface, particles can grow by aggregation with other particles, and this is called secondary growth. The rate of particle growth by aggregation is much larger than that by molecular addition. After the particles grow to a stable size, they will grow by combining with smaller unstable nuclei and not by collisions with other stable particles.

Nanoparticles are small and are not thermodynamically stable for crystal growth kinetically. To finally produce stable nanoparticles, these nanoparticles must be arrested during the reaction either by adding surface protecting reagents, such as organic ligands or inorganic capping materials,[2] or by placing them in an inert environment such as an inorganic matrix or polymers.[4] The nanocrystal (NC) dispersions are stable if the interaction between the capping groups and the solvent is favorable, providing an energetic barrier to counteract the van der Waals and magnetic (magnetic materials) attractions between nanoparticles. To help arrest these nanoparticles, different solvents are also used to change the solubility or the reaction rate.[1,2,4]

2.2. Preparation Methods

2.2.1. Sol Process

As discussed in the previous section, the production of monodisperse colloids requires a temporally discrete nucleation event followed by slower controlled growth on the existing nuclei. A general scheme for preparing monodisperse nanostructures requires a single, temporally short nucleation event followed by slower growth on the existing nuclei.[5] This may be achieved by rapid addition of reagents into a reaction vessel containing a hot, coordinating solvent. Rapid addition of reagents to the reaction vessel raises the precursor concentration above the nucleation threshold. The temperature of the solution is sufficient to decompose the reagents, resulting in a supersaturation of particles in solution. Upon a short nucleation burst, the concentration of these species in solution drops below the critical concentration for nucleation. As long as the consumption of the reactants by the growth of the particles is not exceeded by the rate of precursor addition to the solution, no new nuclei form and the additional material can only add to the existing nuclei. Because the growth of any one NC is similar to that of all others, the initial size distribution is largely determined by the time over which the nuclei are formed and begin to grow. If the time of NC growth during the nucleation period is short compared to the subsequent growth processes, the NCs can become more uniform over time as size focusing takes place.[5−7]

An alternative synthetic approach involves mixing of the reagents in a vessel at a temperature low enough to preclude any appreciable reaction.[2,4−7] A controlled ramp of the solution temperature accelerates the chemical reaction and produces the required supersaturation, which is then relieved by a burst of nucleation. As long as the temperature is adjusted to keep the rate at which the reagents react less than or equal to the rate at which the material is added to the existing nuclei, the supersaturated state is never revisited and no new nuclei form. In either approach, the size distribution of the NC sample is limited primarily by the short time interval in which the initial crystallites form and begin to grow.

In general, NC size increases with increasing reaction time as more material is added to NC surfaces and also with increasing temperature as the rate of addition of material to the existing nuclei increases.[2,4−7]

The systematic adjustment of the reaction parameters, such as reaction time, temperature, concentration, and the selection of reagents and surfactants, can be used to control the size, shape, and quality of NCs. Tailoring the ratio of the concentration of reagents to that of surfactants provides another control over NC size, because high stabilizer-to-reagent concentrations favor the formation of a smaller nuclei and a smaller NC size. During NC growth, the surfactants in solution adsorb reversibly to the surfaces of the NCs, providing a dynamic organic shell (capping layer) that stabilizes the NCs in solution and mediates their growth. Surfactants that bind more tightly to the NC surface or larger molecules providing greater steric hindrance (bulkier surfactants) slow the rate of materials addition to the NC, resulting in smaller average NC size. For example, bulkier trioctylphosphines provide larger steric hindrance than more compact tributylphosphines, resulting in a slower NC growth. An effective strategy involves using a pair of surface agents in which one binds tightly to the NC surface, hindering growth, and the other binds less tightly, permitting rapid growth. For example, adjustment of the ratio of carboxylic acid (tightly bound) and alkylphosphine (weakly bound) stabilizers allows the growth rate and therefore the size and shape of the NCs to be controlled.[2,4−7]

When the NC sample reaches the desired size, further growth is arrested by quickly cooling the solution. The NCs are then isolated from their growth solution. Introducing another solvent that is miscible with the first solvent but has an unfavorable interaction with the capping groups (hence, it can be called a "nonsolvent") reduces the barrier to aggregation and destabilizes the NC dispersion, resulting in their flocculation. Centrifuging the resulting turbid suspension allows the solvent to be decanted and powders of the NCs to be isolated. These powders consist of the desired NCs and their intimate organic capping layer and can be redispersed in a variety of solvents.[2,4−7]

Preparation of II−IV Semiconductor NCs. In the synthesis of II−VI NCs, group II sources can be metal alkyls, metal oxide, or organic salts. The group VI sources are often organophosphine chalcogenides (R_3PE) or bistrimethylsilylchalcogenides TMS_2E (TMS, trimethylsilyl) (where E = S, Se, and Te). In the precipitation method, the sodium salt of X (e.g., Na_2S) or the acid itself (e.g., H_2S) is used. High-boiling coordinating solvents include R_3P, R_3PO, alkyl phosphites, alkyl phosphates, pyridines, alkylamines, and furans. CdO, $CdCO_3$, $Cd(Ac)_2$, Me_2Cd, etc., can be used as Cd sources. By tuning the reaction parameters, different sizes and shapes of CdSe,[5−15] CdS,[6,17,18] CdTe,[6,16,18−21] ZnSe,[22] ZnO,[23] etc., have been successfully prepared.

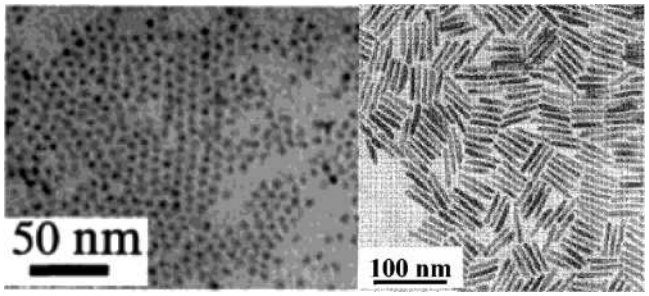

Figure 2. Transmission electron micrographs of wurtzite CdSe nanoparticles, quantum dots (left) and nanorods (right). Reprinted with permission from ref 7 (left) and ref 13 (right). Copyright 2001 and 2001 American Chemical Society.

Figure 2 shows a TEM image of spherical CdSe nanoparticles (left) and CdSe nanorods (right) synthesized using the sol method.[7,13] In a typical synthesis using a stearic acid (SA)/trioctylphosphine oxide (TOPO)/CdO system, CdO is mixed with stearic acid and heated to ~130 °C under argon flow until all of the mixture becomes optically clear. The system is allowed to cool to room temperature, and 2 g of 99% TOPO is added to the flask. The flask is resealed and reheated to 360 °C under argon flow. A selenium solution with selenium powder and toluene dissolved in trioctylphosphine is then quickly injected into the reaction flask. The temperature of the reaction mixture decreases to 300 °C upon injection and is maintained at this temperature during the growth of the nanocrystals. After the reaction is completed, the reaction flask is removed from the heating mantle and allowed to cool to 20−50 °C. Acetone is then added to precipitate nanocrystals. The nanocrystals are further isolated by centrifugation and decantation. In a similar procedure, CdSe nanorods can be synthesized by the substitution of SA with tetradecylphosphonic acid (TDPA) and with multiple injections of Se precursors.[13]

Preparation of Monodisperse III−V Semiconductor NCs. Similarly, high-quality InP and InAs NCs have been synthesized by rapid mixing and heating of group III and V precursors in high-boiling, coordinating solvents. Figure 3 shows a typical TEM image of InP nanoparticles.[22] Typically, $InCl_3$ is employed as an In source with TMS_3P or TMS_3As in R_3P/R_3PO solvents[22−24] to form InP[16,24] and InAs.[1] For example, in a typical synthesis of InP nanocrystals,[24] $In(Ac)_3$ is mixed with ligands and octadecene (ODE) in a three-neck flask and heated to 100−120 °C to obtain an optically clear solution and is pumped for

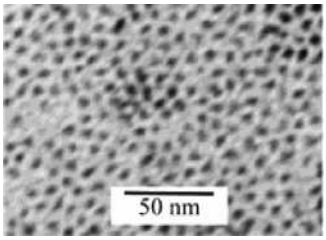

Figure 3. TEM image of InP nanocrystals. Reprinted with permission from ref 22. Copyright 1998 American Chemical Society.

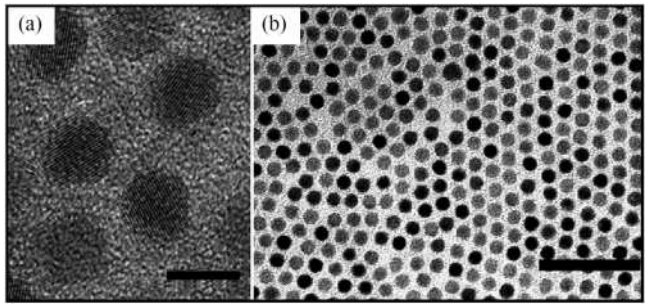

Figure 4. TEM micrographs of PbSe (a) at high resolution (9 nm bar), revealing lattice imaging of the NCs, and (b) at low resolution (70 nm bar), showing an assembly of NCs. Reprinted with permission from ref 27. Copyright 2001 IBM.

2 h. Fatty acids with different chain lengths, amines, phosphines, phosphine oxides, and phosphonic acids were also tested as solvents in ODE. The system is purged with Ar and then further heated to 300 °C under Ar flow. $P(TMS)_3$ dissolved in ODE is then injected into the hot reaction flask. After the injection, the temperature is dropped to 270 °C for the growth of the InP nanocrystals. The resulting InP nanocrystals can be then dissolved in nonpolar solvents. Acetone and methanol can be used to precipitate the nanocrystals to remove excess reagents and side products.

Preparation of Monodisperse IV−VI Semiconductor NCs. PbSe[25−27] nanoparticles have been synthesized by different groups. Their optical transitions are in the infrared range, and they have different potential applications.

Figure 4a shows a high-resolution TEM image of 8 nm PbSe NCs. The internal crystal lattice is clearly resolved in several NCs. Lower magnification imaging, as shown in Figure 4b, conveys the consistent size and shape of the PbSe NCs within a sample.[27] The PbSe nanoparticles are synthesized by rapidly injecting lead oleate and trioctylphosphine selenide (TOPSe) dissolved in trioctylphosphine into diphenyl ether solvent at 150 °C. The reaction temperature is adjusted in the range of 90−220 °C to obtain different sizes of PbSe nanoparticles.[27]

Preparation of Monodisperse Metal NCs. Cobalt serves as a model system for magnetic scaling in materials. Its low to moderate crystal anisotropy allows the effects of size, shape, internal crystal structure, and surface anisotropy to be studied in a single system. Furthermore, synthetic methods allow Co NCs to be produced in several distinct crystal polymorphs with various crystal structures.[27−34] The cobalt carbonylmetal organic precursor is decomposed

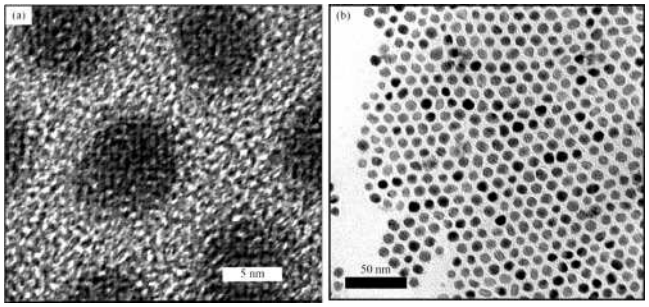

Figure 5. (a) High-resolution TEM image of 7 nm hcp Co NCs revealing subtle lattice imaging of the NCs. (b) Low-resolution TEM images of an ensemble of 10 nm hcp Co NCs. Reprinted with permission from ref 27. Copyright 2001 IBM.

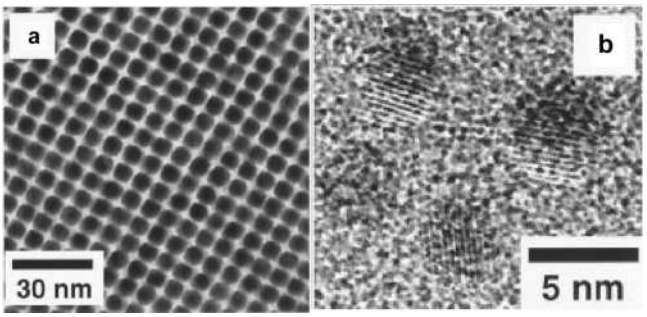

Figure 6. (a) TEM micrograph of a 3D assembly of 6 nm $Fe_{50}Pt_{50}$ sample after replacement of oleic acid/oleylamine with hexanoic acid/hexylamine. (b) High-resolution TEM image of 4 nm $Fe_{52}Pt_{48}$ nanocrystals annealed at 560 °C for 30 min on a SiO-coated copper grid. Reprinted with permission from *Science* (http://www.aaas.org), ref 35. Copyright 2000 American Association for Advancement of Science.

to form Co nanoparticles.[27−30] Puntes et al. have also achieved various particle shapes by varying the reaction conditions.[31−34] Figure 5 shows a typical TEM image of cobalt nanoparticles.[27]

Monodisperse Bimetallic NCs. Progress has also been made in the preparation of monodisperse bimetallic NCs, such as FePt[35−37] and CoPt[38,39] nanoparticles.

Figure 6 shows TEM images for FePt nanoparticles.[35] The 4 nm $Fe_{58}Pt_{42}$ nanoparticles were made by the combination of reduction of $Pt(acac)_2$ and decomposition of $Fe(CO)_5$ in octyl ether solvent. One typical synthetic procedure is as follows. Under air-free conditions, platinum acetylacetonate, 1,2-hexadecanediol, and dioctyl ether are mixed and heated to 100°C. Oleic acid, oleylamine, and $Fe(CO)_5$ are added, and the mixture is heated to reflux temperature (297 °C). Refluxing is continued for 30 min. The heat source is then removed, and the reaction mixture is allowed to cool to room temperature.[35]

NC Core/Shell Structures. Methods for overcoating a semiconductor NC with a second semiconductor material are well developed, and different kinds of core/shell structures have been successfully constructed, including CdSe/ZnS,[40−43] CdSe/ZnSe,[44] and CdSe/CdS,[45−49] FePt/Fe_3O_4,[50] CdTe/CdSe,[51] CdSe/ZnTe,[51] and InP/ZnS [52] core/shell nanoparticles, etc. There are some requirements to prepare core/shell systems by epitaxy growth: (a) The existing NC seeds must withstand the conditions under which the second phase is deposited, (b) the surface energies

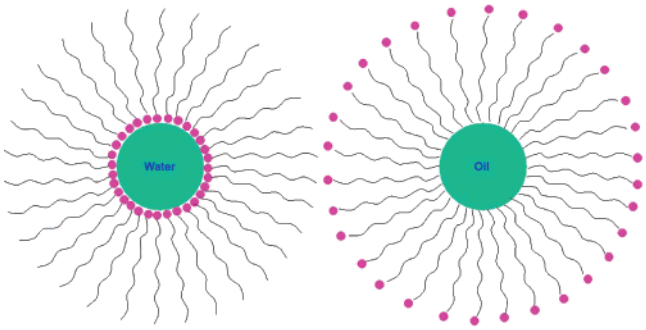

Figure 7. Reverse micelle and normal micelle structures.

of the two phases must be sufficiently similar so that the barrier for heterogeneous nucleation of the second phase is lower than that for homogeneous nucleation, and (c) the seed NC and the overcoat material must not readily interdiffuse under the deposition conditions. Typically, seed NCs are prepared and isolated by one of the standard procedures outlined above, size-selected, and then redispersed in a fresh solution of solvent and stabilizers. The solution is then heated while precursors for the inorganic shell are gradually added to allow the material to heterogeneously nucleate on the seed NCs. If the rate of precursor addition does not exceed the rate of deposition on the seeds, the precursor concentration never reaches the threshold for homogeneous nucleation of a second inorganic phase.[27]

Metal oxide nanoparticles can also be produced using this method. For example, Fe_3O_4,[53] TiO_2,[54] MnO,[55] and $BaTiO_3$[56] nanoparticles have been successfully synthesized.

2.2.2. Micelles

When the surfactant concentration exceeds the critical micelle concentration (cmc) in water, micelles are formed as aggregates of surfactant molecules.[57] In normal micelles, the hydrophobic hydrocarbon chains of the surfactants are oriented toward the interior of the micelle, and the hydrophilic groups of the surfactants are in contact with the surrounding aqueous medium. Above the cmc, the physical state of the surfactant molecules changes dramatically, and additional surfactant exists as aggregates or micelles. The bulk properties of the surfactant change around the cmc, such as osmotic pressure, turbidity, solubilization, surface tension, conductivity, and self-diffusion.

On the other hand, reverse micelles are formed in nonaqueous medium where the hydrophilic headgroups are directed toward the core of the micelles and the hydrophobic groups are directed outward. In the case of reverse micelles, there is no obvious cmc because the number of aggregates is usually small and they are not sensitive to the surfactant concentration.[58]

In both cases, the micelles exist only as a small amount of solubilized hydrophobic or hydrophilic material as illustrated in Figure 7. If the concentration of surfactant is increased further, the solubilization process can be enhanced. The droplet size can increased to a dimension that is much larger than the monolayer thickness of the surfactant because the inside pool of water or oil is enlarged. As the surfactant concentration increases further, micelles can be deformed and can change into different shapes as illustrated in Figure 8,[59] which makes it possible to synthesize different nanoparticle shapes.

The structures of micelles can be determined by the geometric factors of the surfactant at the interface, such as headgroup area α_0, alkyl chain volume V, and the maximum length l_c to which the alkyl chain can extend. The packing considerations govern the geometry of aggregation, which obeys the following rules:

$$\text{(a) spherical micelles: } V/\alpha_0 l_c < {}^1/_3$$

$$\text{(b) nonspherical micelles: } {}^1/_3 < V/\alpha_0 l_c < {}^1/_2$$

$$\text{(c) vesicles or bilayers: } {}^1/_2 < V/\alpha_0 l_c < 1$$

$$\text{(d) inverted micelles: } 1 < V/\alpha_0 l_c$$

Reverse Micelles. Reverse micelles can be formed by ionic surfactants with double-long alkyl chains alone, such as diethyl sulfosuccinate (DES) or a mixture of ionic and nonionic surfactants with a short oxyethylene chain dissolved in organic solvents. Reverse micelles are usually thermodynamically stable mixtures of four components: surfactant, cosurfactant, organic solvent, and water. The surfactants used include AOT, sodium dodecyl sulfate (SDS), cetyltrimethylammonium bromide (CTAB), and Triton-X. Some cosurfactants used are aliphatic alcohols with a chain length of C_6-C_8. Organic solvents used for reversed micelle formation are usually alkanes or cycloalkanes with six to eight carbons. Reversed micelles can solubilize relatively large amounts of water, which makes them suitable for the synthesis of nanoparticles, because the water pool is in the nanometer range and can be controlled.

The general method of using reverse micelles to synthesize nanoparticles can be divided into two cases. The first case involves the mixing of two reverse micelles. Due to the coalescence of the reverse micelles, exchange of the materials in the water droplets occurs, which causes a reaction between the cores, and nanoparticles are formed in the reversed micelles. The second case involves mixing one reactant that is solubilized in the reversed micelles with another reactant that is dissolved in water. The reaction can take place by coalescence or aqueous phase exchange between the two reverse micelles.

Metal nanoparticles can be prepared by reducing metal salts in the reversed micelles. Strong reduction agents such as $NaBH_4$, N_2H_4, and sometimes hydrogen gas were used. Pt, Rh, Pd, Ir,[60,61] Ag,[62] Au,[62-65] Cu,[66-70] Co,[71-73] Ni, FeNi,[74] Cu_3Au,[75] CoNi,[76] etc., have been synthesized using this method.

For example, Cu nanoparticles are produced using reverse micelles, where copper diethyl sulfosuccinate, $Cu(AOT)_2$, water, and isooctane were used.[77] Reverse micelles are formed in two regions for the phase diagram: $0 < w < 5$ and $30 < w < 40$, where w is the ratio $[H_2O]/[AOT]$. Syntheses in these two regions for the phase diagram induce formation of Cu nanoparticles with average particle sizes larger (12 nm)

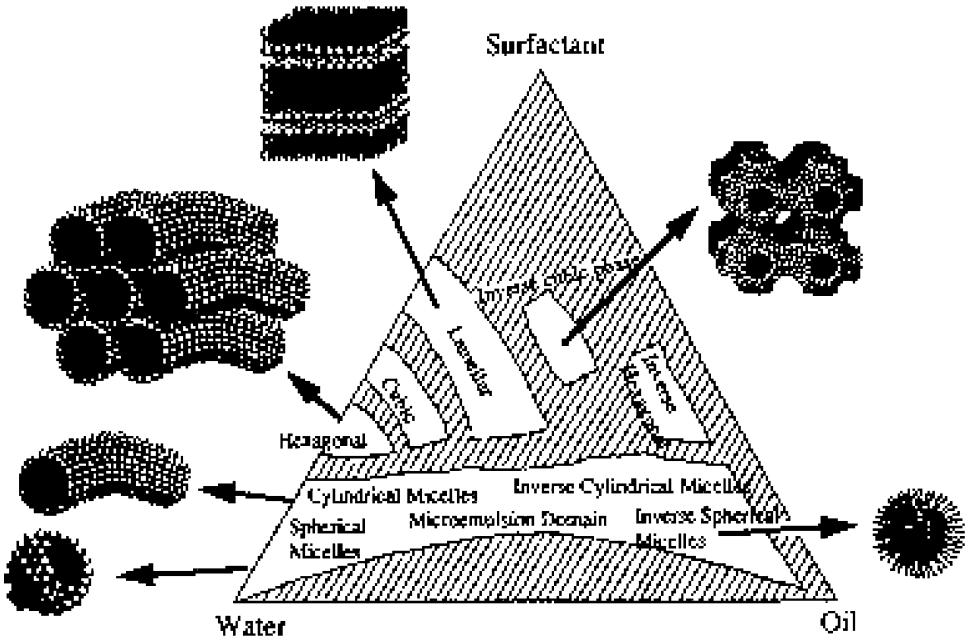

Figure 8. Schematic phase diagram of surfactant−oil−water systems showing a variety of self-assembled structures. Reprinted with permission from ref 59. Copyright 1996 Elsevier.

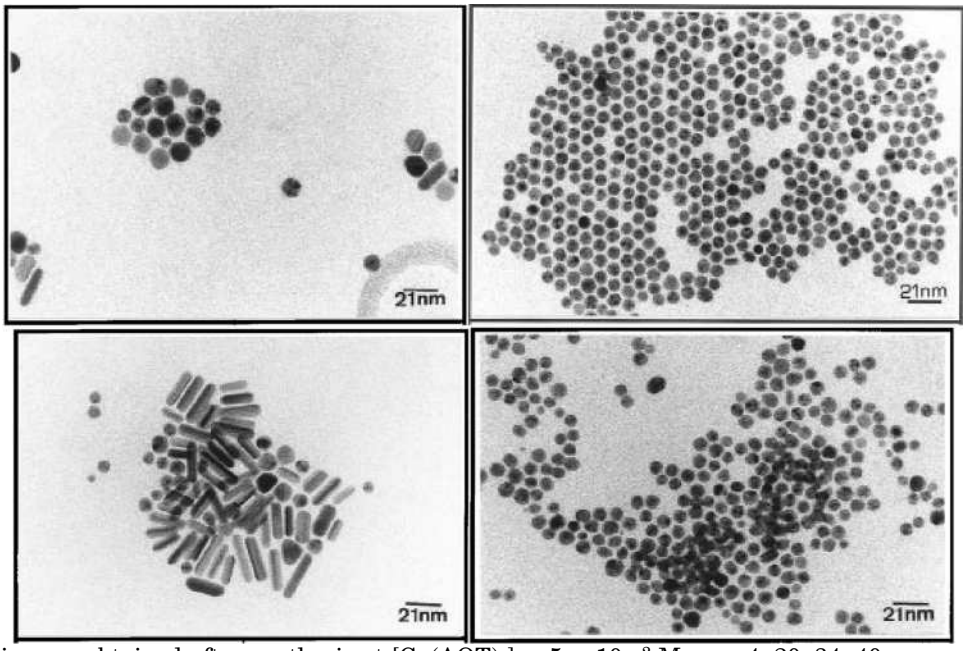

Figure 9. TEM images obtained after synthesis at $[Cu(AOT)_2] = 5 \times 10^{-2}$ M, $w = 4$, 20, 34, 40, respectively. Reprinted with permission from ref 77. Copyright 1997 American Chemical Society.

than those at higher water content (7.5 nm) as shown in Figure 9. This was explained by the fact that the redox potential changes with the water structure inside the water pool. At low water content, the number of nuclei formed is rather small and large nanocrystals are produced.[77] With the increase of the water content, the number of nuclei increases, inducing formation of smaller nanocrystals. By replacing $Cu(AOT)_2$ with $Co(AOT)_2$ and $Cd(AOT)_2$, Co and Cd nanoparticles can be produced.[78]

Metal oxide nanoparticles can be prepared inside reverse micelles by the hydrolysis procedure where metal alkoxide dissolved in oil reacts with water inside the droplets. ZrO_2,[79] TiO_2,[80−82] SiO_2,[83−88] and γ-Fe_2O_3[74] nanoparticles have been prepared in this fashion. Metal sulfate, metal carbonates, metal oxides, and silver halides can also be produced by the precipitation reaction between reactants in reverse micelles. Silver halide,[89−92] AgS,[93] $BaCO_3$, $CaCO_3$, $SrCO_3$,[94,95] and $BaSO_4$[96] nanoparticles have also been prepared using this method.

Water content in the micelles greatly affects the shape of the nanoparticles. Nanowires such as $BaCO_3$[96] and $BaSO_4$[97] have been synthesized using reverse micelles and with different water contents. Figure 10 shows the $BaSO_4$ nanoparticles and $BaCO_3$ nanowires that are prepared at different water contents.

The droplet size controls the size of the particles and can be tuned by changing w. The major change in the particle size is obtained at low water content. When the water content increases, the droplet size

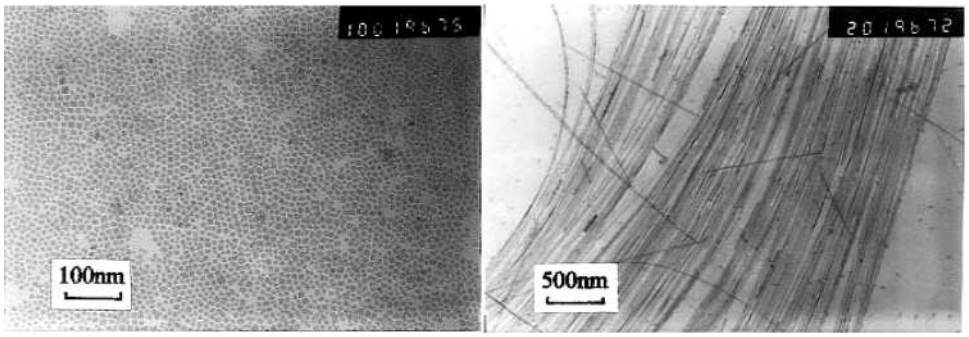

Figure 10. TEM micrographs and electron diffraction pattern of $BaCO_3$ nanowires synthesized in $C_{12}E_4$ reverse micelles. Reprinted with permission from ref 96. Copyright 1997 American Chemical Society.

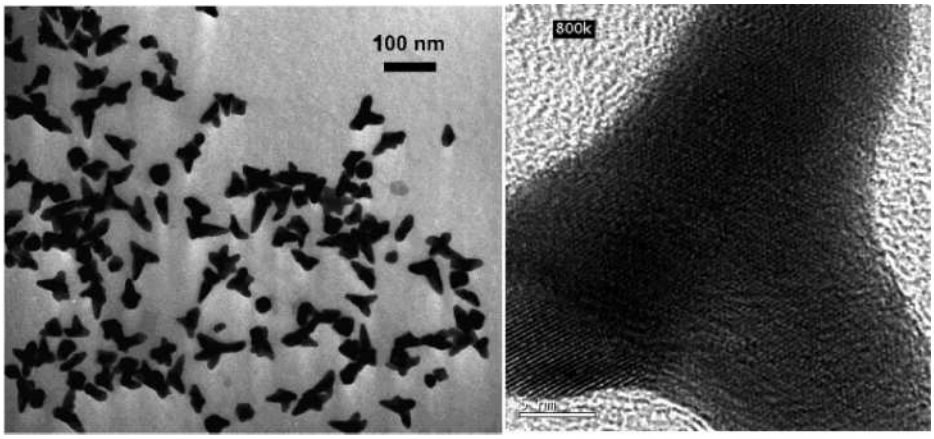

Figure 11. TEM image of branched gold nanocrystals and HRTEM image of an individual gold nanocrystal. Reprinted with permission from ref 105. Copyright 2004 American Chemical Society.

increases, and thus the particle size increases until around $w = 20$, the point when the particle size reaches a plateau. For II−VI semiconductors, such as CdS, ZnS, $Cd_{1-y}Mn_yS$, $Cd_{1-y}Zn_yS$, and CdTe, it is possible to control the particle diameter from 1.8 to 4 nm.[98] Conversely, for Ag_2S and Cu, it can be varied from 2 to 10 nm.[99,100]

Amorphous nanomaterials are formed when the two reactants are present as salts. Nanocrystals are formed when one of the reactants is a functionalized surfactant (the reactant is the counterion of the surfactant). In the latter case, it is possible to make well-defined nanocrystallite alloys such as $Cd_{1-y}Zn_yS$[101] and $Cd_{1-y}Mn_yS$.[102]

Normal Micelles. Normal micelles are oil droplets in water. The length of the surfactant alkyl chain controls the size of the droplets. Most of the nanomaterials produced are made with functionalized surfactants. This induces a marked increase in the local amount of reactants, and a supersaturation regime is formed. In contrast with reverse micelles, there is no confinement of reactants. Normal micelles act as a polymer that controls the nanoparticle size. CdS and Cu nanoparticles are successfully produced[103,104] by using micelles.

By tuning the reaction parameters, different nanoparticle shapes can be produced. Figure 11 shows TEM images of branched gold nanocrystals.[105]

Other interesting metal nanocrystal shapes have also been synthesized. For example, silver nanodisks[106] and high aspect ratio (up to 18) gold nanorods[107] have been synthesized (Figure 12).

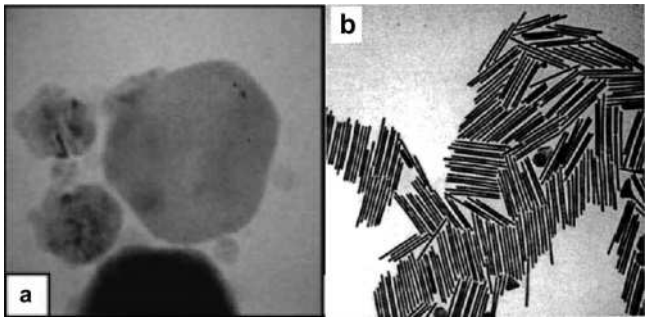

Figure 12. TEM of (a) silver nanodisk[106] and (b) gold nanorods all aspect ratio (length/width) = 18. Reprinted with permission from ref 107. Copyright 2001 American Chemical Society.

Light has been found to play an important role in shaping nanoparticles.[108] Lasers have been used to melt and reshape the nanocrystals formed in solution.[109−113] For example, Au nanorods can be transformed into spherical nanoparticles by using laser pulses as shown in Figure 13.[109−111]

Light plays a role by inducing the coalescence of these nanoparticles into solid particles and their subsequent growth. Spherical silver nanoparticles were converted into silver nanodisks as can be seen in Figure 14.[112] It is possible to control the photochemical growth of metal NCs by choosing the color of the light used to drive the reaction.[112] The size and shape of the resulting NCs can be controlled by selectively exciting the plasmon resonance of a given class of particles.[113]

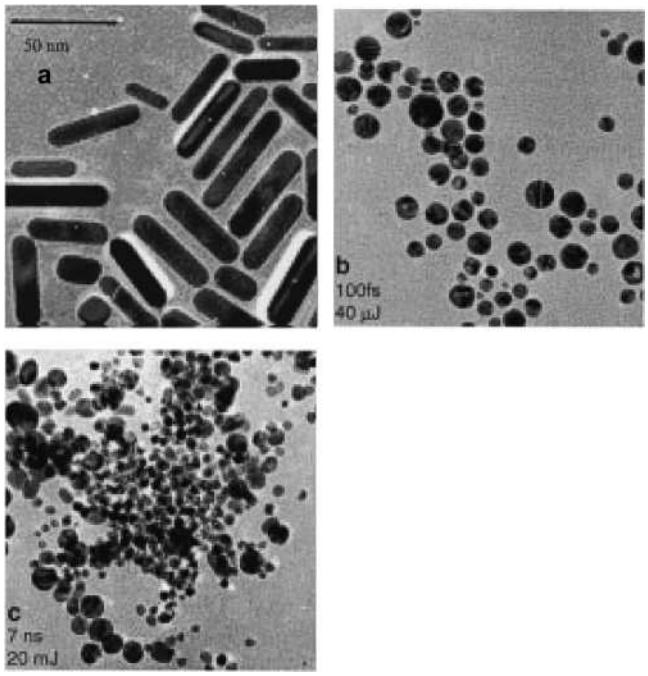

Figure 13. (a) TEM images showing the shape of gold nanorods before laser heating. (b) TEM image of the corresponding solution after exposure to 40 μJ femtosecond pulses (800 nm, 100 fs). (c) TEM image of the evaporated solution after exposure to 20 mJ nanosecond laser pulses (800 nm, 7 ns). Reprinted with permission from ref 109. Copyright 1999 American Chemical Society.

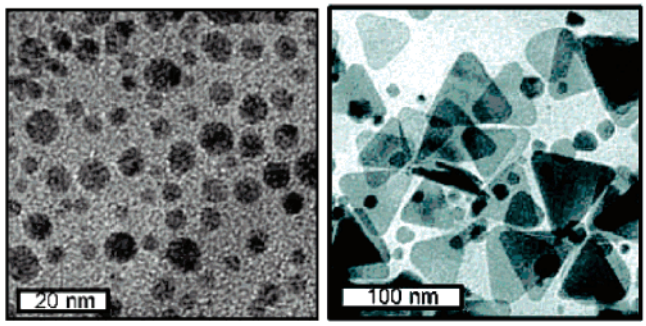

Figure 14. Silver nanoparticles and silver nanotriangles after illumination by a fluorescent lamp. Reprinted with permission from ref 112. Copyright 2003 American Chemical Society.

2.2.3. Sol–Gel Process

The sol−gel method is based on inorganic polymerization reactions. The sol−gel process includes four steps: hydrolysis, polycondensation, drying, and thermal decomposition. Precursors of the metal or nonmetal alkoxides hydrolyze with water or alcohols according to the hydrolysis process

$$M(OR)_x + mH_2O \rightarrow M(OR)_{x-m}(OH)_m + mROH \quad (3)$$

where if m is up to x, the reaction is total hydrolysis, followed by either a water condensation

$$2M(OR)_{x-m}(OH)_m \rightarrow (OH)_{m-1}(OR)_{x-m}-M-O-M(OR)_{x-m}(OH)_{m-1} + H_2O \quad (4)$$

or an alcohol condensation

$$2M(OR)_{x-m}(OH)_m \rightarrow (OH)_{m-1}(OR)_{x-m}-M-O-M(OR)_{x-m-1} + ROH \quad (5)$$

The total reaction can be expressed as

$$M(OR)_x + {}^{x}/_{2}H_2O \rightarrow MO_{x/2} + xHOR \quad (6)$$

In addition to water and alcohol, an acid or a base can also help to hydrolyze the precursor. In the case of an acid, a reaction takes place between alkoxide and the acid.

$$-M-OR + AOH \rightarrow -M-O-A + ROH \quad (7)$$

After the solution has been condensed to a gel, the solvent must be removed. Higher temperature calcination is needed to decompose the organic precursor.

The size of the sol particles depends on the solution composition, pH, and temperature. By controlling these factors, one can tune the size of the particles. This method has been used to synthesize metal oxide nanostructures, such as TiO_2,[114−119] UO_2,[120] TnO_2,[120] ZrO_2,[121] CeO_2,[122,123] SnO_2,[124] SiO_2,[125] CuO,[126] SnO_2,[127] ZnO,[128] Al_2O_3,[129,130] Sc_2O_3,[131] $ZnTiO_3$,[132] $SrTiO_3$,[133] $BaZrO_3$,[134] $CaSnO_3$,[135]and other nanostructures.

2.2.4. Chemical Precipitation

The kinetics of nucleation and particle growth in homogeneous solutions can be adjusted by the controlled release of the anions and cations. Careful control of the kinetics of the precipitation can result in monodisperse nanoparticles. Once the solution reaches a critical supersaturation of the species forming particles, only one burst of nuclei occurs. Thus, it is essential to control the factors that determine the precipitation process, such as the pH and the concentration of the reactants and ions. Organic molecules are used to control the release of the reagents and ions in the solution during the precipitation process. The particle size is influenced by the reactant concentration, pH, and temperature. By engineering these factors, nanoparticles with narrow size distributions, such as $Zr(OH)_4$,[136] $BaTiO_3$,[137,138] $YBaCu_3Oy$,[139] CdS,[140] HgTe,[141] HgTe,[142] and CdTe,[143] have been produced.

Although the method of using precipitation to prepare nanoparticles is very straightforward and simple, very complicated nanostructures can also be constructed using this method such as CdS/HgS/CdS,[144−153] CdS/$(HgS)_2$/CdS,[154] and HgTe/CdS quantum well systems and other core/shell structures.[155,156]

CdS Core. The syntheses of the colloidal solutions were carried out by reacting the cadmium and the sulfide salts in aqueous solution under argon at room temperature.[144] Then the pH was brought to 7.0 using 0.1 M NaOH.

CdS/HgS/CdS Composites. The mercury salt is added to the above CdS colloid solution, and this is followed by readjustment of the pH to 7.0. This procedure results in the substitution of the surface Cd^{2+} ions by Hg^{2+} ions, forming a monolayer of HgS on CdS. The precipitation of Cd^{2+} ions by adding

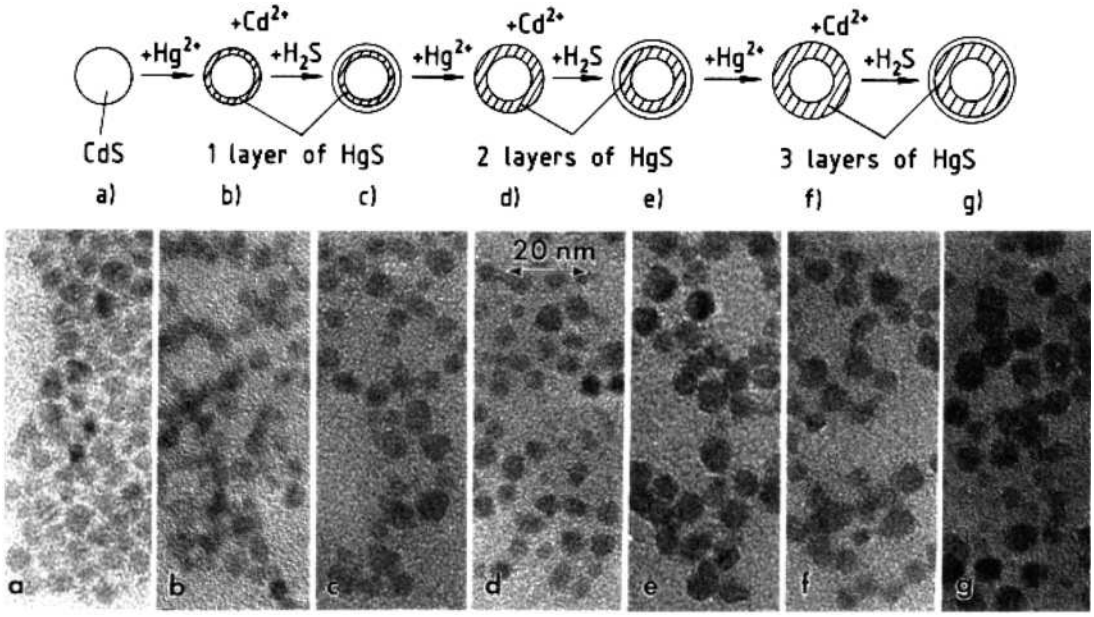

Figure 15. Illustration for the preparation procedure for HgS shell CdS/HgS/Cd quantum wells of different thicknesses and the corresponding TEM images. Reprinted with permission from ref 144. Copyright 1994 American Chemical Society.

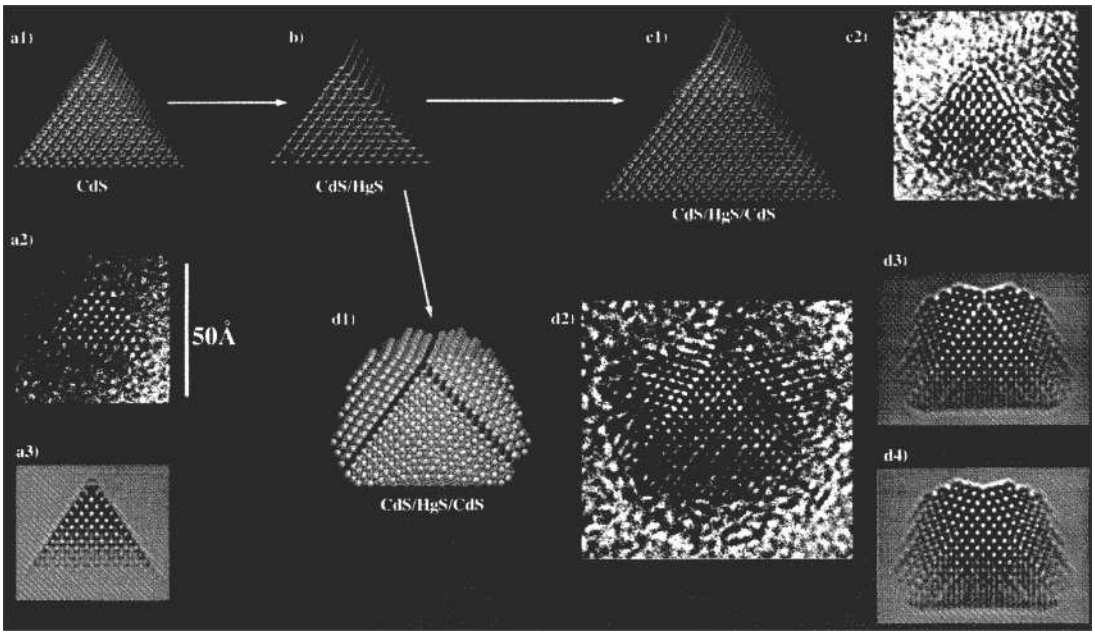

Figure 16. HRTEM study of the structural evolution of the CdS/HgS/CdS nanostructure. The micrograph of a CdS core cluster (a2) exhibits tetrahedral morphology, which is in agreement with the TEM simulation (a3). The corresponding molecular model (a1) shows that all surfaces are cadmium terminated (111). (b) is a model of the CdS particle after surface modification with Hg. A typical micrograph of a tetrahedral CdS/HgS/CdS nanocrystal is shown in (c2) along with a corresponding model (c1). Model (d1) and micrograph (d2) represent a CdS/HgS/CdS nanocrystal after twinned epitaxial growth. The arrow marks the interfacial layer exhibiting increased contrast due to the presence of HgS, in agreement with the simulation (d3). No contrast change is seen in a simulation of a model with all Hg replaced by Cd (d4). Reprinted with permission from ref 145 (Figure 1). Copyright 1996 American Physical Society.

Na_2S or H_2S leads to colloidal particles consisting of a CdS core surrounded by a monolayer of HgS and almost one monolayer of CdS as the outermost shell.[144] Figure 15 shows the illustration to prepare HgS shell CdS/HgS/CdS quantum wells of different thicknesses. Figure 16 shows HRTEM images of the quantum wells and also a simulation of the CdS/HgS/CdS quantum wells.[145]

The thickening of the HgS layer was simply achieved by repeating the substitution and reprecipitation steps described above [80 mL of 10^{-3} M $Hg(C1O_4)_2$ is added to the colloidal solution prepared so far followed by sulfidization with 200 mL of 5×10^{-4} M H_2S/water solution]. This procedure can be repeated up to three times.

An increase in the CdS layer thickness was performed independent of the thickness of the formerly prepared HgS layer in the following manner [2 mL of 0.1 M $Cd(C1O_4)_2$ at pH 7.0 is added to 1 L of a given solution]. During the dropwise addition of 200 mL of 1.2×10^{-3} M H_2S/water solution, the pH decreases to 4.0 within 30 min. The solutions were

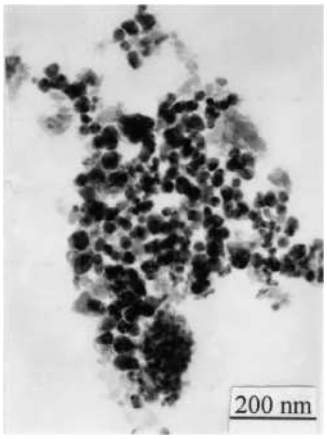

Figure 17. TEM micrograph of nanocrystalline CrN synthesized with hydrothermal method. Reprinted with permission from ref 165. Copyright 1999 Elsevier.

then purged with Ar at pH 7.0 for 15 min, and the solvent was rotovaped until the starting volume was reached again. This procedure can be repeated up to five times.[144]

2.2.5. Hydrothermal Synthesis

Hydrothermal synthesis is a common method to synthesize zeolite/molecular sieve crystals. This method exploits the solubility of almost all inorganic substances in water at elevated temperatures and pressures and subsequent crystallization of the dissolved material from the fluid. Water at elevated temperatures plays an essential role in the precursor material transformation because the vapor pressure is much higher and the structure of water at elevated temperatures is different from that at room temperature. The properties of the reactants, including their solubility and reactivity, also change at high temperatures. The changes mentioned above provide more parameters to produce different high-quality nanoparticles and nanotubes, which are not possible at low temperatures. During the synthesis of nanocrystals, parameters such as water pressure, temperature, reaction time, and the respective precursor−product system can be tuned to maintain a high simultaneous nucleation rate and good size distribution. Different types of nanoparticles such as TiO_2,[157] $LaCrO_3$,[158,159] ZrO_2,[160] $BaTiO_3$,[161] $SrTiO_3$,[162] $Y_2Si_2O_7$,[163] Sb_2S_3,[164] CrN,[165] β-SnS_2,[166] PbS,[167] Ni_2P,[168] and SnS_2 nanotubes,[169] Bi_2S_3 nanorods,[170] and SiC nanowires[171] have been successfully synthesized in this way. The solvent is not limited to water but also includes other polar or nonpolar solvents, such as benzene,[165] and the process is more appropriately called solvothermal synthesis in different solvents.

CrN nanoparticles have also been prepared according to this method, and in this case, toluene was chosen as the solvent.[165] Figure 17 shows a typical TEM image of CrN nanoparticles.[165] An appropriate amount of anhydrous $CrCl_3$ and Li_3N was put into a 50 mL silver-lined stainless steel autoclave with 40 mL of benzene and reacted at 350−420 °C for 6 h. The reaction proceeded as follows:

$$CrCl_3 + Li_3N \rightarrow CrN + 3LiCl \qquad (8)$$

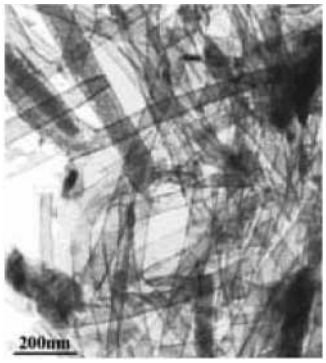

Figure 18. SnS_2 nanotubes sample synthesized with hydrothermal method. Reprinted with permission from ref 169 (Figure 3c). Copyright 2003 Springer.

Figure 18 shows SnS_2 nanotubes that were prepared at 140 °C in an autoclave where anhydrous alcohol was used as solvent, $SnCl_4$ and thiourea were chosen as reactants, and anodic aluminum oxide was used to guide the growth of nanotube shape during the reaction.[169]

Figure 19 shows SiC nanowires prepared in an autoclave using this method, where appropriate amounts of CCl_4, Si powder, and Na were put into a titanium alloy autoclave and reacted at 700 °C for 10−48 h.[171] The reaction can be expressed as follows:

$$Si + CCl_4 + 4Na \rightarrow SiC + 4NaCl \qquad (9)$$

The nanocrystals prepared according to this method usually have high crystallinity and poor size distribution. Fine control of the size and shape of the targeted nanoparticles using this process therefore needs further investigation.

The solvothermal synthesis also includes the use of supercritical fluids as solvents, and different types of nanostructures have been obtained, including Ag,[172−174] Cu,[173,175−178] Ni,[79] Co,[179] Pt,[179] Ge,[180,181] Au,[182] PdS,[183] ZnS,[184] and CdS[184−186] nanoparticles, Ge,[187,188] GaAs,[189] and GaP [189] nanowire, and carbon nanotube.[190]

In addition, a new approach, named solventless synthesis, has recently been developed,[191−193] and various shapes of nanostructures have been synthesized, including Cu_2S nanoparticles,[191,192] nanorods,[191,192] nanodisks,[191,192] nanoplates,[191,192] NiS nanorods, and triangular nanoprisms.[193] Figure 20 shows the NiS nanorods and triangular nanoprisms prepared with this method.[193]

2.2.6. Pyrolysis

Pyrolysis is a chemical process in which chemical precursors decompose under suitable thermal treatment into one solid compound and unwanted waste evaporates away. Upon completion, the desired new substance is obtained. Generally, the pyrolytic synthesis of compounds leads to powders with a wide size distribution in the micrometer regime. To get a uniform nanosized material, some modifications or revisions of the pyrolytic preparation procedure and reaction conditions are needed such as slowing of the reaction rate or decomposition of the precursor in the inert solvent. MCO_3, MC_2O_4, $M(C_2O_2)$, $M(CO)_x$, MNO_3,

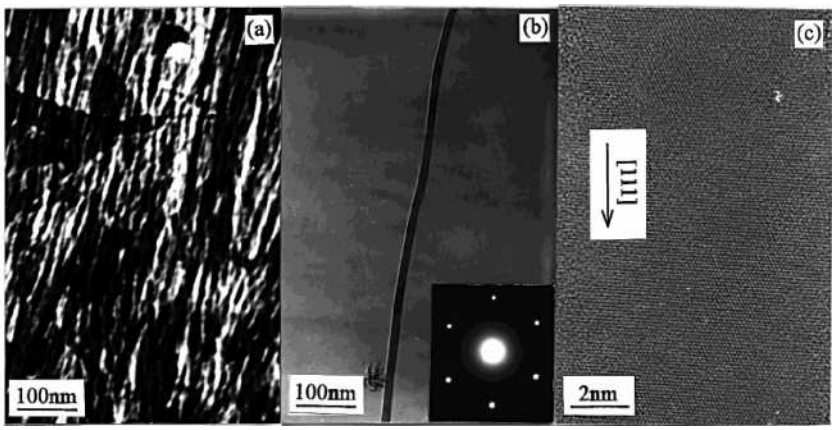

Figure 19. (a) TEM image of SiC nanowires. (b) TEM images of a straight single SiC nanowire and its ED pattern. (c) HRTEM image of the nanowire SiC shown in (b). Reprinted with permission from ref 171. Copyright 2000 American Chemical Society.

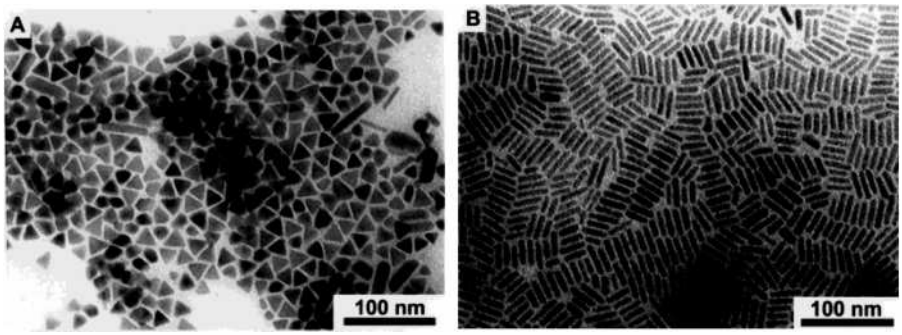

Figure 20. TEM image of the NiS nanorods (A) and triangular nanoprisms (B) prepared according to the solventless method. Reprinted with permission from ref 193. Copyright 2004 American Chemical Society.

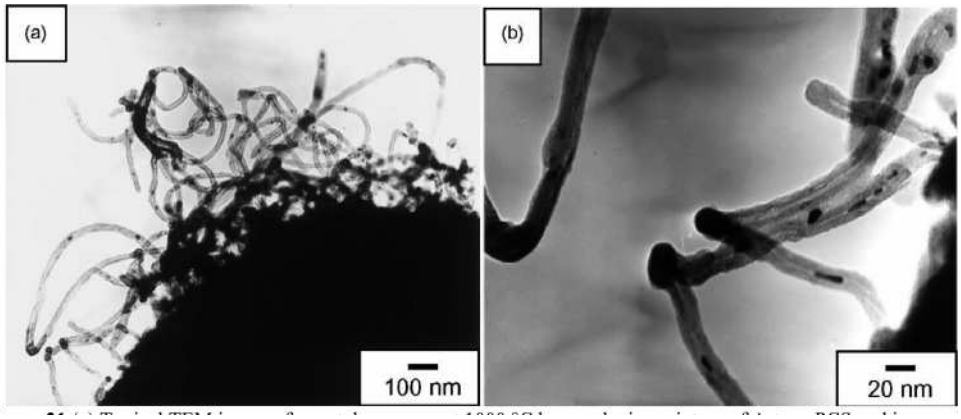

Figure 21. (a) Typical TEM image of nanotubes grown at 1000 °C by pyrolyzing a mixture of A-type PCS and iron nanoparticles. (b) Enlarged TEM image showing V-shape CNTs and adhered films. Reprinted with permission from ref 203. Copyright 2004 Elsevier.

glycolate, citrate, and alkoxides are the common precursors that are used. Poly(vinyl alcohol) (PVA) and poly(ethylene glycol) (PEG) are commonly used as protecting agents. Pyrolysis can be used to prepare different kinds of nanoparticles including metals, metal oxides, semiconductors, and composite materials such as Ag,[194] Au,[195] ZrO_2,[196] Al_2O_3, SnO_2,[197] TiO_2,[198] GaN,[199] ZnS,[200] $YBa_2Cu_3O_{7-x}$,[201] Ni,[202] and carbon nanotubes.[203−213]

Figure 21 shows TEM images for the nanotubes prepared by pyrolysis of organic precursors.[203] In a typical experiment, both low molecular mass (990 g/mol, L-type) and medium molecular mass (1290 g/mol, A-type) polycarbosilane (PCS) with a structural formula of $-(HSiCH_3-CH_2)_n-$ were used as the source materials and 17 nm iron nanopowder was used as the catalyst. The mixtures of about 0.2 g of PCS powder and 0.08 wt % iron nanopowder in toluene were spun-coated onto silicon wafers in air and subsequently pyrolyzed in a vacuum furnace between 700 and 1100 °C. The pressure was kept lower than 1.33×10^{-3} Pa during the high-temperature pyrolysis and cooling step.

Figure 22 shows Fe−C nanocomposites that have also been prepared by pyrolysis.[204] The carbon-embedded iron nanocores were synthesized in a flow reactor. A focused continuous-wave (CW) CO_2 laser radiation crossed the gas flows emerging through

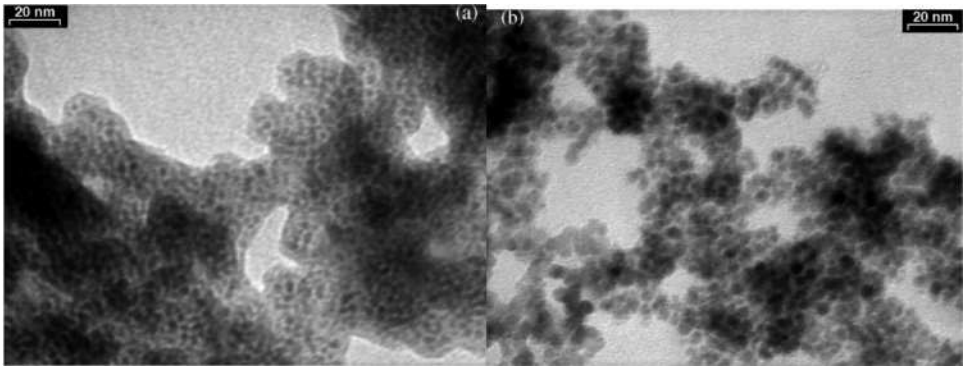

Figure 22. TEM images of FeC nanocomposite by pyrolysis [204]. Reprinted with permission from ref 204. Copyright 2004 Elsevier.

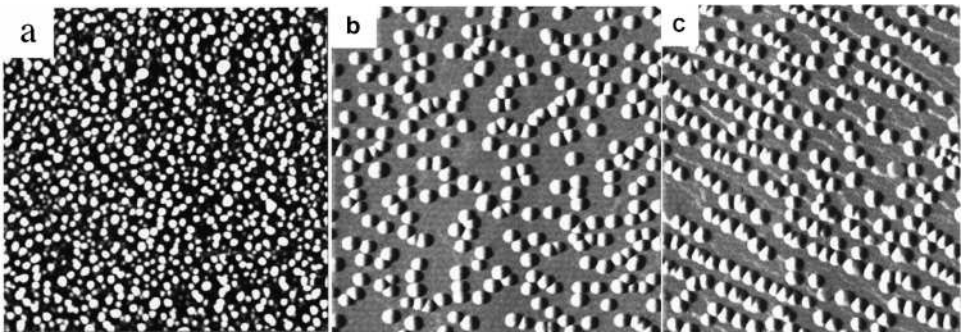

Figure 23. (a) Islands formed at growth temperature $T_g = 600$ °C and substrate miscut angle $\theta_m = 0.05$. Scans are 1 μm by 1 μm. AlInAs islands were grown on AlGaAs surface. Average diameter $d = 21$ nm. (b) Island density obtained for AsH_3 partial pressure of 1×10^{-6}, d =36 nm. (c) Partial InGaAs/GaAs island alignment at multiatomic step edges, obtained for high values of miscut angles $\theta_m = 1.25$, $T_g = 550$ °C, $d = 33$ nm. Reprinted with permission from ref 221. Copyright American Institute of Physics.

three concentric nozzles at right angles. $Fe(CO)_5$ vapors entrained by C_2H_4 were admitted through the central inner tube, while a hydrocarbon mixture including C_2H_4 and C_2H_4 entered in the reaction cell through an intermediate, middle tube. The reactive flow gas was confined to the flow axis by a coaxial Ar stream. During the experiment, the reactor was maintained at a constant pressure (700 mbar). Nucleated particles that are formed during the reaction are entrained by the flow to the cell exit into a trap, which is closed with a microporous filter in the direction of the rotary pump.

The pyrolysis of organic precursors seems to provide a direct and effective method of producing nanotubes of various kinds such as the one-step synthesis of aligned carbon nanotubes and Y-junction nanotubes. Carbon nanotubes produced from organometallic precursors can be used to further prepare gallium nitride nanowires, silicon nitride nanotubes, and boron nitride nanotubes.[213−215]

2.2.7. Vapor Deposition

2.2.7.1. Chemical Vapor Deposition (CVD). In CVD, the vaporized precursors are introduced into a CVD reactor and adsorb onto a substance held at an elevated temperature. These adsorbed molecules will either thermally decompose or react with other gases/vapors to form crystals. The CVD process consists of three steps: (a) mass transport of reactants to the growth surface through a boundary layer by diffusion, (b) chemical reactions on the growth surface, and (c) removal of the gas-phase reaction byproducts from the growth surface. Nucleation in the gas phase is homogeneous, whereas nucleation on the substrate is heterogeneous. Catalysts, usually transition metal particles such as Fe, Ni, and Co, are also used in the CVD process. Strained-induced Stranski−Krastanow growth is used to produce nanoparticles in the CVD process.[216−220]

Figure 23 shows the InGaAs nanoparticle structures grown on AlGaAs substrate by CVD.[221] For the growth of InGaAs islands, $(CH_3)_3Ga$, $(CH_3)_3In$, and AsH_3 were used as precursors. The H_2 carrier flow rate was 17.5 L/min. After growth of GaAs buffer layers at 650 °C, the temperature was lowered within the range of 490−630 °C and nanometer-sized InGaAs islands were grown by depositing five monolayers (ML) of $In_{0.6}Ga_{0.4}As$. Growth rates used for both compositions were nominally 0.5 ML/s. Substrates were (100) semi-insulating GaAs with miscut angles (θ_m) ranging from 2 to (110) to very close to the exact (100). $Al_{0.4}In_{0.6}As/Al_{0.31}Ga_{0.69}As$ quantum dots were grown in a similar fashion, using $(CH_3)_3Al$ and $(CH_3)_3In$ as precursors and growth temperatures ranging from 550 to 675 °C. Different sizes and shapes of nanoparticles can be produced by tuning the reaction parameters (see Figure 23).

Figure 24 shows the highly oriented carbon nanotubes grown by plasma-enhanced hot filament chemical vapor deposition.[222] These carbon nanotubes were grown in a pressure of 1−20 Torr maintained by flowing acetylene and ammonia gases with a total

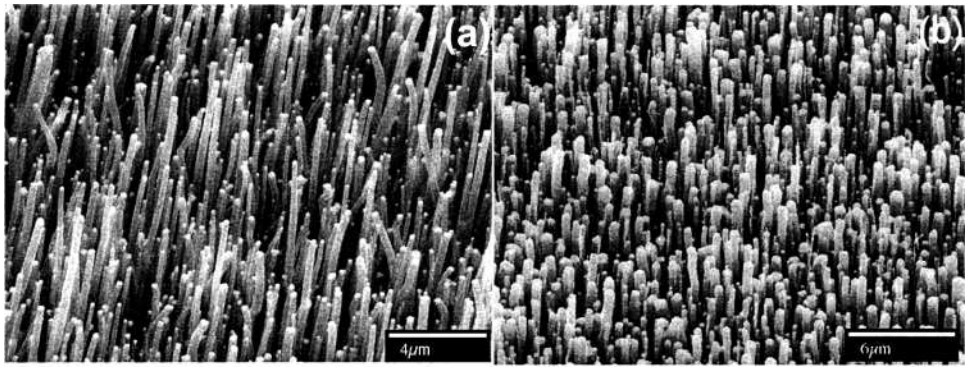

Figure 24. SEM micrograph of carbon nanotubes grown on polycrystalline Ni substrate. Most of the tube diameters are 250 nm in (a) and from 60 to 500 nm in (b). From a comparison of (a) to (b), the diameter uniformity is substantially narrowed and the average diameter size is reduced, by tuning the reaction parameters. Reprinted with permission from ref 222. Copyright 1998 American Institute of Physics

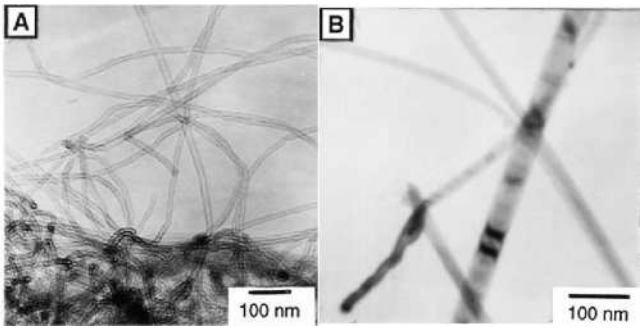

Figure 25. (A) Carbon nanotubes used as starting material and (B) GaN nanorods produced by CVD. Reprinted with permission from *Science* (http://www.aaas.org), ref 223. Copyright 1997 American Association for Advancement of Science.

flow rate of 120−200 standard cm^3/min. The acetylene-to-ammonia volume ratio varied from 1:2 to 1:10. Growth durations varied from 10 min to 5 h depending on the desired carbon nanotube lengths. Changing the parameters produces different size and length distributions of carbon nanotubes as shown in Figure 24.

GaN nanotubes were also successfully produced by CVD.[223] The reaction can be expressed as

$$2Ga_2O(g) + C(\text{nanotubes}) + 4NH_3 \rightarrow 4GaN(\text{nanorods}) + H_2O + CO + 5H_2 \quad (10)$$

This reaction was carried out in a conventional furnace with a horizontal quartz tube, where a 4:1 molar mixture of Ga and Ga_2O_3 was placed in an alumina crucible and covered with a porous alumina plate with 3−5 mm diameter channels. The carbon nanotubes were placed on the porous alumina plate. The crucible was placed in the hot zone inside the quartz tube and was held in a flowing ammonia atmosphere (400 standard cm^3/min) at 1173 K for 1 h. The Ga_2O gas generated from the $Ga-Ga_2O_3$ powder mixture flies up toward the region of carbon nanotubes through the porous plate and reacts with the nanotubes and the NH_3 gas and produces GaN nanotubes. Figure 25 shows the TEM images of the starting carbon nanotube materials and the resulting GaN nanotubes.

Various nanoparticles, including InGaAs,[221] Fe2O3,[224] TiO2,[225] SiC,[226,227] TiN,[228] SiC_xN_y,[229,230] and carbon nanotubes,[222,231−234,246] GaN nanorod,[223] and GaAs,[235,236] InAs,[237,238] ZnSe,[239] GaSe,[240] β-SiC,[241,242] SiN,[243] Si,[244] and p-type GaN nanowires[245] have been successfully produced using the CVD synthesis method.

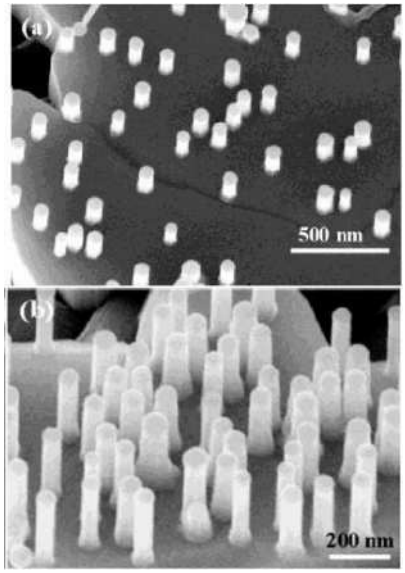

Figure 26. Perpendicular growth of nanorods on the *c* plane of ZnO nanorods. Dispersively oriented nanorods with inter-rod distances of 400 (a) and 100 nm (b), respectively. Reprinted with permission from ref 250. Copyright 2003 American Chemical Society.

2.2.7.2. Physical Vapor Deposition (PVD). PVD involves condensation from the vapor phase. The PVD process is composed of three main steps: (a) generating a vapor phase by evaporation or sublimation of the material, (b) transporting the material from the source to the substrate, and (c) formation of the particle and/or film by nucleation and growth. Different techniques have been used to evaporate the source such as electron beam, thermal energy, sputtering, cathodic arc plasma, and pulsed laser. Si nanowire,[247,240] GeO_2 nanowire,[248] Ga_2O_3[249] nanowire, ZnO[250] nanorod, GaO nanobelt and nanosheet,[251] SnO_2 nanowire, nanoribbon, nanotube,[252] etc., have been synthesized using PVD.

Figure 26 shows the ZnO nanorods grown on alumina substrate by the PVD method.[250] The experimental apparatus includes a horizontal tube

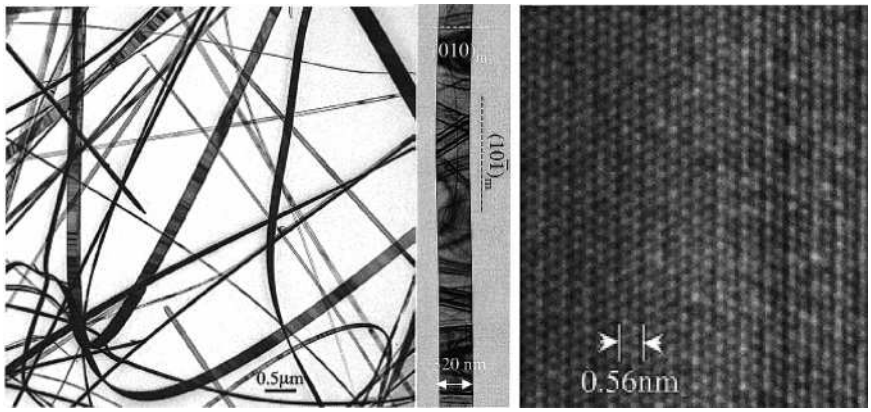

Figure 27. Flexibility of the ceramics increases dramatically with its size: (left) low-magnification TEM image of Ga_2O_3 nanoribbons; (middle) nanoribbon lying on the carbon substrate; (right) HRTEM image. Reprinted with permission from ref 251. Copyright 2002 American Chemical Society.

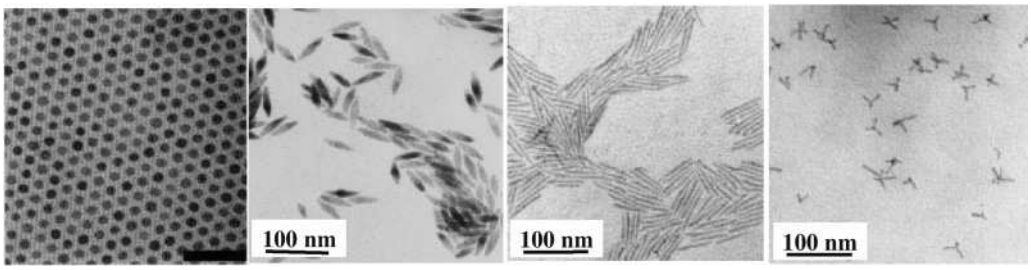

Figure 28. Different shapes of CdSe nanoparticles (from left to right): dots (reprinted with permission from *Annual Reviews in Materials Science* (http://www.AnnualReviews.org), ref 2. Copyright 2000 Annual Reviews); spindle-shaped, rod-shaped, and tetrapod-shaped (reprinted with permission from ref 253. Copyright 2003 Wiley). Scale bar = 50 nm.

furnace, a rotary pump system, and a gas supply system. A mixture of commercial ZnO, SnO_2, and graphite powder in a certain ratio (2:1:1 Zn/Sn/C) was placed in an alumina boat as the source material and positioned at the center of an alumina tube. The deposition process was conducted at 1150 °C. The desired nanostructures were deposited onto an alumina substrate located 21 cm away from the center of the furnace in a temperature range of 550−600 °C. Graphite was introduced as a vapor generation agent for the growth of the desired nanostructures because graphite can increase the creation rate of Zn and Sn vapors and also reduce ZnO and SnO_2 to Zn and Sn vapors at relatively low temperatures.

Figure 27 shows the GaO_3 nanoribbons prepared with PVD based on thermal evaporation of GaN powders under controlled conditions in the presence of oxygen.[251] The commercially supplied GaN powders (99.99% metals basis, Alfa Aesar) were placed at the center of an alumina tube that was inserted in a horizontal tube furnace. The furnace was heated at a rate of 10−15 °C/min to 1100 °C and then maintained at this temperature for 2 h before being cooled to room temperature. The pressure in the growth chamber was 300 Torr, and the Ar flow rate was 50 sccm. During evaporation, the products were deposited onto polycrystalline alumina plates placed at the downstream end of the alumina tube where the temperature is ~800−850 °C. The formation of Ga_2O_3 rather than GaN was due to the high combinability of Ga with oxygen leaked into the growth tube.

2.3. Growth Mechanism of Nanostructures of Different Shapes

2.3.1. Effect of Monomer Concentration on the Shape of the Semiconductor QDs

Nanocrystals of various shapes have been successfully synthesized over the past years. In particular, dot-,[2] rod-,[253−255] spindle-,[253,254] and tetrapod-shaped[253,254,256] semiconductor quantum dots have been fabricated (Figure 28). Because the properties of nanosized materials are strongly influenced by their shape, it is very important to explore the growth mechanisms that lead to a particular nanocrystal shape to systematically produce the desired material. In past years, Peng et al. have investigated the growth mechanisms for developing various shapes of II−VI type semiconductors using the hot TOPO/TOP method.[253] From the previous sections, we have learned that for a given monomer concentration, there is a critical nanoparticle size formed. The solubility of particles of this critical size equals exactly the monomer concentration in the solution. Any crystals with smaller sizes will have higher solubility and, thus, will dissolve in the solution. On the other hand, when the nanocrystals present in solution are slightly larger than the critical size, narrowing or focusing of the size distribution occurs, whereby the smaller nanocrystals in the distribution grow more rapidly than the larger ones. Finally, when the monomer concentration is depleted due to particle growth, the critical size becomes larger than the average size present. Consequently, Ostwald

ripening or defocusing occurs, where the size distribution broadens because some smaller nanocrystals are shrinking and eventually disappear, whereas the larger ones are still growing. The distribution can be refocused by injection of additional monomer, which compensates for the depletion due to the growth and shifts the critical size back to a smaller value. In this step of nanocrystal growth, the focusing time as well as the focused size changes with the different initial concentration of the monomer as the time for depleting the monomer concentration varies. For example, in synthesizing CdSe nanocrystals, when the initial Cd/Se molar ratio in the stock solution is about 1.4:1, the focusing time is shortened from 22 to 11 min and the focused size decreases from 3.3 to 2.7 nm. Decreasing the volume of the first injection by ~15% and keeping all of the other conditions the same achieve an initial Cd/Se ratio of 1.9:1, and the nanocrystals can be maintained at the growth temperature for hours after reaching the focused size before any defocusing occurs.[1]

The nucleation stage for the growth of anisotropic shapes plays a key role in determining the size/shape of the resulting nanocrystals. The critical nuclei can be much smaller than the ones for the synthesis of dots. In the extremely small size range, the relative chemical potential is highly size-dependent, and even very sensitive to the configuration of the nuclei. Thermodynamically, all of the nanocrystals will grow toward the shape having the lowest energy at equilibrium, which is governed by the classic theory. However, the formation dynamics can affect the shape of the formed nanocrystals. Indeed, the formation of nanocrystals is found to be a highly kinetics-driven process. In principle, before the reaction reaches the equilibrium stage, any metastable nanocrystal shapes can be arrested by tuning the reaction conditions. Even spherical or dot-shaped nanocrystals are not thermodynamically stable unless they are arrested or capped by different protecting groups, which is true in the case of most nanocrystal systems.[1,253]

In summary, essentially at low monomer concentrations or long enough growth time, all nanocrystals grow toward the lowest chemical potential environment, and this leads to the generation of only dots. On the other hand, a median monomer concentration can support only an isotropic growth in a three-dimensional growth stage and produces spindle-shaped nanocrystals. At high monomer concentrations, the magic-sized nanoclusters promote the formation of rods or other elongated structures having metastability. If the remaining monomer concentration in the growth solution is extremely high, the solution could supply a sufficient amount of monomers for each seed to fully grow arms on the four (111) facets of the zinc blende structure of the tetrahedral seeds and yields tetrapod-shaped nanoparticles as shown in Figure 29. [253]

In reality, the monomer concentration remaining in the reaction solution is always depleted by the nucleation and growth of the nanocrystals. If the reaction time is sufficiently long, the monomer concentration should drop to a level lower than that

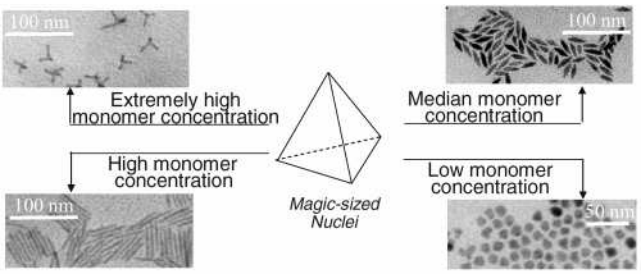

Figure 29. Illustration of the growth conditions for different nanocrystal shapes. Reprinted with permission from ref 253. Copyright 2003 Wiley.

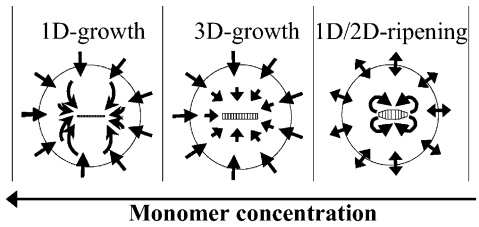

Figure 30. Illustration of the three growth stages of elongated CdSe nanocrystals at different monomer concentrations. Reprinted with permission from ref 253. Copyright 2003 Wiley.

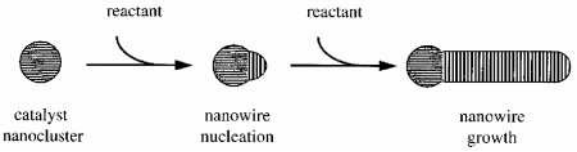

Figure 31. Schematic diagram illustrating the catalytic synthesis of nanowires. Reactant material, which is preferentially absorbed on the catalyst cluster, is added to the growing nanowire at the catalyst−nanowire interface. Reprinted with permission from ref 257. Copyright 1999 American Chemical Society.

required for a given shape, and the nanocrystals should eventually evolve to the most stable dot shape if no additional monomers are added to the reaction system. Figure 30 illustrates the three stages for the shape evolution of a rod-shaped nanocrystal as the monomer concentration decreases. The third stage is one-dimensional-to-two-dimensional intraparticle ripening. During this stage, there is no net monomer exchange between the nanocrystals and the solution, and the number of nanocrystals remains constant. Due to the differences in chemical potential between different facets of the nanocrystals, the monomers on the nanocrystals move in an intraparticle manner to convert the rod-shaped nanocrystals to the dot-shaped ones.[253]

2.3.2. Vapor–Liquid–Solid Growth for Nanowire by CVD and PVD Methods

Figure 31 illustrates the growth process of nanowires in many CVD and PVD processes, where catalysts are usually employed.[257] The growth of nanowires follows the vapor−liquid−solid growth mechanism, in which the vapor phase condenses on the catalyst and forms a co-alloy in liquid phase, and target solid wire grows after nucleation from this liquid phase resulting from the continuing condensation of the vapor phase. Usually, the catalyst defines

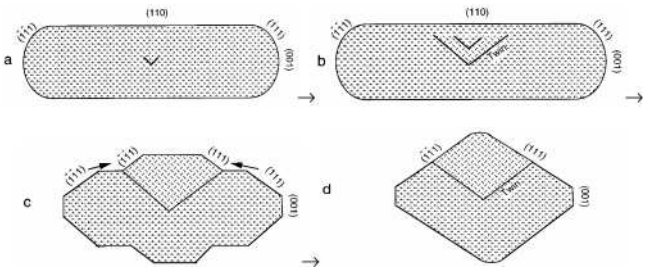

Figure 32. Illustration of the structural transformation process from nanorod to gold nanodot. Reprinted with permission from ref 258. Copyright 2000 American Chemical Society.

the diameter of the structure and localizes the reactant at the end of the growing nanowire. The liquid catalyst alloy cluster serves as a preferential site for absorption of reactant (i.e., there is a much higher sticking probability on liquid vs solid surfaces) and, when supersaturated, acts as the nucleation site for crystallization. Preferential one-dimensional growth occurs in the presence of the reactant as long as the catalyst remains as a liquid. The specific composition (catalyst, nanowire material) to form a liquid alloy with the nanowire material of interest and the synthesis temperature are key components to the growth of well-controlled nanowires.

2.3.3. Light-Induced Shape Change Mechanism of Metal Nanorods

We previously reported that Au nanorods could melt into Au nanodots with femtosecond laser pulses.[255,258−260] Figure 32 illustrates a proposed mechanism of the rod-to-sphere shape transformation process. The sides of defect-free single crystal Au nanorods are enclosed by {110} and {100} facets, and its growth direction is [001] (Figure 32a), with the small {111} facets present at the corners. While being illuminated by pulsed laser light, point defects are first created in the body of the nanorods (Figure 32b), which serve as the nuclei for the formation of twins and stacking faults (Figure 32c). The melting first takes place at the defect sites in order to form a twinned crystal. Surface diffusion takes place simultaneously to enhance the growth of the twinned crystal, which is driven by reduction of the surface energy through the decrease of the {110} surface area and the increase of the {111} surface (Figure 32d). A continuation of the growth of the twinned crystal finally eliminates the unstable {110} surface and induces the more stable {111} and/or {100} faces, which cover the whole nanoparticle and transform the Au nanorods into spherical nanoparticles.[258]

In other studies, the growth of bigger nanodisks from small nanoparticles induced by light has also been reported, such as for silver nanoparticles. In this process, the proposed mechanisms include the initial melting of small silver nanoparticles and the subsequent disintegration into smaller particles. This step is then followed by nucleation and growth,[261] and the bigger silver nanoparticles can be grown from the coalescence of the aggregate of several small nanoparticles.[112]

3. Surface Chemical Modification of Nanoparticles

The surface plays an important role in the properties of nanoparticles, including the solubility, reactivity, stability, melting point, and electronic structure.[262] At the same time, the surface is the connection of the nanoparticles to other materials and objects nd plays a vital role in the construction of superlattices in the fabrication of new devices and in the conjugation with target molecules for drug delivery applications. Thus, the chemical modification of the surface of nanoparticles is a very important field.

During growth of the nanoparticles, stabilizing agents are present to prevent nanoparticle aggregation and precipitation. Various organic and inorganic materials have been utilized as capping materials on the surface of nanoparticles through covalent or ionic interactions.[2,263] These capping groups can stabilize nanocrystals in solution and passivate surface electronic states in semiconductor QDs. For example, many nanoparticles are capped with inorganic materials to improve the photoluminescence quantum yield.[47,49,264] Besides modifying the properties of the bare nanoparticles, they also play a role as the connecting media of the nanoparticles to the outside world. For example, in the superlattices of nanoparticles, they define the space distances between nanoparticles.[2,265] On the other hand, in nanoparticle-based drug delivery, they connect the nanoparticles to the therapeutic agents.[266]

The techniques for tuning the surface capping materials of nanoparticles allow more methods to tailor the properties of these materials. For organic capping, the tail and head groups can be varied independently through well-established chemical substitutions by ligand exchange. This involves repeated exposure of the nanocrystals to an excess competing capping group, followed by precipitation to isolate the partially exchanged nanocrystals.[2,5,267]

4. Assembly of Nanoparticles

The assembly of synthetic colloidal nanoparticles to construct interesting materials for their potential applications has been the subject of great interest recently.[2,265,268,269] Nanoparticle superlattices can be obtained by slowly evaporating the solvent that the monodisperse nanoparticles are dissolved in.[2,265,268,269] The spacing between nanoparticles in the solids can be tuned with the modification of the capping materials.[2,265]

Glassy solids, with only short-range order and random nanocrystal orientation, can be prepared by tailoring the solvent composition to maintain stability of the nanoparticle dispersion during solvent evaporation.[2,270−273] When the interaction between the nanocrystals is weak and repulsive, there is no significant energy driving the formation of an ordered lattice. However, as the concentration increases with solvent evaporation, the viscosity of the dispersion increases until it freezes the local liquid-like structure in the solid.[274,275] Very rapid destabilization forms low-density fractal aggregates as particles quickly add and stick to one another.[276] When introduced to a nonsolvent, nanoparticle dispersions become un-

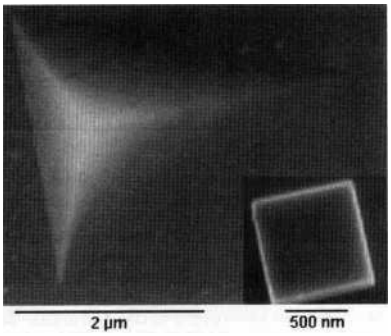

Figure 33. Colloidal crystals grown with 48 CdSe nanocrystals show a characteristic pyramidal shape of $(111)_{SL}$ facets. The inset shows a $(100)_{SL}$ oriented colloidal crystal. Reprinted with permission from *Annual Review of Materials Science* (http://www.AnnualReviews.org), ref 2. Copyright 2000 Annual Reviews.

stable, and the nanoparticles aggregate and precipitate from solution. The structure of the aggregates depends on the rate of destabilization and the sticking coefficient between the particles. At slower rates of destabilization, the particles form close-packed but amorphous aggregates. The formation of nanocrystal glasses is reversible at any step by gradual addition of fresh solvent. These solids have liquid-like radial distribution functions, resembling the random packing of hard spheres with soft shells.[2,265]

Tailoring the composition of the dispersing medium to provide a slow destabilization of the nanocrystal dispersion as the solvent evaporates allows the production of three-dimensional nanocrystal superlattices with long-range order over hundreds of micrometers. For example, semiconductor nanocrystals with organic stabilizers having long-chain alkyl tail groups can be induced to order by evaporating the nanocrystal dispersion composed of a low-boiling alkane and a high-boiling alcohol. As the dispersion is concentrated, the relative concentration of the alcohol rises, which slowly reduces the steric barrier to aggregation and causes slow separation of the nanocrystals from the dispersed state. On the other hand, dipolar coupling between polarizable metal nanocrystals provides an attractive interaction that allows metal nanocrystal superlattices to assemble from single-component solvents.[277−279] If the rate of the transition is carefully controlled, the sticking coefficient between the nanocrystals remains low and the arrival time is such that the nanocrystals have sufficient time to find equilibrium superlattice sites on the growing structure.[276] For example, slowly destabilizing the dispersion by evaporating it from a mixture of solvents and nonsolvents will result in ordered superlattices that are also known as colloidal crystals, which homogeneously nucleate in solution. Mild destabilization provides a weakly attractive potential and sufficient time for colloidal particles or nanocrystals to find equilibrium superlattice sites.

Ordered NC superlattices have been prepared from semiconductor nanocrystals such as CdSe,[2,265] AgS,[93] TiO_2,[280] Au,[278,281] Ag,[277,282] Co,[27,29,71,283] Ni,[29] Fe,[29,284] Fe_2O_3,[268,269] CoO,[285] $BaCrO_4$,[286] and FePt.[35,36,287,288] Assembly of nanoparticles into wires and rings has also been reported recently.[37,289]

Figure 33 shows a colloid crystal grown with 48 CdSe nanocrystals with a characteristic pyramidal shape of $(111)_{SL}$ facets, and the inset shows a $(100)_{SL}$ oriented colloidal crystal by the method mentioned above;[2,265] $(111)_{SL}$ indicates the (111) face of the superlattice composed of CdSe nanoparticles, and $(100)_{SL}$ indicates the (100) face of the superlattice.

Figure 34a shows TEM images of a $(100)_{SL}$ projection through a three-dimensional superlattice of 48 Å CdSe nanocrystals. At high magnification, the internal lattice structure of the nanocrystal building blocks is resolved as shown in Figure 34b. Small-angle electron diffraction pattern demonstrates the lateral perfection of the superlattice domain (Figure 34c). Very similar results were obtained along the (101) projection and the (111) projection for other superlattices[2,265]

Recently, binary superlattice structured solids composed of PbSe/γ-Fe_2O_3 nanoparticles have been successfully prepared.[288] The 6 nm PbSe nanoparticles were prepared using the method mentioned under section 2.2.1. The 11 nm γ-Fe_2O_3 nanocrystals were synthesized with a similar method [decomposition of iron pentacarbonyl in trioctylamine (boiling point = 365 °C) with oleic acid as surfactant, and a subsequent oxidation with trimethylamine *N*-oxide following a general one-pot synthesis]. Various size ratios between PbSe and γ-Fe_2O_3 particles were

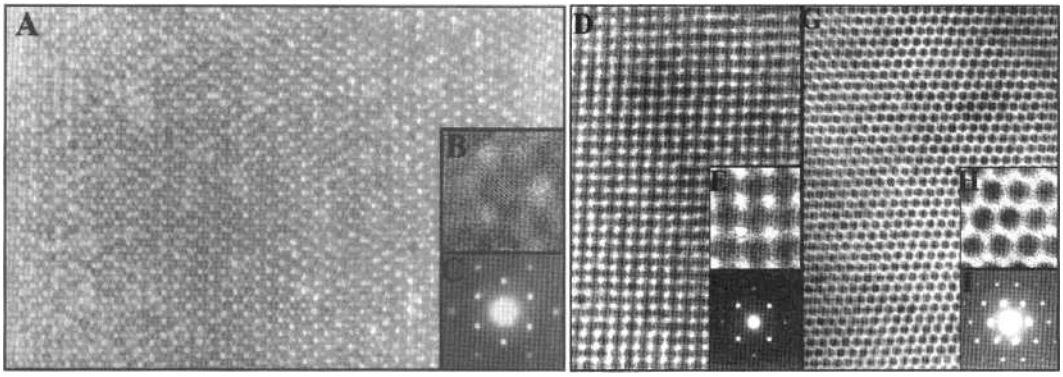

Figure 34. TEM images (A), at high magnification (B), and small-angle electron diffraction pattern (C) of a $(100)_{SL}$ projection through a three-dimensional superlattice of 48 CdSe NCs. TEM image (D), at high magnification (E), and small-angle electron diffraction (F) of a (101) projection for a superlattice of 48 NCs. TEM image (G), high magnification image (H), and small-angle electron diffraction pattern (I) of a (111) projection of a superlattice of 64 CdSe NCs. Reprinted with permission from *Annual Review of Materials Science* (http://www.AnnualReviews.org), ref 2. Copyright 2000 Annual Reviews.

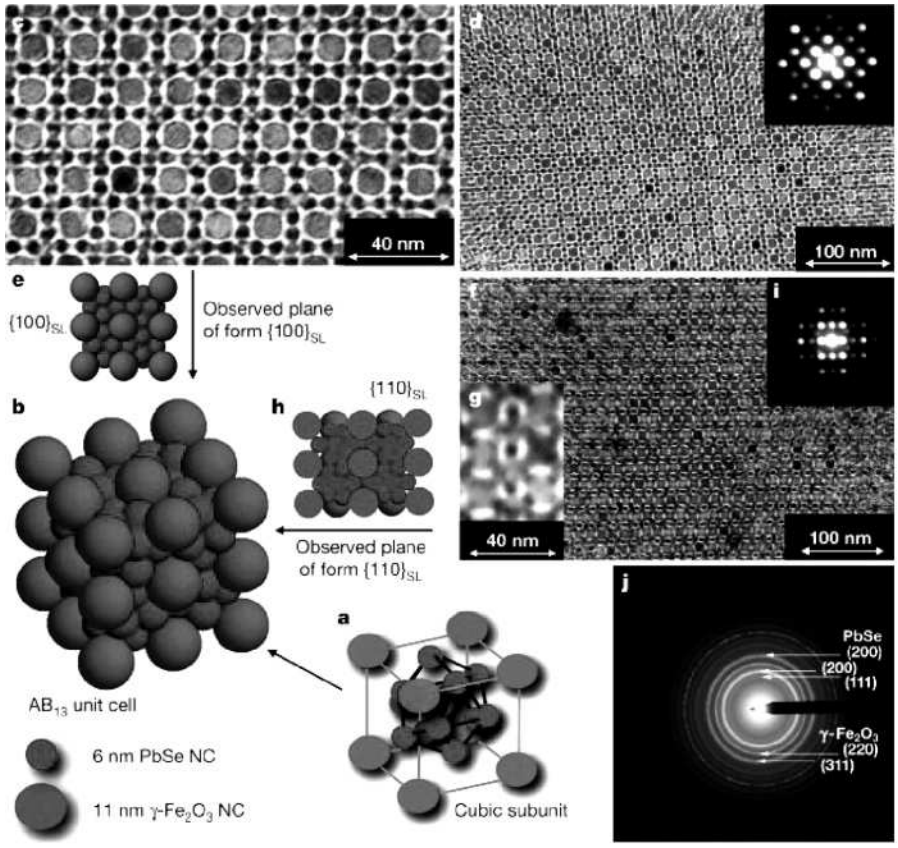

Figure 35. TEM micrographs and sketches of AB_{13} superlattices of 11-nm γ-Fe_2O_3 and 6-nm PbSe NCs: (a) cubic subunit of the AB_{13} unit cell; (b) AB_{13} unit cell built up of eight cubic subunits; (c) projection of a $\{100\}_{SL}$ plane at high magnification; (d) same as (c) but at low magnification [(inset) small-angle electron diffraction pattern from a corresponding 6-μm^2 area]; (e) depiction of a $\{100\}$ plane; (f) projection of a $\{110\}_{SL}$ plane; (g) same as (f) but at high magnification; (h) depiction of the projection of the $\{110\}$ plane; (i) small-angle electron diffraction pattern from a 6-μm^2 $\{110\}_{SL}$ area; (j) wide-angle electron diffraction pattern of an AB_{13}-superlattice (SAED of a 6-μm^2 area) with indexing of the main diffraction rings for PbSe and γ-Fe_2O_3. Reprinted with permission from *Nature* (http://www.nature.com), ref 288. Copyright 2003 Nature Publishing Group.

obtained (0.4−0.7), whereas the relative concentrations were adjusted around the optimal composition of the target structure (for example, 1:13 for AB_{13}). Hexane, octane, and dibutyl ether were tested as solvents in the drying process, and the temperature of evaporation was increased from room temperature to 60 °C. The deposition rate is adjusted by controlling the solvent vapor pressure above samples during drying. By systematic variation of nanocrystal sizes, concentrations, and deposition rates to optimize assembly conditions, three-dimensional assembly assigned to crystal structures known from the intermetallic compounds $NaZn_{13}$, AlB_2, and $CaCu_5$ has been successfully constructed.[288]

A unit cell of the AB_{13} superlattice is composed of eight cubes by twisting adjacent icosahedrons by 90° as shown in Figure 35b. The larger γ-Fe_2O_3 nanoparticles form a cubic framework, with an icosahedron of smaller PbSe nanoparticles in the middle and the 13th PbSe nanoparticle in the center of the icosahedron (Figure 35a). One of the $\{100\}_{SL}$ planes of a superlattice with each γ-Fe_2O_3 nanoparticle spaced with eight small PbSe nanoparticles (Figure 35c,d) forms a square array (Figure 35e). A $\{110\}$ plane of the AB_{13} superlattice (Figure 35f−h) consists of γ-Fe_2O_3 nanoparticles forming rectangles with a ring of PbSe nanoparticles in the middle surrounding an additional γ-Fe_2O_3 nanoparticle (the icosahedron is cut through the middle). The average cubic unit cell has an edge length of ~36 nm, consisting of 8 γ-Fe_2O_3 and 104 PbSe nanocrystals, $\sim 4.5 \times 10^6$ atoms in total.[288]

The hexagonal unit cell of the AB_2 superlattice consists of parallel layers of hexagonally ordered γ-Fe_2O_3 nanoparticles with PbSe nanoparticles in every trigonal prismatic interstice (Figure 36a,b). In the $(001)_{SL}$ plane of the AB_2 structure, the particles appear to touch each other in the two-dimensional projection, but in fact the PbSe nanoparticles form a second layer above the hexagonal layer of iron oxide nanocrystals, and each one of the PbSe nanocrystals is occupying the gap between three touching γ-Fe_2O_3 nanoparticles (Figure 36c,d). The $\{111\}_{SL}$ planes are composed of parallel rows of γ-Fe_2O_3 nanoparticles forming an array of parallelograms or alternative distorted hexagonal packing, which was confirmed in the selected-area electron diffraction (SAED) pattern (Figure 36g−j). The $\{112\}$ planes project an image with wavelike alternating layers of large and small particles (Figure 36k,l). The lattice constants are 12−13 nm for a and 15 nm for c, respectively, and the elongation in the c direction is caused by the intermediate layer of small PbSe particles.

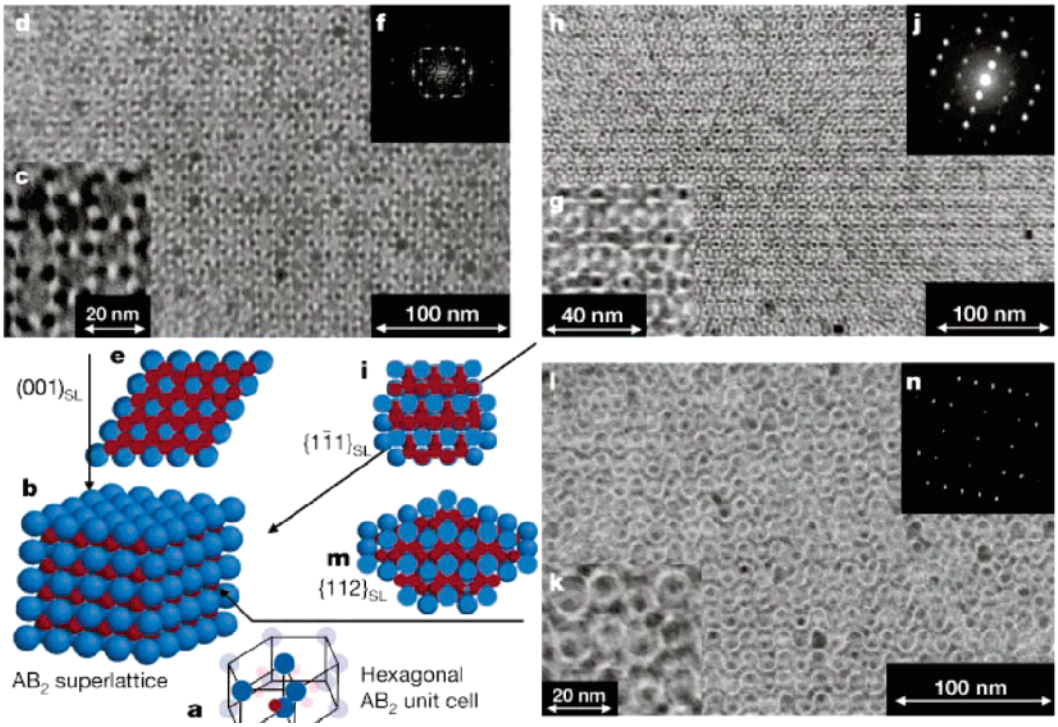

Figure 36. TEM micrographs and sketches of AB_2 superlattices (isostructural with intermetallic phase AlB_2) of 11-nm γ-Fe_2O_3 and 6-nm PbSe NCs: (a) hexagonal unit cell of the AB_2 lattice; (b) AB_2 superlattice built up of alternating layers of large and small particles; (c) projection of the $(001)_{SL}$ plane; (d) same as (c) but at lower magnification; (e) depiction of the (001) plane; (f) FFT of (d); (g) projection of a $\{111\}_{SL}$ plane; (h) same as (g) but at lower magnification; (i) depiction of the projection of a $\{1\bar{1}1\}_{SL}$ plane; (j) small-angle electron diffraction pattern from a 6-μm^2 $\{112\}_{SL}$ area; (k) projection of the $\{112\}_{SL}$ plane; (l) same as (k) but at lower magnification; (m) depiction of the projection of a $\{112\}_{SL}$ plane; (n) FFT of (l). Reprinted with permission from *Nature* (http://www.nature.com), ref 288. Copyright 2003 Nature Publishing Group.

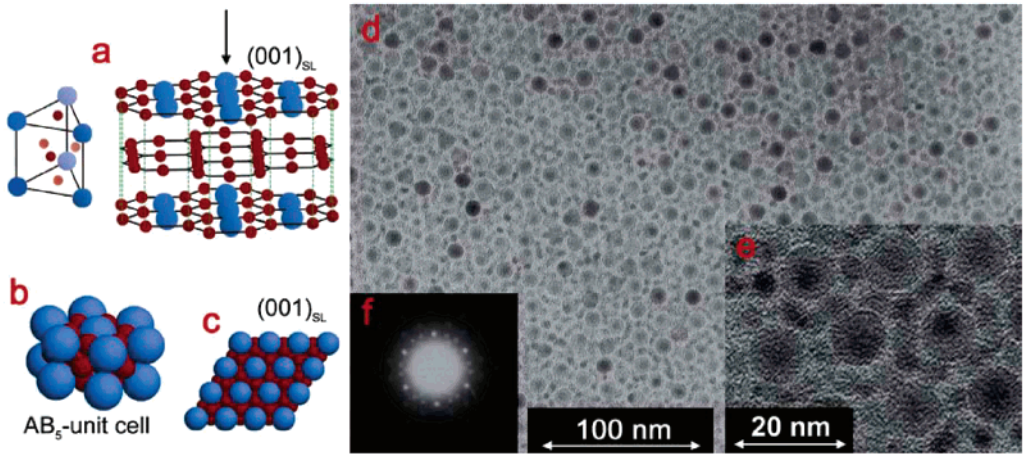

Figure 37. TEM micrographs and sketches of AB_5 superlattices of 11-nm γ-Fe_2O_3 and 6.3-nm PbSe NCs: (a) depiction of the AB_5 structure as trigonal face-centered prism or layers; (b) hexagonal AB_5 unit cell; (c) depiction of the (001) plane; (d) projection of the $(001)_{SL}$ plane; (e) projection of the $(001)_{SL}$ plane at high magnification; (f) small-angle electron diffraction pattern from a 6 μm^2 (001) SL area. Reprinted with permission from *Nature* (http://www.nature.com), ref 288. Copyright 2003 Nature Publishing Group.

Figure 37a−e shows the unit cell, the (001) plane, and the structure of the AB_5 superlattice, based on 11 nm γ-Fe_2O_3 nanoparticles and 6.3-nm PbSe nanoparticles. The average unit cell length a_{SL} is 17 nm. γ-Fe_2O_3 nanoparticles in a hexagonal array are separated by PbSe nanoparticles occupying the trigonal interstices. Parallel layers of this arrangement are separated by a hexagonal net of PbSe nanoparticles.[288]

The size and shape distributions and the thickness and the type of organic capping materials influence the assembly of the nanoparticles. In the assembly of spherical nanoparticles, the nanoparticles with the surfactants on the surface can be treated as hard spheres, and the arrangement of the nanoparticles obeys the traditional prediction in a crystal model, where the structures of the crystals are quite predictable on the basis of the ratio of the sizes of different

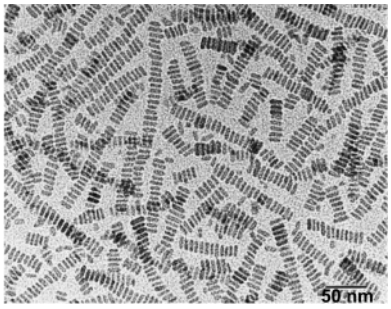

Figure 38. TEM image showing ordered chains of $BaCrO_4$ nanorods. Reprinted with permission from *Nature* (http://www.nature.com), ref 293. Copyright 1999 Nature Publishing Group.

units, such as the sizes of nanoparticles, for example, R_A/R_B in the assembly of nanoalloys of two different sizes of nanoparticles.[290,291]

Unlike the isotropic hexagonal arrangement of spherical or near spherical nanoparticles during the assembly, the assembly of anisotropic nanostructures, including nanotubes and nanowires, requires more effort and remains a good challenge. Fortunately, recent progress demonstrated the good manipulation on the assembly of these more complex structures, including nanorods and nanowires. The alignment of nanowires made of silver nanoparticles was demonstrated using a Langmuir trough by Heath and co-workers,[292] without elucidating the mechanism behind. Ordered chains of $BaCrO_4$ nanorods as shown in Figure 38 were observed by Mann and co-workers,[293] and the assembly of these structures was attributed to the interactions between the surfactants on the surface of the adjacent nanorods. Nikoobakht and co-worker suggested that in the assembly of nanorods, the interacting forces determining the parallel alignment between nanorods include higher lateral capillary forces along the length of the nanorod than its width, and van der Waals attraction and a screened Coulomb repulsion between nanorods.[294] This explanation is adopted by other researchers.[295,296]

Yang and co-workers adopted the technique of Langmuir−Blodgett assembly of monolayers to assemble and align $BaCrO_4$ and $BaWO_4$ nanorods.[295−297] They not only demonstrated the ordered side-by-side alignment of these nanorods but also found singularity structures in the assembly of multilayered nanorod structures,[295,296] which was also found by Alivisatos and co-worker in the assembly of CdSe nanorods.[298] Besides the directional capillary force and van der Waals attraction as mentioned above, the consideration that the maximization of the entropy of the self-assembled structures by minimizing the excluded volume per particle in the array by Onsager was also taken into account in their explanation.[295,296] They also illustrated the pressure-induced phase transition when the nanorods are compressed at the water−air interface, which could help the assembly of other nanorod materials using this technique. Figure 39 shows two singularity structures within the multiplayer nanorods (Figure 39a,b) and one ordered monolayer with nematic configuration (Figure 39c).[295]

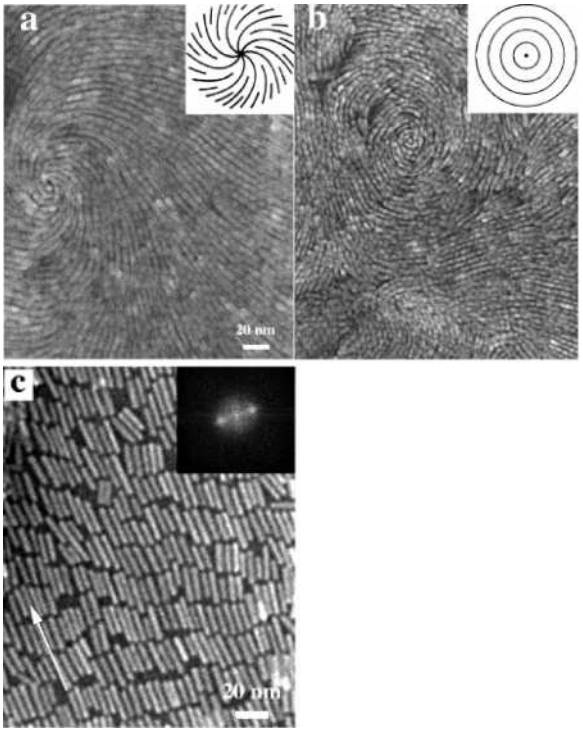

Figure 39. TEM images for two singularity structures within the multiplayer nanorods (a, b) and one ordered monolayer with nematic configuration (c). Insets in (a) and (b) show the nanorod director orientation in the vicinity of the singularity structures, and the inset in (c) shows the Fourier transform of the image. Reprinted with permission from ref 295. Copyright 2001 American Chemical Society.

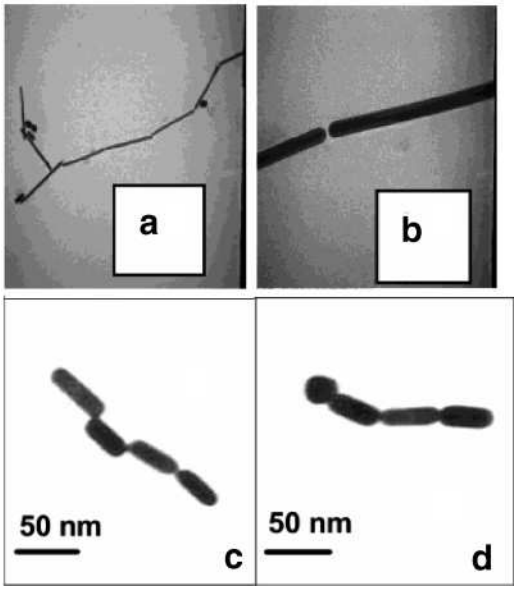

Figure 40. TEM images of the end-to-end aligned Au nanorods (a); (b) see ref 301; (c, d) see ref 302. Parts b−d were reprinted with permission from refs 301 and 302. Copyright 2003 and 2004 American Chemical Society.

The assembly of nanorods is also demonstrated by other researchers.[299−302] Besides the above side-by-side alignment of nanorods, recent achievements on the end-to-end alignment of gold nanorods are also worthy of the special emphasis by choosing appropriate linking molecules between nanorods,[301,302] which could expand the manipulation of nanoscale materials. Figure 40 shows the TEM images of the end-to-

end aligned Au nanorods using this method,[301,302] and readers are strongly urged to study their original contributions. The different reactivities of the different faces' ending surfaces of the sides and ends of these nanorods allow the selective binding with the linkage, which finally connects the nanorods in a linear way.[301,302]

The assembly of nanowires has also been demonstrated, for example, by Lieber's group [303,304] and by Yang's group [305] recently. This is not addressed here, because it could be addressed in Lieber's review in this issue.

5. Optical, Thermal, and Electrical Properties of Particles of Different Sizes and Shapes

5.1. Semiconductor Nanoparticles

5.1.1. Discrete Electronic Structure

Quantum confinement is a widely used terminology in the study of nanocrystals. In a bulk crystal, the properties of the material are independent of the size and are only chemical composition-dependent. As the size of a crystal decreases to the nanometer regime, the size of the particle begins to modify the properties of the crystal. The electronic structure is altered from the continuous electronic bands to discrete or quantized electronic levels. As a result, the continuous optical transitions between the electronic bands become discrete and the properties of the nanomaterial become size-dependent.[262,306−308] Furthermore, depending on the relationship of the radius of the crystal to the Bohr radius of the bulk exciton, $a_B = \epsilon\hbar^2/\mu e^2$, where μ is the exciton-reduced mass and ϵ is the dielectric constant of the semiconductor,[309,310] the quantum confinement effect can be divided into three regimes: weak confinement, intermediate confinement, and strong confinement regimes, which correspond to $a \gg a_B$, $a \sim a_B$, and $a \ll a_B$, respectively.[308−311]

For small semiconductor nanocrystals, both linear and nonlinear optical properties arise as a result of transitions between electron and hole quantum-size levels. In a spherical nanocrystal surrounded by an infinite potential barrier, the energy of the electron and hole quantum-size levels can be written in parabolic approximation as[5,309,311,312]

$$E_{l,n}^{e,h} = \frac{\hbar^2 \phi_{l,n}{}^2}{2m_{e,h}a^2} \quad (11)$$

where l is the angular momentum quantum number, $m_{e,h}$ is the electron and hole effective mass, respectively, a is the crystal radius, and $\phi_{l,n}$ is the nth root of the spherical Bessel function. Thus, with decreasing nanocrystal size, the energy of the lowest electron and hole quantum-size levels increase as well as the total energy of optical transitions between these levels. In addition, between the optically created electron and hole, there exists the Coulomb interaction, which strongly affects the nanocrystal's optical spectra. The Coulomb energy of the electron and hole interaction is on the order of $e^2/\epsilon a$. Because the quantization energy increases with decreasing size by $1/a^2$, whereas the Coulomb energy grows only as $1/a$, the Coulomb energy varies in a less pronounced manner than the quantization energy as the size of the nanocrystal changes. Specifically, in small nanocrystals, the Coulomb energy becomes a small correction to the quantization energies of electrons and holes. In large nanocrystals, the Coulomb interaction is more important than the quantization energies of the electrons and holes.

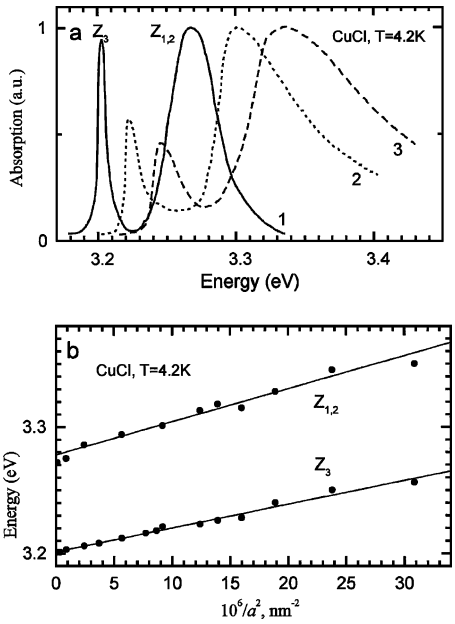

Figure 41. (a) Absorption spectra of 310 (1), 29 (2), and 20 (3) CuCl nanocrystals in radius. (b) Size dependence of the exciton line peak position as a function of $1/a_2$; solid lines are theory. Reprinted with permission from *Annual Review of Materials Science* (http://www.AnnualReviews.org), ref 311. Copyright 2000 Annual Reviews.

Weak Confinement Regime. When $a \gg a_B$, the binding energy of an exciton, E_{ex}, is larger than the quantization energy of both the electrons and holes, and it is called the weak confinement regime. The optical spectra of these nanocrystals are determined by the quantum confinement of the exciton center of mass, and the exciton energy is given by

$$\hbar\omega = E_g - E_{ex} + \frac{\hbar^2 \phi_{l,n}}{2Ma^2} \quad (12)$$

where E_g is the semiconductor energy gap and $M = m_e + m_h$ is the exciton translation mass.[309] CuCl nanocrystals are a very good system to study the weak confinement effect because $a_B = 7$ and the condition $a \gg a_B$ can be easily met.[313−316] The evolution of the absorption spectrum of CuCl nanocrystal with size is described very well by eq 12 (Figure 41), where these spectra exhibit two exciton lines connected with two hole subbands.[310,315]

Intermediate Confinement Regime. The intermediate confinement regime corresponds to $a_e > a > a_h$, in which $a_e = \epsilon\hbar^2/m_e e^2$ and $a_h = \epsilon\hbar^2/m_h e^2$ are the Bohr radii of the electrons and holes, respectively, assuming that the electron and hole have different values of effective masses. In this case, the electron moves much more quickly than the hole, which is

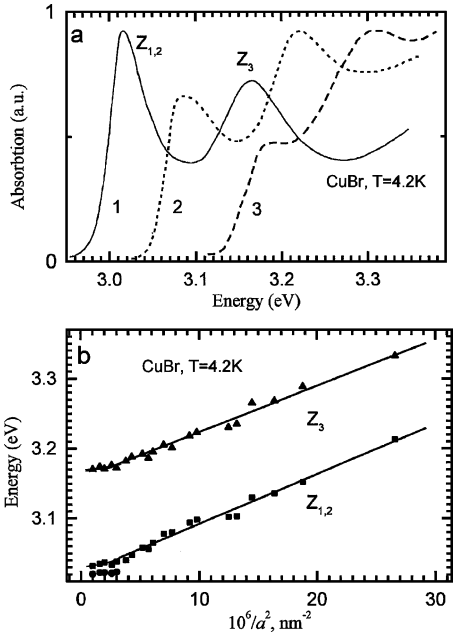

Figure 42. (a) Absorption spectra of 240 (1), 36 (2), and 23 (3) CuBr nanocrystals in radius. (b) Size dependence of the exciton line peak position as a function of $1/a^2$; solid lines are theoretical results for a donor-like exciton. Reprinted with permission from *Annual Review of Materials Science* (http://www.AnnualReviews.org), ref 311. Copyright 2000 Annual Reviews.

confined in the average potential of the much faster electron and is localized at the center of the nanocrystal. The hole moving area around the crystal center is much smaller than the nanocrystal radius, and the size dependence of the exciton can be described as the behavior of a donor localized at the nanocrystal center. The excitation spectrum of such a donor-like exciton can be described as oscillation of the hole about the crystal center and has been observed in the absorption spectra of moderately sized CdS and CuBr nanocrystals.[317−319] Figure 42 shows the size dependence of two exciton lines in CuBr nanocrystals, where the bulk electron Bohr radius is 18.

Strong Confinement Regime. Strong confinement corresponds to $a \ll a_B$ in small nanocrystals, where the electron−hole Coulomb interaction lowers the energy of these transitions only slightly. The optical spectra can be considered as spectra of transitions between electron and hole quantized electronic levels. Transitions are allowed only between levels with the same quantum numbers in the interband transitions between quantum-size levels of conduction and valence bands. The transition energy can be expressed as

$$\hbar\omega_\nu = E_g + E_\nu^h(a) + E_\nu^e(a) - 1.8\frac{e^2}{\kappa a} \qquad (13)$$

where the Coulomb correction is calculated by first-order perturbation theory.[312] Figure 43 shows the absorption spectra and their size dependence in CdS nanocrystals.[320]

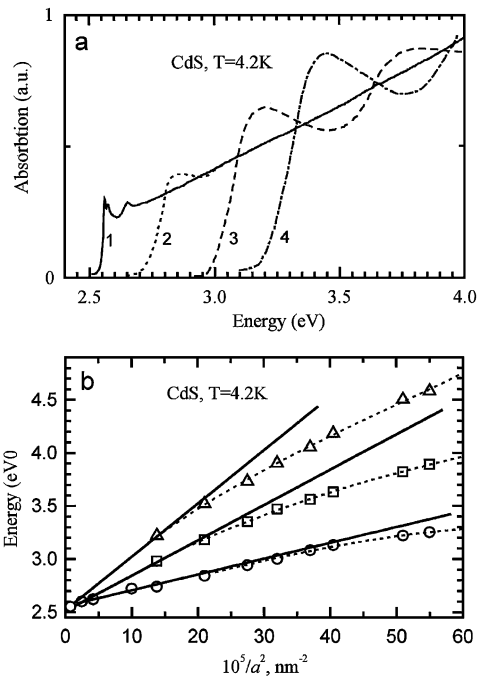

Figure 43. (a) Absorption spectra of 330 (1), 33 (2), 15 (3), and 12 (4) CdS nanocrystals in radius. (b) Size dependence of the exciton line peak position as a function of $1/a^2$. Solid lines are results of parabolic band approximation theory. Reprinted with permission from *Annual Review of Materials Science* (http://www.AnnualReviews.org), ref 311. Copyright 2000 Annual Reviews.

5.1.2. Optical Transitions in Nanostructures of Different Shapes

5.1.2.1. Optical Transitions in Semiconductor Nanocrystals. The most striking property of semiconductor nanocrystals is the massive changes in electronic structure as a function of size. As the size decreases, the electronic excitations shift to higher energy, and the oscillator strength is concentrated into just a few transitions.[5,262] The optical properties of semiconductor nanoparticles have been studied extensively with different optical techniques and theoretical considerations.[2,5,262,321−324] In the following, the optical properties of semiconductor nanoparticles are summarized on the basis of the research on the model semiconductor CdSe nanoparticle system.

5.1.2.1.1. Optical Transition from Intrinsic States. *A. Theoretical Consideration of Optical Transitions in Semiconductor Nanoparticles. Exciton Structure.* CdSe nanocrystal is a model semiconductor system and has been extensively studied over the past years.[2,5,262,321−324] The bulk material adopts two distinct crystalline phases, which consist of the wurtzite and cubic zinc blende structures. Shown in Figure 44 is an illustration of the electron energy level scheme for a CdSe semiconductor that has a cubic zinc blende structure.[324,325] When the size of the nanocrystal is smaller than the Bohr radius of the exciton of the corresponding bulk material, the band energy evolves into discrete energy levels, and the optical transitions near the band edge involve only the s conduction band level for electrons and the top three p levels in the valence band levels for holes. The optical transitions can be regarded as the energy

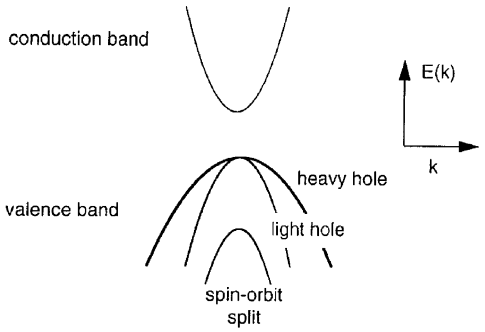

Figure 44. Illustration of the band structure for cubic zinc blende CdSe nanoparticles near Γ (**k** = 0). Reprinted with permission from ref 324. Copyright Taylor and Francis.

levels for electrons plus holes, and the relevant nomenclature for the semiconductor QDs can be derived from the atomic quantum numbers n (principal), l (angular momentum), m, and ms, to obtain their $J(L + S)$ values, where L represents the total angular momentum and S the multiplicity term. For example, in CdSe QDs, $1S_{3/2} - 1Se$, $2S_{3/2} - 1Se$, $1S_{1/2} - 1Se$, and $1P_{3/2} - 1Pe$ are the commonly observed transitions.[324−326] When the spin−orbit coupling needs to be included in the energy level scheme, then the higher atomic number elements comprising the anions play an important role. Then, for the cadmium chalcogenides, the order for the spin−orbit splitting for the valence energy levels is Te > Se > S > O.

When the radius of the QD $R < a_B$, both the energy spectrum and the wave functions for the electron (e) and hole (h) in the e−h pair can be approximated by using an independent quantization approach to the e and h motion, which is a multiband effective mass approximation. The effective mass approximation requires an external potential that is smooth, and $2R \gg a_0$, where a_0 is the lattice constant. The effective mass approximation also requires that the e and h energies lie close to the bottom of the conduction band and the top of the valence band, respectively, and the next energy levels for both the conduction band and the valence band to the ones already involved must be further away than the quantization energy, which is the case when $R \ll a_B$. For a spherically symmetric QD with a cubic structure, the first level for the e is a doubly degenerate (spin included) $1S_e$ state, but the first level for the h is a $1S_{3/2}$ state.[311,324,327]

The energies for the electrons can be derived from the using the parabolic approximation:

$$E_{1s} = \frac{\hbar^2 \pi^2}{2m_e^* R^2} \tag{14}$$

On the other hand, information for the holes can be approximated as follows:

for the 4-fold degenerate valence band (Γ_8)

$$E_{3/2}(\beta) = \frac{\hbar^2 \varphi^2(\beta)}{2m_{hh}^* R^2} \tag{15}$$

with $\beta = m_{lh}^*/m_{hh}^*$, the ratio of the light to heavy hole effective masses, whereas $\varphi(\beta)$ involves solutions using Bessel functions.[311,324,327]

For the ideal case of a spherical QD with a triply degenerate valence band derived from p states and an s-like conduction band, the exciton (e−h) pair ground state is 8-fold degenerate (spin included) with the label of $1S_{3/2}1Se$. When the internal crystal structure shape anisotropy and e−h exchange energy are considered, the hole valence states split into two 2-fold degenerate states with $|M| = {}^1/_2$ and ${}^3/_2$, with the $M = {}^3/_2$ state being the ground state, that is, $1S_{3/2}$. The splitting resulting from the hexagonal character of the lattice structure involves the crystal field splitting ($\Delta_{CF} = 25$ meV for bulk CdSe). In reality, the splitting is modified for the nonspherical shape. For example, in prolate shapes, the ellipticity μ is given by the relationship

$$c/b = 1 + \mu \tag{16}$$

for the ratio of the major to minor axes. The net splitting of the hole states for a QD of radius R, with $R = (b^2c)^{1/3}$, is given by

$$\Delta(R, \beta, \mu) = \Delta_{sh}\Delta_{CF} \tag{17}$$

where Δ_{sh} represents the shape contribution of the splitting. For prolate CdSe nanoparticles with $\mu > 0$ and $\beta = 0.28$, the net splitting can decrease with size. The order of the hole states can also alter, and the $|M| = {}^1/_2$ state becomes the ground-state level if R is sufficiently small.[311,324,327]

The ideal 8-fold degeneracy of the band edge e−h pair or exciton can also be lifted by e−h exchange interaction. For bulk crystals, it is split into a 5-fold degenerate and is in the optically passive state with a total angular momentum of 2 and a 3-fold degenerate and optically active state with a total angular momentum of 1. For hexagonal nanoparticles, the degenerate ground state is split into five levels, labeled according to the total angular momentum projection

$$F = M + s_z \tag{18}$$

giving one level with $F = \pm 2$, two levels with $F = \pm 1$, and two levels with $F = 0$.

The energies for the various levels ($\epsilon_{|F|}$) are estimated by the use of the appropriate exciton wave functions for different values of the ellipticity (μ). Figure 45 shows the dot size dependence of the band edge splitting for the spherical and prolate QDs with ellipticity ($\mu = 0.28$), where the letters U and L refer to upper and lower states, respectively.[311,327] In the above figure, the dashed lines correspond to the optically passive or "dark" exciton levels. Depending on shape, the order of the levels as R is varied can be different. For the spherical QDs, the $F = \pm 2$ state corresponds to the exciton ground state for all dot sizes R and is optically passive, that is, dark. For prolate QDs, the order of the exciton levels can change at a specific R value, such as when R is small, the optically passive or dark $F = 0$ state becomes the ground state for the exciton.[311,324,327]

When levels cross at a specific value for R, the shape asymmetry term can compensate for the asymmetry due to having a hexagonal rather than a cubic lattice. In this case, the exciton levels may

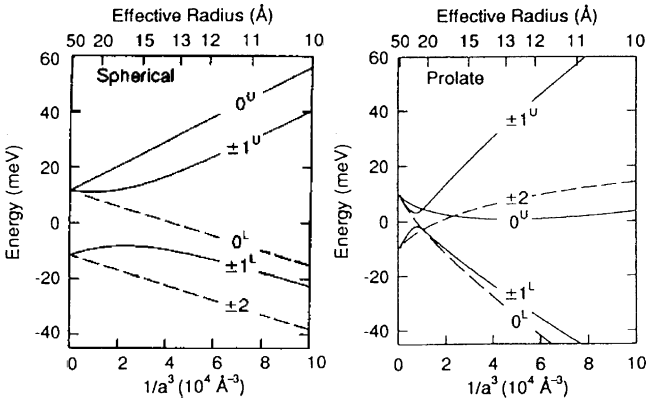

Figure 45. Size dependence of the exciton band edge energy for spherical shape and prolate QDs with ellipticity $\mu = 0.28$. Solid lines are for optically active levels, whereas dashed lines correspond to passive levels. Reprinted with permission from *Annual Review of Materials Science* (http://www.AnnualReviews.org), ref 311. Copyright 2000 Annual Reviews. Also, reprinted with permission from ref 327 (Figure 2a,c). Copyright 1996 American Physical Society.

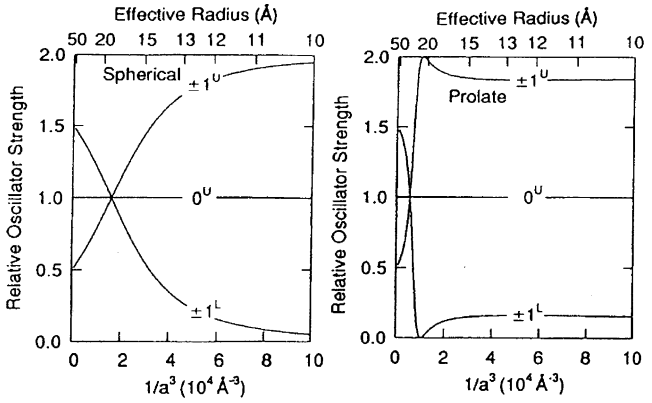

Figure 46. Size dependence of the oscillator strengths relative to the O^U state for spherical and prolate QDs with $\mu = 0.28$. Reprinted with permission from *Annual Review of Materials Science* (http://www.AnnualReviews.org), ref 311. Copyright 2000 Annual Reviews. Also, reprinted with permission from ref 327 (Figure 4a,c). Copyright 1996 American Physical Society.

resemble those for dots having spherical symmetry, and there develops one 5-fold degenerate exciton (e−h) pair level with total a angular momentum of 2, which is reflected by the crossing of the 0^L as well as the $\pm1^L$ levels with the ±2 level. In addition, there is one 3-fold degenerate exciton state that has a total angular momentum of 1, as reflected by the crossing of the 0^U and the $\pm1^U$ levels.[311,324,327]

Selection Rules and Transition Oscillator Strengths. Figure 46 shows the calculated oscillator strengths for both spherical and prolate-shaped QDs as the sizes (R) vary for $\mu = 0.28$.[311,327] The optical transition probabilities change because of the mixing of the e and h spin momentum states due to e−h exchange interaction. However, the wave functions of the $|F| = 2$ exciton state do appear to remain unaltered by this interaction, and it is in fact optically passive (dark) in the dipole approximation, because any emitted or absorbed photon during a transition cannot have an angular momentum projection of ±2, but only ±1. The $\pm1^L$, 0^L, and ±2 exciton states all represent the optically passive (dark) exciton states, whereas the $\pm1^U$ and 0^U remain as the three states that carry nearly all of the oscillator strength.[311,325,327]

B. Quantized Optical Transitions in Experimental Studies. Figure 47 shows an illustration of the optical absorption and emission transitions as well as the vibrational levels in a configurational coordinate diagram. Furthermore, it illustrates the optical absorption of the lowest transition, the photoluminescence emission peak, and the Stokes shift for a QD. After excitation by light, the optical transitions can occur as nonresonant, resonant, and interband transitions, which correspond to the transition energies below, equal to, and above the band gap of the semiconductor, respectively.[325] Because the electronic structures of nanomaterials are quantized, the electronic transitions between these levels are also quantized. To probe the quantized optical transitions in semiconductor nanoparticles, different techniques have been employed, including absorption spectroscopy, photoluminescence excitation spectroscopy, transient differential absorption spectroscopy, and fluorescence line or photoluminescence narrowing spectroscopy.

Absorption Spectra of Semiconductor Nanoparticles. Optical absorption spectroscopy is the most commonly used technique in exploring the quantum effects in semiconductor nanoparticles. By using this method, one can observe the development of discrete features in the spectra and the enlargement of the energy gap in semiconductor QDs.[2,5,262,321,322] However, many times, the discrete states are not readily visible in the absorption spectra due to inhomogeneous broadening, which can be traced to the size, shape, and surface defect distributions in the nanoparticles.

The number of occupied levels in the ground state, the unoccupied levels in the excited state, and the transition probability can also determine the absorption intensity, where the absorption constant is given by

$$K = \frac{\pi e^2}{nm} N(E) f_{ij} \tag{19}$$

where $N(E)$ is the density of state function and f_{ij} is the oscillator strength determining the transition probability.[328] The inhomogeneous distribution of the samples (including the surface defect distributions) can change $N(E)$, which may change the overlaps of the transitions and result in the broadening of the absorption bands.

The discrete optical transitions in the absorption spectra have been observed in many monodisperse nanoparticle systems.[2,7,10] Figure 48 shows the absorption spectra for a series of CdSe nanoparticles of different sizes. In addition, it shows how the first absorption peak changes as the nanoparticle size changes for CdSe, CdS, and CdTe QDs. The absorption spectra show a consistent red shift as the size of the particle increases, and up to 10 discrete optical transitions can be resolved, which corresponds to the transitions between the discrete energy levels of the QDs. A high-quality absorption spectrum for monodisperse QDs can be used to calculate and calibrate the size and size distribution of the synthesized

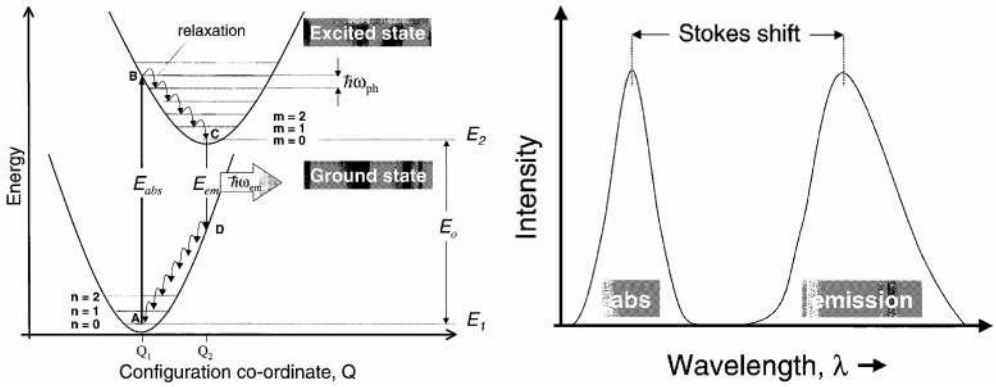

Figure 47. (Left) Illustration of optical absorption and emission transitions as well as the vibrational levels in a configurational coordinate diagram. (Right) Simple illustration of an optical absorption, a PL emission peak, and the Stokes shift for a QD. Reprinted with permission from ref 324. Copyright 2001 Taylor and Francis.

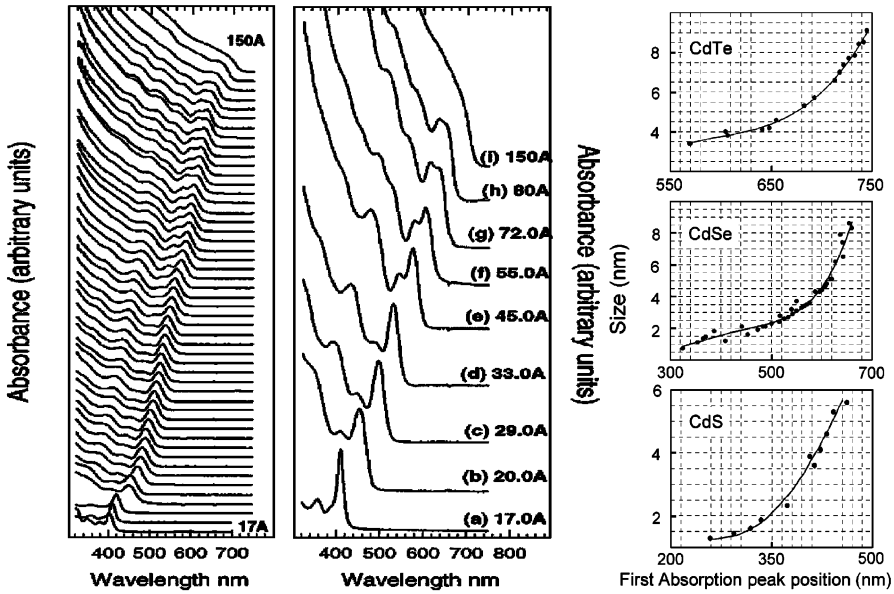

Figure 48. (Left, middle) Observation of discrete electronic transitions in optical absorption for a series of sizes of monodisperse CdSe NCs. Reprinted with permission from Annual Reviews in Materials Science (http://www.AnnualReviews.org), ref 2. Copyright 2000 Annual Reviews. (Right) First absorption peak change versus the size of the nanoparticle. Reprinted with permission from ref 10. Copyright 2003 American Chemical Society.

nanoparticles directly. For example, empirical relationships between the size and the first absorption wavelength can be derived for various types of semiconductor QDs, and the size can be read out after determination of the first absorption wavelength from the absorption spectra.[10]

However, line shape discrete optical absorption has not been observed even in the best samples reported due to the broadening effect. The broadening of the absorption results from intrinsic (homogeneous) and extrinsic (inhomogeneous) broadenings. The former includes dephasing due to the exciton−phonon interaction and carrier−carrier (or exciton−exciton) interactions. Lattice vibrations give rise to stochastic fluctuations of the exciton energy, which in turn manifest themselves in the exciton line broadening. Exciton−phonon coupling in an ideal nanocrystal can be attributed to the interactions with optical phonons and acoustic phonons. All of the above broadenings give rise to a Lorentzian line shape. The inhomogeneous broadening can be attributed to the size, shape dispersions, and scattering of the surface defects. These broadenings lead to a Gaussian line shape.[308] The features of interband optical transitions in the absorption spectra of CdSe nanoparticles couple different electron and hole states, and the spectra can be fitted by sums of Gaussians.[329]

For the series of CdSe QDs, although distinct optical transitions are well resolved within ~1 eV on the high-energy side of the 1S resonance of the absorption spectra,[329] the optical transitions merge into the bulk structureless absorption at higher energies.[329−331] The optical absorption of the nanocrystal samples only determined by the volume fraction (ξ) of the semiconductor material can be expressed as

$$\alpha_0(\hbar\omega \geq 3.5\ \text{eV}) = \xi|\eta(\hbar\omega)|^2\alpha_b(\hbar\omega) = n_0 V_0|\eta(\hbar\omega)|^2\alpha_b(\hbar\omega) \quad (20)$$

where $\alpha_b(\hbar\omega)$ is the bulk material absorption, V_0 is

the volume of a single nanocrystal, and n_0 is the nanocrystal concentration in the sample. Thus, the nanocrystal absorption cross section $\sigma_0 = \alpha_0/n_0$ can be expressed as

$$\sigma_0(\hbar\omega \geq 3.5\text{eV}) = V_0|\eta(\hbar\omega)|^2\alpha_b(\hbar\omega) = \frac{4\pi}{3}R^3|\eta(\hbar\omega)|^2\alpha_b(\bar{\lambda}\omega) \quad (21)$$

suggesting a strong nanocrystal size dependence of σ_0 ($\sigma_0 \propto R^3$). The oscillator strength shows a linear dependence for the 1S transition ($f_{1s} \propto R$) and a quadratic dependence for the 2S transition in the size range from 1 to 4 nm. The absorption cross section for transition with lower energy (1S) exhibits a much weaker size dependence ($\propto R$) at high spectral energies ($\propto R^2$ for 2S and $\propto R^3$ or higher). The size dependence of high-spectral-energy absorption cross sections is significantly affected by size-dependent changes in both the oscillator strength of an individual transition and the spectral density of optical transitions.[329]

For optical transitions that are far from any strong resonance and the band edge, where the QD density of states may be approximated as a continuum, the QD absorption cross section may be modeled from the light scattering of small particles.[334] The extinction cross section is the sum of the absorption (C_a) and scattering cross sections (C_s):

$$C_{ex} = C_{abs} + C_{scat} \quad (22)$$

As light propagates a distance (l) through a medium with a refractive index (ϵ) containing N particles per unit volume, its intensity is reduced by $e^{-C_{ex}Nl}$. Because the radius (a) of nanoparticles is much smaller than the wavelength in the medium (λ/ϵ_m, λ is the wavelength in a vacuum), C_{scat} is much smaller than C_{abs} and can be neglected. The extinction coefficient can then be calculated using Beer's law, $\epsilon_\lambda = A_\lambda/cl$, where A_λ is the absorbance at wavelength (λ), c is the concentration of nanoparticle, and l is the path length (cm) of the sample cell.[10,332]

Shown in Figure 49 is the extinction coefficient per mole of CdTe, CdSe, and CdS nanocrystals.[10] The extinction coefficient per mole of the nanoparticles is size-dependent, and it can be fitted as follows:

for CdTe: $\epsilon = 3450\Delta E(D)^{2.4}$ (solid line) or $\epsilon = 10043(D)^{2.12}$(dotted line)

for CdSe: $\epsilon = 1600\Delta E(D)^{3}$ (solid line) or $\epsilon = 5857(D)^{2.65}$(dotted line)

for CdS: $\epsilon = 5500\Delta E(D)^{2.5}$ (solid line) or $\epsilon = 21526(D)^{2.3}$(dotted line)

ΔE (in eV) is the transition energy of the first absorption peak, and D is the diameter or size of the nanocrystals.[10]

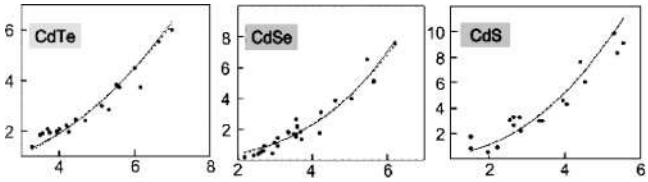

Figure 49. Extinction coefficient $\times 10^5$ cm^{-1} M^{-1} of particles at the first absorption peak position curves for CdTe, CdSe, and CdS nanocrystals as a function of size.[10]

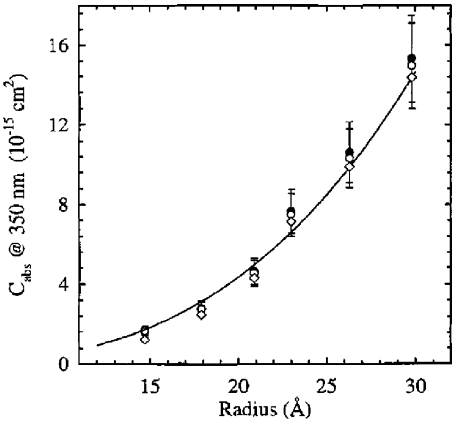

Figure 50. Observed and theoretical absorption cross section as a function of size for CdSe QDs dispersed in hexane. The symbols represent the experimental data. The solid line is the theoretical calculation.[332]

On the other hand, the nanoparticle absorption cross section (cm^2) can be obtained from the relationship

$$C_{abs} = \frac{2303\epsilon_\lambda}{N_A} \quad (23)$$

where N_A is Avogadro's number. Figure 50 shows observed and theoretical absorption cross section as a function of size for CdSe QDs dispersed in hexane, suggesting that the absorption cross section increases as the radius of the nanoparticle increases.[332]

Figure 51 (left side) shows the absorption cross section and the total oscillator strength per CdSe unit. Over this limited energy range, the total oscillator strength per CdSe unit varies weakly with QD radius. As the QD radius decreases, the oscillator strength per CdSe unit of the lowest energy transition ($1S_e1S_{3/2h}$) increases. Figure 51 (right side) shows the absorption cross section per QD for CdSe QDs. The integrated oscillator strength per particle for the lowest energy transition $1S_e1S_{3/2h}$ increases linearly with the particle radius. [332]

Photoluminescence Excitation (PLE) Spectra of Semiconductor Nanoparticles. PLE is a very useful technique adopted to explore the optical properties of the semiconductor nanoparticles, which is achieved by monitoring a narrow spectral region of the full luminescence while scanning the excitation energy.[322,325,328,333−335] The photoexcitation rate is given by

$$R = \int Cq(\nu)K\,d\nu \quad (24)$$

where C is the radiation velocity within the material, $q(\nu)$ is the photon density of radiation, and K is the

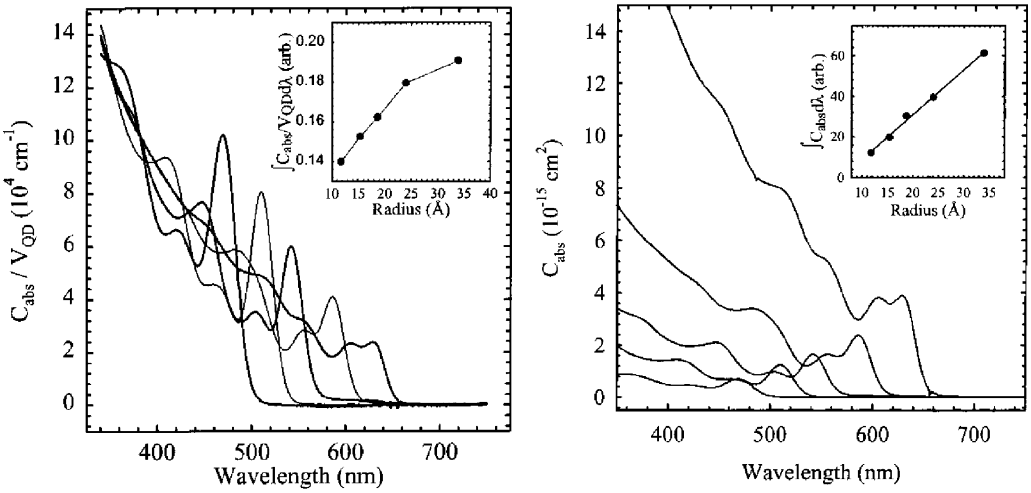

Figure 51. (Left) Room temperature absorption cross section per CdSe unit versus wavelength for CdSe QDs dispersed in hexane. Each spectrum is divided by the volume of the QD to give the absorption cross section per CdSe unit. From right to left, spectra are shown for QDs with radii of 33.9, 24.0, 18.7, 15.4, and 11.8. (Inset) Integrated area per unit volume as a function of the QD radius. (Right) Room temperature absorption cross section per QD for CdSe QDs dispersed in hexane. From right to left, spectra are shown for QDs with radii of 33.9, 24.0, 18.7, 15.4, and 11.8. (Inset) Integrated oscillator strength per particle for the lowest energy transition $1S_e1S_{3/2h}$) plotted versus particle radius. Reprinted with permission from ref 332. Copyright 2002 American Chemical Society.

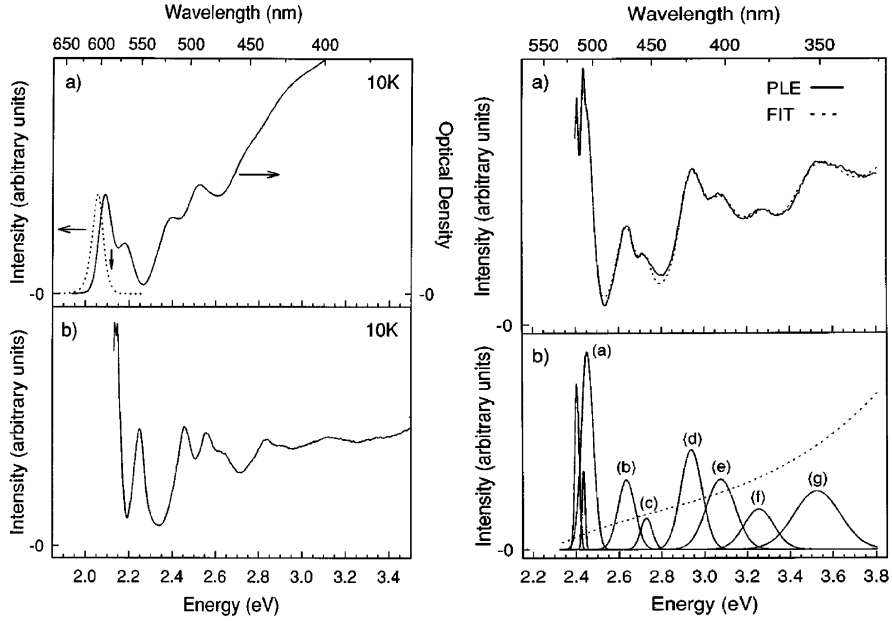

Figure 52. (Left) (a) Absorption (solid line) and photoluminescence (dashed line) spectra for 28-radius quantum dots. In luminescence the sample was excited at 2.655 eV (467.0 nm). The downward arrow marks the emission position used in PLE. (b) PLE scan for 28-radius dots. (Right) (a) Demonstration of the fitting procedure used to extract PLE peak positions. The PLE scan (solid line) is compared to the fit (dashed line) for an 18-radius sample. The structure on the first absorption is clearly visible in this plot. (b) Individual Gaussian components (solid lines) and cubic background (dashed line), which combine to form the fit. Reprinted (Figures 1a,b, 3a,b) with permission from 325. Copyright 1996 by the American Physical Society.

absorption constant. As $q(\nu)$ increases very rapidly with increasing wavelength, the significant part of the integral in the above equation is concentrated around the absorption edge. The transition may not be observed in the PLE if $q(\nu)$ is zero, even if the absorption transitions between the two states occur. The transition between two states may be detected by absorption as long as the transition is allowed. On the other hand, with PLE, only the radiative transition can be observed.[322,325,328,333−335]

PLE spectroscopy is a very useful and cheap technique that helps to remove the size distribution broadening effect on the absorption spectrum of QDs and assists in assigning the discrete optical transitions.[322,325,328,333−335] By probing the high-energy emission end of the luminescence, only emission from the smaller nanoparticles is monitored (Figure 52, left). By using this technique, up to 10 discrete optical transitions have been obtained in near-monodisperse CdSe QD samples. Figure 52 (right) shows the resolved discrete transitions of the QDs obtained by fitting with Gaussian functions.

Shown in Figure 53 are the normalized PLE scans for seven different sizes of QD samples. In addition,

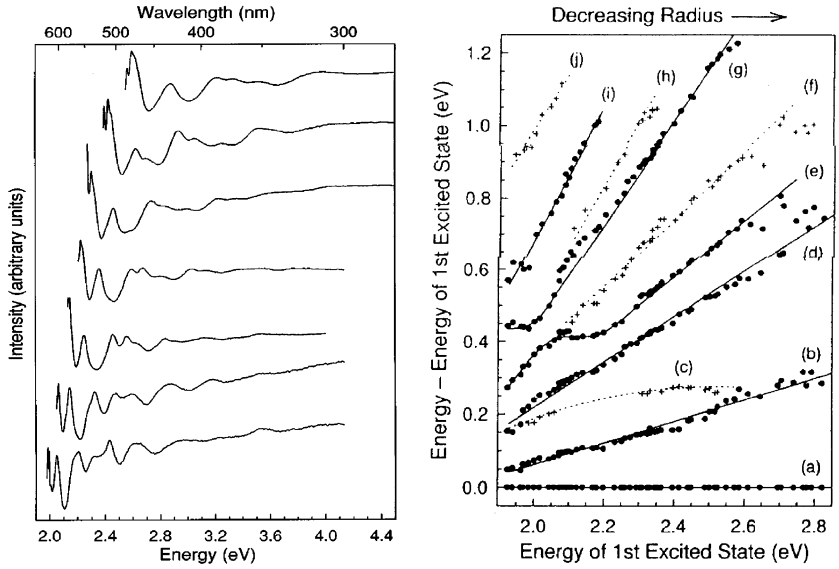

Figure 53. (Left) Normalized PLE scans for seven different size CdSe quantum dot samples. Size increases from top to bottom and ranges from 15 to 43 in radius. (Right) Transition energies relative to the first excited state as a function of the energy of the first excited state and derived from the PLE spectra. Strong transitions are indicated by circles, weak transitions by crosses. The solid and dashed lines are visual guides for the strong and weak transitions to indicate their size evolution. (a), (b), (c), (d), (e), (f), (g), (h), (i), (j) refer to the optical transition of $1S_{3/2}Se$, $2S_{3/2}1Se$, $1S_{1/2}1Se$, $1P_{3/2}1Pe$, $2S_{1/2}1Se$, $1P_{5/2}1Pe$ and $1P'_{1/2}1Pe$, $3S_{1/2}1Se$, etc. Reprinted (Figures 2 and 4) with permission from ref 325. Copyright 1996 American Physical Society.

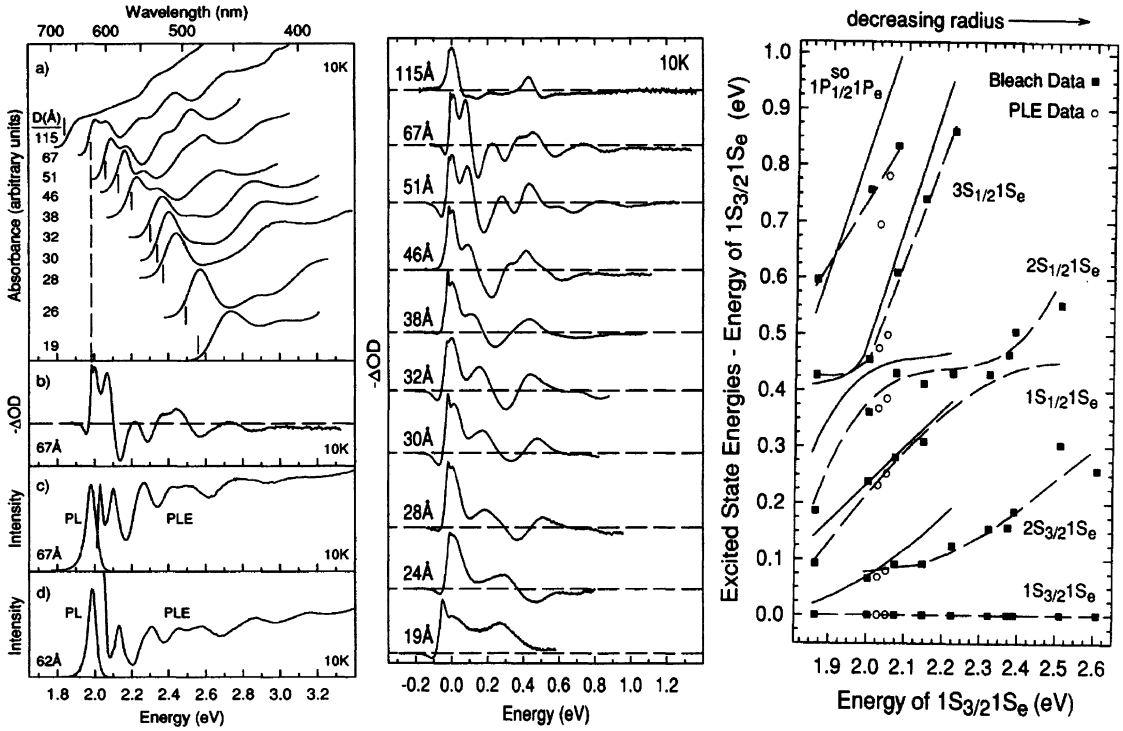

Figure 54. (Left) (a) Absorption spectra (10 K) for CdSe dots embedded in poly(vinyl butyral) (PVB) films; (b) bleach spectrum for 67 dots at 10 K; (c) PL and PLE spectra for 67 dots at 10 K; (d) PL and PLE spectra for 62 dots at 10 K. (Middle) Bleach spectra at 10 K, with pump energies at 1.842, 1.984, 2.060, 2.130, 2.198, 2.296, 2.339, 2.366, 2.490, and 2.557 eV for 115 to 19 dots. $1S_{3/2}1S_e$ transitions were set to zero energy. (Right) Excited-state spacings from TDA spectra (solid squares) plotted relative to $1S_{3/2}1S_e$. The x-axis is the size-dependent energy of $1S_{3/2}1S_e$. Dashed lines are visual guides. Solid lines are predictions. PLE data are plotted (open circles). Reprinted (Figures 1−3) with permission from ref 321. Copyright 1994 American Physical Society.

the transition energies relative to the first excited state are presented as a function of the energy of the first excited state.[325] For the CdSe QDs, 10 discrete optical transitions were resolved and assigned correspondingly (Figure 53). With the increase of the first transition energy or the decrease of the nanoparticle size, the optical transition energy increases monotonically.

Transient Differential Absorption Spectra of Semiconductor Nanoparticles. Pump−probe or transient differential absorption spectroscopy can also help in resolving the discrete optical transitions in semicon-

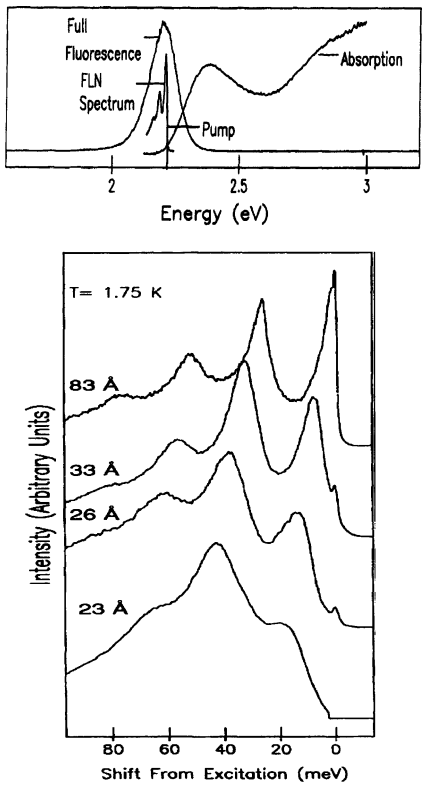

Figure 55. (Top) Illustration of fluorescence line narrowing (FLN) measurement. (Bottom) Size dependence of the FLN spectrum at 1.75 K showing the decrease in LO-phonon coupling with increasing size. Reprinted (Figures 1a and 9a) with permission from ref 336. Copyright 1994 American Physical Society.

ductor QDs.[321] By exciting on the red edge of its first transitions with a spectrally narrow pump beam, only the bigger sizes of the nanoparticles are pumped. The pump-induced change in optical density contains both bleached and induced absorption arising from particles already containing an electron−hole pair. Comparison of the pump−probe spectra with the absorption data shows that bleach features correspond to ground-state transitions, but are more clearly resolved in the former. Compared to the PLE spectrum for the same sample, the spectrum is very similarly featured with discrete transitions. However, there is a shift in energy because PLE monitors the smaller particles, whereas pump−probe monitors the bigger ones. Discrete optical transitions can also be assigned using the pump−probe technique shown in Figure 54. Similar to the PLE technique, results on the dependence of the transition energy on the size of particle can be concluded from pump−probe measurements.

Photoluminescence or Fluorescence Line Narrowing (PLN or FLN) Spectra of Semiconductor Nanoparticles. FLN or PLN is a similar technique, which involves the excitation on the red side of the absorption spectrum to probe the bigger sized nanoparticles in an inhomogeneous sample.[336] Using this technique, the LO−phonon progression can be well-resolved, and the exciton−LO−phonon coupling strength can be monitored. For example, shown in Figure 55 is the size dependence of the FLN spectrum at 1.75 K, where the decrease in LO−phonon coupling with increasing size is presented.[336]

C. Comparison of Experimental Results with Theory. Figure 56 shows a comparison of both experimental and calculated exciton energies for the wurtzite form of CdS QDs.[324,337] After removal of the degeneracy of the valence bands at Γ by crystal field and spin−orbit interactions, a higher 2-fold spin degenerate band, followed by a lower 2-fold degenerate band with $(j; m_j) = (3/2; \pm 1/2)$ and a 2-fold degenerate band with $(j; m_j) = (1/2; \pm 1/2)$ were obtained, as indicated in the three distinct optical transitions labeled A−C. From this analysis, a reasonable agreement was shown between the predicted and the experimental values.

Shown in Figure 57 is the size dependence of the resonant and nonresonant Stokes shift of CdSe nanoparticles.[267,311,324,327] Both the resonant and nonresonant Stokes shifts increase as the size of the semiconductor nanoparticles decreases. The resonant Stokes shift corresponds to the difference in energy between the pump energy and the zero LO phonon line (ZPL) in the FLN spectra. The FLN spectra are obtained by excitation of the TOPO-capped CdSe QDs with a Q-switched Nd-doped YAG−dye laser system operating with ~7 ns pulses. The spectra show good band edge fine structure for the FLN spectra and well-resolved LO phonon spectra. The resonant Stokes shift shows good agreement with the theoretical calculations, and the nonresonant Stokes shift was found to depend on the size distribution. Further-

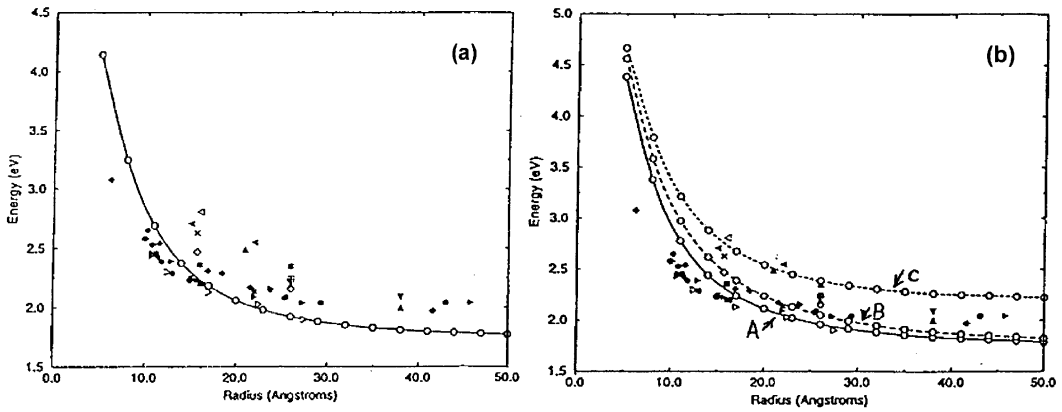

Figure 56. (a) Direct exciton energies of wurtzite CdSe QDs (full line) and comparison with available experimental data; (b) three calculated optical transition energies, *A*, *B*, and *C*, as a function of dot radius. Reprinted with permission from ref 324. Copyright 2001 Taylor and Francis.

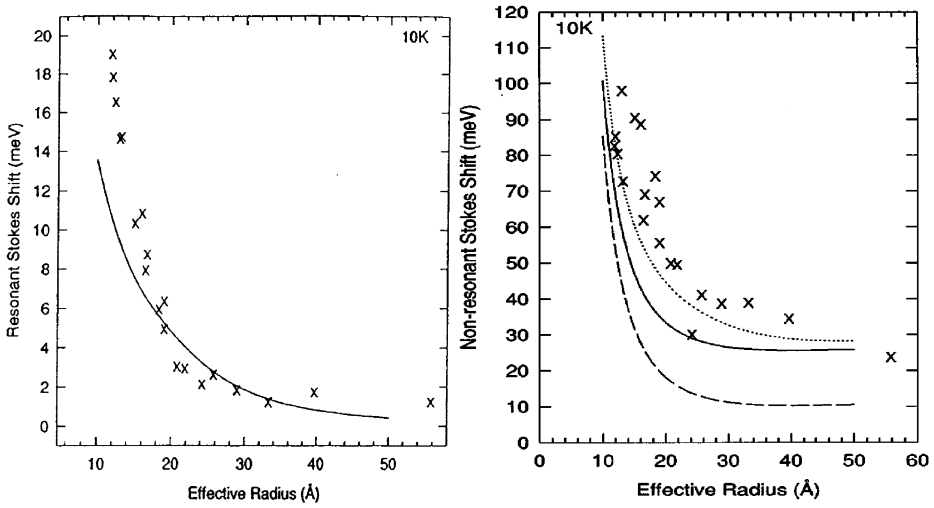

Figure 57. (Left) Size dependence of the resonant Stokes shift, which corresponds to the difference in energy between the pump energy and the zero LO phonon line (ZPL) in the FLN spectra. The solid line is the theoretical size-dependent splitting between the $\pm 1^L$ state and the ± 2 exciton ground state; experimental values are shown as $\times$. (Right) Size dependence of the nonresonant Stokes shift. This Stokes shift is considered to be the difference in energy between the peak of the band-edge absorption and the peak of the full luminescence. Experimental values are represented by $\times$. The dashed line is the theoretical Stokes shift calculated for a sample with a 5% size distribution. It is the difference between the mean energy of the three light exciton states and the mean position of the ± 2 exciton ground states of the participating crystals. The solid line includes the contribution of phonons to the theoretical splitting. The dotted line shows the theoretical results for a sample with a 10% size distribution. Reprinted with permission from ref 324. Copyright 2001 Taylor and Francis. Also, reprinted (Figures 7 and 9) with permission from ref 327 (Figures 7 and 9). Copyright 1996 American Institute of Physics.

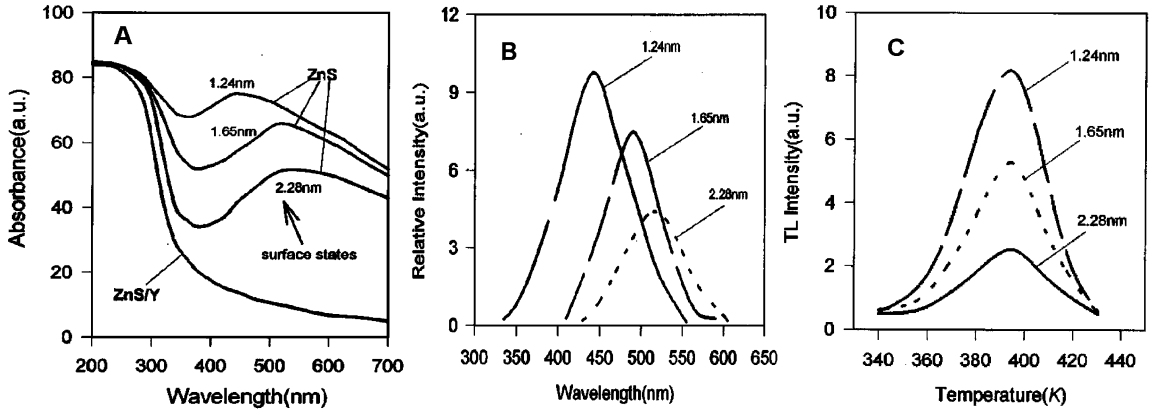

Figure 58. (A) Reflectance absorption, (B) photoluminescence (PL), and (C) thermoluminescence (TL) spectra of ZnS nanoparticles and of the ZnS clusters in zeolite Y (ZnS/Y). For photoluminescence spectra of ZnS nanoparticles ($\lambda_{exc} = 280$ nm). Reprinted with permission from ref 340a. Copyright 1997 American Institute of Physics.

more, the nonresonant Stokes shift contains contributions from shape, structure, and differences in chemical environment experienced by the dots. Any other type of inhomogeneous broadening leads to an additional Stokes shift at the nonresonant excitation conditions. Thus, the nonresonant Stokes shift shows deviation from the theoretical calculations.

5.1.2.1.2. Optical Transition from Surface States. Surface states and optical transition are important topics, which have been investigated with different techniques, including up-conversion and extended X-ray absorption fine structure (EXAFS), etc. Here we focus our review on the optical techniques. Luminescence is one of the most important methods to reveal the energy structure and surface states of semiconductor nanoparticles and has been studied extensively. Whenever a semiconductor is irradiated, electrons and holes are created. If electron−hole pairs recombine immediately and emit a photon that is known as fluorescence and if the electrons and holes created do not recombine rapidly, but are trapped in some metastable states separately, they need energy to be released from the traps and recombine to give luminescence. If they spontaneously recombine after some time, it is called photoluminescence (PL). It is reported that the fluorescence process in semiconductor nanoparticles is very complex, and most nanoparticles exhibit broad and Stokes shifted luminescence arising from the deep traps of the surface states. Only clusters with good surface passivation may show high band-edge emission.[5,267,338,339] If the detrapping process is caused by heating or thermostimulation, the luminescence is called thermoluminescence (TL), and the energy corresponding to the glow peak is equal to the trap depth. The TL process is different from the PL

process because the energy of thermostimulation is not sufficiently high to excite the electrons from their ground states to their excited states. Only the carriers ionized from the surface states or defect sites are involved in the TL process; that is, the thermoluminescence has arisen from the surface states. Thermoluminescence is a good way to detect the recombination emission caused by the thermal detrapping of carriers.[328,340a]

Figure 58 shows the reflectance absorption, PL, and TL spectra of ZnS nanoparticles. Two broad absorption bands appear in the absorption spectra of the ZnS nanoparticles. The absorption band around 300 nm was attributed to the interband transition or exciton absorption of the particles. The absorption bands in the long-wavelength regimes were caused by the surface states of the ZnS nanoparticles because the absorption was lying below the absorption edge of the particles. As the size decreases, the absorption of the surface states becomes more intensive and the absorption peak shifts to the blue. This indicates that the contents of the surface states increase as the size of the particles decreases. Because the surface-to-volume ratio increases as the size decreases, ions at the surface increase rapidly, and surface states (dangling bonds, defect sites, or traps) increase rapidly via surface reconstruction.

The broad and Stokes-shifted emission band in PL was attributed to the so-called trapped luminescence arising from the surface states. The surface emission becomes more intensive and shifts to the blue as the size of the particles is decreased.

An obvious glow peak around 396 K in TL was observed. The three samples show the glow peaks at almost the same position, and the TL intensity increases as the particle size decreases. The increase in the TL intensity upon decreasing size reveals the increase in the surface states as the size is decreased. This result is in agreement with that obtained from the fluorescence and absorption measurements. TL information provides other evidence to show that the long-wavelength absorption is caused by the surface states.

Recently, we found that optical transitions in the absorption spectrum involving the surface states can be clearly observed in the process of the gradual crystallization of small CdSe nanoparticles.[340b] The small CdSe nanoparticles had similar sizes around 2.0 nm during the crystallization process. The initially formed amorphous CdSe nanoparticles crystallized slowly by reconstructing the surface atoms, moving the deeper surface states to shallower ones, resulting in a blue-shift absorption during the crystallization process and highly crystallized nanocrystals after the crystallization. The gradual crystallization process is also reflected in the PL spectra as well.

5.2. Metallic Nanoparticles

Surface Plasmon Resonant Transitions in Metal Nanoparticles. Colloidal solutions of spherical gold nanoparticles exhibit a deep red color due to the well-known surface plasmon absorption. The surface plasmon resonance is caused by the coherent

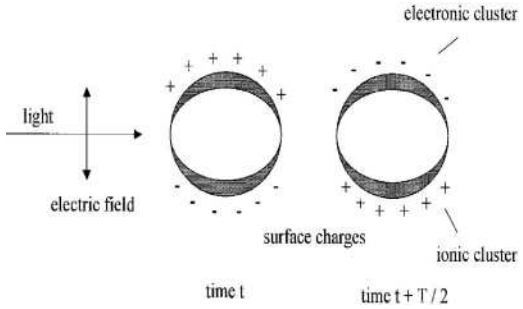

Figure 59. Illustration of the excitation of the dipole surface plasmon oscillation. A dipolar oscillation of the electrons is created with period *T*. Reprinted with permission from ref 259. Copyright 2000 Taylor and Francis.

motion of the conduction band electrons, which interact with an electromagnetic field.[259,260,341−343] In a classical picture, polarization of the electrons with respect to the much heavier ionic core of a spherical nanoparticle is induced by the electric field of an incoming light wave. A net charge difference exists only at the nanoparticle surface, which in turn acts as a restoring force. In the simplest case, a dipolar oscillation of all the electrons with the same phase is created, as shown in Figure 59. The observed color originates from the strong absorption of the metal nanoparticles when the frequency of the electromagnetic field becomes resonant with the coherent electron motion.

The frequency and width of the surface plasmon absorption depends on the size and shape of the metal nanoparticles as well as on the dielectric constant of the metal itself and the surrounding medium.[259,260,341−343] Noble metals such as copper, silver, and gold have a strong visible-light plasmon resonance, whereas most other transition metals show only a broad and poorly resolved absorption band in the ultraviolet region.[259,260,344] This difference is attributed to the strong coupling between the plasmon transition and the interband excitation. In addition, the conduction band electrons of the noble metals can move freely, independently from the ionic background, and the ions act only as scattering centers.[345,346] This gives the electrons in the noble metals a higher polarizability, which shifts the plasmon resonance to lower frequencies with a sharp bandwidth. The surface plasmon resonance was theoretically explained by Mie in 1908, including linear optical properties such as extinction and scattering of small spherical metal particles.[347]

Mie's theory and experimental spectra agree well in the size regime >20 nm until the normal incidence absorption no longer shows a plasmon resonance for bulk metals. The spectrum is composed of the sum of size-dependent absorption and scattering modes. Higher order modes become more dominant with increasing particle size, causing the plasmon absorption band to red shift and resulting in increased bandwidth, because for larger particles, the light cannot polarize the nanoparticles homogeneously and retardation effects lead to the excitation of higher order modes.[341] The optical absorption spectra depend directly on the size of the nanoparticles, which is called the extrinsic size effect.[341] Figure 60 shows the

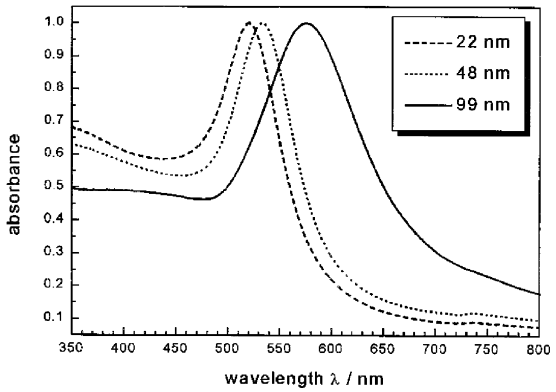

Figure 60. Optical absorption spectra of 22, 48, and 99 nm spherical gold nanoparticles. The broad absorption band corresponds to the surface plasmon resonance. Reprinted with permission from ref 259. Copyright 2000 Taylor and Francis.

absorption spectra of Au spherical nanoparticles with different sizes. As the size increases, the plasmon band shifts to the red.

When the size of nanoparticles is much smaller than the wavelength (<20 nm) of the interacting light, only the dipole oscillation contributes significantly to the extinction cross section. Mie's theory can be approximately expressed[259,260,341−344]

$$\sigma_{\text{ext}} = \frac{9V\epsilon_{\text{m}}^{3/2}}{c} \cdot \frac{\omega\epsilon_2(\omega)}{[\epsilon_1(\omega) + 2\epsilon_{\text{m}}]^2 + \epsilon_2(\omega)^2} \quad (25)$$

where V is the particle volume, ω is the angular frequency of the exciting light, and c is the speed of light. ϵ_{m} and $\epsilon(\omega) = \epsilon_1(\omega) + i\epsilon_2(\omega)$ are the dielectric functions of the surrounding medium and the metal, respectively. For the metal, the dielectric function is complex and depends on the frequency. The resonance condition is fulfilled roughly when $\epsilon_1(\omega) = -2\epsilon_{\text{m}}$ if ϵ_2 is small or weakly dependent on ω.

Within the dipole approximation (eq 25), the surface plasmon resonance is independent of the particle size. This is contradicted with experimental results on metallic nanoparticles much smaller than 10 nm,[341] where the plasmon band shows a size dependence for small particles and even disappears completely for nanoparticles of $<\sim$2 nm.[278,348,349] Thus, the assumption of a free electron gas is no longer valid in the size range below 2 nm. Very small nanoparticles are better treated as molecular clusters with discrete electronic states. The question arises about the validity of bulk optical properties stemming from a bulk dielectric function, even for particles within an intermediate size range from 2 to 20 nm with established electronic bands. Thus, the dielectric function is modified for the smaller sized nanoparticles. The dielectric function is decomposed into the interband transitions and a free electron part; the latter can be modified to account for enhanced electron-surface scattering as a function of the particle radius (R) within the Drude free-electron model. Therefore, the dielectric function becomes size dependent [$\epsilon(\omega, r)$], and this explains the observed $1/r$ dependence of the plasmon bandwidth.[341] The size effects for smaller nanoparticles are called intrinsic size effects because the dielectric function of the material itself is size-dependent.[341] Many other effects such as the spill out of the conduction electrons have also been considered and were incorporated by changing the bulk dielectric function appropriately.[350−360]

Mie's theory for spherically shaped particles was extended within the dipole approximation by Gans for cylindrical or oblate nanoparticles.[361] The particles are usually characterized by their aspect ratio (ratio between the length and width of the particle). For elongated ellipsoids, the extinction cross section σ_{ext} is given by[362]

$$\sigma_{\text{ext}} = \frac{\omega}{3c}\epsilon_{\text{m}}^{3/2}V\sum_j \frac{(1/P_j^2)\epsilon_2}{\{\epsilon_1 + [(1-P_j)/P_j]\epsilon_{\text{m}}\}^2 + \epsilon_2^2} \quad (26)$$

where P_j are the depolarization factors along the three axes A, B, and C of the nanorod with $A > B = C$, defined as

$$P_A = \frac{1-e^2}{e^2}\left[\frac{1}{2e}\text{In}\left(\frac{1+e}{1-e}\right) - 1\right] \quad (27)$$

$$P_B = P_C = \frac{1-P_A}{2} \quad (28)$$

and the aspect ratio (R) is included in e as follows:

$$e = \left[1 - \left(\frac{B}{A}\right)^2\right]^{1/2} = \left(1 - \frac{1}{R^2}\right)^{1/2} \quad (29)$$

The plasmon resonance for nanorods splits into two bands. As the aspect ratio increases, the energy separation between the resonance frequencies of the two plasmon bands also increases.[108,363−365] The high-energy band corresponds to the oscillation of the electrons perpendicular to the major axis of the rods and is referred to as the transverse plasmon absorption. The other absorption band, which is red-shifted to lower energies, is caused by the oscillation of the electrons along the major axis of the nanorods and is known as the longitudinal surface plasmon absorption. The transverse plasmon absorption has linear dependence on the aspect ratio and the dielectric constant of the medium.

Figure 61 shows the experimentally observed absorption spectrum of a nanorod sample having an aspect ratio of 3.3 compared to the 22 nm nanodots.[260] The inset shows how the maxima of the transverse (squares) and longitudinal (spheres) surface plasmon modes vary with aspect ratio. The transverse plasmon absorption band is relatively insensitive to the nanorod aspect ratio and coincides spectrally with the surface plasmon oscillation of the nanodots.

Photoluminescence from bulk copper and gold has been used extensively in characterizing the carrier relaxation and the band structure of metals.[366−371] The emission peak is centered near the interband absorption edge of the metal and attributed to direct radiative recombination of the excited electrons with holes in the d band. In bulk noble metals, the quantum efficiency of the photoluminescence is very low, typically on the order of 10^{-10}.[372] On rough metal

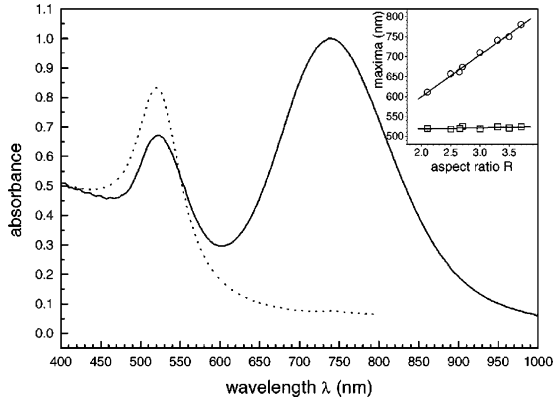

Figure 61. Absorption spectrum of a nanorod sample having an aspect ratio of 3.3 compared to the 22-nm nanodots. The inset shows how the maxima of the transverse (squares) and longitudinal (spheres) surface plasmon modes vary with aspect ratio. Reprinted with permission from *Annual Reviews of Physical Chemistry* (http://www.AnnualReviews.org), ref 260. Copyright 2003 Annual Reviews.

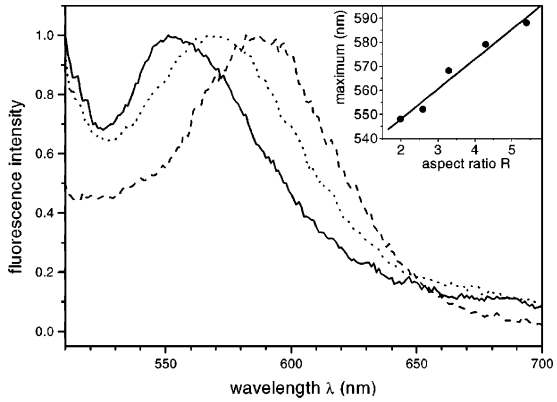

Figure 62. Luminescence spectra of colloidal gold nanorods with aspect ratios of 2.6, 3.3, and 5.4 (480-nm excitation). The inset shows the linear dependence of the luminescence maximum on the aspect ratio. Reprinted with permission from *Annual Reviews of Physical Chemistry* (http://www.AnnualReviews.org), ref 260. Copyright 2003 Annual Reviews.

surfaces, the luminescence is enhanced by several orders of magnitude, known as the lightning rod effect.[367,373,374] Rough metal surfaces can be treated as a collection of randomly oriented nanometer hemispheroids on the smooth surfaces, which have a surface plasmon resonance similar to the gold nanorods, and therefore the incoming and outgoing electric fields are amplified by the plasmon resonances around the hemispheroids. The luminescence efficiency of gold nanorods increases by 6 orders of magnitude by this lightning rod effect.[375]

Figure 62 show the absorption and steady-state fluorescence spectra, respectively, of three gold nanorod samples having average aspect ratios of 2.6, 3.3, and 5.4.[260] The spectra reveal the presence of an emission band between 550 and 600 nm. The luminescence quantum efficiency increases linearly with the square of the aspect ratio, and the fluorescence maximum red-shifts linearly with increasing nanorod aspect ratio as shown in the inset.[375] On the other hand, gold nanodots with diameters between 20 and 30 nm prepared according to the same method do not show a comparable emission. Thus, the longitudinal plasmon resonance absorbing at longer wavelengths is more effective in amplifying the fluorescence in gold nanoparticles compared to the surface plasmon resonance of spheres, and this is consistent with the longer dephasing times measured for the rods.[376]

Luminescence was also found to be absent in 15 nm spherical nanoparticles, whereas the enhancement of the photoluminescence was found for very small gold clusters (<5 nm).[377] The origin of the photoluminescence was attributed to the radiative recombination of an electron−hole pair. The electrons from the filled d band to electronic states were promoted to the sp conduction band above the Fermi level by the incident photons. Both electrons and holes relax by scattering with phonons and recombine radiatively to emit luminescence, which is modified by the local field created around the nanoparticles caused by excitation of the plasmon resonance. The theory of the local field effect has been successfully applied in various cases, including second harmonic generation, surface-enhanced Raman scattering, luminescence from rough noble metal surfaces,[367,373,374] and luminescence of gold nanorods, where the observed linear dependence of the luminescence maximum and quadratic dependence of the quantum yield on the aspect ratio can be reproduced.[375]

Triangle-branched Au nanocrystals have been recently synthesized and characterized.[378] In contrast to the characteristic red color of spherical Au nanoparticles, the colloidal triangle-branched Au nanocrystals are blue. The measured extinction spectrum is shown in Figure 63, and the plasmon resonance peak is red-shifted from 500 to 530 nm for spheres to 690 nm for the branched particles. The plasmon band can be varied in the range from 650 to 700 nm, and the narrower plasmon band centered at 657 nm corresponds to smaller average sizes. The plasmon resonance for the triangle-branched Au nanocrystals has three bands, corresponding to two in-plane or longitudinal surface plasmon absorptions at the longer and shorter wavelength and one out-of-plane or transverse plasmon absorption present between.

Plasmon resonance spectra with three or more resonance bands are also observed for silver nanocrystals with different shapes, such as silver nanodisks[106,112,379,380] and silver nanoprisms.[113] It could be concluded that the number of asymmetric dimensions in the shape of metal nanocrystals can break the plasmon band. The number of plasmon bands increases from one to two, three, or more as the shape changes from sphere to rod, disk, or irregular. This is because the plasmon band breaks or degenerates from one band into two, three, or more bands.

5.3. High Surface-to-Volume Ratio

Two key factors controlling the properties of nanomaterials are the size and surface characteristics of nanoparticles.[5,262,323,346,381] These two factors are interrelated because the S/V ratio increases as the size decreases. For a spherical particle, the S/V ratio is inversely proportional to its radius, R ($S/V = 3/R$).

Full-shell clusters are built up by hexagonal (hcp) or cubic (ccp) close-packed atoms. This assumes that

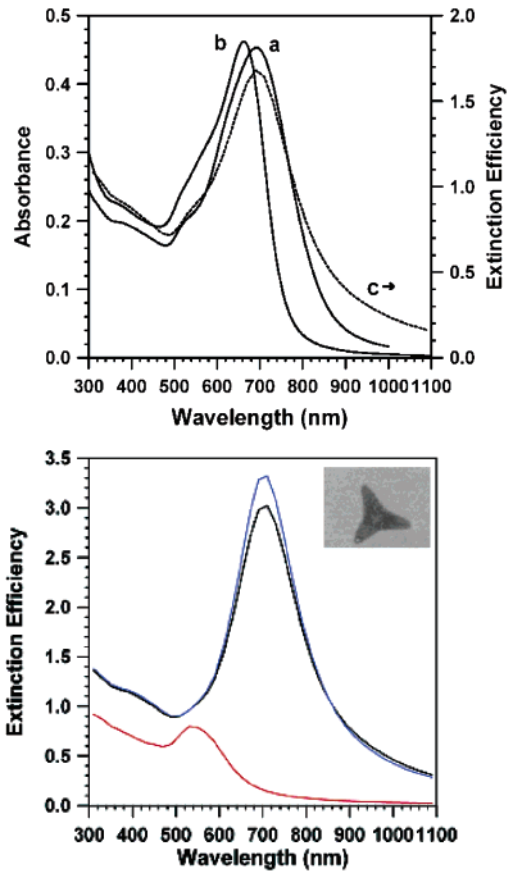

Figure 63. (Top) UV−visible spectra of branched gold nanocrystals with bigger size (a) and smaller size (b). The dashed line (c) shows the calculated extinction spectrum using the discrete dipole approximation (DDA) method. (Bottom) Calculated extinction spectra of a single gold nanocrystal for two in-plane polarization directions and one out-of-plane direction. The upper right shows one illustration of the branched gold. Reprinted with permission from ref 378. Copyright 2004 American Chemical Society.

the particles are built on a center atom by adding one, two, or three dense-packed shells. The number of atoms per shell is $N_s = 10n^2 + 2$, where n is the number of the shell.[346] The total number (N) of atoms of the n shell is $N = (10n^3 + 15n^2 + 11n + 3)/3$. Thus, the surface/volume ratio is N_s/N. For example, when the smallest full-shell cluster consists of 13 atoms, the surface atom ratio is 12/13 = 92.3%. Assuming that the thickness per shell is 6 Å, we can calculate the surface/volume ratio as shown in Figure 64, where the surface/volume ratio increases as the radius of the particle decreases, that is, in the regime of fewer than 10 layers, corresponding to ~3 nm.

It is clear that the surface of nanoparticles plays an important role in their fundamental properties, from structural transformation via light emission to solubility. The surface atoms are chemically more active compared to the bulk atoms because they usually have fewer adjacent coordinate atoms and unsaturated sites or more dangling bonds. At the same time, the imperfection of the particle surface induces additional electronic states in the band gap, which act as electron or hole trap centers. At high densities of surface defects, a decrease in the observed transition energy and a red-shifted emission

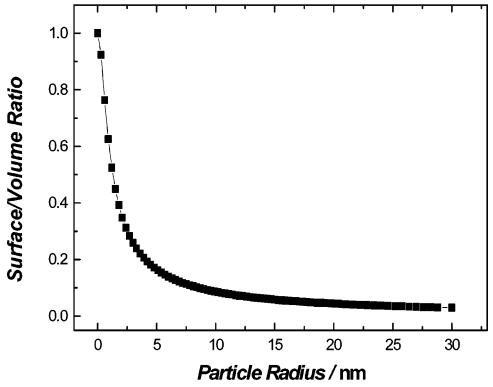

Figure 64. Surface/volume ratio as a function of the particle size.

band can be observed due to defect band formation. As the size of the materials decreases, the surface-to-volume ratio increases and the surface effects become more apparent and thereby easier to explore. In addition, the surface states near the gap can mix with the intrinsic states to a substantial extent, and these effects may also influence the spacing of the energy levels of nanoparticles.[5,262,323,346,381]

In a system containing only a few hundred atoms, a large fraction of these atoms will be located on the surface. Because surface atoms tend to be coordinatively unsaturated, there is a large energy associated with this surface. The smaller the nanocrystal, the larger the contribution made by the surface energy to the overall energy of the system and, thus, the more dramatic the melting temperature depression as discussed later.[262]

5.4. Melting Point

In a wide variety of materials ranging from metals to semiconductors to insulators, a decrease in solid to liquid transition temperature has been observed with decreasing nanocrystal size.[382−386] Because surface atoms tend to be coordinatively unsaturated, there is a large energy associated with this surface. The key to understanding this melting point depression is the fact that the surface energy is always lower in the liquid phase compared to the solid phase. In the dynamic fluid phase, surface atoms move to minimize surface area and unfavorable surface interactions. In the solid phase, rigid bonding geometries cause stepped surfaces with high-energy edge and corner atoms. By melting, the total surface energy is thus reduced. This stabilizes the liquid phase over the solid phase. The smaller the nanocrystal, the larger the contribution made by the surface energy to the overall energy of the system and thus, the more dramatic the melting temperature depression. As melting is believed to start on the surface of a nanocrystal, this surface stabilization is an intrinsic and immediate part of the melting process.[387,388] Figure 65 shows the relationship between particle size and melting point of gold and CdS nanoparticles. It is clear that the melting point decreases as the size of the particles decreases, and there is a dramatic decrease in the melting points for particles that are smaller than 3−4 nm.[262,346]

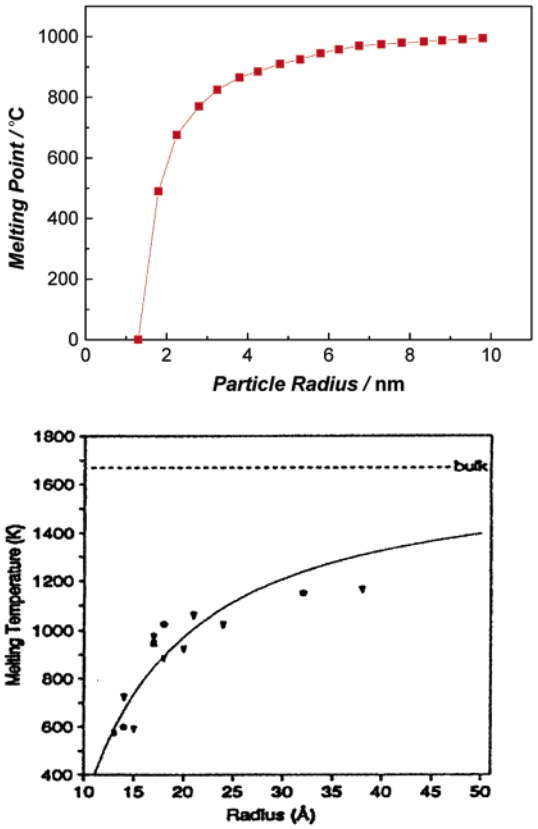

Figure 65. Relationship between the melting points and the sizes of gold (top) (reprinted with permission from ref 346; copyright 2001 Wiley) and CdS nanoparticles (bottom) (reprinted with permission from ref 262; copyright 1996 American Chemical Society).

5.5. Conductivity and Coulomb Blockade

Electrical conductivity of bulk metals is based on their band structures. The mobility of electrons is described by

$$\mu = \frac{e\lambda}{4\pi\epsilon_0 m_e V_F} \tag{30}$$

where λ is the mean free path of the electrons between two collisions, m_e is the effective mass of the electron in the lattice, V_F is the speed of the electrons (Fermi speed), and ϵ_0 is the dielectric constant of vacuum. The expression λ/V_F can be interpreted as the mean time, τ, between two collisions of electrons. For example, in copper, V_F is $\sim 1.6 \times 10^6$ ms^{-1} and λ is $\sim 4.3 \times 10^{-8}$ m (43 nm), and as a result, τ is equal to 2.7×10^{-14} s (270 fs). In any metal, there are two scattering mechanisms: by lattice defects (foreign atoms, vacancies, interstitial positions, and grain boundaries) and by phonons (thermal lattice vibrations). The collective motion of electrons in a bulk metal obeys Ohm's law $U = RI$, where U is the applied voltage, R is the resistance of the material, and I is the current.[346]

As the electron band becomes discrete energy levels, the above Ohm's law is no longer valid. If an electron is transferred to the particle, its Coulomb energy (E_C) increases by $E_C = e^2/(2C)$, where C is the capacitance of the particle. Thermal motion of the atoms in the particle can initiate a change in the charge and the Coulomb energy so that further electrons may tunnel uncontrolled. To produce single-electron tunneling processes, the thermal energy of the particle must be much smaller than the Coulomb energy, $kT \ll e^2/(2C)$, to keep the energy on the particle. With an additional charge, a voltage $U = e/C$ is produced, leading to a tunneling current $I = U/R_T = e/(R_T C)$, where R_T is the tunnel resistance. The resulting additional charge has a mean lifetime of $\tau = R_T C$. The related Heisenberg uncertainty of energy, $\delta E = h/\tau = h/(R_T C)$, leads to unexpected tunneling if it exceeds the Coulomb energy. The Heisenberg fluctuation energy is expressed as $E = h/R_{QH}C$, where R_{QH} is the quantum Hall resistance. Thus, a second condition for single-electron tunneling is $R_{QH} \ll R_T$. The quantum resistance can also be elucidated from classical transport as follows: quantum $\Rightarrow \delta e \delta t \sim h \Rightarrow e^2/RC \times RC \sim h \Rightarrow R \sim 2h/e^2$, where much lower R means classical.

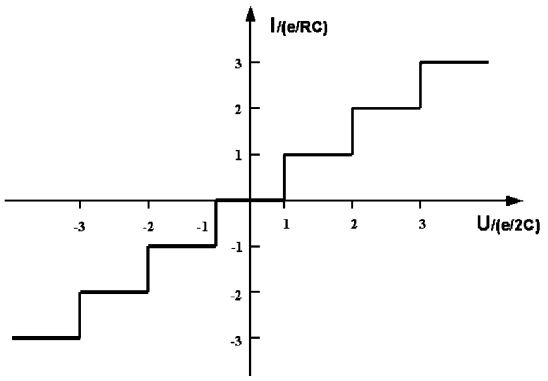

Figure 66. $I-U$ characteristic of ideal single electron transport, where Coulomb blockade is shown as the step function.

The current–voltage characteristic for an ideal quantum dot shows no current up to $U_{Coulomb} = \pm e/2C$. If this value is reached, an electron can be transferred. Following this, an electron tunneling process occurs if the Coulomb energy of the quantum dot is compensated by an external voltage of $U = \pm ne/(2C)$. An idealized "staircase", resulting from the repeated tunneling of single electrons, is shown in Figure 66. The step height ΔI corresponds to $e/(RC)$, and the width ΔU corresponds to $e/(2C)$.

As the size of semiconductors and metals approaches nanometer length scales, the finite size of the materials also leads to unique electronic properties. To add a single charge to a semiconductor or metal NC costs energy because a charge carrier is no longer solvated in an effectively infinite medium. For a NC surrounded by a medium of dielectric constant, ϵ, the capacitance of the nanoparticle, depends on its size as $C(r) = 4\pi\epsilon r\epsilon_0$ and the energy required to add a single charge is given by the charging energy $E_C = e^2/2C(r)$. Tunneling of single charges onto metal or semiconductor nanoparticles can be seen at temperatures $k_{BT} < E_C$ in the I–V characteristics from devices containing single nanoparticles[391,392] or from STM measurements of NCs on conductive surfaces.[393,394]

Figure 67 shows one approach to measure the Coulomb blockade.[391] First, leads with a spacing of a few nanometers are fabricated using electron beam

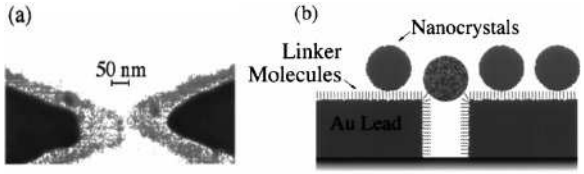

Figure 67. (a) Field emission scanning electron micrograph of a lead structure before the nanocrystals are introduced. The light gray region is formed by the angle evaporation and is 10 nm thick. The darker region is from a normal angle evaporation and is 70 nm thick. (b) Schematic cross section of nanocrystals bound via a bifunctional linker molecule to the leads. Transport between the leads occurs through the mottled nanocrystal bridging the gap. Reprinted with permission from ref 391. Copyright 1996 American Institute of Physics,

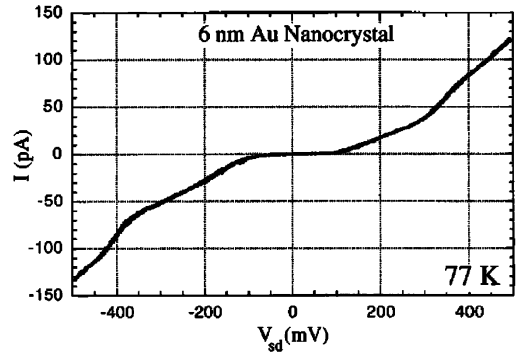

Figure 68. $I-V$ characteristic of a 5.8-nm diameter Au nanocrystal measured at 77 K. Several Coulomb steps of period ΔVsd = 200 mV can be seen. Reprinted with permission from ref 391. Copyright 1996 American Institute of Physics.

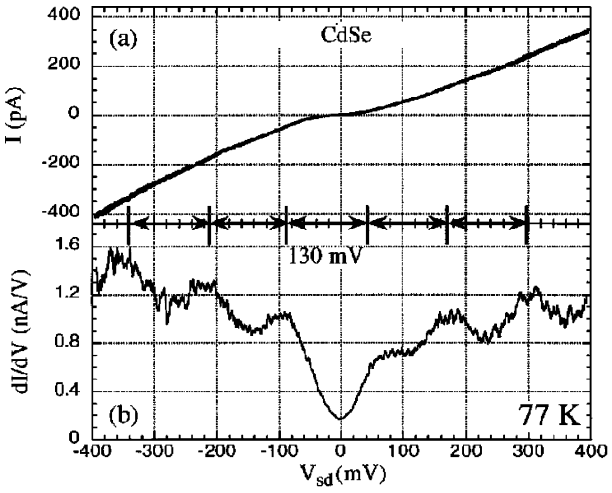

Figure 69. (a) I versus Vsd and (b) dI/dVsd versus Vsd for a 5.8-nm diameter CdSe nanocrystal measured at 77 K. In (b), Coulomb peaks with a spacing of 130 mV are clearly visible. Reprinted with permission from ref 391. Copyright 1996 American Institute of Physics.

lithography and shadow evaporation. Then, an organic monolayer is used to bind nanocrystals to the leads and serve as a tunnel barrier. When a nanocrystal bridges the gap between the leads, it can then be electrically investigated.

Figure 68 shows the measured current (I) as a function of the source-drain bias, V_{sd}, for a 5.8 nm Au nanoparticle system at 77 K. A Coulomb staircase is observed due to incremental charging of the dot

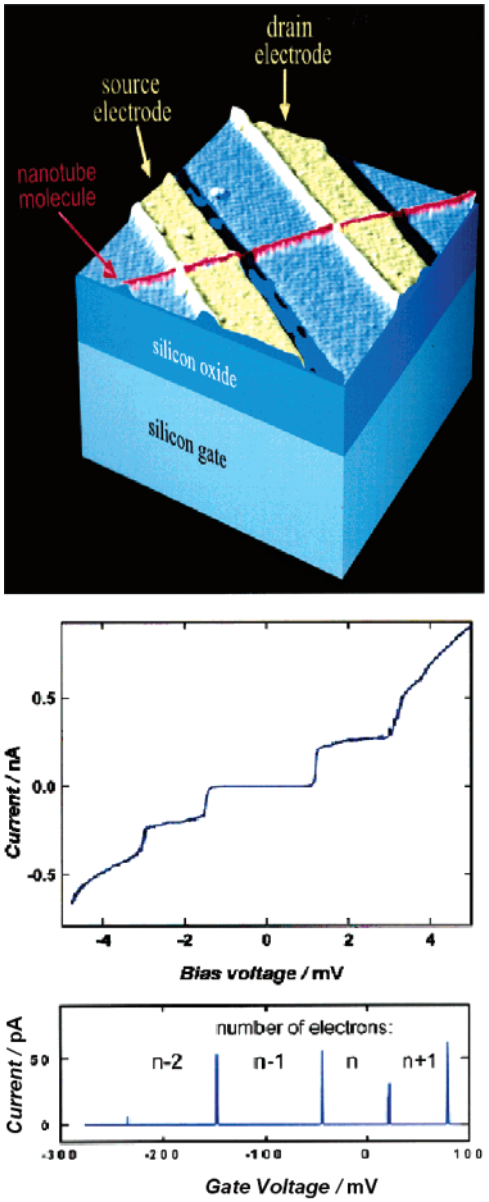

Figure 70. (Top) Illustration of STM spectroscopy measurements on a carbon nanotube. (Middle) $I-V$ characteristics of the tube on a straight line along the tube axis. Current steps correspond to discrete energy states entering the bias window. (Bottom) Discrete charging exhibits Coulomb blockade. Reprinted with permission from *Science* (http://www.aaas.org), ref 400. Copyright 1999 American Association for Advancement of Science.

by single electrons with increasing V_{sd}. The period of these steps, ΔV_{sd}, is 200 mV. Figure 69 shows I and dI/dV_{sd} versus V_{sd} for a 5.8 nm CdSe nanocrystal measured at 77 K. Here, a Coulomb staircase with a period of 130 mV is observed.[391]

STM is commonly employed to study the electronic and conductivity properties of metallic carbon nanotubes.[2,395−401] Figure 70 shows an illustration of STM spectroscopy measurements on a carbon nanotube (top). The $I-V$ characteristics of the tube were measured on a straight line along the tube axis, and current steps correspond to discrete energy states entering the bias window (middle). Also, discrete charging was observed (bottom). The above observations clearly exhibit Coulomb blockade in carbon nanotubes.[400−401]

6. Nonradiative Relaxation of Nanoparticles of Different Shapes

6.1. Nonradiative Relaxation in Metal Nanostructured Systems

6.1.1. Background

Time-resolved transmission, reflectivity,[259,260,402−413] and two-photon photoemission spectroscopies[414−419] have been used to study the interaction between the electrons and the lattice vibrations (phonons) in bulk metallic materials. The electrons of the metal can be selectively excited, and the electron−phonon coupling can be studied in real time, with the advancement of ultrashort laser pulses, which are shorter than the electron−phonon energy relaxation time.[402,403] Electron−electron interactions are strong enough to thermalize the electron gas within the duration of the laser pulse excitation due to the high electron density in metals. Because of the large difference in their heat capacities, the electrons and the lattice can be treated as two coupled subsystems according to the two-temperature model (TTM).[420]

In interband transitions, the holes in the low-lying d band recombine with the excited electrons above the Fermi level or the unexcited electrons below the Fermi level in the time range of tens of femtoseconds,[421−423] which is faster than or comparable with the duration of the laser pulse excitation. It is the high density of the charge carriers in the conduction band that leads to fast interband relaxation. If an Auger-type recombination mechanism process takes place for the interband relaxation, then after the excitation pulse, highly excited electrons are present within the conduction. These electrons have an average excess energy above the Fermi level, which is equal to the exciting photon energy as the holes in the d band have already been filled by the initial electron−electron scattering.[259,260] In the case of gold thin films, a typical electron−phonon relaxation process occurs within a few picoseconds.[259,260,402−419]

The effect of size on the electron−phonon coupling can be directly analyzed by measuring the transient optical response of metal nanoparticles. In the nanoparticle, the reduction in the size and dimensionality of the material introduces new boundaries at the surface. Enhanced electron-surface scattering[424,425] could also be important for the energy relaxation of hot electrons. The relaxation dynamics in these zero-dimensional dots could be further altered by the reduction in the density of electron and phonon states. The bulk band structure of the nanoparticles is well-developed in the size range of 10−100 nm gold nanoparticles.[37,260] Compared with the thermal energy, the average energy spacing between adjacent energy levels within the conduction band is small. Thus, quantum size effects in the relaxation dynamics are expected to occur only in very small gold clusters, which lack intense plasmon absorptions. The presence of a well-developed plasmon band can, however, be very advantageous in following the optical response of excited metal nanoparticles.[426−449] For a 20 nm gold nanoparticle with ~200 000 atoms, a transient broadening of the surface plasmon absorption results in a bleach at the plasmon absorption band maximum with two positive absorption features at higher and lower energies. The rate of the bleach recovery directly monitors the rate of the electron−electron, electron−phonon, and phonon−phonon dynamics.[259,260]

6.1.2. Theoretical Modeling of the Transient Optical Response

Theoretically, the changes in the real ϵ_1 and imaginary ϵ_2 parts of the complex dielectric function induce the broadening of the plasmon band.[405,408,409,430,447,448] For continuous-wave thermomodulation experiments, the changes in ϵ_1 and ϵ_2 are related to the changes in the electron distribution function.[450,451] In the constant-matrix approximation, the change in ϵ_2 is given by the equation[409]

$$\Delta\epsilon_2 \propto \frac{1}{(h\nu)^2}\int D(E,h\nu)\Delta\rho \, \mathrm{d}E \tag{31}$$

where $D(E, h\nu)$ is the joint density of states of the final state with respect to the energy E[450] and $\Delta\rho$ denotes the change in the electron distribution, f. The change ($\Delta\rho$) in the electron distribution for a thermalized electron gas is calculated from the difference between the two Fermi electron distributions at room temperature and at a higher temperature after laser excitation. A given change in $\Delta\rho$ in the electron distribution corresponds to a $\Delta\epsilon_2$. The change $\Delta\epsilon_1$ in the real part of the dielectric constant is then computed from $\Delta\epsilon_2$ using the Kramers−Kronig relationship[345]

$$\Delta\epsilon_1(h\nu) = \frac{2}{\pi}P\left(\int \frac{h\nu'\Delta\epsilon_2(h\nu)}{(h\nu')^2 - (h\nu)^2}\,\mathrm{d}(h\nu')\right) \tag{32}$$

where P denotes a Cauchy principal value integral that extends over the whole frequency range.

The differential transmission $\Delta T/T$ of the gold nanoparticles at low excitation levels is approximately equal to the change in absorption and can be expressed as[409]

$$\frac{\Delta T}{T} = \frac{\delta(\mathrm{In}T)}{\delta\epsilon_1}\Delta\epsilon_1 + \frac{\delta(\mathrm{In}T)}{\delta\epsilon_2}\Delta\epsilon_2 \tag{33}$$

The coefficients of proportionality can be calculated using the theoretical expression for the plasmon band absorption. This model has been used successfully in describing the optical response of metal nanoparticles excited by an ultrashort laser pulse.[259,260,430,447,448]

6.1.3. Electron–Electron Thermalization in Gold Nanoparticles

Using pump−probe laser spectroscopy (transient absorption, transmission, or reflectivity), the thermal response of an excited sample, expressed as temperature changes, can be obtained from the optical changes induced by the pump pulse. Fermi−Dirac statistics describe the electron distribution within the conduction band of the metal after a rapid internal electron relaxation.[345] Each Fermi electron distribu-

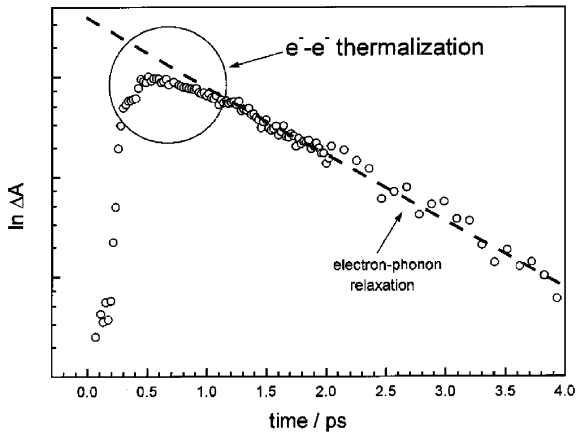

Figure 71. Electron−electron thermalization in spherical gold nanoparticles. The plasmon bleach recovery of 22-nm gold nanoparticles probed at 530 nm is plotted against a logarithmic scale. Reprinted with permission from *Annual Reviews in Physical Chemistry* (http://www.AnnualReviews.org), ref 260. Copyright 2003 Annual Reviews.

tion is associated with an electronic temperature. Therefore, the electronic temperature can be used to follow the energy relaxation of the electron gas into the lattice motion, as will be discussed in the following section.[259,260]

Shown in Figure 71 is the kinetic bleach recovery trace recorded for 22 nm gold nanoparticles at 530 nm after excitation with 800 nm femtosecond laser pulses.[260,448] If the long-time component of phonon−phonon interactions is neglected, a single-exponential decay should be obtained due to electron−phonon scattering. However, due to the nonthermal electron distribution, deviations at early times are clearly visible.[410] The bleaching of the plasmon band is less intense for a nonthermalized than for a thermalized electron distribution, which is consistent with the calculation of the transient absorption spectrum.[260,409,448]

The electron thermalization time is on the scale of <500 fs[259,260,448] and is much longer than a scattering event involving only two electrons, which is on the order of 10 fs according to the Fermi-liquid theory,[452] because it requires all of the electrons to scatter with each other to reach a Fermi distribution. The effect of these processes on the transient absorption spectra is rather small (compared with theoretical results) and only detectable at low pump powers,[448] because the processes of electron−electron, electron−phonon, and phonon−phonon scattering are not really sequential but overlapping processes. Before an equilibrium Fermi electron distribution can be fully established via electron−electron scattering, electron−phonon coupling occurs.[259,260,448]

6.1.4. Electron–Phonon Relaxation in Gold Nanoparticles

Figure 72 shows the steady ground-state absorption (top half with positive absorption) and transient absorption spectra (bottom half with negative absorption, thus bleach) of 15 nm gold particles at different delay times after the excitation pulse of 400 nm.[259] Compared with the ground-state absorption, a bleach and two positive absorptions in the transient

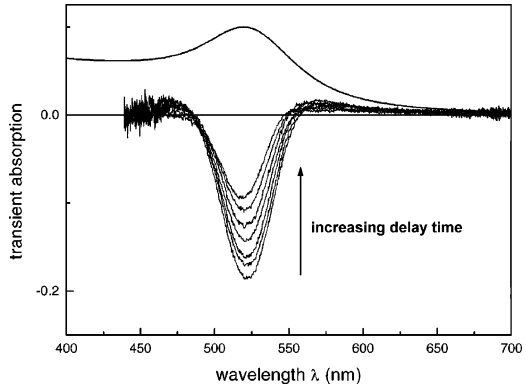

Figure 72. Steady-state absorption and transient absorption spectra of 15-nm gold nanoparticles after excitation with 400-nm laser light. The series of spectra corresponds to different delay times between the pump and probe pulses. Reprinted with permission from ref 259. Copyright 2000 Taylor and Francis.

spectrum (difference spectrum) is observed due to a broader but less intense plasmon absorption at a higher electronic temperature after laser excitation. The plasmon band bleaches at its maximum, corresponding to a higher transmission of light of the excited solution. Two weaker absorption bands are also visible at lower and higher energies than the plasmon band maximum,[426−428,446−448] which is attributed to a broadening of the surface plasmon resonance at higher electronic temperatures.

The optical response is independent of the excitation wavelength.[259,260,448] At 400 nm or shorter wavelengths than the plasmon absorption, interband transitions from the d band to above the Fermi level are excited. Excitation at the plasmon resonance causes the oscillation of the conduction electrons and the collective excitation of all the conduction electrons. This could be regarded as intraband transitions, which are also excited to the red of the plasmon band. All of these excitation processes result in heating of the electron gas.[259,260,448]

After the thermal equilibration is established, the laser-induced optical changes decay via electron−phonon scattering between the electrons and the lattice.[259,260,427,430,446] The absorbed laser energy is then released to the surrounding medium by phonon−phonon interactions.[427,430,446] The electron−phonon and phonon−phonon relaxation times can be obtained by measuring the bleach recovery as a function of time as shown in Figure 73. The transient signal is most sensitive at the wavelength of 520 nm, coinciding with the plasmon band bleach maximum. The plasmon bleach recovery can be fitted to a biexponential decay function with relaxation times of about 3.4 and 100 ps, corresponding to the electron−phonon interactions and the energy relaxation of the hot lattice via phonon−phonon interactions to the surrounding medium, respectively.[259,260,446] At 480 nm, the signal first shows absorption and then bleaches at later times, which is explained by a red shift of the plasmon resonance due to a volume expansion of the hot particles and, hence, a lower electron density and lower plasmon frequency.[259,260,430] At 550 nm, the transient absorption signal changes from a bleach into an absorption at a comparable

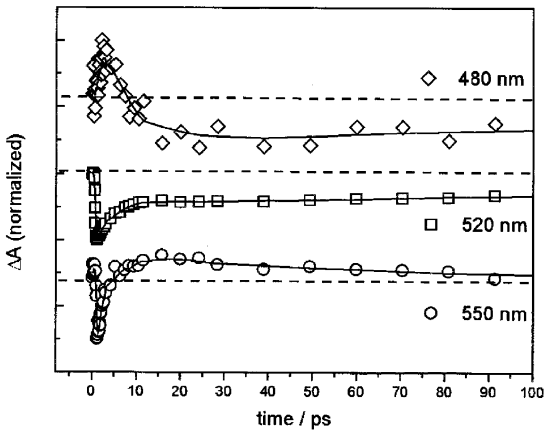

Figure 73. Temporal evolution of the plasmon bleach spectra at certain wavelengths: (◇) 480 nm; (□) 520 nm; (○) 550 nm. Reprinted with permission from *Annual Reviews in Physical Chemistry* (http://www.AnnualReviews.org), ref 260. Copyright 2003 Annual Reviews.

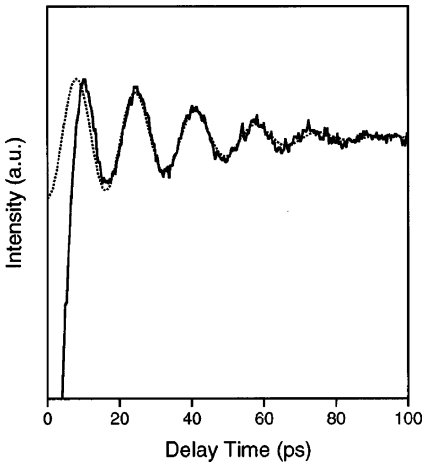

Figure 74. Transient absorption data obtained for 60 nm diameter Au particles (solid line) and signal calculated with a distribution of cosine functions with frequencies and weights determined by the measured size distribution of the sample (dashed line). Reprinted with permission from ref 432. Copyright 1999 American Institute of Physics.

time delay of ~10 ps, resulting from a red shift and the narrowing of the plasmon bleach.[259,260]

A 5−20 ps periodic oscillation of the transient absorption signal as shown in Figure 74 is found at a longer wavelength than the plasmon band maximum.[259,260,432] These oscillations result from the low-frequency acoustic breathing modes of the hot nanoparticles, which are excited by the rapid heating of the particle lattice after laser excitation as suggested by del Fatti et al.[440,441] and Hartland et al.[431,432] Because of the excitation of these modes, the volume of the nanoparticles periodically increases and decreases, leading to a shift in the plasmon band maximum as the free-electron density changes with the volume, because a volume expansion causes a drop in the free-electron density and a red shift of the plasmon, whereas volume contraction has the opposite effect. The frequencies of the acoustic modes are inversely proportional to the nanoparticle radius.[431,432,440,441]

Physically, the transient behavior of the plasmon band broadening is also associated with a faster

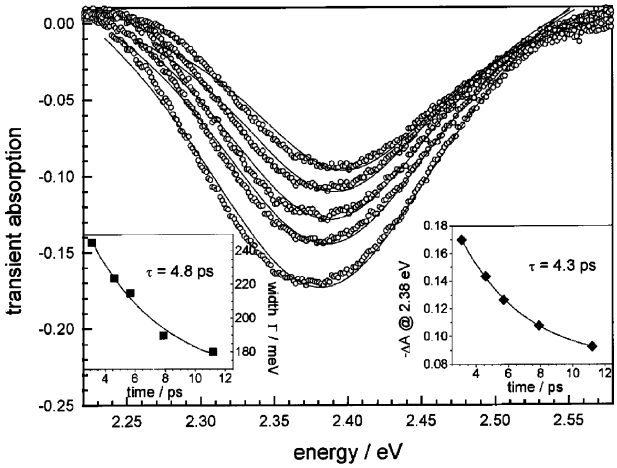

Figure 75. Transient absorption spectra of 15-nm gold nanoparticles after excitation at 400 nm with 100-fs laser pulses recorded at different delay times. The left inset shows the decrease in the bleach line width with increasing delay time. The line width was obtained by fitting a Lorentzian function (−) to the experimental spectra (○). The right inset illustrates the decay of the transient bleach signal monitored at 2.38 eV. Reprinted with permission from ref 259. Copyright 2000 Taylor and Francis.

dephasing time (T_2) of the coherent plasmon oscillation.[426−428] At higher temperatures, the occupation of higher electronic states leads to an increased electron scattering rate[452] and thus to an increased damping of the plasmon oscillation. For gold nanoparticles embedded in a sol−gel matrix, an increase by 120 meV in the plasmon bandwidth was found, and for a hot electron distribution at 4000 K, an average electron−electron scattering rate was calculated to be (10 fs)$^{-1}$ by Perner et al.[427]

Figure 75 shows the decay of the transient plasmon band broadening following the same kinetics as the decay of the bleach intensity for 15 nm gold nanoparticles. This was concluded from transient absorption spectra obtained with excitation at 400 nm with 100 fs laser pulses at different delay times. The line width decays with a lifetime of 4.8 ps, whereas the plasmon bleach intensity at its maximum (2.38 eV) decays with a lifetime of 4.3 ps.

6.1.5. Shape and Size Dependence on the Electron−Phonon Relaxation Rate

Figure 76 shows the transient absorption and steady-state absorption spectra of gold nanorods with a mean aspect ratio of 3.8. The spectra were recorded at a delay time of 6 ps after excitation with 100 fs laser pulses having a center wavelength of 400 nm. Both the transverse and longitudinal surface plasmon bands are bleached due to a hot electron gas.[449] The bleach of the two bands and the positive absorption around 600 nm are consistent with a broadening of these bands. The magnitude of the bleach is less pronounced for the longitudinal plasmon band than for the transverse plasmon band, which is evaluated by comparing the intensity ratio of the two bands in the transient absorption spectrum with that for the steady-state spectrum.[259,260]

Because increased electron-surface scattering is thought to be responsible for the plasmon band broadening in the intrinsic size region, femtosecond

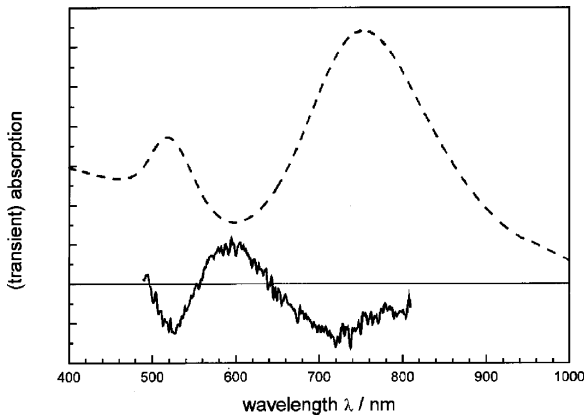

Figure 76. Optical response of gold nanorods after excitation with a femtosecond laser pulse. Transient absorption (—) and steady-state absorption spectrum (- - -) of gold nanorods with a mean aspect ratio of 3.8 are shown. Both spectra are scaled to arbitrary units. The transient absorption spectrum was recorded at a delay time of 6 ps after excitation with 100-fs laser pulses having a center wavelength of 400 nm. Reprinted with permission from ref 259. Copyright 2000 Taylor and Francis.

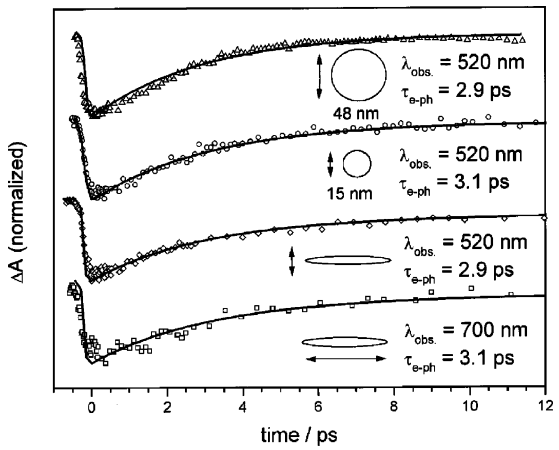

Figure 77. Size and shape dependence of the electron–phonon relaxation time. Plasmon bleach recovery was measured for 48- and 15-nm gold nanoparticles and for the transverse and longitudinal modes of gold nanorods with an average aspect ratio of 3.8 (from top to bottom). Reprinted with permission from ref 250. Copyright 2000 Taylor and Francis.

transient absorption experiments are carried out to determine whether electron-surface collisions are mainly inelastic and contribute effectively to energy relaxation. With a mean free path of ~40–50 nm in gold and silver,[345] the measured electron–phonon relaxation time should increase with decreasing particle radius if electron-surface scattering becomes an important relaxation pathway for small particles. Figure 77 shows the plasmon bleach recovery measured for 48 and 15 nm gold nanoparticles in comparison to the bleach recovery of the transverse and longitudinal modes of gold nanorods with an average aspect ratio of 3.8 (top to bottom). The laser pump power and optical densities of the samples at the excitation wavelength were adjusted to induce comparable initial electron temperatures by the exciting femtosecond laser pulse to ensure the measured relaxation times can be directly compared with each other. For 48 and 15 nm gold nanoparticles, no significant difference in the electron–phonon relaxation dynamics can be observed,[259,260,448] and the relaxation dynamics appear to be independent of the particle shape and the specific plasmon band excitation mode (transverse or longitudinal mode).[259,260,449] The electron-surface scattering as a dominant energy relaxation pathway was excluded from these experiments and other studies and on other metal nanoparticles such as silver nanoparticles.[432,439,447]

In other experiments, however, contradicting results were also observed.[438,441,453–455] For example, a size dependence was found by Smith et al. in the comparative study of 15 nm gold nanoparticles with small Au_{13} and Au_{55} clusters.[438] The electron–phonon coupling decreases and the electron-surface scattering increases as the nanoparticle size decreases. Furthermore, enhanced electron-surface scattering was found for tin, gallium, and silver nanoparticles as the size of the particles decreased[441,453–455] from >10 to <1 nm.

The difference in the size dependence of the electron–phonon relaxation in different metallic nanoparticles was explained by Hodak et al. by the contribution of the electron-surface coupling constant to the total (bulk) coupling constant.[456–458] In gold nanoparticles as small as 2.6 nm, the excitation of capillary and acoustic surface modes by the scattering of the electrons with the particle surface is calculated to account for <10% of the electron energy loss. The ratio of the electron density to the metal density in a specific metal determines the relative magnitude of the electron-surface coupling constant compared with the total electron–phonon coupling constant. In nanoparticles consisting of heavy atoms such as gold, the excitation of surface vibrations is suppressed as the electrons scatter rather elastically. In nanoparticles made of lighter atoms, a size-dependent energy relaxation becomes possible via electron-surface interactions with more valence electrons contributing to the conduction band and smaller atomic mass.[456]

6.1.6. Pump Power Dependence of the Electron–Phonon Relaxation Rate

The electron–phonon relaxation times are pump power dependent[429,430,447,448] as demonstrated in Figure 78.[259,260,448] The measured lifetimes increase from 1.5 to 3.6 ps as the pump power increases from 50 to 160 nJ. With increasing pump power and, hence, increasing electron temperature, the electron–phonon relaxation time increases.[429,430,447,448] However, the effective rate constant $[g/C_e(T_e)]$ of the thermal relaxation of the electron gas (dC_e/dT_e) is temperature dependent, because the electronic heat capacity depends on the electron temperature ($C_e \propto T_e$).[345] From a plot of the measured electron–phonon relaxation times versus power, the electron–phonon coupling constant can be obtained,[429,430] which compares well with the value measured for bulk gold films.[405]

6.2. Nonradiative Relaxation in Semiconductor Nanostructured Systems

Time-resolved nonlinear optical spectroscopy is a powerful tool for studying the energy structures and

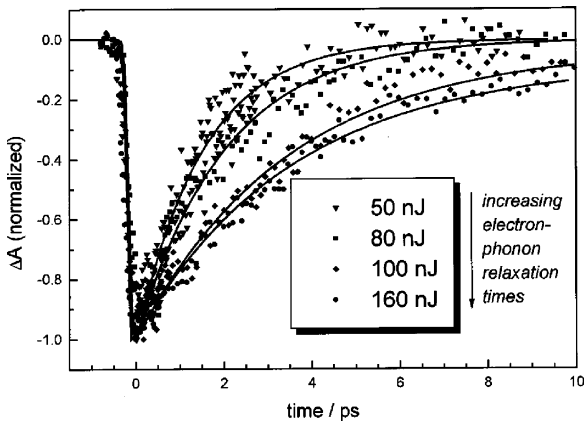

Figure 78. Pump power dependence of the electron−phonon relaxation time in gold nanoparticles. The plasmon bleach recovery of 15-nm gold nanoparticles is probed at 520 nm after excitation at 400 nm with laser pulses of various energies. Reprinted with permission from ref 259. Copyright 2000 Taylor and Francis.

carrier dynamics in bulk and low-dimensional materials.[329,459−462] In nanoparticles, state-filling and Coulomb multiparticle interactions (the carrier-induced Stark effect) primarily cause resonant optical nonlinearities.[459,460] State-filling leads to bleaching of the interband optical transitions involving populated quantized states proportional to the sum of the electron and hole occupation numbers. If the linear absorption spectrum of nanocrystals is expressed as a sum of separate absorption bands corresponding to different quantized optical transitions, the induced absorption changes ($\Delta\alpha$) can be expressed as

$$\Delta\alpha(\hbar\omega) = -\sum_i a_i G_i(\hbar\omega - \hbar\omega_i)(n_i^{\mathrm{e}} + n_i^{\mathrm{h}}) \quad (34)$$

where $G_i(\hbar\omega - \hbar\omega_i)$ is the unit-area absorption profile of the $\hbar\omega_i$ transition, a_i is the transition area (proportional to its oscillator strength), and n_i^{e} and n_i^{h} are occupation numbers of electron and hole states involved in the transition, respectively. The occupation numbers can be found using the Fermi distribution function under thermal quasi-equilibrium after the intraband relaxation is finished.[329,459−462] After the electrons and holes are excited far from the equilibrium, both will return to the ground state after radiative and nonradiative relaxations, via carrier−carrier (electron−electron, hole−hole, and electron−hole), carrier−phonon, and phonon−phonon interactions. In the following, the carrier relaxation dynamics will be focused on the systems of nanoparticles, because detailed reviews regarding the carrier relaxation dynamics in quantum well systems have already been conducted.[462]

6.2.1. II–VI Semiconductor Systems

6.2.1.1. Nonradiative Relaxation by Pump−Probe Technique. The carrier relaxation dynamics in semiconductor nanomaterials have been studied extensively by different research groups.[329,462−465] Very good reviews on this topic have been written by V. I. Klimov, J. Z. Zhang, and A. J. Nozik over the past few years.[329,462−464] In these studies, the pump−probe technique is a common method used in exploring the carrier relaxation dynamics in these systems.[329,462−465] In a typical pump−probe experiment, the sample is excited by an ultrafast narrow laser pulse and is probed with a continuous band (usually white light) laser pulse. The absorption change is monitored as a function of the delay time between the excitation and the white light pulses. This provides information about the relaxation of the excited states or that of the excited electrons and holes.[329,462−465] In the II−VI semiconductor nanoparticle system, CdSe nanoparticles are the most extensively studied materials,[329,465−475] and the review will focus on this system to elucidate the general relaxation process and phenomena in similar semiconductor nanoparticles.

The absorption changes in the visible and UV regions due to state-filling are dominated by electrons,[476] because the occupation probabilities of electron states are much greater than those of the coupled hole states at room temperature. This is due to the degeneracy of the valence band and the large hole to electron mass ratio (in CdSe, $m_{\mathrm{h}}/m_{\mathrm{e}} = 6$), which makes the hole populations spread over many adjacent levels by thermal distribution. The extremely fast depopulation of the initially excited valence-band states [sub-picosecond to picosecond (ps) time scales] further reduces the role of holes in transitions' bleaching.[329,474,477]

The local fields generated by photoexcitation of carrier populations lead to a shift of optical transitions and changes in transition oscillator strengths due to the Stark effect (specified as follows), caused by Coulomb interactions between one or several e−h pairs excited by the pump pulse and the e−h pair generated by the probe pulse.[329] Unlike state-filling, which selectively affects only transitions involving populated states, the carrier-induced Stark effect modifies all transitions and comes into play when charge separated e−h pairs are formed.[321,478]

The early-time TA spectral shape of CdSe nanocrystals, taken at low pump intensities corresponding to initial populations $\langle N_0 \rangle$ of fewer than one e−h pair per nanoparticle on the average, is similar to that of the second derivative of the absorption spectra.[329,478−480] The carrier-induced Stark effect is manifested both as bleaching features ($\Delta\alpha < 0$) at the positions of the steady-state transitions and as photoinduced absorption (PA) features ($\Delta\alpha > 0$) at the positions of the new (shifted) transitions in TA spectra.[329] The contribution of state-filling to band-edge signals at $\Delta t \leq 100$ fs is not significant.[329] As the time Δt increases, the carriers relax into low-energy quantized states, leading to increasing contribution from state-filling to the band-edge absorption changes.[329] The 0.1 ps TA spectrum is entirely due to the carrier-induced Stark effect, and at 0.5 ps, the bleach of the 1S and 1P electron states increases due to increasing population or an increased state-filling effect. After the time of the electron relaxation into the 1P state delayed by ~400 fs, the bleach of 1P decreases due to relaxation of the 1P electrons into the lower 1S state and the bleach of 1S is further enhanced.[329,475]

6.2.1.2. Pump Dependence of Band-Edge Bleaching Signals. After the high-energy relaxation is complete and the 1S electron state is populated, the bleaching of the 1S state can be attributed to both the Stark effect and state-filling. If only one electron occupies the 1S state, the state-filling process completely saturates one of the two spin-degenerate 1S transitions, whereas the absorption changes for the unpopulated transition are due to the Stark effect. State-filling-induced signal within the 1S and 2S transitions estimated from the product of the population factor $n_{1S}^{e} = \langle N_0 \rangle/2$ and α_0 indicates that state-filling provides a dominant contribution to $\Delta\alpha$.[329]

In the pump-dependent TA spectra, the relative contribution of state filling to transitions bleaching increases as the average nanocrystal population increases.[329] PA features due to Stark effect can be observed in the spectrum taken at $\langle N_0 \rangle = 0.9$, whereas bleaching is observed over the entire spectral range at pump levels above $\langle N_0 \rangle \geq 2$. The pump-dependent $\Delta\alpha d$ spectra were fitted to a sum of four Gaussian bands, with the positions and the widths of the bands derived from the linear absorption spectrum. The transitions areas were presented as $a_i = p_i a_{0i}$, where a_{0i} are the areas of transitions in the linear absorption spectrum and $p_i(\langle N \rangle)$ are "saturation" coefficients describing the pump-dependent transition bleaching. In terms of the state-filling model, these coefficients account for the population factors as follows:

$$p_i = n_i^{e} + n_i^{p} \tag{35}$$

The pump-density dependences for p_1 and p_2 are almost identical, as expected for the 1S and 2S transitions due to a population increase of the same 1S electron state. The p_3 shows a delayed growth with the onset at $\approx$2 as expected for the filling of the 1P electron level. The growth of p_4 is further delayed (onset at $\sim$5), and this indicates the beginning of the filling of the next (1D) electron level.[329] A good match of the pump dependence of the normalized saturation coefficients p_1 and p_2 was found with pump-dependent occupation numbers of the 1S and 1P electron states calculated within the state-filling model.[329] The bleaching of nanocrystal transitions involving occupied states is primarily due to state-filling by populating of electron quantized states. The sequential filling of electron shells in QD artificial atoms is analogous to filling of electron orbitals in atoms of natural elements.[329]

The pump dependence of the normalized 1S absorption changes for nanocrystals of different sizes as shown in Figure 79. The spectrum measured immediately after the intraband relaxation is complete (Δt from 1 to 2 ps) and is normalized with 1S absorption changes and can be fitted to the equation[329]

$$-\Delta\alpha/\alpha_0 = k_1\langle N_0 \rangle/(k_2 + N_0) \tag{36}$$

with $k_1 = 1.05 \pm 0.15$ and $k_2 = 1.6 \pm 0.3$,[1] which allows the accurate determination of instant nanocrystal populations as derived from the measured $\Delta\alpha$ dynamics.[329]

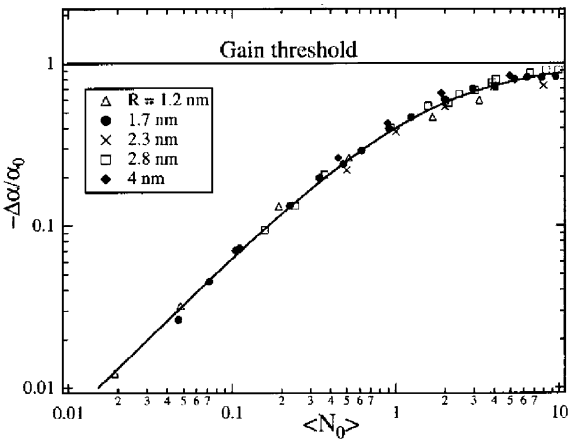

Figure 79. Pump dependence of normalized 1S absorption changes for NCs of different sizes (symbols) fit to the universal pump dependence $-\Delta\alpha/\alpha_0 = k_1\langle N_0 \rangle/(k_2 + \langle N_0 \rangle)$, with $k_1 = 1.05$ and $k_2 = 1.6$ (line). Reprinted with permission from ref 329. Copyright 2000 American Chemical Society.

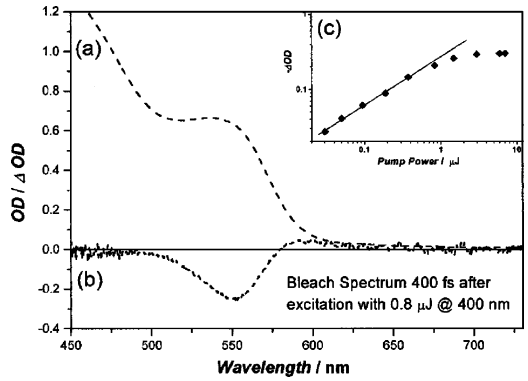

Figure 80. (a) Absorption spectrum of the CdSe NP solution showing an onset of absorption at 600 nm. The lowest energy transition is found at 560 nm. (b) Excitation leads to a bleaching of the absorption spectrum. The bleach intensity of the lowest exciton transition (560 nm) depends on the excitation power. In our experiment, for 0.8 μJ per pulse, half of the absorption is bleached at a delay time of 400 fs. (c) Saturation of the bleaching occurs between 1 and 2 μJ excitation power. Reprinted with permission from ref 465a. Copyright 2002 American Institute of Physics.

In nanocrystals, the bleaching at room temperature induced by state-filling is primarily due to electron populations.[329] In a simple two-level system, both electrons and holes contribute to the 1S bleaching when the 1S optical gain is at $\langle N_0 \rangle > 1$.[474] However, no crossover from absorption is shown to gain at the position of the 1S transition. The maximum $\Delta\alpha$ measured experimentally corresponds to the complete bleaching of the 1S transition ($\Delta\alpha \approx \alpha_0$), for the case of only electrons contributing to the state-filling-induced signals.[474]

In some other pump−probe experiments, the CdSe nanoparticles were pumped at high energies and probed from the visible to the infrared.[465] Figure 80 shows the absorption and bleaching spectra of CdSe nanoparticles 4.5 nm in diameter.[465] The bleach spectrum at 400 fs delay time after 400 nm excitation reflects the bleaching of the lowest energy transitions. The bleaching of the lowest energy transitions increases as the pump power increases and levels off

at certain pump power (1.5 μJ), which is consistent with the previous analysis.[465]

6.2.1.3. Nanocrystal Size Dependence on Intraband Relaxation Rates. In bulk II−VI semiconductors, fast (typically sub-picosecond) carrier cooling dynamics is observed, which is dominated by the Frhlich interactions with longitudinal optical (LO) phonons.[329,481,482] In nanocrystals, the carrier relaxation mediated by interactions with phonons is hindered dramatically because of restrictions imposed by energy and momentum conservation leading to a phenomenon called a "phonon bottleneck".[308,329,462,483,484] For example, reduction in the energy loss rate is expected in the regime of strong confinement because the level spacing can be much greater than LO phonon energies; hence, carrier−phonon scattering can occur only via weak multiphonon processes.[308,329,462,483,484]

However, a number of recent experimental results indicate that carrier relaxation in II−VI nanocrystals is not significantly slower than that in bulk materials.[329,462,477,478,485,486] In CdSe nanocrystals, strong evidence against the existence of the phonon bottleneck was found in the sub-picosecond 1P-to-1S electron relaxation even in samples where the 1S−1P energy separation is >10 LO phonon energies.[329,473−475] The decay of the 1P bleaching and the complementary growth of the 1S bleaching provide a measure of the rate of the 1P-to-1S energy relaxation, for example, with a 540 fs time constant for 4.1 nm NCs.[329,473−475]

Intraband relaxation becomes more rapid with decreasing nanocrystal size, where the 1S state population dynamics in nanoparticles of different radii show a linear decrease in the 1S buildup time with decreasing nanoparticle radius, from 530 fs for R = 4.1 nm to 120 fs for R =1.7 nm.[329] The energy relaxation rate (dE_e/dt) is size-dependent in nanocrystals and rapidly increases (roughly as $R^{-2.6}$) with decreasing particle size. In nanoparticles, the energy loss rate is greater than the rate expected for a multiphonon emission.[329]

6.2.1.4. Electron−Hole Interactions and Intraband Energy Relaxation. Energy relaxation in nanoparticles is dominated by *nonphonon* energy-loss mechanisms, such as Auger-type e−h energy-transfer processes, which is based on the extremely fast electron relaxation as well as a confinement-induced enhancement in the relaxation process.[329] Auger-type e−h energy transfer involves transfer of the electron excess energy to a hole with subsequent fast hole relaxation through its dense spectrum of states based on the intrinsic Auger-type e−h interactions and leads to significantly faster relaxation times than those for the multiphonon emission.[487]

In three-pulse femtosecond TA experiments,[329] the carrier relaxation is affected by the surface of the nanoparticles because electron and hole wave functions in nanoparticles are strongly affected by nanocrystal surface properties. The sample is excited by a sequence of two ultrashort visible and infrared (IR) pulses and probed by broad-band pulses of a femtosecond white-light continuum.[329] The visible interband pump is used to create an e−h pair in the nanocrystal, whereas a time-delayed intraband IR pump is used to re-excite an electron within the conduction band. Electron intraband dynamics for different delays between the visible and the IR pump pulses were monitored. The electrons generated directly in the lowest quantized 1S state remain in this state until they are re-excited by the IR pulse. However, holes initially populating the excited $2S_{3/2}$ state rapidly relax due to transitions into lower energy quantized states inside the nanocrystal or due to charge transfer to a capping group. By varying the IR re-excitation time, the effect of modification in the hole wave function (during hole relaxation/transfer) on electron intraband dynamics can be evaluated.[329] In ZnS-overcoated nanocrystals, the 1P-to-1S relaxation is extremely fast (320 fs time constant) for all Δt_{IR} delays from 100 fs to 1 ps, but in the case of pyridine-capped nanocrystals, the electron dynamics show a strong dependence on the delay between visible and IR pulses. At Δt_{IR} = 70 fs, the relaxation constant is 250 fs, similar to that in the ZnS-capped particles. By increasing the visible−IR pump delay, the time for the electron to relax gradually increases to 3 ps at Δt_{IR} = 430 fs. A further increase in Δt_{IR} does not lead to significant changes in electron intraband dynamics.[329] In CdSe nanoparticles passivated with pyridine, an efficient hole acceptor, the electron intraband relaxation is strongly affected due to the e−h interactions, because the e−h coupling is strong immediately after photoexcitation and is reduced dramatically after the hole is transferred to a capping group.[329] The threshold delay of roughly 400 fs found in the three-pulse experiments is very close to the hole-transfer time to a capping molecule inferred from visible TA measurements of pyridine-capped nanocrystals.[329,470] The pyridine cation (formed by hole transfer) is observed in the TA spectra as a long-lived broad PA band below 2.5 eV and has a rise time of ~450 fs. In ZnS-capped samples, the holes are confined within the dot during the first 600 fs after excitation,[329,474] and the e−h coupling changes significantly. In pyridine-capped nanocrystals, the e−h coupling is strong immediately after photoexcitation and significantly smaller after the hole transfers to the pyridine, inducing the >10-fold slowing in the electron intraband relaxation.[329]

These observations are consistent with the electron-relaxation mechanism involving Coulomb-interaction-mediated e−h energy transfer.[487] Although the above results on well-capped nanoparticles could be successfully discussed in terms of lowest electron and hole coupling mechanism, one must always be aware of the surface involvement in the relaxation of hot electrons in these small nanoparticles. First of all, small nanoparticles will always have their excited electrons with a nonvanishing amplitude at the surface. Second, it is difficult to synthesize these nanocrystals with surfaces that are free of surface states, trapping sites, and large organic molecules as capping material that could act either as an electron acceptor or as an excellent heat bath. The hotter the electron is in a nanoparticle, the larger its amplitude is at the surface and the more probable its relaxation or capture is by the surface. Recently, a number of

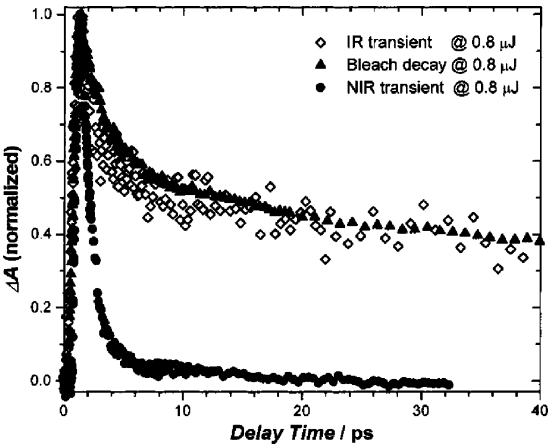

Figure 81. Femtosecond time-resolved kinetic traces that describe the response of the visible bleaching (570 nm probe wavelength, ▲), the IR (4.8 μm, ◇), and the NIR (1960 nm, ●) after excitation with 0.8 μJ at 400 nm. In this representation it becomes evident that the bleach (which actually is a negative signal) and the IR transient absorption occur on the same time scales (2 and 30 ps) and could be due to the same decay process. On the other hand, the NIR transient absorption seems to describe an independent event with a fast time constant of 1.2 ps. Reprinted with permission from ref 466a. Copyright 2001 American Chemical Society.

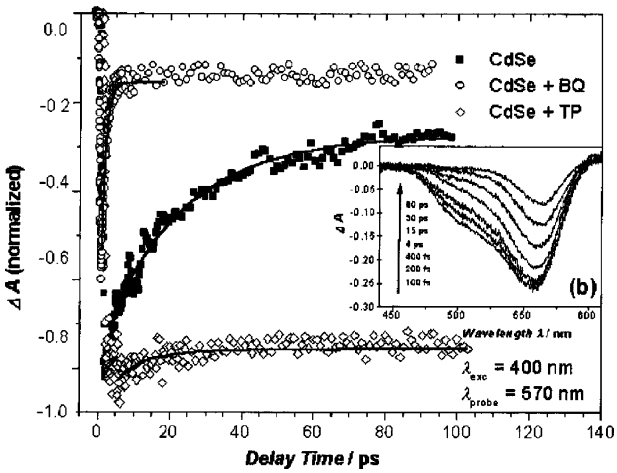

Figure 82. Kinetic behavior of the bleach as monitored at 570 nm for CdSe nanoparticles without the addition of quenchers (■). The decay times are fitted to be 2 and 30 ps. After addition of benzoquinone (BQ), the bleach decay (○) is accelerated to a monoexponential decay with a 2.7 ps lifetime. A weak off-set is observed for lower BQ concentrations, which is probably due to NPs that do not undergo electron transfer. Addition of 4-aminothiophenole (TP) extends drastically the lifetime of the bleach (◇) due to hole trapping and elimination of electron traps. The time-resolved spectra in the visible spectral range are shown inset (b). The bleach maximum is reached after 200 fs at 560 nm. Reprinted with permission from ref 466a. Copyright 2001 American Chemical Society.

observations such as the dependence of the hot electron relaxation rates on size, shape, and excitation energies could be discussed in terms of the calculated hot electron density on the surface of the nanoparticles.[491]

6.2.1.5. Electron and Hole Relaxation Paths in Nanocrystals. *6.2.1.5.1. IR-Pump Probe Technique.* Intraband relaxation leads to a fast establishment of quasi-equilibrium populations of electron and hole nanocrystal quantized states. Besides the radiative mechanism, depopulation of these states occurs via a variety of nonradiative mechanisms, including carrier trapping at surface/interface states and Auger recombination.[329] In CdSe nanocrystals, the 1S bleaching decay shows two distinct regions with a relatively fast sub-100 ps relaxation due to trapping at surface defects and due to slower nanosecond decay. The amplitude of the fast component is sensitive to the degree of surface passivation. The improvement in surface passivation leads to the suppression of the fast decay component, where the repaired electron traps are likely associated with metal dangling bonds.[329] Separation of electron and hole signals is achieved using intraband TA spectroscopy with an IR probe tuned in resonance with either electron or hole intraband transitions.[474,489] In the near-IR range from 0.4 to 1 eV, intraband TA of CdSe nanocrystals can be attributed to electron and hole intraband absorptions.[329,473,474] The hole intraband transitions are at much lower energies due to higher density of states and small energy separation. The fast hole relaxation is independent of surface properties and is likely due to relaxation into intrinsic nanocrystal states.[329]

6.2.1.5.2. Electron and Hole Quencher Technique. The dynamics of electron and hole relaxation processes can be investigated using the technique of electron and hole quenching.[466a] Figure 81 shows three transient signals measured in the visible, NIR, and IR range after identical excitation conditions (excitation with 400 nm pulses of 0.8 μJ energy). The dynamics of the bleaching at 560 nm and the transient absorption at 4800 nm are very similar with time constants of 2 and 30 ps. The NIR signal decays much more quickly (1.2 ps) and is therefore assigned to a different process.[466]

Figure 82 shows the dynamics of the bleach after CdSe nanoparticles were excited with 400 nm femtosecond laser pulses.[466a] The inset shows the resulting bleach which monitors the population of the lowest excitonic states. The population reaches its maximum at 560 nm after excitation for 200 fs. The bleach signal of CdSe nanocrystals (squares) was found to decay with three components (2, 30, and ~200 ps).[466]

By selectively and rapidly removing either the electron or the hole from the photoexcited nanoparticle (NP), the electron or hole relaxation can be distinguished from the bleach signal, respectively.[468] In these experiments, benzoquinone was chosen as the electron acceptor (electron quencher, BQ) and 4-aminothiophenol as the electron donor (hole quencher, TP). The addition of benzoquinone (BQ) to a colloidal solution of CdSe rapidly removes the electrons from the conduction band of the photoexcited NP and forms a short-lived charge-transfer complex that monoexponentially decays with a lifetime of 2.7 ps.[468] The repopulation of the ground state is thereby rate limited by the lifetime of the NP^+BQ^- charge transfer (CT) complex. Because the lifetime of the CT state is 2.7 ps, the excited-state lifetime of the CdSe−BQ conjugate is actually drastically shorter than that of the CdSe NPs. BQ removes the excited electron

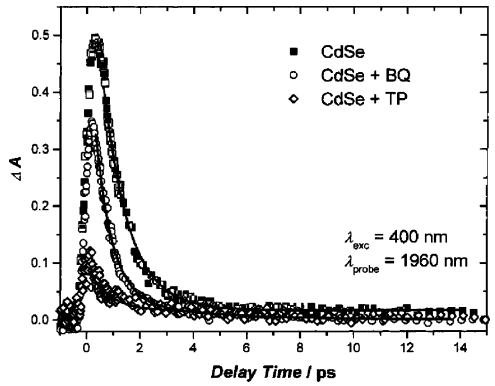

Figure 83. Relaxation dynamics of the transient absorption observed at 1960 nm in the NIR. The CdSe NP without quencher and the CdSe NP−BQ conjugate show the same relaxation dynamics with a 1.2 ps decay time. Therefore, it is likely that the transient is due to the relaxation of the hole. Indeed, the addition of hole quencher (TP) reduces the lifetime to 850 fs, which supports the assignment to a hole transition. Reprinted with permission from ref 466a. Copyright 2001 American Chemical Society.

very efficiently and acts like an additional electron trap.

The curve denoted BQ (circles) shows the bleach dynamics after fast removal of the electron. After depopulating the conduction band edge and forming the CT state, the spectral bleach at 560 nm is still observed in the time frame of 200 fs to 2.7 ps until the CT state decays.[468] Therefore, the photoexcitation of an electron and its removal from the band edges cause bleaching. When lower concentrations of BQ were used, incomplete quenching was observed due to incomplete conjugation of the NPs with BQ.[468]

On the other hand, the addition of the electron donor, 4-aminothiophenol, leads to a rapid neutralization of the photogenerated hole in the valence band and can be considered to be a hole quencher or hole trap. The addition of TP removes the electron traps on the nanoparticle surface. The excited-state lifetime of CdSe NPs was considerably longer when TP was added, and the bleach lifetime ($\gg$1 ns) exceeds the time window of the femtosecond experiment; this is due to the reduced electron−hole overlap[488] and the reduced electron surface traps because of the presence of TP.[489] The dynamics indicate that the electron, which populates the conduction band edge, contributes to the transient bleach. On the other hand, the removal of an electron, which leaves back a p-doped NP, shows that the hole in the valence band also causes part of the overall bleach in photoexcited samples.[466]

Figure 83 shows the dynamics of the transient absorption at 1960 nm.[466a] For the CdSe NP solution without added quenchers (squares), the transient absorption is very short-lived, with a 1.2 ps decay time. The addition of the electron quencher BQ (circles) does not reduce the lifetime but rather the intensity by 40% of the original transient. On the other hand, the addition of TP hole quencher (diamonds) reduces the lifetime of the transient absorption from 1.2 ps to 850 fs and the intensity by 80% of its original value. These results suggest that the NIR transient feature is mainly due to the hole.[267,338] On

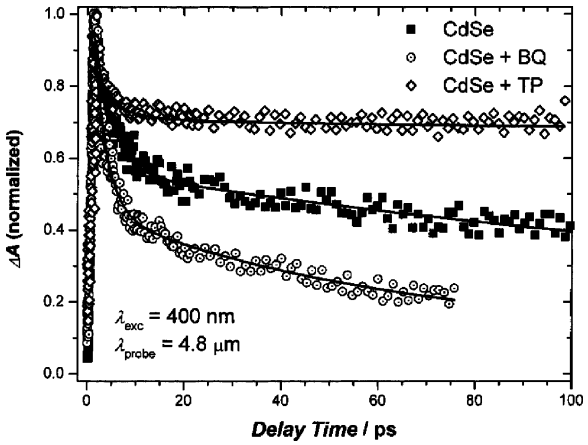

Figure 84. Relaxation dynamics of the transient absorption observed at 4.8 μm. The CdSe NP sample without quencher shows transients with 3 and 30 ps lifetimes. The CdSe−BQ sample relaxes more rapidly with 2.6- and 12-ps lifetime components. In addition, the long lifetime contribution is partly quenched for the CdSe−BQ sample but clearly not quantitatively as was observed for the visible transient. The CdSe−TP conjugate shows long lifetimes of 2 and 0.100 ps. Because the excited hole in the valence band is efficiently neutralized (trapped on the TP), the transient absorption in CdSe−TP is due to the remaining electron in the valence band. This dynamical behavior is very similar to the one observed for the bleach at 570 nm. Therefore, the transients are assigned to be mainly electron transitions. Reprinted with permission from ref 466a. Copyright 2001 American Chemical Society.

the basis of the accelerated transient decay and the fact that $k_{dec} = \Sigma k_i$ (the sum of the individual relaxation processes), the hole transfer to TP (trapping) is estimated to be on the order of $k_{ht} \approx 3 \times 10^{11}$ s^{-1}, requiring a lifetime of the hole in the valence band to be 3 ps or longer. Indeed, the quenching experiments with BQ already suggested that the hole lifetime is >2.7 ps.[466]

Figure 84 shows the dynamics of transient absorption of the CdSe NP sample while probing in the IR spectral range from 4000 to 5000 nm after 400 nm excitation.[466a] For bare CdSe NPs, the transient absorption decays with 2 and 30 ps time constants. The electron quencher BQ reduces the long-lifetime component of the transient from 30 to 12 ps. A clear quenching of the IR transient is observed, and the short lifetime component of 2.6 ps appears. However, the transient absorption does not decay completely due to trap-state absorption. The addition of TP hole quencher leads to an extended lifetime. The effect of the additional quenchers on the monitored IR kinetics is very much like the one observed in the visible range (except that the observed transient at 4.8 μm is absorption and the transient at 570 nm is bleach). These quenching experiments suggest that the IR transient absorption is due to electronic transitions in the conduction band.[466]

Figure 85 summarizes the electron-transfer dynamics when BQ or TP is added to the NP.[466a] Possible relaxation pathways are carrier recombination,[267] trapping,[336,338,490] and population of the spin-forbidden dark state.[327,339] The electron donor TP extends the initial bleach decay time to nanoseconds because the hole is efficiently trapped by TP and

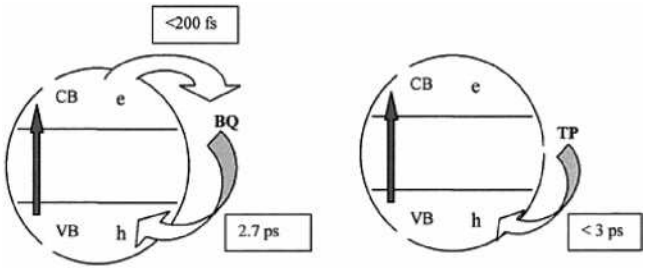

Figure 85. Schematic of the electron relaxation mechanism that takes place after benzoquinone (BQ) is attached to the CdSe NP surface (left). BQ serves as an electron shuttle, which pumps the excited electron in <3 ps from the conduction band back to the hole in valence band. The thiophenol (TP, right), is a hole trap (or electron donor) due to its low ionization potential. The hole transfer to TP is estimated to be on the order of 3 ps, on the basis of the quenching kinetics. This agrees with the fact that the lifetime of the hole on the conduction band edge is found to be longer than the NP^+BQ^- lifetime (2.7 ps). Reprinted with permission from ref 466a. Copyright 2001 American Chemical Society.

coupling to the hole is reduced. Moreover, the fast electron surface trapping processes are eliminated. The electron acceptor BQ accelerates the bleach decay because additional electron trapping is induced with the BQ on the NP surface. After removal of the conduction band electron during the lifetime of the NP−BQ CT complex (200 fs−2.7 ps), the hole still occupies the valence band and the ground-state absorption still bleaches.[468] Therefore, the lifetime of the hole on the valence band edge has to be longer than the 2.7 ps lifetime of the NP−BQ CT complex. Also, the removal of the hole by TP does not recover the bleach. Therefore, the quenching experiments with BQ and TP show that it is the electron occupying the conduction band and the hole populating the valence band that cause the excited CdSe NPs to be temporarily bleached, and consequently it needs both carriers to be removed from the band edges for the ground-state absorption to be recovered.[466]

Overall, the quenching experiments reveal that the 1.2 ps component at 1960 nm is due to an intraband transition of the hole, which is rate limiting to the intraband relaxation process of the excited CdSe NPs, because the electron conduction band relaxation occurs within 400 fs. The conduction band edge population by the electron is then found to occur within 200−400 fs (bleach rise time) when CdSe NPs are excited at 400 nm. The hole relaxes within 1.2 ps (NIR absorption decay) to the valence band edge and remains there for >3 ps. At longer times, induced absorptions are due to trap-state transitions. The PL occurring on the nanosecond time scale is due to radiative recombination from trap states. The PL redshifts drastically for longer observation times, and this suggests that a trap-hopping mechanism into subsequently lower trap states takes place and is summarized in Figure 86.[466a]

6.2.1.6. Shape-Dependent Relaxation Dynamics of CdSe Nanoparticles. Shown in Figure 87 are the TEM images and the absorption of the CdSe nanodots and nanorods in the study.[466b] Figure 88 compares the change in the bleach spectrum of the nanorods with that of the nanodots using the same

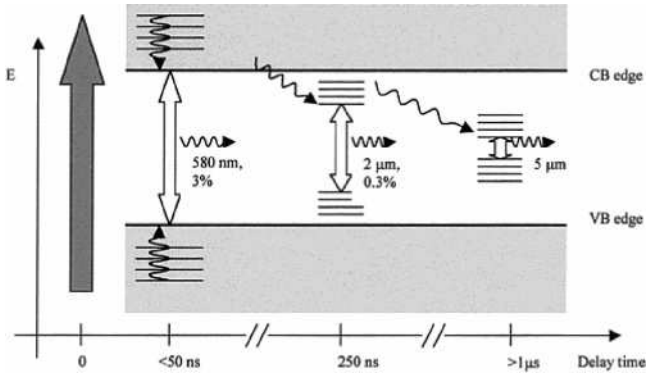

Figure 86. Scheme summarizing the relaxation process observed by time-resolved transient absorption and photoluminescence spectroscopy in the spectral range from 450 to 5000 nm. The PL decay times are 43 ns, 130 ns, and ~1 μs at 580-nm, 1000-nm, and 5-μm emission wavelengths, respectively. Reprinted with permission from ref 466a. Copyright 2001 American Chemical Society.

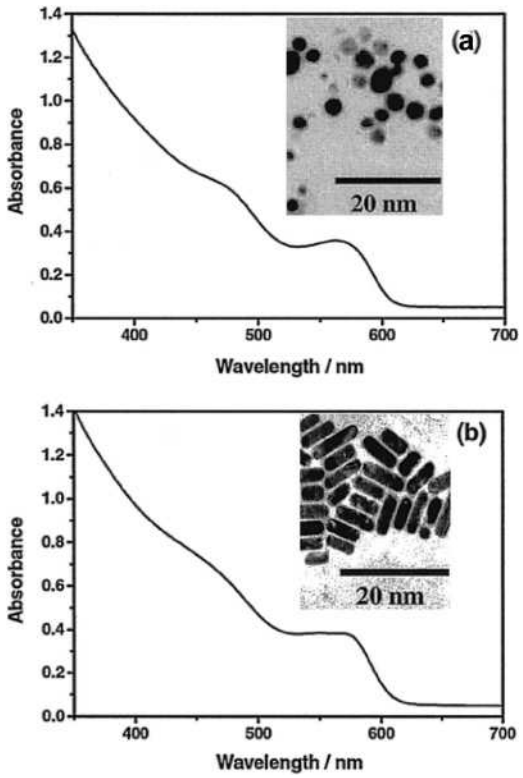

Figure 87. TEM image and absorption spectra of CdSe nanodot (a) and nanorod (b) solutions. Reprinted with permission from ref 466b. Copyright 2001 American Chemical Society.

delay times of 200 fs, 400 fs, 1.2 ps, and 2.4 ps.[466b] Within 200 fs, the carriers seem to distribute themselves among fewer energy states in the dots compared to the rods. This allows the $1S_e - 1S_h(^3/_2)$ (band gap state at 585 nm) to have a higher population than the corresponding state in the quantum rods. As the delay time increases, the dot spectrum does not change much, whereas in the nanorod spectrum, the population of the higher excitonic states relaxes rapidly to the lower states and finally to the band gap state.

The deconvolution of the bleach spectra at early time (1 ps)[466b] is shown for both the dots and the rods

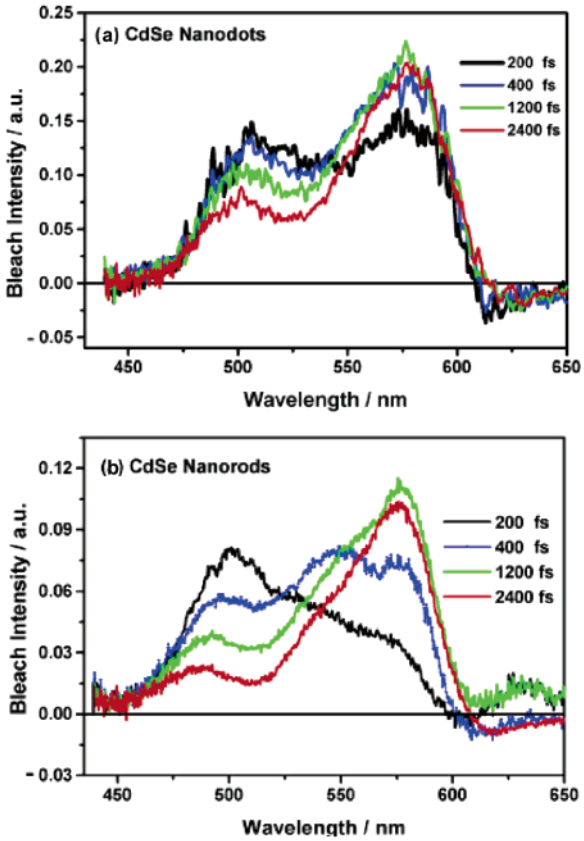

Figure 88. Shape-dependent ultrafast electron−hole relaxation in CdSe nanocrystals in early time 200 fs−2.4 ps at the spectral range 440−650 nm. The change in dynamics over the same spectral range is less pronounced for nanodots (a) than for nanorods (b). Reprinted with permission from ref 466b. Copyright 2001 American Chemical Society.

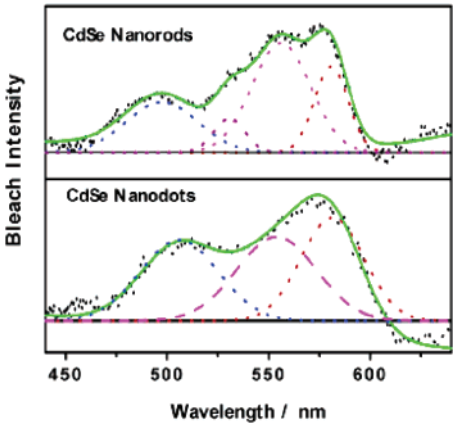

Figure 89. Deconvolution of the early time bleach spectra of CdSe nanorods and nanodots. Reprinted with permission from ref 466b. Copyright 2001 American Chemical Society.

in Figure 89. The bands of the dots are much broader than those of the rods (which have very narrow size distributions) and are deconvoluted into three bands with energies in agreement with those reported in the literature.[308,481] In comparison, the rods have more absorption bands than the dots because in the dots, there is splitting of the corresponding degenerate states.

Figure 90 shows the band gap bleach kinetics of the CdSe nanorods (blue squares) and nanodots (red circles); both the rise and decay times are longer for the rods compared to those for the dots.[466b] Table 1 shows a summary of the kinetic results of the rise and the bleach decay monitored for the different peaks appearing in the spectra for both the rods and dots. From the table, the following points are observed: (1) The rise time of the high-energy states (at 480 nm) is very fast in both particles (within the laser pulse width of 100 fs). (2) The rise time of the band gap state is faster in the dots (400 fs) compared with the rods (~1.0 ps). (3) The decay of the higher energy state is much faster in the rods compared with the dots (300 fs vs 2 ps). (4) For the rods, the decay time becomes longer as the energy decreases (300 fs for states in the 480−515 nm range, a few picoseconds for states in the 530−575 nm range, and 50 ps at the band gap state). (5) The decay time of the band gap state (585 nm) is longer for the rods (50 ps) compared with that for the dots (2.0 or 36 ps). This might be due to less effective surface trapping in the rods due to the smaller electron density of the excited electrons[491] due to its larger surface area.

The fast carrier relaxation dynamics of the higher energy states in the rods compared with that in the dots could be explained by the fact that lowering the symmetry in the rods leads to splitting of the

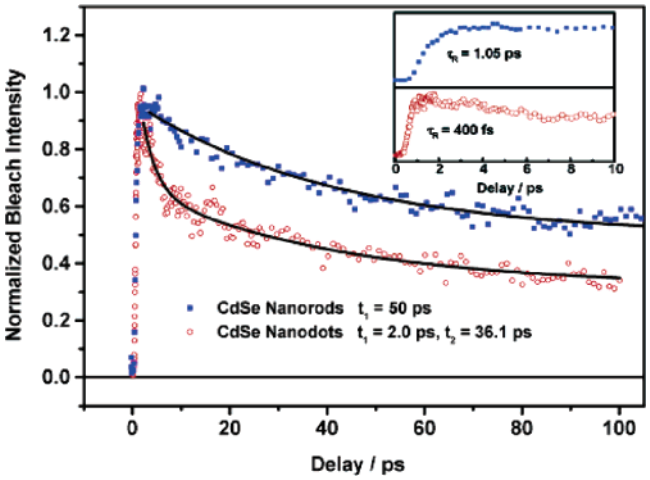

Figure 90. Comparison between the rise and the decay kinetics of the CdSe nanorods and nanodots at 585-nm wavelength (at the band gap) showing that the rise and decay in the case of nanorods is much slower than that of the dots. Reprinted with permission from ref 466b. Copyright 2001 American Chemical Society.

Table 1. Comparison of the Exciton Relaxation Dynamics of the Different States in CdSe Nanodots and Nanorods[a]

	CdSe nanodots			CdSe nanorods		
probe wavelength, nm	decay times t_1, ps	decay times t_2, ps	rising times, fs	decay times t_1	decay times t_2, ps	rising times, fs
585	2.05	36.1	~400	50.0 ps		~1000
575				3.5 ps	47.0	~750
550	2.2	33.0	~350	4.3 ps	43.0	~540
530				4.1 ps	20.0	~470
515	2.25	28.0	<100	330 fs	3.7	<100
500				350 fs	3.1	<100
480	2.6	21.9	<100	310 fs	2.1	<100

[a] The excitation wavelength is 400 nm and the laser pulse width is 100 fs [466B].

degeneracy of the energy levels in the dots. It should be mentioned that the increase in the density of states leads to an increase in the relaxation process involving either electron−phonon or electron−hole coupling.[481] The smaller the electron energy separation, the more likely phonons or holes can be found to accept the released energy and, thus, the faster the relaxation would be.

6.2.2. I–VII Semiconductor Systems

The ultrafast charge carrier dynamics has also been studied on AgI nanoparticles and related systems.[492] The electronics relaxation has been shown to consist of two components (a 2.5 ps and another component longer than 0.5 ns). In addition, the relaxation dynamics was found to be independent of the excitation power. The observed fast decay was attributed to the trapping and nonradiative electron−hole recombination, which is dominated by a high density of trap states, whereas the slow decay was attributed to the reaction of deeply trapped electrons with silver cations to form silver atoms. For the AgBr/Ag_2S core/shell system, there was a new component of 4 ps, which can be attributed to a transient bleach signal due to the Ag_2S shell.[493]

6.2.3. III–V Semiconductor Systems

The III−V semiconductor system, which includes InP, GaN, and GaAs nanoparticles, has been studied extensively in the past years.[494−498] Hot carrier relaxation measurement on the InP nanocrystals by time-resolved photoluminescence and transient absorption spectroscopy has revealed that increasingly efficient relaxation with decreasing excitation energy for the 1S exciton relaxation occurs.[494,495] Additionally, a 1.3 ps relaxation component was found to be due to a hole relaxation process between VB states near the band edge. The photoluminescence lifetime was found to be ∼10 ns, and the rise time for the 1S bleaching was found to be 280 fs. Furthermore, at least one charge carrier, an electron or a hole, was found to remain hot or exit the relaxation channel involving core electronic states in favor of capping molecule states, thus leading to nonradiative recombinations. A bleaching due to higher energy transitions (e.g., 1P) was also observed, which persisted after charge carrier cooling. Holes cooling to states lying near the VB edge contributed to the bleaching of transitions probed by the 1P exciton energy, even in the absence of electrons occupying the $1P_e$ CB level. The origin of the bleach signal at early times is a combination of both state-filling and carrier-induced Stark effect. The bleach signal of the 1S transition was similar to that of the 1P transition with a fast component of 20 ps and a slower component of 170 ps. The 1P state relaxed to the 1S state very quickly at ∼1 ps. The hot electron was found to stay at the 1S state for >300 ps, which was suggested due to the phonon bottleneck effect. On the other hand, the excess thermal energy was suggested to transfer to the hole via an Auger process.

The transient bleaching revealed that the number of electron−hole pairs reaching the lowest 1S state was independent of the excitation energy, whereas the number reaching the emitting state depended on the excitation energy. It was found that the number of electron−hole pairs relaxing to the emitting 1S state was proportional to the amount of light that is absorbed. A recent study also showed that for the 1S relaxation, a biexponential process with 500−750 fs and 2−4 ps time constants is observed by IR probe technique.[496] A dependence of the relaxation process on the size of the InP nanocrystals was found. Both rates increased as the size decreased. Furthermore, the relaxation in both exciton-confined and charge-separated nanocrystals was explained by using the Coulomb electron−hole interactions. A reduction in the relaxation rate of electrons was found when the hole was absent or trapped at the surface of the nanocrystal due to the intrinsic surface state related to the dangling bonds. The relaxation process has also been studied on other systems, such as GaAs nanocrystals.[500]

6.2.4. Group IV Semiconductor Systems

Time-resolved carrier dynamics have also been investigated in group IV semiconductor nanocrystal systems, which includes the industrially important silicon and germanium materials. Transient absorption spectroscopy studies conducted on ion-planted Si nanocrystals in SiO_2 matrix revealed that the photoinduced absorption spectra exhibited two components due to the carrier in the quantized states (high-energy band) of the Si nanocrystals and the Si/SiO_2 interface state (low-energy band).[501] The population of the quantized states was short-lived, and it decays on the sub-10-ps time scale with the latter attributed to efficient surface trapping. The nonlinear optical response in an indirect-gap semiconductor was found to be dominated by the free-carrier absorption due to intraband transitions, and the relaxation in the wave-vector conservation leads to the enhancement of this process. The red emission was not attributed to the carrier in quantized states, but was due to the deactivation of surface traps.[501]

The ultrafast carrier dynamics has also been investigated on a nanocrystalline silicon thin film system, where a multicomponent response was observed due to the separate phases of the heterogeneous materials.[502] A 240 fs component of the relaxation process was observed and attributed to the intraband carrier relaxation in the silicon crystallites. A response characteristic of bimolecular recombination in the amorphous silicon matrix and a long-lived component due to the grain-boundary states or surface states was observed.[502] The dynamics of excited carrier has been investigated in a silica matrix by pump−probe technique with a laser duration of 35 ps, where the excited carriers were found to depopulate with a lifetime of ∼70 ps.[504] In another experiment on Ge nanocrystals by the pump−probe technique, the photoexcited electrons were found to be rapidly scattered out of the Γ valley into the X valleys with a time constant of ∼230 fs and then into the L valleys in the time range of ∼1.5 ps, which involved the carrier−phonon couplings.[505]

6.2.5. Metal Oxides Systems

TiO_2 has received much attention because of its promising application prospects in solar energy conversion and photocatalysis.[507−509] The charge carrier dynamics have been investigated on bare TiO_2 nanoparticles and on TiO_2 nanoparticles coupled with dyes.[510−515] For bare TiO_2 nanoparticles, the photoinduced electrons were found to decay following a second-order kinetics with a second-order recombination rate constant of 1.8×10^{-10} cm^3/s.[510] In this measurement, an electron-trapping process was found to occur on the time scale of 180 fs.[511]

On the other hand, in dye-sensitized TiO_2 nanoparticles, the electron is injected from an excited dye molecule on the surface of TiO_2 nanoparticle. Usually the dye that is used absorbs visible light and the excited state of the dye molecule lies above the conduction band edge of the TiO_2 nanoparticle. In these systems, the back electron transfer to the dye following injection can be ignored. The electron injection and back electron-transfer rates depend on the nature of the dye molecule, the properties of the TiO_2 nanoparticle, and the interactions between the dye and the nanoparticle.[512,513] The electron injection occurs in ~100 fs. For example, the electron injection happens around 200 fs, 50 fs, and <100 fs for the systems of coumarin 343,[8] N_3,[515,516] and anthocyanin[517] dye-sensitized TiO_2 nanoparticles, respectively. The back electron transfer occurs much more slowly, usually from 10 ps to μs, and also depends on the nature of the dye and the nanoparticles.[517−520]

The electron relaxation dynamics have also been investigated in Fe_2O_3.[520] The relaxation dynamics was found to be very similar in the α- and γ-phases of Fe_2O_3 nanoparticles, which featured a multiexponential decay with time constants of 360 fs, 4.2 ps, and 67 ps. The nonradiative relaxation process is very efficient in this system and can be related to the weak fluorescence and low photocurrent efficiency of the Fe_2O_3 electrode due to the intrinsic dense band structure or the high density of trap states.[520]

6.2.6. Other Systems

PbS is a good system to investigate the strong quantum confinement in semiconductor nanoparticles because it has a relatively large Bohr radius of 18 nm and a narrow bulk band gap of 0.41 eV.[464,521] The dynamics of photoinduced electrons have been investigated using femtosecond laser spectroscopy in PbS nanoparticles capped with different protecting groups such as polyvinyl-alcohol (PVA), polyvinylpyrrolidone (PVP), gelatin, DNA, polystyrene (PS), and polymethyl-methacrylate (PMMA).[464,521] The electronic relaxation was found to be very similar and follows a double-exponential decay with time constants of 1.2 and 45 ps for all of the samples studied, independent of particle size, shape, surface capping, probe wavelength, and excitation intensity. The fast decay was attributed to trapping from the conduction band to shallow traps or from shallow traps to deep traps, and the slower decay was due to electron−hole recombination mediated by a high density of surface trap states within the band gap.[464]

Another interesting system that was investigated is the copper sulfide family of semiconductors. It has been observed that the electronic relaxation in Cu_2S has a dominant fast decay component of 1.1 ps due to charge carrier trapping at shallow trap sites, and a slower decay component of 80 ps due to deep trapping, which is independent of excitation intensity, probe wavelength, and capping agent.[464,522] On the other hand, the dynamics of the crystalline form of CuS shows an interesting power dependence due to trap state saturation. At low excitation intensities, the bleach has a fast recovery of 430 fs due to carrier trapping, which leads to an increase in transient absorption. Then a long time offset due to relaxation from shallow to deep traps and further relaxation of charge carriers from deep traps were observed. At high excitation intensities, a transient absorption signal with a 1.1 ps decay and a slow rise with a lifetime >1 ns was observed.[522]

In the case of Ag_2S nanoparticles with cysteine (Cys) and glutathione (GSH) as capping agents, the dynamics of photoinduced electrons had a quick (<150 fs) rise followed by a fast decay (750 fs) due to the fast trapping into shallow trap states, and a slower rise (4.5 ps) due to the deep trapping process.[464,523] The initial photoexcitation populated the conduction band and depleted the valence band within the laser pulse (<150 fs). The decay signal overlaps with both transient absorption and bleach, where the transient absorption contribution becomes more dominant over bleach with increasing excitation intensity due to shallow trap state saturation at high intensities. On longer time scales, Ag_2S nanoparticles capped with Cys-1, Cys-2, and GSH-2 have a recovery of 4.5 ps time constant that goes above the baseline and then decays gradually toward the baseline with a time constant of >1 ns. This process is attributed to the recombination of deeply trapped electrons with the hole. The nanoparticles capped with GSH-1 show a bleach recovery with a similar time constant (>1 ns) following the fast 4.5 ps rise.[464,523]

The relaxation in PbI_2 nanoparticles was also investigated and found to be dominated by surface properties and independent of particle size in the size range of 3−100 nm. The relaxation dynamics in this system was found to also be strongly dependent on the solvent used.[464,524,525] The early dynamics times were found to show some signs of oscillation with a period varying with solvent but not with size (6 ps in acetonitrile, 1.7 ps in alcohol). The relaxation was dominated by a 75 ps decay in acetonitrile and a fast additional 6 ps decay in alcohol. On the other hand, the relaxation in aqueous PVA solution features a double-exponential decay with time constants of 1 and 40 ps. These decays have been attributed to trapping and recombination mediated by trap states.[464,524,525]

The electronic relaxation dynamics observed for BiI_3 nanoparticles in different solvents was also found to be sensitive to solvent and insensitive to particle size. It was also observed to be somewhat dependent on the probe wavelength and independent of the excitation intensity.[464,525] The relaxation in BiI_3 nanoparticles was dominated by a 50 ps decay and a

long-lived component of 1.3 ns in acetonitrile, and with an additional fast 9 ps decay in alcohol. The influence of particle size was small in the size range studied (2−100 nm), and the relaxation was dominated by surface characteristics because spatial confinement was not significant in affecting the relaxation process due to the small exciton Bohr radius of the material (0.61 nm for bulk BiI_3).[464,525]

The electron−hole dynamics was also investigated in the CdS/HgS/CdS quantum dot-quantum well system.[151] Four bleach bands and a stimulated emission signal in the visible spectral range between 450 and 780 nm were resolved in the transient absorption spectra, and a transient induced absorption was found to be due to the intraband transitions by using an IR probe pulse at 4.7 μm. All four bleach signals have rise times between 200 and 300 fs, whereas the stimulated emission signal rises at 1.5 ps. From the 1.5 ps rise time of the stimulated emission originating from the HgS well and the intraband hole IR absorption (150 fs) after excitation into the CdS core, the electron localization time (transfer time from the core to the well) was found to be 1.5 ps, whereas that of the hole was on the order of ~150 fs. There is a large difference in the transfer time of the electron and hole across the CdS/HgS interface. This was explained by the fact that the hole transfer occurs from excited S^- in the CdS system to S^{2-} in the HgS system, whereas the electron is transferred from the excited S^- to Hg^{2+}. The energetics and Franck−Condon factor are good for the hole transfer between the surface MOs but are not very good for the electron transfer as it involves change of chemical species with large differences in their energies and overlap.[152]

The exciton dynamics was also investigated in a double-layer-QW CdS/$(HgS)_2$/CdS quantum-dot−quantum-well system and was compared to the dynamics of the QDQW system with a single-layer HgS QW.[154] A fast relaxation component of ~5 ps at wavelengths <700 nm was found, and this is due to an energy relaxation process of the two $1P_e-1P_h$ exciton state. At longer wavelengths, a slow decay component that increases in decay time with increasing wavelength was found, and this is due to the decay of the dim $1S_e-1S_{3/2}$ state. The inhomogeneously broadened absorption band and the wide distribution of decay times in the low-energy region gave strong evidence for a broad inhomogeneous energy distribution of the lowest energetic $1S_e-1S_{3/2}$ dim state, which was discussed in terms of the morphological structure of the quantum well.

The kinetic measurements of the optical transitions in the double-layer-QW system were correlated with their symmetry and overlap of carrier wave functions. A rapid relaxation among the higher excitonic states leads to the population of the lowest state, which decayed more slowly than the upper states via trapping processes. The tetrahedral shape and the CdS/HgS interfaces were considered to be the source of both the broad distribution of the excitonic energies and the large density of trapping sites, which can lead to the observed distribution of energy states and decay times of the lowest exciton state.[154]

6.3. Hot Electrons and Lattice Temperatures in Nanoparticles

The electrons of the metal can be selectively excited, and the electron−phonon coupling can be studied in real time with the advancement of ultrashort laser pulses, which are shorter than the electron−phonon energy relaxation time.[402,403] Electron−electron interactions are strong enough to thermalize the electron gas within the duration of the laser excitation pulse due to the high electron density in metals. Because of the large difference in their heat capacities, the electrons and the lattice can be treated as two coupled subsystems according to the two-temperature model (TTM).[420] A nonequilibrium temperature difference between the electron gas and the lattice is created directly after the electrons absorb the photon energy from the laser pulse. A new Fermi electron distribution with a higher electron temperature is reached via an internal electron thermalization by electron−electron scattering within the electron gas,[259,260,408,409] where electron−electron interactions are elastic and the overall energy is conserved during this first relaxation process. A temperature equilibration between the electron and the lattice subsystems is established via external thermalization by electron−phonon collisions, which exchanges the excitation energy between the electron subsystem and the lattice (energy relaxation T_1).[259,260,408,409] During the external thermalization, the temperature of the electron gas (and the lattice) decreases steadily and the whole system returns to its original (ground) state prior to laser excitation. The time evolution of the electron and the lattice temperatures are expressed as[420,406,407,526]

$$C_e(T_e)\frac{\partial T_e}{\partial t} = -g(T_e - T_1) + \nabla(\kappa'\nabla T_e) + \mathrm{LP}(z,t) \quad (37)$$

$$C_1\frac{\partial T_1}{\partial t} = g(T_e - T_1) \quad (38)$$

where C_e and C_l are the electronic and lattice heat capacities, respectively, g is the electron−phonon coupling constant, and κ' is the electronic thermal conductivity. LP(z,t) is the spatial and temporal evolution of the exiting laser pulse. The electronic heat capacity $C_e(T_e)$ is usually assumed to vary linearly with the electron temperature T_e.

The optical (transient absorption, transmission, or reflectivity) changes induced by the pump pulse can be expressed in terms of temperature changes.[345] Fermi−Dirac statistics

$$f = \frac{1}{1 + \exp(E - E_F/kT)} \quad (39)$$

describe an electron distribution within the conduction band of the metal[345] after a rapid internal electron relaxation by elastic electron−electron collisions, where k, T, E_F, and E are the Boltzmann constant, temperature, Fermi energy, and energy of the electronic energy levels, respectively. An electronic temperature is associated with each Fermi electron distribution and can describe the energy

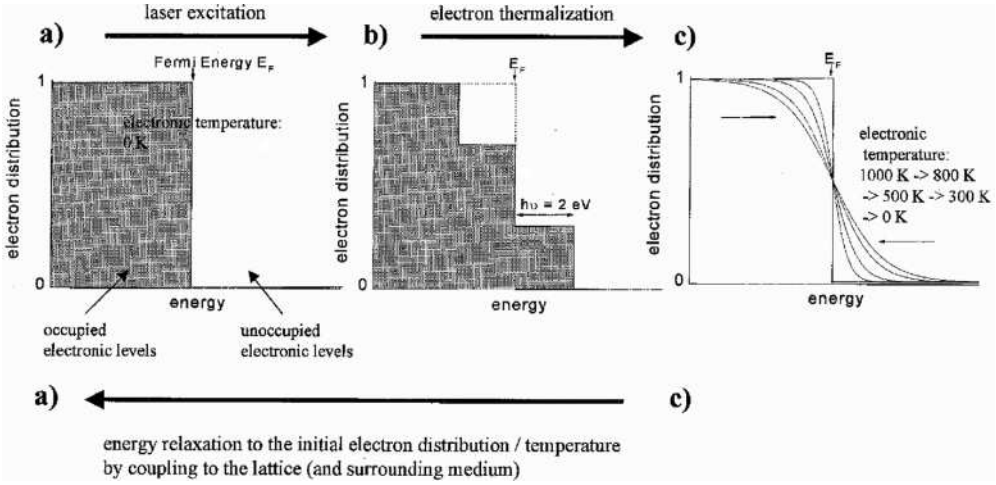

Figure 91. Schematic illustration of the electron distribution in the conduction band of a metal (nanoparticle). (a) Before laser excitation all states below the Fermi energy are occupied, whereas all states above the Fermi energy are unoccupied at an initial temperature of 0 K. (b) Electrons with energies of up to the excitation energy below the Fermi energy to states are promoted above the Fermi energy having a maximum energy equal to the excitation energy after excitation with a laser pulse (2 eV in this illustration). This electron distribution is a nonthermal electron distribution with regard to Fermi–Dirac statistics. This nonthermal electron distribution relaxes (thermalizes) by electron–electron scattering without losing the absorbed photon energy to a certain electron temperature. (c) In this case an electron temperature of 1000 K is reached. [Energy conservation requires that the areas under the curves in (b) and (c) for energies greater than the Fermi energy have to be equal.] The electron gas is cooled via electron–phonon coupling and phonon–phonon interactions with the surrounding medium as illustrated by the other curves in (c). Finally, the system returns to its starting electron temperature (*a*). Reprinted with permission from ref 259. Copyright 2000 Taylor and Francis.

relaxation of the electron gas into the lattice motion. Figure 91 illustrates the changes in the electronic energy distribution within the conduction band of the metal after laser intraband excitation at an initial temperature of 0 K, where the electron distribution *f* is calculated according to the Fermi–Dirac statistics.[345]

The electrons having an energy of ≤2.0 eV below the Fermi level are excited to electronic levels up to 2 eV above the Fermi level after laser excitation with a wavelength of 620 nm, which leads to a nonequilibrium distribution according to the occupation dictated by the Fermi–Dirac statistics for fermions as plotted in Figure 91b. A new Fermi electron distribution with a higher electron temperature is reached after electron–electron scattering within the electron gas as shown in Figure 91c, which is also called an internal electron thermalization process,[259,408,409] because the overall energy is conserved during this relaxation process. The latter event is attributed to elastic electron–electron interactions, assuming there is no energy exchange between the electrons and the lattice. A temperature equilibration between the electron and the lattice subsystems is established after an external thermalization[259,408,409] with the phonon bath, where the excited electrons above the Fermi level lose their energy to the phonons via electron–phonon interactions. Finally, the temperature of the electron gas (and the lattice) decreases steadily and the Fermi distribution narrows until the whole system returns to its original (ground) state before laser excitation is reached (Figure 91a), assuming that there is also heat release to the surrounding system.

Interband transitions lead to a very similar but complicated picture, where the holes in the low-lying d band can recombine with any of the excited

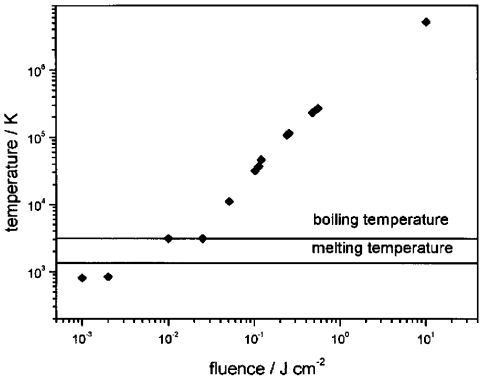

Figure 92. Dependence of the estimated lattice temperature of the gold nanoparticles as a function of the laser fluence. The two horizontal lines represent the bulk melting and boiling temperature, respectively. Reprinted with permission from ref 527. Copyright 2000 American Chemical Society.

electrons above the Fermi level or the unexcited electrons below the Fermi level occurs on the tens of femtoseconds time scale[421–423] due to the high density of the charge carriers in the conduction band. If the interband relaxes via an Auger-type recombination mechanism process, then highly excited electrons are present within the conduction shortly after the excitation pulse. These electrons have an average excess energy above the Fermi level equal to the exciting photon energy as the holes in the d band have already been filled by the initial electron–electron scattering.[259]

The temperature change of the nanoparticle lattice has also been examined.[527] Figure 92 shows the temperature of the gold nanorods after excitation with femtosecond pulses as a function of the laser fluence.[527] The bulk melting and boiling temperatures of gold (1337 and 2929 K, respectively) are indicated

with the two horizontal lines. The number of gold nanorods in the excitation volume can be calculated, given the beam diameter of the laser pulse, optical path length, and an overall nanorod concentration. The amount of energy per nanorod can be obtained with this value together with the absorbed photon energy, E_{abs}. The temperature (T) of the nanoparticle lattice is then given by eqs 46−48, where the initial temperature was assumed to be room temperature (293 K)

$$T = \frac{E_{abs}}{mc_p} + 293 \quad (40)$$

$$T = \frac{E_{abs} - \Delta H_{melt}}{mc_p} + 293 \quad (41)$$

$$T = \frac{E_{abs} - \Delta H_{melt} - \Delta H_{vap}}{mc_p} + 293 \quad (42)$$

where ΔH_{melt} and ΔH_{vap} are the heats of melting and vaporization, respectively, c_p is the specific heat capacity of gold, and m is the mass of the nanoparticle. Equation 39 is valid for temperatures below the melting point, whereas eqs 40 and 41 are valid when the temperatures have reached values above the melting and boiling points, respectively. The temperatures represent an upper limit because no heat losses are considered, assuming that all of the absorbed laser energy is transferred into the lattice. The temperatures of the nanoparticles exceed the melting and boiling points of bulk gold where temperatures on the order of 10^4-10^5 K are easily achieved with the femtosecond pulses.[527]

6.4. Phonon Bottleneck

In a crystal consisting of N elementary cells with n atoms in each, $3nN-6$ independent elementary oscillations exist, which are called normal modes. Each crystal state can be described in terms of superposition of normal modes. The six modes are usually ignored compared to the large number of modes. All of these normal modes can be classified into $3n$ different branches containing N oscillations each. Three of them are called acoustic branches, and the others are called optical branches. In a three-dimensional lattice with more than one atom in the primitive cell, there are always three types of acoustic modes and three types of optical modes, namely, one longitudinal and two transversal modes. Every vibrational state of a lattice can be described in terms of the state of an ideal gas of noninteracting quasiparticles called phonons. In nanocrystals, acoustic phonon modes become discrete because of finite size and can be described in terms of elastic vibration of homogeneous particles in a spherical crystallite. Optical modes in nanocrystals experience some modifications as well, and a number of surface modes appear.[308,462]

Consider the simplified scheme of the optical transitions including the ground and the two lowest excited states of a nanocrystal. In the ground state, no exciton exists. The first excited state corresponds to one exciton in its ground state, that is, the 1s state in a weak confinement case and the $1s_e1S_{3/2}$ state in the strong confinement limit. The second state is then the 2s state or $1s_e2S_{3/2}$ state, respectively. The energy difference between the two excited states, ΔE_{12}, grows rapidly with decreasing nanoparticle size. For CdSe nanocrystal with $a = 2$ nm, $\Delta E_{12} \cong 200$ meV (1600 cm^{-1}). This is a very large value compared with LO−phonon energy, which is ~26 meV for CdSe nanoparticles. The latter is close to the thermal fluctuation energy $E_T = kT$ value at room temperature. Therefore, for rather large sizes and temperature ranges, $\Delta E_{12} \gg E_{LO}, E_T$. In this case, relaxation between these two excited states is possible via multiple emissions of optical and acoustical phonons. In bulk semiconductors, exciton energy relaxation results mainly from cascade LO−phonon emissions, where interaction with acoustic phonons is less important. In nanocrystals that are smaller than 10 nm, when the discreteness of electron−hole states becomes essential, optical phonons cannot provide an efficient relaxation channel. The dispersion curve of optical phonons is nearly independent of wavenumber, and LO−phonon energies can only be weakly deviated from the E_{LO} value. Therefore, the relaxation via multiple LO−phonon emission requires $\Delta E_{12} = nE_{LO}$, where n is an integral number. Unlike in bulk crystals where there exists a continuous spectrum for quasi-particles, there is no intermediate state that exists between the lowest two excited states in nanocrystals. Therefore, the probability of the above process is very low because multiple phonon emission should occur via virtual intermediate states. The corresponding relaxation rate is lower than the typical electron−hole recombination rates. Thus, the relaxation between the excited states in nanocrystals is essentially inhibited. This effect is often called phonon bottleneck.[308,462]

Phonon bottleneck in nanoparticles has been studied in the past years,[308,462] and the results are controversial.[475,485,489,528−554] The excited carriers should have an infinite relaxation lifetime for the extreme, limiting condition of a phonon bottleneck; thus, the carrier lifetime would be determined by nonradiative processes, and PL would be absent.[308,462] In the case that the relaxation times are not excessively long and PL is observed, the results are not indicative of a phonon bottleneck, although relatively long hot-electron relaxation times (tens of picoseconds) compared with what is observed in bulk semiconductors are observed.[555−557] The time of electron transfer from bulk III−V semiconductors to redox molecules (metallocenium cations) adsorbed on the surface can be sub-picosecond to several picoseconds;[558−560] hence, photoinduced hot electron transfer can be competitive with electron cooling and relaxation if the latter is greater than tens of picoseconds. If the relaxation/cooling times are >10 ps (about an order of magnitude greater than for bulk semiconductors), slower relaxation/cooling of carriers is observed in nanoparticles.[462]

Slow hot electron cooling with times ranging from 10 ps to 1 ns was observed in self-assembled InGaAs QDs produced by Stranski−Krastinow (SK) growth

on lattice-mismatched GaAs substrates by Sugawara and colleagues.[530−533] The relaxation time increased with electron energy up to the fifth electronic state. Slow electron cooling was also reported in InAs/GaAs nanoparticles by Kamat et al.[541] In strain-induced GaAs QDs formed by depositing tungsten stressor islands on a GaAs QW with AlGaAs barriers, slow cooling of up to 1 ns was observed by Gfroerer et al.[542]

On the other hand, slow hole cooling with a lifetime of 400 ps was reported in SK InAs/GaAs nanoparticles by Adler et al.[538,539] In stacked layers of SK InAs nanoparticles deposited on GaAs, hole relaxation times of ∼40 ps were observed by Heitz et al.[534] Klimov et al. also found very fast electron relaxation dynamics on the order of 300 fs from the first-excited 1P to the ground 1S state on II−VI CdSe colloidal QDs using interband pump−probe spectroscopy, which was attributed to an Auger process for electron relaxation that bypassed the phonon bottleneck.[462,470,475] Guyot-Sionnest et al.[489] conducted experiments to separate electron dynamics from hole dynamics with CdSe QDs coated with different capping molecules (TOPO, thiocresol, and pyridine), which exhibit different hole-trapping kinetics. The rate of hole trapping increased in the order of TOPO, thiocresol, and pyridine, with a fast relaxation component (1−2 ps) due to the Auger relaxation process and a slow relaxation component (≈200 ps) attributed to the phonon bottleneck, which is most prominent in pyridine-capped CdSe QDs. In the Auger process, the excess electron energy is rapidly transferred to the hole, which then relaxes rapidly through its dense spectrum of states. The relative weight of these two processes in a given QD system depends on the hole-trapping dynamics of the molecules surrounding the QD. The relaxation times follow the hole-trapping ability of the different capping molecules and are longest for the QD systems having the fastest hole-trapping caps; the slow component dominates the data for the pyridine cap, which is attributed to its faster hole-trapping kinetics.[462,489]

Klimov et al. further studied the presence of the Auger mechanism for carrier relaxation dynamics in CdSe QDs with a ZnS cap and a pyridine cap.[329,470,471] The relaxation time from the 1P to 1S state was ∼250 fs with the ZnS-capped CdSe, whereas for the pyridine-capped CdSe, the relaxation time increased to 3 ps, which was attributed to a phonon bottleneck produced by rapid hole trapping by the pyridine.

6.5. Quantized Auger Rates

In the regime of multiple e−h pair excitation, depopulation of nanocrystal quantized states can occur via Auger recombination, a nonradiative multiparticle process, leading to the recombination of e−h pairs via energy transfer to a third particle (an electron or a hole) that is re-excited to a higher energy state.[329,472,561,562] The Auger recombination occurs as a sequence of quantized steps from N to $N - 1$, $N - 2$, ..., and finally to the 1 e−h pair state and is characterized by a set of discrete recombination constants, characteristic of the decay of the two, three, ..., e−h pair NC states.[329,472] The multiparticle decay process has been studied by monitoring the relaxation of the 1S bleaching using pump−probe techniques.[329,472] Single-exponential dynamics of different multiple-pair nanocrystal states can be obtained by subtraction from the experimental $\langle N(t)\rangle$ time transients normalized to the long-time decay values.[329,472] The carrier decay becomes progressively faster with increasing number of e−h pairs per nanocrystal. The ratio 0.22:0.47:1 of the experimentally determined times of four-, three-, and two-pair relaxations (10, 21, and 45 ps, respectively) is close to the predicted ratio of $\tau_4/\tau_3/\tau_2 = 0.25:0.44:1$ in bulk semiconductor with $\tau_N^{-1} = C_A(N/V_0)^2$ ($N \geq 2$), where τ_N is the effective decay time constant in the Auger regime. The quantitative match of scaling for the multiparticle relaxation times indicates that the decay rates for quantum-confined Auger recombination are cubic with respect to the carrier density ($dn_{eh}/dt \propto -n_{eh}^3$), just as in bulk materials.[329,472] The time constants measured for the two-, three-, and four-pair decays rapidly decrease with decreasing nanocrystal size following a cubic size dependence, such that the time-constant ratios predicted by the bulk-semiconductor model holds for all nanocrystal sizes.[329,472] The R^3 size dependence of relaxation times in nanocrystals are different from the R^6 dependence predicted by the bulk-semiconductor model, and this shows that in three-dimensionally-confined systems, the Auger constant depends on the particle size. For the size between 1 and 4 nm, the Auger constant decreases with reducing nanocrystal radius as R^3 and the C_A values calculated by using lifetimes of two, three, and four e−h pair states are similar to each other.[329,472]

6.6. Trapping Dynamics

Recently, it was demonstrated that $Cu_{1.8}S$ is a good system for studying the trapping dynamics in nanoparticles.[563,564] In the absorption spectra shown in Figure 93 (top), the red shift from 450 to 510 nm during the particle growth is due to the quantum confinement effect on the excitation into intrinsic electronic states as the quantum dot size increases. The emission spectrum of the $Cu_{1.8}S$ quantum dots reveals a bathochromic shift and occurs from trapping sites. Upon femtosecond laser excitation of the quantum dots, strong bell-shaped excited-state absorption from 450 to 750 nm was observed, resulting from the population of trapping sites with a maximum around 600 nm and a dip between 450 and 550 nm due to the superposition of transient absorption and transient bleach in this spectral range. The overall peak intensity was excitation power dependent, as illustrated in the inset of Figure 93. The pump power utilized caused multiple excitations but was still in the linear range and no saturation occurred, where the highest pump power corresponds to 20 excitations per particle and ∼1 excitation at the lowest applied pump power. The linearity of the absorption intensity suggested that the number of surface traps exceeds the number (20) of excited carriers.[563,564]

If transient absorption is indeed from populated trap states, the decay dynamics, due to the detrapping process of the carriers, should be temperature

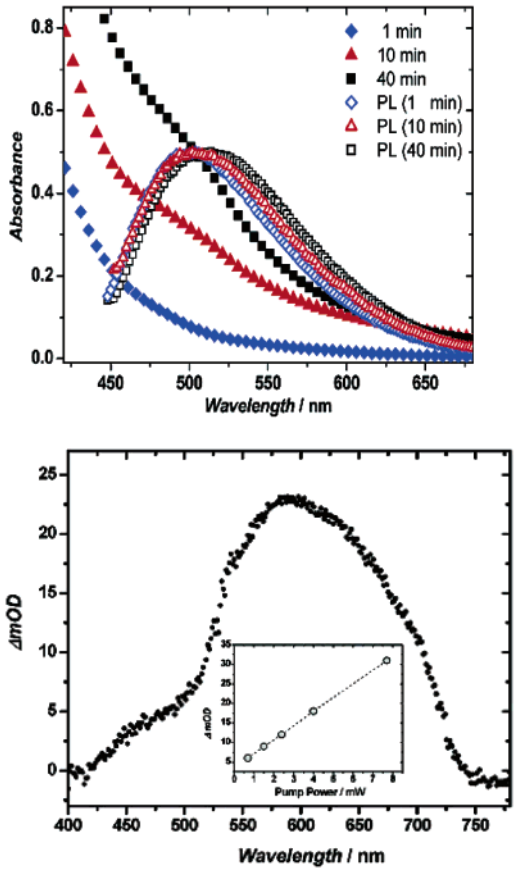

Figure 93. (Top) Absorption spectra (solid symbols) of aliquots drawn at 1 (diamonds), 10 (triangles), and 40 (squares) min of reaction time during the synthesis of CuxS quantum dots. The absorption spectra show shoulders around 480, 495, and 510 nm. The corresponding photoluminescence spectra are shown for the three samples on an arbitrary scale, displaying a decreasing Stokes shift for larger quantum dots. (Bottom) Transient absorption spectra of Cu1.8S quantum dots after femtosecond laser excitation at 5-ps delay time. The inset shows the pump power dependence of the signal intensity. No saturation was observed up to 22 excitations per quantum dot. Reprinted with permission from ref 563. Copyright 2003 American Chemical Society.

dependent (thermal activation for escaping the trap potential) and should be largely independent for the number of populated trapping sites. The decay time (2.55 ± 0.5 ns) of this transient absorption does not change with excitation power variation when excitation powers between 0.5 and 10 μJ/pulse or 1−20 excitations per quantum dot were applied as shown in Figure 94.

Transient bleach occurs in quantum dots as a result of excited-state-filling, which leads to a partial saturation of the band gap transition as long as the excited states are populated. The combination of transient bleach and absorption should result in a more complex relaxation dynamics in the 500 nm range compared to the 600 nm (intraband gap) range, which is less than the band gap energy of the investigated quantum dot. Transient absorption in this energy range was previously assigned[470] to excited-state absorption originating from surface states, which occurs as a result of lattice defects and dangling bonds on the surface of the nanocrystals.

Figure 95 shows the rise of the transient absorption monitored at 600 nm with a fast increase in absorption that is observed within the first 400 fs due to excited-state absorption of the delocalized hot carriers. A slower component (35%) with a rise time of 16.8 ps assigned to the trapping process of carriers and the concomitant depopulation of the band edge is also observed.[563]

The adsorbed benzoquinone (BQ) acts then as an electron acceptor and removes the photoexcited electron from the conduction band in less time than the laser pulse duration (<120 fs). Therefore, the electron-transfer rate is faster than the experimental time resolution, and as a result, the pump−probe measurements in the presence of BQ provide information about the remaining hole dynamics in the quantum dot. Thereby, detailed information about the dynamics of the electron or the hole can be obtained.[468,470,565,566]

Figure 96 shows the kinetics monitored at 500 nm (black open circles) with a fast relaxation component of 350 fs, a slower component of 2.2 ps, and a rise time of 16 ps. The 350 fs and 2.2 ps decays at 500 nm are actually the rise time of the bleach at the band edge due to the intraband relaxation of the electron and hole, respectively, and the 16 ps rise time at 500 nm is actually the decay of the band edge bleach via trapping.[563,564]

After the addition of the electron acceptor BQ, the quenched 350 fs component can be assigned to the intraband relaxation of the hot electron, whereas the unquenched 2.2 ps component is assigned to the relaxation of the hot hole. The quenched 16 ps rise time suggests that with BQ on the surface, no electrons can reach the trapping sites. A slower decay component of 39.7 ps is then observed, and this is due to the trapping of the hole or the recombination of the carriers.

The addition of BQ completely removes the 16 ps component that is due to the trapping of electrons and is shown in Figure 97. A new decay with a 2 ps component and a long lifetime component was observed, and this is due to the intraband relaxation of the hole as a result of the recombination of the electron and the hole (in the presence of the electron acceptor on the surface), respectively (shown in Figure 97, top left).

Through the localization of the carriers during the trapping process, the overlap between electron and hole wave function can be drastically reduced, resulting in longer time components for the decay of the transient signals. The decay of the transient absorption monitored at 600 nm takes place on the 2.5 ns time scale. A similarly long lifetime component was also measured for the transient absorption at 500 nm, as presented in Figure 97. The addition of BQ reduced the lifetime of the recombination transient drastically from 2.5 ns to 471 ps. The decay of the transient absorption could be due to the depopulation of the hole trap states into deeper traps, and the recovery of the ground-state spectrum suggests an electron−hole recombination on the 471 ps time scale.[563,564]

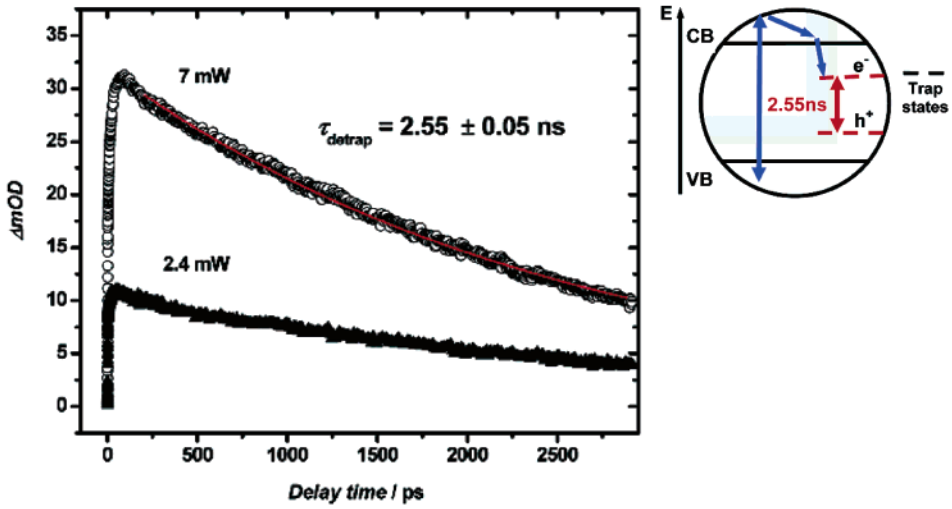

Figure 94. Nanosecond decay curve of the laser-induced transient absorption monitored at 600 nm, revealing the recombination time of the trapped electron and holes. Reprinted with permission from ref 563. Copyright 2003 American Chemical Society.

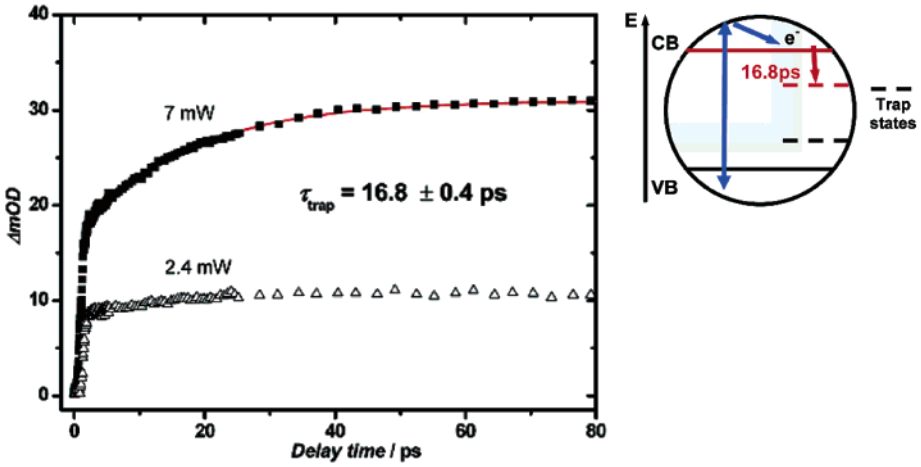

Figure 95. Picosecond rise time of the laser-induced transient absorption monitored at 600 nm, monitoring the conduction band depopulation and trapping of the photoexcited electron. Reprinted with permission from ref 563. Copyright 2003 American Chemical Society.

7. Nanocatalysis

7.1. Introduction

The field of nanocatalysis (in which nanoparticles are used to catalyze reactions) has undergone an exponential growth during the past decade. Two types of studies have been carried out, homogeneous catalysis in solution and heterogeneous catalysis in which the nanoparticles are supported on a substrate. Because nanoparticles have a large surface-to-volume ratio compared to bulk materials, they are attractive to use as catalysts. In 1996, it was demonstrated that transition metal nanoparticles can be synthesized with different shapes, and the potential of using different shapes to catalyze different reactions was discussed.[567] Recently, it has been shown that the activities of platinum nanoparticles of different shapes are indeed different for the same electron-transfer reaction in colloidal solution.[568] This potential shape-dependent catalysis adds to the advantage of using nanoparticles as catalysts. Of course, being small with corners and edges could make their surface atoms unstable during the chemical reaction they catalyze, and shape changes could occur.[570]

7.2. Homogeneous Catalysis

In homogeneous catalysis, transition metal nanoparticles in colloidal solution are used as catalysts. In this type of catalysis, the colloidal metal nanoparticles are dispersed in an organic or aqueous solution or in a solvent mixture. The colloidal nanoparticles must be stabilized to prevent their aggregation and also to be good potential recyclable catalysts. However, it was shown that the better the capping, which makes the nanoparticles stable in solution, the lower the catalytic activity becomes because the active surface sites are better protected.[569]

Being small has the advantage that a larger fraction of the atoms is used in the catalysis process. Furthermore, surface atoms can occupy the corners and edges of the nanoparticles and thus become chemically unsaturated and also much more active. Recently, Narayanan and El-Sayed[568] showed that there is a reasonable correlation between the cata-

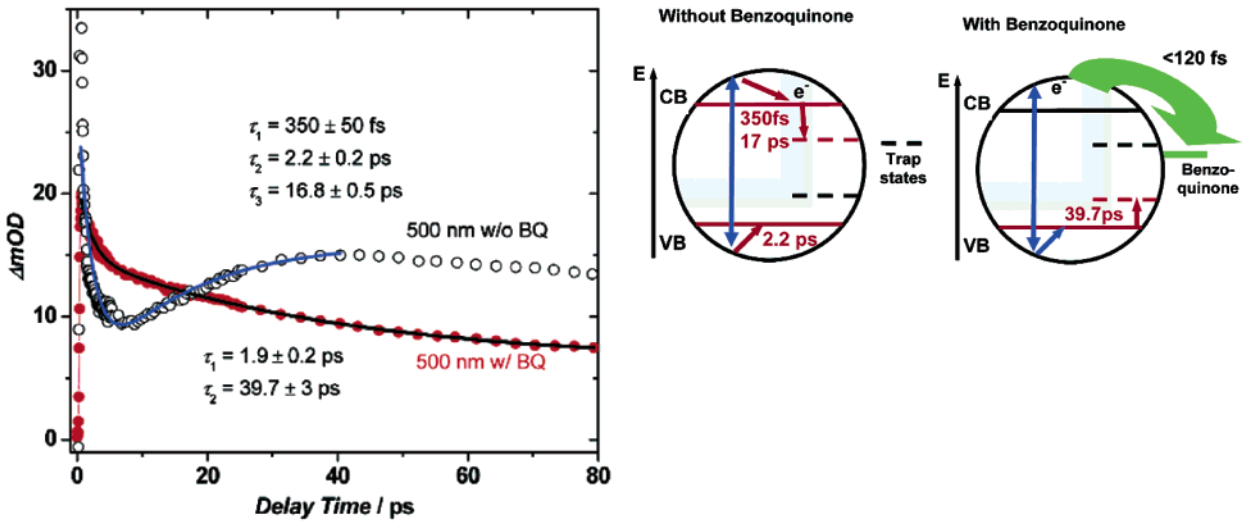

Figure 96. Relaxation dynamics of the transient absorption observed at 500 nm in a time window up to 80 ps. A fast decay (350 fs) and slower rise time (16.8 ps) are observed for the original sample without benzoquinone, indicating intraband relaxation and trapping of the photoexcited electrons. The 2.2 ps time component was identified as hole-cooling dynamics. Reprinted with permission from ref 563. Copyright 2003 American Chemical Society.

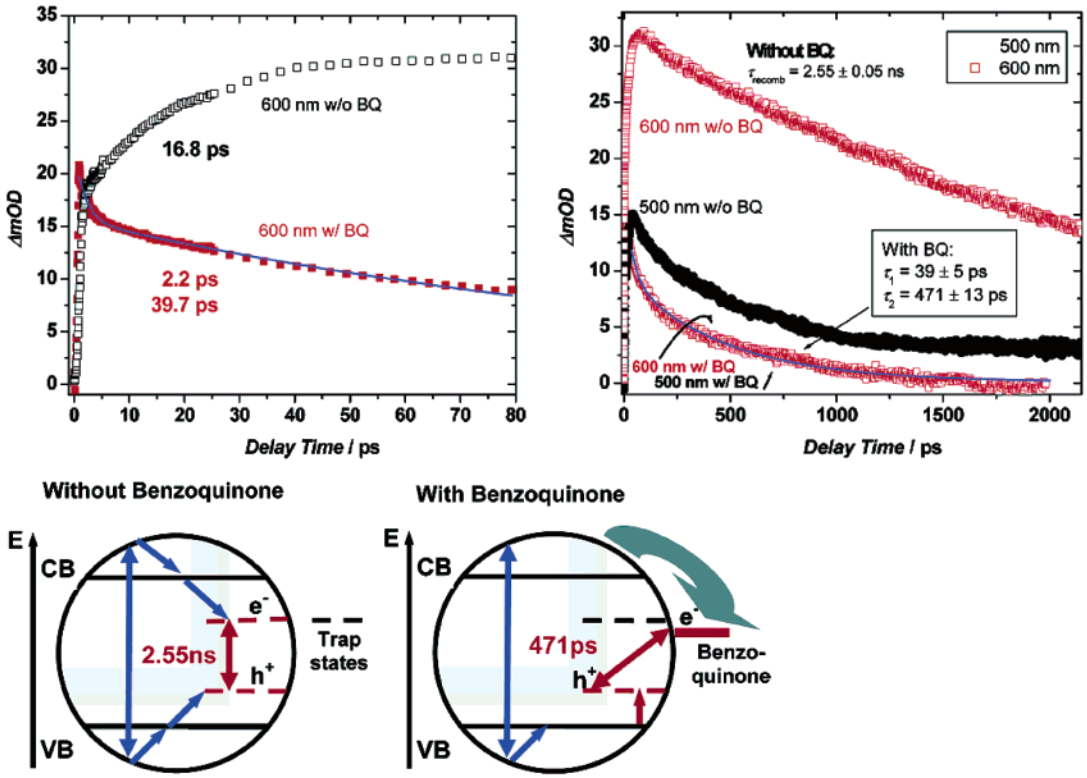

Figure 97. (Top left) Relaxation dynamics of the transient absorption observed at 600 nm, measured up to 80-ps delay. (Top right) Decay dynamics of the transient absorption observed at 600 (red squares) and 500 nm (black circles) in a time window up to 2000 ps. (Bottom left) Without benzoquinone, the trap-state absorption displays a lifetime of several nanoseconds (≥2.5 ns). (Bottom right) After adsorption of benzoquinone, the transient absorption is reduced in lifetime to <500 ps. This could be due to accelerated recombination of the electron with the hole due to trapping of the hole in the field of the BQ anion. Reprinted with permission from ref 563. Copyright 2003 American Chemical Society.

lytic activity of nanoparticles with different shapes and the fraction of atoms located on corners or edges. However, this high reactivity could lead to surface reconstruction and shape changes in colloidal solution.[570] Thus, being small could make the surface atoms dynamically active and could also lead to surface reconstruction. In the electron-transfer reaction catalyzed with tetrahedral shaped Pt nanoparticles in colloidal solution, it is found that the activity of the nanoparticles decreases during the course of the reaction as a result of changes toward a spherical shape (which has the most stable surface).[571]

There have been a number of reviews that discuss the use of colloidal transition metal nanoparticles as catalysts for homogeneous catalysis and also some of the major reactions that this type of nanoparticles has catalyzed. One review has focused on whether transition metal colloidal nanoparticles are potential

Table 2. References to the Common Reducing Agents and Stabilizers Used in the Synthesis of Nanoparticles in Colloidal Solution as well as the Important Reactions Studied

important factors for colloidal transition metal nanoparticles	examples
reducing agents	alcohols[569,579−593]
	hydrogen gas[567−568,570−571,594−601]
	sodium borohydride[569,602−620]
	hydrazine[621−626]
	sodium citrate[627−628]
	thermal reduction[629−634]
	photochemical reduction[635−640]
	sonochemical reduction[641−648]
	ligand displacement of organometallics[649−658]
	metal vapor condensation[659−667]
	electrochemical reduction[668−670]
stabilizers	polymers[567−571,579−583,671−677]
	block copolymers[569,678−681]
	dendrimers[569,602,682−687]
	surfactants[688−692]
	other ligands[693−700]
chemical reactions	Suzuki cross-coupling reactions[569,580−582,602,604,701−706]
	Heck cross-coupling reactions[686,701,704−705,707−711]
	electron-transfer reactions[568,570−571,583,594,712−715]
	hydrogenations[716−720]
	oxidations[721−727]

recyclable catalysts.[572] The synthesis, structure, and catalytic properties of ligand-stabilized giant palladium clusters and nanosized palladium complexes have also been reported.[573] The use of transition metal nanoparticles stabilized with various polymers as homogeneous catalysts has been reviewed.[574] The use of monometallic and bimetallic nanoparticles stabilized by solvent and surfactants as catalysts has been surveyed.[575] PVP-stabilized bimetallic catalysts in colloidal dispersions have also been reviewed as potential catalysts.[576] The use of colloidal transition metal catalysts as low-temperature oxidation catalysts has been reviewed.[577] There has also been a general review on nanoscale transition metal nanoparticles and a description of transition metal colloids.[578]

Table 2 summarizes the common reduction methods used to synthesize transition metal nanoparticles in colloidal solution, the common stabilizers used to cap the colloidal transition metal nanoparticles, and the common reactions that have been conducted using the colloidal transition metal nanoparticles. Some common reducing agents and reduction methods that have been used to synthesize colloidal transition metal nanoparticles include chemical reduction with alcohols,[569,579−593] hydrogen gas,[567,568,570,571,594−601] sodium borohydride,[569,602−620] hydrazine,[621−626] and sodium citrate;[627,628] thermal reduction;[629−634] photochemical reduction;[635−640] sonochemical reduction;[641−648] ligand displacement of organometallics;[649−658] metal vapor condensation;[659−667] and electrochemical reduction.[668−670] Some common stabilizers used to cap transition metal nanoparticles in colloidal solution include polymers,[567−571,579−583,671−677] block copolymers,[569,678−681] dendrimers,[569,602,682−687] surfactants,[688−692] and other ligands.[693−700]

7.2.1. Chemical Reactions Catalyzed Using Colloidal Transition Metal Nanocatalysts

Some types of chemical reactions that have been catalyzed using transition metal nanocatalysts in colloidal solution include cross-couplings,[569,580−582,602,604,686,701−711] electron transfers,[568,570,571,583,594,712−715] hydrogenations,[716−720] and oxidations.[721−727] There are many other types of reaction that have also been catalyzed using transition metal nanoparticles in colloidal solution, but due to the vast volume of literature, we focus on only the above four types of reactions in this review. Table 2 summarizes some of the major reactions that have been catalyzed using colloidal transition metal nanocatalysts.

7.2.1.1. Cross-Coupling Reactions. Two main types of cross-coupling reactions that have been catalyzed using colloidal transition metal nanoparticles are the Suzuki and the Heck cross-coupling reactions. The Suzuki reaction is a C−C bond formation reaction that couples arylboronic acids and aryl halides to form biaryls, whereas the Heck reaction is a C−C bond formation reaction that occurs by the arylation of alkenes with aryl halides.

The use of transition metal nanoparticles to catalyze the Suzuki reaction[569,580−582,602,604,701−706] has been fairly recent. Palladium nanoparticles[569,580−582,602,604,701−704] are most commonly used to catalyze the Suzuki reaction, whereas ruthenium,[705,706] copper,[706] and bimetallic[706] nanoparticles have also been used to a much smaller extent. Many different capping agents have been used to stabilize the palladium nanoparticles that are used to catalyze the Suzuki reaction such as PVP,[569,580−582,602] PAMAM-OH dendrimers,[569,602,604] polystyrene-*b*-poly(sodium acrylate),[569] poly(*N*,*N*-dialkylcarbodiimide,[703] and G-3 dendrimer.[704] The Suzuki reaction has been conducted in aqueous solution using the 3:1 acetonitrile/water solvent[569,580−582,602] with palladium nanoparticles. The reaction has also been catalyzed with palladium nanoparticles under microwave heating conditions.[703] It has been shown that when PVP−Pd nanoparticles[582] and PAMAM−OH generation 4 dendrimer-stabilized Pd nanoparticles[602] are used to catalyze the Suzuki reaction between phenylboronic acid and iodobenzene, the palladium nanoparticles grow larger in size due to the Ostwald ripening process and the presence of unreduced Pd ions, partly reduced Pd ions, and Pd atoms in solution. After the second cycle, in the case of the PVP−Pd nanoparticles, the larger nanoparticles aggregate and precipitate out of solution, leaving the smaller nanoparticles left in solution. Figure 98 summarizes the TEM images and Gaussian fits of the size distributions of the PVP−Pd nanoparticles after the first and second cycles of the Suzuki reaction.

In the case of the dendrimer−Pd nanoparticles, the nanoparticles continue to grow in size during the second cycle of the reaction, and this could be due to a greater amount of partly reduced and unreduced Pd ions in solution as well as the stronger encapsu-

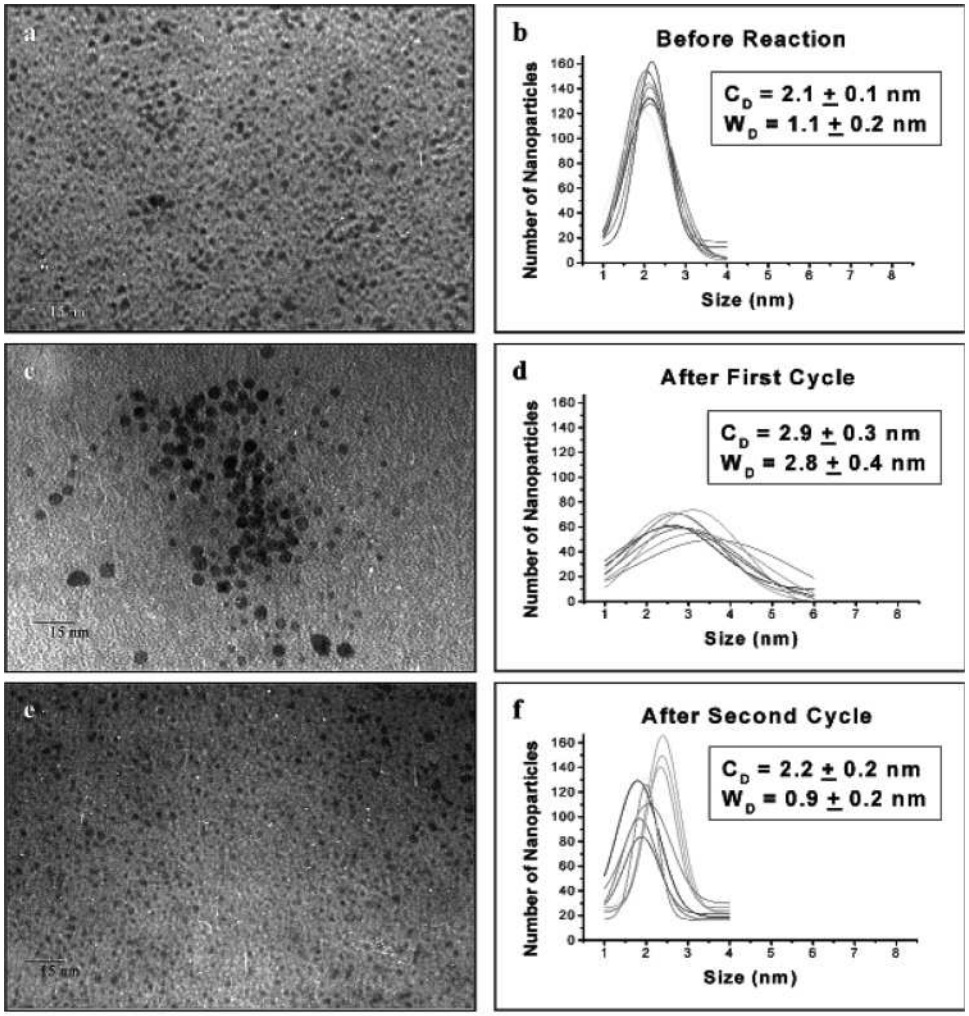

Figure 98. TEM images and Gaussian fits of the size distributions of PVP−Pd nanoparticles before the Suzuki reaction (a, b), after the first cycle of the reaction (c, d), and after the second cycle of the reaction (e, f). Reprinted with permission from ref 582. Copyright 2003 American Chemical Society.

lating action of the dendrimer. Also, it is found that the growth process occurs in the presence of iodobenzene, whereas it is inhibited in the presence of phenylboronic acid, the other reactant. On the basis of these results, it is proposed[582,602] that the mechanism of catalyzing the Suzuki reaction involves phenylboronic acid binding to the nanoparticle surface and reacting with the iodobenzene in solution. Palladium nanoparticles stabilized with 1,5-bis[4,4′-bis(perfluorooctyl)phenyl]-1,4-pentadien-3-one (I) have been shown to be efficient recoverable catalysts for the Suzuki reaction.[701] Palladium nanoparticles that are stabilized by a Keggin-type polyoxometalate have also been used to catalyze Suzuki reactions efficiently.[702] Palladium nanoparticle-cored G-3 dendrons were shown to be 90% unpassivated and were found to inhibit metal agglomeration without affecting chemical reactivity when catalyzing various Suzuki reactions.[704]

Another cross-coupling reaction that has been catalyzed using transition metal nanoparticles in colloidal solution is the Heck reaction[686,701,704−705,707−711] between alkenes and aryl halides for C−C bond formation. The Heck reaction has also been conducted mainly using palladium nanoparticles.[686,701,704,707−710] Ruthenium nanoparticles[705] and trimetallic (gold−silver−palladium) nanoparticles[711] have also been used as catalysts for the Heck reaction. PAMAM−dendrimer encapsulated palladium nanoparticles have also been used to catalyze the Heck reaction and were found to be an efficient catalyst in phosphine-free conditions.[686] Palladium nanoparticles stabilized with 1,5-bis[4,4′-bis(perfluorooctyl)phenyl]-1,4-pentadien-3-one (I) have been used as efficient recoverable catalysts for the Heck reaction between ethyl cinnamate and iodobenzene.[701] The palladium nanoparticle-cored G-3 dendrons with their highly unpassivated surface have also been used to efficiently catalyze Heck reactions.[704] Heck reactions have also been catalyzed with palladium nanoparticles in the presence of ionic liquids such as tetrabutylammonium bromide as the solvent and tetrabutylammonium acetate as the base.[608−709] Palladium nanoparticles encapsulated in PPI dendrimers have been used to catalyze Heck reactions between nonactivated aryl halides and butyl acrylate, and the recovered nanocatalysts were found to retain a significant fraction of their original catalytic activity.[710] Figure 99 shows a HRTEM image of the PPI dendrimer stabilized palladium nanoparticles used to catalyze Heck reactions.

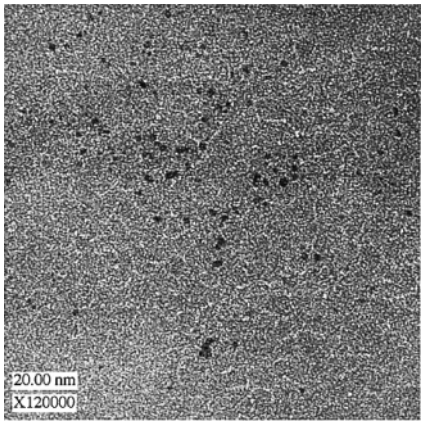

Figure 99. High-resolution TEM image of palladium nanoparticles stabilized with PPI dendrimers. Reprinted with permission from ref 710. Copyright 2001 American Chemical Society.

7.2.1.2. Electron-Transfer Reactions. Electron-transfer reactions[568,570,571,583,594,712−715] have also been catalyzed using transition metal nanoparticles in solution. There have been studies using spherical,[568,571,583] tetrahedral,[568,570,571] and cubic[568,570,571] shaped platinum nanoparticles to catalyze the electron-transfer reaction between hexacyanoferrate(III) ions and thiosulfate ions to understand what happens to the nanoparticles during the course of the reaction[570,571,583] and also to determine the catalytic activity.[568,571] Figure 100 shows TEM images of tetrahedral, cubic, and spherical platinum nanoparticles, their shape distributions, and the activation energy obtained when catalyzing the electron-transfer reaction.

The tetrahedral nanoparticles with their (111) facets and also a great fraction of surface atoms on edges and corners are found to be the most catalytically active.[568] The cubic nanoparticles with their (100) facets and a very small fraction of surface atoms on edges and corners are found to be the least catalytically active. The spherical nanoparticles are actually nearly spherical because they are composed of many (111) and (100) facets with many edges at their interfaces. As a result, the activation energy of the nearly spherical nanoparticles is intermediate to that of the tetrahedral and cubic nanoparticles. All of these results were obtained at the early stages of the reaction and before shape changes occur.[568] It has been observed that during the course of the reaction, there are changes in the tetrahedral and cubic shapes[570] with corresponding changes in the activation energies.[571] Figure 101 shows HRTEM images of tetrahedral and cubic platinum nanoparticles before and after the reaction, and it can be seen that there are distortions that occur in the corners and edges of the two types of nanoparticles.

A size-dependent study has also been conducted using platinum nanoparticles[712] to catalyze this electron-transfer reaction. It was observed that particles below 38 nm exhibit a trend of decreasing reaction rate with decreasing particle size, whereas those above 38 nm show a steady decline of reaction

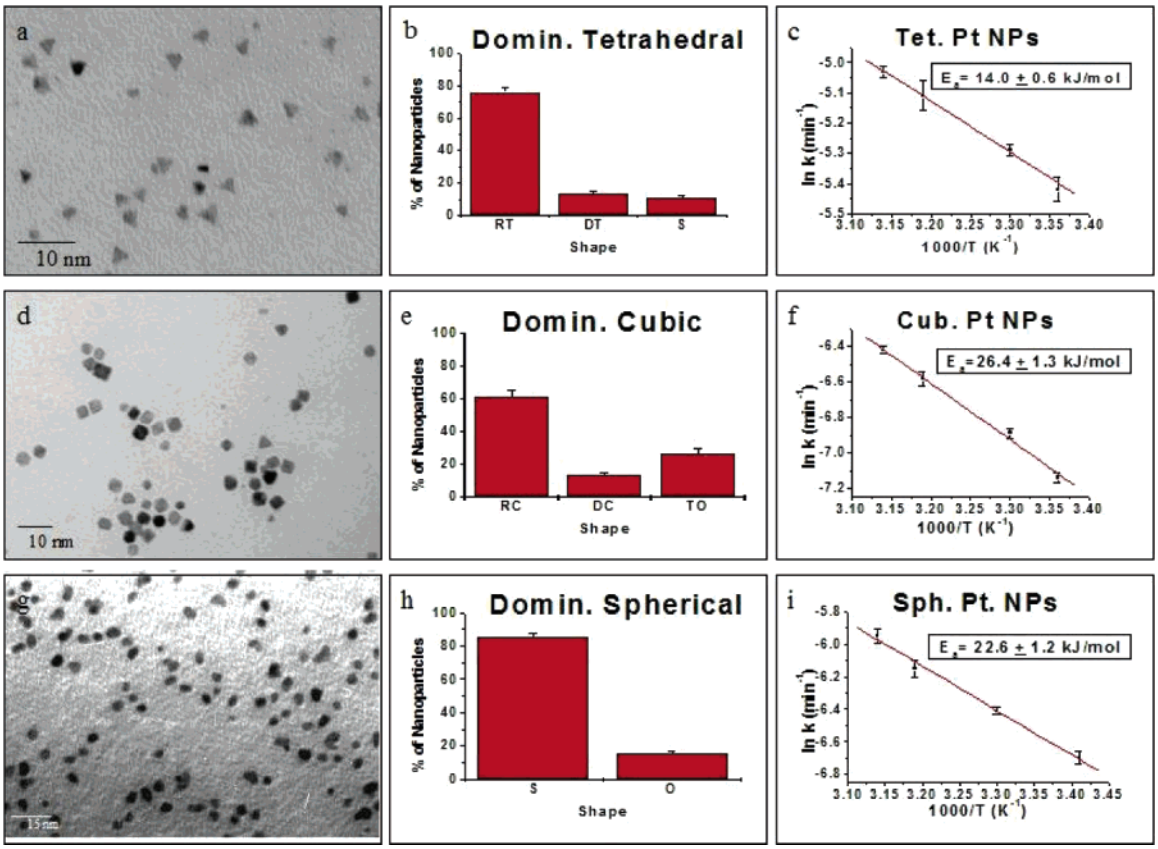

Figure 100. TEM images and shape distributions of dominantly tetrahedral, cubic, and spherical platinum nanoparticles (a, b; d, e; and g, h), activation energy obtained for catalyzing the electron-transfer reaction with tetrahedral, cubic, and spherical platinum nanoparticles (c, f, and i). Reprinted with permission from ref 568. Copyright 2004 American Chemical Society.

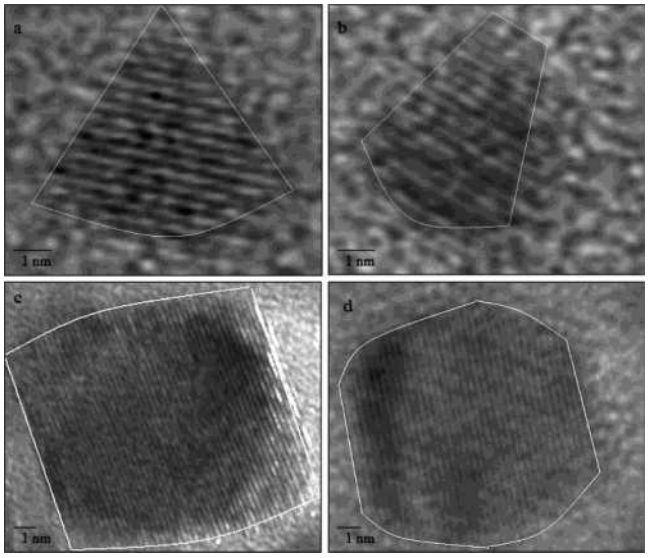

Figure 101. HRTEM image of a tetrahedral platinum nanoparticle before the electron-transfer reaction (a), after the reaction (b), cubic platinum nanoparticle before the electron-transfer reaction (c), and after the reaction (d). Reprinted with permission from ref 570. Copyright 2004 American Chemical Society.

rate with increasing size. The authors propose that when the nanoparticles are smaller than 38 nm, there is a downward shift in the Fermi level with a consequent increase in the band gap energy. As a result, the nanoparticles require more energy to pump electrons to the adsorbed ions for the electron-transfer reaction. This leads to a reduced reaction rate by the smaller nanoparticles. For nanoparticles larger than 38 nanometers, the change in Fermi level is not appreciable, and they exhibit less surface area for adsorption due to the larger size of the nanoparticles.

Platinum nanoparticles that are stabilized in an aerosol−OT (AOT)−water−heptane system[713] have also been used to catalyze this reaction. In this case, it was observed that the initial rate of the reaction increased linearly with the concentration of the Pt nanoparticles and that the rate constant data suggested that the rate-determining step occurs at the surface of the Pt nanoparticles. In addition, citrate-stabilized gold nanoparticles[714,715] were also used to catalyze this reaction. It was found that the catalytic rate increased linearly with the concentration of the catalysts for gold nanoparticles of different sizes, and the magnitude of the rate constant suggested that the rate-determining step occurs at the gold nanoparticle surface.

7.2.1.3. Hydrogenation Reactions. Hydrogenation reactions[716−720] are the most common reactions that have been conducted using transition metal nanoparticles in colloidal solution. Examples of some types of hydrogenation reactions that have been catalyzed with colloidal transition metal nanoparticles include hydrogenation of benzene,[716,717] cyclooctene hydrogenation,[718] hydrogenation of dehydrolinalool,[719] hydrogenation of cinnamaldehyde,[720] etc. There are many more kinds of hydrogenation reactions that have been conducted and are too numerous to list. Palladium and rhodium nanoparticles that are stabilized with plastic have catalyzed the complete hydrogenation of benzene in the presence of supercritical carbon dioxide as the solvent and were found to be highly efficient and reusable catalysts.[716] Iridium and rhodium nanoparticles that were formed and stabilized in the presence of ionic liquids have been shown to be efficient catalysts for the hydrogenation of arenes.[717] Chitosan-stabilized platinum and palladium nanoparticles have been used to catalyze the octene and cyclooctene hydrogenation reactions, and it was observed that the catalytic activity is greater when the platinum nanoparticles are used as catalysts for both reactions.[718] Poly(ethylene oxide)-*block*-poly-2-vinylpyridine micelles filled with Pd nanoparticles were used as catalysts for the selective hydrogenation of dehydrolinalool to form linalool.[719]

7.2.1.4. Oxidation Reactions. Oxidation reactions[721−727] are very important in many industrial processes and have been catalyzed by transition metal nanoparticles. Some oxidation processes that are important in the color photography industry include the oxidation of DMPPD[721] and TMPPD,[722] which have been shown to be catalyzed by palladium nanoparticles in water/AOT/heptane microemulsions. The oxidation of ethylene has been conducted with silver colloidal nanoparticles[723] that are stabilized with poly(sodium acrylate) and also with gold nanoparticles[724,725] stabilized with sodium polyacrylate. It was found that the rate of oxidation with polyacrylate capped silver nanoparticles as catalysts increased with increasing reaction temperature.[723] In the case of PVP-stabilized silver nanoparticles catalyzing the oxidation of ethylene, it was found that the addition of alkali metal ions increased the catalytic activity remarkably.[724] The cyclohexane *tert*-butyl peroxidation reaction catalyzed with iron oxide nanoparticles was found to occur at anaerobic conditions, and this made it an interesting alternative to other methods of catalyzing this reaction.[726] The oxidation of alkanes[727] has also been catalyzed by iron oxide nanoparticles in reverse microemulsions.

7.3. Heterogeneous Catalysis on Support

In heterogeneous catalysis, transition metal nanoparticles are supported on various substrates and used as catalysts. There have been a number of reviews that discuss various reactions conducted using supported transition metal nanoparticles as catalysts.[728−737] There has been a review on highly active supported transition metal nanocatalysts for hydrogenations and enantioselective synthesis of organic compounds.[728] Functional resins are reviewed as potential supports for transition metal nanoparticles as complements to traditional supports.[729] The effect of the support used on the catalytic activity of monometallic and bimetallic nanoparticles has been surveyed.[730] The catalytic properties of transition metal nanoparticles that are supported on oxide supports have been reported.[731] A review of supported transition metal nanoparticles as catalysts for oxidations and epoxidations has been conducted.[732] The impact of nanoscience on heterogeneous catalysis has been reviewed.[733] The use of supported bimetallic

Table 3. References to the Common Supports Used in Heterogeneous Nanocatalysis and Examples of Reactions Studied

important factors for supported transition metal nanoparticles	examples
supports	carbon[738−749]
	silica[750−758]
	alumina[759−767]
	titanium dioxide[768−773]
	grafting onto polymeric support[774−781]
	lithographically fabricated onto supports[782−789]
chemical reactions	fuel cell reactions[738−743,746,748,790−794]
	oxidations[739−740,791,795−800,802,804]
	hydrogenations[750,751,756,758,760,762,767,773,782−784,789]
	reduction reactions[759,761,763,764,781,809]
	decompositions[744,782,810−812]

nanoparticles for catalyzing a variety of hydrogenation reactions has been reviewed.[734] A review has been conducted suggesting that the focus of transition metal nanoparticles as catalysts in heterogeneous catalysis should be on 100% selectivity of the product to be formed.[735] Adsorbate-induced restructuring of supported transition metal nanocatalysts has been surveyed.[736] A survey of supported transition nanoparticles fabricated by using electron beam lithography and pulsed laser deposition has been conducted.[737]

There are three major ways through which heterogeneous transition metal nanocatalysts are prepared: adsorption of the nanoparticles onto supports, grafting of the nanoparticles onto supports, and fabrication of nanostructures onto supports by lithographic techniques. Some common supports that have been used in the preparation of supported transition metal nanoparticles include carbon,[738−749] silica,[750−758] alumina,[759−767] titanium dioxide,[768−773] grafting onto polymeric supports,[774−781] and lithographic fabrication[782−789] on supports. Table 3 gives a summary of the different types of supports that have been used to prepare supported transition metal nanoparticles and also some common reactions that have been catalyzed using supported transition metal nanoparticles.

7.3.1. Lithographically Fabricated Supported Transition Metal Nanocatalysts

Electron beam lithography[782−789] has been used to fabricate arrays of transition metal nanoparticles onto different supports such as silica and alumina. Platinum nanoparticles that are 50 nm have been fabricated onto silicon wafers and have been used to catalyze the ethylene hydrogenation at high pressures.[782,784] Studies on the reaction intermediates and surface restructuring of platinum nanoparticle arrays formed on silica, alumina, and titania that are used to catalyze olefin hydrogenations have been conducted.[783] The stability of lithographically fabricated supported silver arrays in both oxidizing and reducing conditions has been investigated.[785] Twenty nanometer silver arrays supported on a silicon wafer have been used to catalyze the ethylene epoxidation reaction.[786] The thermal, chemical, and adhesion

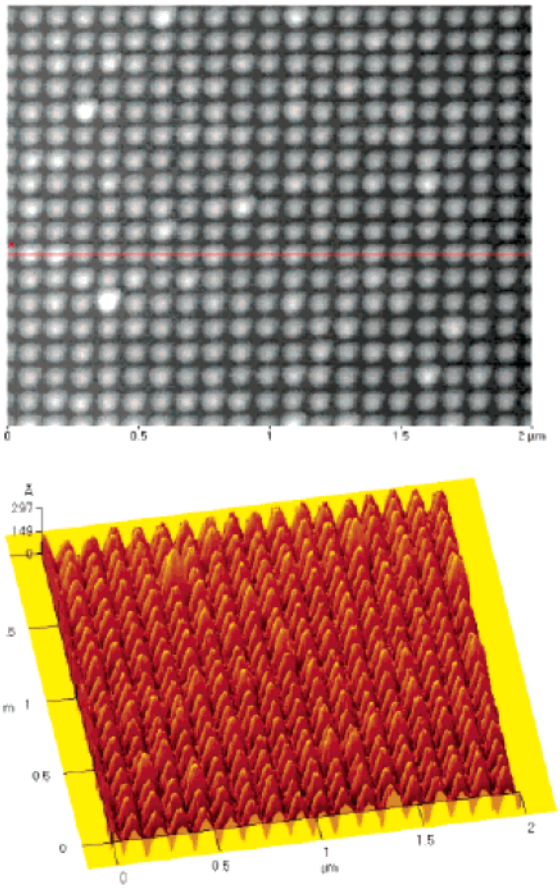

Figure 102. AFM images of the platinum nanoparticle arrays fabricated using electron beam lithography (nanoparticle height = 15 ± 2 nm with interparticle spacing of 100 ± 1 nm). Reprinted with permission from ref 789. Copyright 2002 American Chemical Society.

stabilities of platinum nanoparticle arrays supported on silica were studied.[787] It was found that at high temperature (1000 K) and high vacuum (10^{-7} Torr) and in the presence of 1 atm of hydrogen gas, the domain sizes within individual particles grew larger without any noticeable deformation of the arrays. Platinum nanoparticles that are lithographically fabricated and supported on silica have been used to catalyze the hydrogenation and dehydrogenation of cyclohexane.[788] Figure 102 shows AFM images of the platinum nanoparticle arrays fabricated using electron beam lithography. The nanoparticles in the arrays have an average height of 15 ± 2 nm, and the interparticle spacing is 100 ± 1 nm. The ethylene hydrogenation reaction has been catalyzed using these nanoparticle arrays as catalysts, and the active metal surface area in this type of nanocatalyst has been determined on the basis of the calculated turnover frequency.[789]

7.3.2. Chemical Reactions Catalyzed Using Supported Transition Metal Nanocatalysts

Many different kinds of chemical reactions have been catalyzed using heterogeneous transition metal nanocatalysts. A major industrial area that utilizes supported transition metal nanocatalysts is the fuel cell industry for catalyzing fuel cell reactions. Some types of reactions that have been catalyzed using

heterogeneous metal nanocatalysts include fuel cell reactions,[738−743,746,748,790−794] oxidations,[739−740,791,795−800,802,804] hydrogenations,[750,751,756,758,760,762,767,773,782−784,789] reductions,[759,761,763−764,781,809] decompositions,[744,782,810−812] etc. There are many other types of chemical reactions that have been conducted using supported transition metal nanoparticles in heterogeneous catalysis, but due to the huge volume of literature, we will focus only on the above reactions in this review. Table 3 summarizes some of the major reactions that have been catalyzed using supported transition metal nanoparticles.

7.3.2.1. Fuel Cell Reactions. Supported metal nanoparticles have been widely used in catalyzing many reactions associated with direct methanol and ethanol fuel cells. A majority of the fuel cell reactions[738−743,746,748,790−794,808] have been conducted using transition metal nanoparticles that are supported on various forms of carbon. Some fuel cell reactions that have been conducted using heterogeneous supported transition metal nanoparticles include methanol oxidation,[738,742−743,746,748,790,792−794,808] oxidation reduction,[741] etc. Platinum and platinum−ruthenium nanoparticles supported on various forms of carbon are the most commonly used supported transition metal nanoparticles for catalyzing a variety of fuel cell reactions. Platinum and PtRu nanoparticles that are supported on Vulcan XC-72 carbon have been used as catalysts for the methanol oxidation reaction in direct methanol fuel cells (DMFCs).[738,743] Carbon-supported platinum nanoparticles have also been used to catalyze the oxidation reduction reaction in solid polymer electrolyte fuel cells.[741] Platinum−ruthenium bimetallic nanoparticles supported on Vulcan XC-72 and carbon nanotubes have been used as catalysts for the electro-oxidation of methanol in DMFCs.[742,748,793] Platinum−ruthenium bimetallic nanoparticles supported on carbon black have also been used as catalysts for the electro-oxidation of methanol.[746]

Figure 103 shows high-resolution TEM images of the platinum nanoparticles supported on carbon after nanogluing with silica sol to form the Pt-modified carbon−silica composite aerogels and both types of nanoparticles after heating them to 900 °C.[790] The heating process is conducted to yield more uniformly distributed platinum nanoparticles. This highly active electrocatalytic architecture consisting of colloidal platinum-modified carbon−silica composite aerogels has been shown to have electocatalytic activity that is 4 orders of magnitude greater than that of a native Pt-modified carbon powder.[790] It has been found that PtRu bimetallic nanoparticles are not the most active for methanol electro-oxidation and that a catalyst consisting of a mixture of Pt metal and hydrous ruthenium oxide is more catalytically active for this fuel cell reaction.[792] Osmium and platinum−osmium nanoparticles supported on carbon have been tested as potential methanol oxidation catalysts in DMFCs, but were found to have low catalytic activity.[794]

7.3.2.2. Oxidation Reactions. Some common oxidation reactions that have been catalyzed using

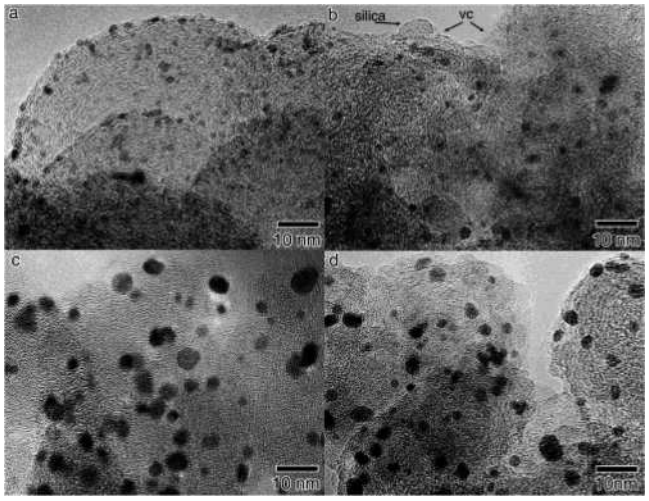

Figure 103. High-resolution TEM images of the Pt nanoparticles supported on Vulcan carbon (a), after nano gluing with silica sol to form Pt-modified carbon−silica composite aerogel, and both types of nanoparticles after heating to 900 °C (c, d). Reprinted with permission from ref 790. Copyright 2002 American Chemical Society.

supported nanoparticles are the CO oxidation reaction,[739−740,791,795−800,802,804] oxidation of ethylene glycol,[792,793,803] oxidation of diesel soot,[801] oxidation of glycerol,[805] oxidation of benzene,[806] and oxidation of SO_2.[807] Gold nanoparticles supported on activated carbon fibers have been found to be highly active for the CO oxidation reaction.[739] Gold nanoparticles supported on various reducible and nonreducible oxides have also been used to catalyze the low-temperature CO oxidation reaction.[740] Gold-supported titanium dioxide composite aerogels have also been shown to have high catalytic activity for the CO oxidation reaction.[791] When gold nanoparticles supported on silica are prepared using chemical vapor deposition (CVD), it is observed that the nanoparticles have enhanced catalytic activities for the CO oxidation reaction compared to the nanoparticles prepared using liquid-phase methods.[794] A comparison of the catalytic activity of gold nanoparticles prepared using CVD and supported on silica, alumina, and titania was conducted, and it was found that there are no differences in the catalytic activity for the oxidation of CO.[795] Gold nanoparticles supported on iron oxide and titanium dioxide have also been used to catalyze the CO oxidation reaction and were found to have different catalytic activities that arise from changes in the gold nanoparticle size distribution.[797] Gold nanoparticles that are deposited onto metal oxides by liquid-phase grafting of di-Me gold acetylacetonate have been shown to be highly active for the CO oxidation reaction.[798] Gold nanoparticle−nylon 11 nanocomposites supported on titania were shown to be highly active for the CO oxidation reaction with a 50% conversion of CO.[799] Gold nanoparticles supported on titanium dioxide nanorods have also been used to catalyze the CO oxidation reaction and were found to be as catalytically active as gold nanoparticles supported on spherical titanium dioxide nanoparticles.[800] Gold nanoparticles supported on SBA-15 silica that is functionalized with positively charged groups were shown to be

more active for the CO oxidation reaction than other silica supported gold nanoparticles that were prepared using a solution technique.[802] The CO oxidation reaction has also been catalyzed with Pt−Ru bimetallic nanoparticles, and it was found that the rate-determining step was the oxidation of Ru atoms on the PtRu nanoparticles.[796] Platinum nanoparticles adsorbed on alumina have also been used as catalysts for the CO oxidation reaction.[804]

Gold nanoparticles that were immobilized on activated carbon and titania have been used as catalysts for the oxidation of ethylene glycol to form glycolate.[792,793] Gold nanoparticles stabilized with *N*-dodecyl-*N*,*N*-dimethyl-3-amino-1-propane sulfonate and immobilized in activated carbon were found to have superior catalytic activity for the oxidation of ethylene glycol than other kinds of carbon-supported gold nanoparticles.[803] The oxidation of diesel soot has been catalyzed with gold nanoparticles supported on vanadia−titania and vanadia−zirconia, and it was observed that the catalytic activity was higher at higher loadings of vanadia.[801] Platinum, palladium, and gold nanoparticles supported on activated carbon and graphite have been used to catalyze the oxidation of glycerol.[805] Gold nanoparticles supported on vanadia−ceria have been used to catalyze the complete oxidation of benzene and were found to have a high and stable catalytic activity.[806] Titania-supported platinum nanoparticles were shown to have a high catalytic activity for the SO_2 oxidation reaction.[807]

7.3.2.3. Hydrogenation Reactions. Numerous hydrogenation reactions[750,751,756,758,760,762,767,773,782−784,789] have also been catalyzed by many different types of heterogeneous supported transition metal nanoparticles. Some specific hydrogenation reactions that have been catalyzed using supported transition metal nanocatalysts include hydrogenation of benzene,[750,758] hydrogenation of cinnamaldehyde,[751] hydrogenation of *N*-heterocycles,[756] hydrogenation of arenes,[760] hydrogenation of propene,[762,767] hydrogenation of crotanaldehyde,[773] ethylene hydrogenation,[782,784,789] hydrogenation of olefins,[783,808] etc. There are many more kinds of hydrogenation reactions that have been catalyzed using supported transition metal nanoparticles, and the above reactions mentioned are examples of some typical hydrogenation reactions. Nickel and palladium nanoparticles supported on silica have been used as catalysts for the hydrogenation of benzene.[750,758] Palladium nanoparticles supported on silica monolith have been used to catalyze the hydrogenation of cinnamaldehyde.[751] Silica-supported ruthenium nanoparticles were shown to be efficient catalysts for the hydrogenation of *N*-heterocycles and simple aromatic hydrocarbons, but were found to be unsuccessful in catalyzing the hydrogenation of *S*-heterocycles.[756] Alumina-supported ruthenium nanoparticles were also used to catalyze the hydrogenation of arenes such as methyl benzoate and 2-(methoxycarbonylphenyl)-1,3-dioxane.[760] Platinum nanoparticles prepared using the hydrogen reduction method and supported on alumina have been used to catalyze the propene hydrogenation reaction.[762,767] Silica- and titania-supported silver nanoparticles have been used as catalysts for the hydrogenation of crotanaldehyde, and it was determined that this reaction is structure-sensitive with the rate-determining step depending critically on the silver nanoparticle size and surface structure.[773] Arrays of disk-shaped platinum nanoparticles on silicon wafers that were prepared using electron beam lithography (EBL) have been used as catalysts for the hydrogenation of ethylene at high pressures.[782−784] Arrays of platinum nanoparticles on alumina support that were prepared by EBL were also used to catalyze the ethylene hydrogenation reaction and were used to determine the active metal surface area in the nanoparticles.[789]

7.3.2.4. Reduction and Decomposition Reactions. There are many kinds of reduction[759,761,763,764,771,809] and decomposition[744,772,810−812] reactions that have been catalyzed by heterogeneous supported transition metal nanocatalysts. Some types of reduction reactions include NO reduction,[759,761,763,764,809] reduction of SO_2,[772] etc. Some decomposition reactions that have been catalyzed using heterogeneous supported transition metal nanoparticles include decomposition of methane,[744] decomposition of formic acid,[772] decomposition of chlorodifluoromethane,[810] ammonia decomposition,[811] decomposition of acetylene,[812] etc.

The relationship between the morphology of alumina-supported platinum nanoparticles and their catalytic activity was investigated for the NO reduction reaction. For the mainly cubic Pt nanoparticles, it was found that there was a conversion of the low index facets to higher plane facets, and this was also associated with substantial changes in the catalytic activity and selectivity of the products obtained.[759] Platinum nanoparticles of different morphologies that are supported on alumina have been used as catalysts for the NO reduction reaction, and it was observed that the catalytic behavior can be tuned by the morphology of the nanoparticles.[761] Alumina-supported ruthenium nanoparticles were found to have high catalytic activity and selectivity for the NO reduction reaction.[763,764] Platinum−rhodium bimetallic nanoparticles were also used to catalyze the NO reduction reaction, and it was found that alloys with a higher percentage of Pt are more catalytically active than pure Pt nanoparticles.[809] On the other hand, alloys with a greater percentage of Rh were found to have a low catalytic activity for this reaction. The SO_2 reduction reaction has been catalyzed using titania-supported ruthenium sulfide nanoparticles, and it was found that this catalyst has high catalytic activity even at low temperatures.[771]

Palladium and nickel nanoparticles supported on oxidized diamond have been used as catalysts for the methane decomposition reaction to produce carbon nanowhiskers.[744] Figure 104 shows TEM images of carbon nanowhiskers that have been formed during the decomposition of methane with nickel and palladium nanocatalysts supported on oxidized diamond.

Titania-supported palladium nanoparticles were used to catalyze the formic acid decomposition reaction, and it was found that the catalytic activity for the supported Pd nanoparticles is slower than for Pd single crystals.[772] This could be due to alloying with Ti originating from the interstitial Ti^{3+} cations in the

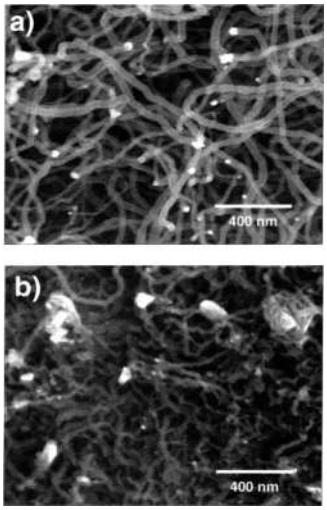

Figure 104. TEM images of carbon nanowhiskers that have been formed during the methane decomposition reaction catalyzed by nickel nanoparticles supported on oxidized diamond (a) and palladium nanoparticles supported on oxidized diamond (b). Reprinted with permission from ref 744. Copyright 2003 American Chemical Society.

oxide. This results in a reduced electron density at the Fermi level of the nanoparticles. Gold nanoparticles supported on thiol-functionalized titanium oxide−zirconium oxide were tested as catalysts for the chlorodifluoromethane decomposition reaction and were found to have only a small increase in selectivity of the products obtained compared to without the catalyst.[810] Small ruthenium nanoparticles supported on carbon nanotubes have been found to be highly active and stable for catalyzing the ammonia decomposition reaction.[811]

8. Summary

This review is intended to demonstrate the richness and maturity that nanoscience and nanochemistry in particular have achieved in recent years. Although the elemental composition and size control of nanostructures have been a major topic over the past decade, it is the shape that is now a third major coordinate in the chemistry of nanostructures. This clearly enriched the field of nanochemistry enormously, which is reflected in a large number of recent books and overview-type papers. Below, we present a short survey of the different reviews and books written in the field as a summary.

8.1. Reviews

Numerous reviews have been written about the synthesis and properties of different kinds of nanoparticles such as metal nanoparticles, semiconductor nanoparticles, and carbon-based nanoparticles. There have also been many reviews written about nanoparticles in general. Table 4 summarizes the references to the reviews that have been written about the different kinds of nanoparticles.

8.1.1. Synthesis

8.1.1.1. Metal Nanoparticles. There have been many reviews on the synthesis of metallic[613,813−819] nanoparticles. Some reviews deal with the synthesis of metallic nanoparticles in general.[813,828] Some reviews deal with the synthesis of gold nanoparticles.[814,817] The synthesis of dendrimer encapsulated metal nanoparticles has been reviewed.[613] The use of lithographic techniques to fabricate metallic nanoparticles has also been surveyed.[4,816,817,819]

Table 4. References to Review Articles and Books That Have Been Written on Different Kinds of Nanoparticles

publishing medium	type of nanoparticles
review articles on the synthesis of nanoparticles	metal nanoparticles[4,613,813−819,828] semiconductor nanoparticles[820−825] carbon-based nanoparticles[213,826−832]
review articles on the properties of nanoparticles	metal nanoparticles[260,281,833−839] semiconductor nanoparticles[2,311,323,329,462,463,840−850] carbon-based nanoparticles[257,851−865]
review articles on nanoparticles in general	nanoparticles in general[866−876]
books	metal nanoparticles[877,878] semiconductor nanoparticles[308,878−887] carbon-based nanoparticles[888−897] nanoparticles in general[898−921]

8.1.1.2. Semiconductor Nanoparticles. Many reviews have also been written on the synthesis of semiconductor[820−825] nanoparticles. Some reviews deal with the synthesis of quantum dot semiconductor nanoparticles,[820−822,824] whereas another discusses the synthesis of semiconductor nanowires and nanotubes.[823] The synthesis of semiconductor nanocrystal superlattices has also been surveyed.[825]

8.1.1.3. Carbon Nanotubes and Nanoparticles. Because many papers have been written in this active field, we did not include it in this review. Here we give references to only some of the reviews. Numerous reviews have been written on the synthesis of carbon-based[213,826−832] nanotubes and nanoparticles. A review has also been written on the synthesis of carbon nanocones.[827]

8.1.2. Properties

8.1.2.1. Metal Nanoparticles. Many reviews have been written on the properties of metal nanoparticles.[260,281,833−839] The assembly of metallic nanoparticles has been surveyed.[833,838] A review on the crystal structure of gold nanoparticle arrays has been conducted.[281] The optical properties and ultrafast dynamics of metal nanoparticles have been reviewed.[260,837] The properties of gold nanoparticles and its applications in biology, catalysis, and nanotechnology have been surveyed.[834] The potential for using metal nanoparticles for optical devices is examined.[835] The photocatalytic aspects of metal nanoparticles have been reviewed.[836] The synthesis, properties, and applications of one-dimensional metal nanostructures have been surveyed.[839]

8.1.2.2. Semiconductor Nanoparticles. Many reviews have been published on the properties of different kinds of semiconductor nanoparticles.[2,311,323,329,462,463,840−850] The interfacial charge carrier dynamics of semiconductor nanoparticles has been reviewed.[329,463] The size- and composition-de-

pendent properties of semiconductor nanoparticles have been examined.[840] The luminescent properties of semiconductor nanocrystals have been surveyed.[840,847] A review has been conducted on the size and shape of strained germanium nanoparticles grown on silica substrate.[841] The spectroscopy of single CdSe nanocrystals has been examined.[842] The characterization of semiconductor nanoparticles has also been reviewed.[843,848] A survey of semiconductor nanoparticles and their applications has been conducted.[2,311] The self-assembly of semiconductor nanoparticles is surveyed.[844] The hot electron dynamics of quantum wells and quantum dots is examined.[462] The tunneling and optical spectroscopy of semiconductor nanoparticles has also been reviewed.[845] Magnetic resonance studies on semiconductor nanoparticles have been conducted.[846,850] The photophysics of semiconductor nanoparticles has been examined.[849]

8.1.2.3. Carbon Nanotubes and Nanoparticles. Many review articles have been written on the properties of carbon-based[257,851−865] nanotubes and nanoparticles. The characterization of carbon nanotubes using electron microscopy has been examined.[851] The properties of carbon nanotubes and applications have been reviewed.[257,852,856−858,860−864] Chemical doping of carbon nanotubes has been studied.[853] The molecular electronic applications of carbon nanotubes have also been surveyed.[854] Defects in carbon nanotubes have been studied.[855] The Raman spectroscopy of single carbon nanotubes has been surveyed.[859] The ballistic conduction properties of carbon nanotubes have also been studied.[865]

8.1.3. General

Several reviews have been published on nanoparticles in general.[866−876] The synthesis of nanoparticles in general has been reviewed.[866] The properties and applications of functional oxide nanobelts have been surveyed.[867] The self-assembly of nanostructures has been examined.[868,870] Scanning probe microscopy studies of single nanostructures have been conducted.[869] Nanoengineering of particle surfaces has also been studied.[871] The applications of nanoparticles have also been reviewed.[872,873] The use of transmission electron microscopy in characterizing nanoparticles has been examined.[874,875] The self-assembly of coated nanoparticles has also been surveyed.[876]

8.2. Books

Many books have been written on different types of nanoparticles such as metal nanoparticles, semiconductor nanoparticles, and carbon-based nanoparticles. Numerous books have also been written on the synthesis, properties, and applications of nanoparticles in general. Table 4 summarizes the books that have been written about the different kinds of nanoparticles.

8.2.1. Metal Nanoparticles

There have been a couple of books that have been written on metal nanoparticles.[877,878] A book on the synthesis, characterization, and applications of metal nanoparticles has been written.[877] It also focuses on the structural, optical, and electronic properties of the nanoparticles and emphasizes that the size, shape, and surface chemistry can affect the performance of the nanoparticles. In another book, the synthesis, electronic, and optical properties of metal nanoparticles have also been examined.[878] It documents advances in nanocrystal synthesis and assembly and discusses various applications such as optical amplification and bio-labeling.

8.2.2. Semiconductor Nanoparticles

Many books have been written on semiconductor nanoparticles.[308,878−887] The synthesis, electronic, and optical properties of semiconductor nanoparticles have been discussed in many books.[308,878,879,882,887] The optical properties of quantum dots with coverage of both theoretical and experimental results have been examined in great detail.[270] The synthesis of quantum dots and their applications in photovoltaic and electroluminescent devices have been reviewed.[878] The optical properties of quantum-confined semiconductor nanostructures have been discussed from both a theoretical and experimental point of view.[879] The theory, spectroscopic investigation, and methods of producing semiconductors such as quantum dots, II−IV semiconductors, and photonic crystals have been examined.[882] One book examines synthetic strategies and characterization methodologies for ultrasmall semiconductor nanoparticles, films, and wires as well as the fate of photoinduced charge carriers in these materials and the phenomena of charge transfer across interfaces.[887]

Books have also been written on quantum dots and nanowires.[880,881,883−886] Some emerging aspects of quantum dots and nanowires such as advances in physical and chemical synthetic approaches, processing and fabrication of quantum-dot arrays, self-assemblies, spectroscopic characterization, and their properties have been examined.[880] One book provides comprehensive reviews on many aspects of quantum dot systems such as their growth, structure, self-assembly, energy states, and optical properties.[881] The properties of quantum dots have also been discussed in great detail.[883,885] The key phenomena and principles of quantum dots have been examined such as their fabrication, self-organization, geometric structure, chemical composition, theoretical and experimental properties, and their use for photonic devices.[884] Another book focuses on the theoretical study of size confinement, dipole interaction, spin−orbital coupling, third-order linearities, and the influence of lattice phonons and external magnetic fields on quantum dots grown on glass and also comments on the experimental results that have been obtained.[886]

8.2.3. Carbon Nanotubes and Nanoparticles

There have been many books written on carbon-based nanotubes and nanoparticles.[888−897] A book has been written on the use of electron microscopy to characterize carbon nanotubes.[888] Many books have been written on the properties and applications of carbon nanotubes.[889−891,893−897] Many important areas of carbon nanotube research have been covered such

as the synthesis and growth mechanisms as well as theoretical approaches to the electronic properties and structure.[889] One book provides a comprehensive review on the status of carbon nanotube research and discusses various synthetic techniques and growth mechanisms.[890] The synthesis of carbon nanotubes, their mechanical, chemical, and electronic properties, and their applications have been examined.[891] The physics of fullerene and fullerene-based nanomaterials have been examined.[892] One book focuses on the basic principles behind the physical properties of carbon nanotubes and also discusses their transport and elastic properties.[893] Other carbon nanostructures such as carbon nanocapsules, onion-like graphite particles, and metal-coated fullerenes are discussed in addition to the traditional carbon nanotubes.[894] This textbook introduces the physical concepts that are needed for investigating carbon nanotubes and other one-dimensional solid-state systems and gives a combined theoretical and experimental description of topics such as luminescence, Raman scattering, and transport measurement.[895]

8.2.4. Nanoparticles in General

Numerous books have also been written about nanoparticles in general.[898−921] Books have been written on the application of nanoparticles.[898,899,904,909,913−914,916,921] The synthesis, assembly, fundamental physical properties, and pragmatic applications of nanoparticles have been discussed in great detail from a chemist's standpoint rather than one oriented toward materials science or physics.[898] A reference book has been published that provides fundamental knowledge of nanoscopic materials and covers topics such as metal nanoparticles for catalysis, synthesis for microemulsions, spectroelectrochemistry of semiconductor quantum dots, properties and applications of Langmuir−Blodgett films, and magnetic thin films.[899] A book has been written on the use of nanoparticles in catalysis and electrocatalysis.[900] The synthesis, characterization, and properties of nanoparticles have been discussed as well as applications in single-electron devices, ultradense recording media, bioelectronic sensors, and biolabeling.[902] Advances in molecularly designed nanostructured materials have been covered such as flame synthesis of nanosized powders, nanodispersed metal nanoparticles in polymeric matrices, and monodisperse sol−gel materials.[907] One book focuses on nanostructures and how they can be synthesized and also discusses useful implementations and applications of nanotechnology.[911] The innovative synthesis of nanomaterials, characterization, and some of their properties such as quantum size effects, superparamagnetism, and field emission have been covered.[912] The synthesis and processing of different classes of nanomaterials as well as their mechanical, magnetic, electronic, optical, chemical, and structural properties have been discussed.[914] A reference book has been written on the bottom-up approach to designing nanostructured systems for a variety of chemical, physical, and biological applications.[919]

There have also been books written about nanoparticles in a general manner.[901−906,908−912,915,917,919,921] Supramolecular and other approaches for synthesizing polymer colloids have been covered along with an emphasis on the use of the polymer colloids for biological and biomedical applications.[901] Developments in nanoscale and molecular electronics, biotechnology, carbon nanotubes, and nanocomputers have been examined.[902] Books have also been written on self-assembled nanoparticles.[903] The synthesis of nanoparticles and controlling their morphology has been reviewed.[904] An introductory textbook has been written that covers the basic background on nanoparticles and also covers topics such as molecular nanotechnology, nanomaterials and nanopowders, nanoelectronics, and nanobiomimetics.[905] The science and technology of nanostructured metallic and ceramic materials have been examined such as the synthesis, characterization, assembly, properties, and applications.[920] A book has been written on nanostructured materials such as nanocrystals, semiconductor heterostructures, nanotubes, and nanowires.[909] The course of nanoscience research has been delineated, and a vision has been articulated for the development of nanoscale frontiers in electronics, mechanics, chemistry, magnetics, materials, and biology.[909] Many nanotechnology areas have been covered such as the synthesis and characterization of nanomaterials, quantum theory, nanocomposites, and applications in electronics, sensors, ceramics, magnetics, polymers, and membranes.[910] Many aspects of nanoclusters and nanocrystals have been covered such as their fabrication, morphology control, growth mechanism, spectroscopic characterization, physical properties, and potential industrial applications.[913] Novel nanostructures such as fullerenes, nanotubes, nanocomposites, and semiconductor nanostructures have been reviewed.[915] There has also been a book on the characterization of nanomaterials and their assemblies.[918] A book has been written that details the developments that will revolutionize many industrial processes and products currently used.[920] The nanoengineering of nanomachines, nanoclusters, functional nanostructures, and their characterization have been examined.[920] Table 4 summarizes some important articles, books and reviews regarding the important areas in this part of this field.

9. Acknowledgment

C.B. and X.C. acknowledge the financial support by NSF Chemistry Division (#0239688) and ACS-PRF (#39881-G5M). M.A.E. and R.N. acknowledge the financial support by NSF Chemistry Division (#0240380).

10. References

(1) Peng, X.; Wickham, J.; Alivisatos, A. P. *J. Am. Chem. Soc.* **1998**, *120*, 5343.
(2) Murray C. B.; Kagan, C. R.; Bawendi, M. G. *Annu. Rev. Mater. Sci.* **2000**, *30*, 545.
(3) Pamplin, B. R. *Crystal Growth*; Pergamon Press: New York, 1975.
(4) Jiang, Y. Forced Hydrolysis and Chemical Co−Precipitation. In *Handbook of Nanophase and Nanostructured Materials*; Wang, Z. L., Liu, Y., Zhang, Z., Eds.; Kluwer Academic: New York, 2003; p 59.
(5) Murray, C. B.; Norris, D. J.; Bawendi, M. G. *J. Am. Chem. Soc.* **1993**, *115*, 8706.

(6) Peng, Z. A.; Peng, X. *J. Am. Chem. Soc.* **2001**, *123*, 183.
(7) Qu, L.; Peng, Z. A.; Peng, X. *Nano Lett.* **2001**, *1*, 333.
(8) Qu, L.; Yu, W. W.; Peng, X. *Nano Lett.* **2004**, *4*, 465.
(9) Wang, X.; Qu, L.; Zhang, J.; Peng, X.; Xiao, M. *Nano Lett.* **2003**, *3*, 1103.
(10) Yu, W. W.; Qu, L.; Guo, W.; Peng, X. *Chem. Mater.* **2003**, *15*, 2854.
(11) Chen, X.; Nazzal, A. Y.; Xiao, M.; Peng, Z. A.; Peng, X. *J. Lumin.* **2002**, *97*, 205.
(12) Peng, X.; Wilson, T. E.; Alivisatos, A. P.; Schultz, P. G. *Angew. Chem., Int. Ed.* **1997**, *36*, 145.
(13) Peng, Z. A.; Peng, X. *J. Am. Chem. Soc.* **2002**, *124*, 3343.
(14) Yen, B. K. H.; Stott, N. E.; Jensen, K. F.; Bawendi, M. G. *Adv. Mater.* **2003**, *15*, 1858.
(15) Liberato, M.; Erik, C. S.; Alivisatos, A. P. *J. Am. Chem. Soc.* **2000**, *122*, 12700.
(16) Talapin, D. V.; Rogach, A. L.; Mekis, I.; Haubold, S.; Kornowski, A.; Haase, M.; Weller, H. *Colloids Surf., A* **2002**, *202*, 145.
(17) Yu, W. W.; Qu, L.; Guo, W.; Peng, X. *Chem. Mater.* **2003**, *15*, 2854.
(18) Yu, W. W.; Peng, X. *Angew. Chem., Int. Ed.* **2002**, *41*, 2368.
(19) Yu, W. W.; Wang, Y. A.; Peng, X. *Chem. Mater.* **2003**, *15*, 4300.
(20) Talapin, D. V.; Haubold, S.; Rogach, A. L.; Kornowski, A.; Haase, M.; Weller, H. *J. Phys. Chem. B* **2001**, *105* (12), 2260.
(21) Gaponik, N.; Talapin, D. V.; Rogach, A. L.; Hoppe, K.; Shevchenko, E. V.; Kornowski, A.; Eychmueller, A.; Weller, H. *J. Phys. Chem. B* **2002**, *106* (29), 7177.
(22) Hines, M. A.; Guyot-Sionnest, P. *J. Phys. Chem. B* **1998**, *102*, 3655.
(23) Shim, M.; Guyot-Sionnest, P. *J. Am. Chem. Soc.* **2001**, *123*, 11651.
(24) Battaglia, D.; Peng, X. *Nano Lett.* **2002**, *2*, 1027.
(25) Steckel, J. S.; Coe-sullivan, S.; Bulovic, V.; Bawendi, M. G. *Adv. Mater.* **2003**, *15*, 1862.
(26) Wehrenberg, B. L.; Wang, C.; Guyot-Sionnest, P. *J. Phys. Chem. B* **2002**, *106*, 10634.
(27) Murray, C. B.; Sun, S.; Gaschler, W.; Doyle, H.; Betley, T. A.; Kagan, C. R. *IBM J. Res. Rev.* **2001**, *45*, 47.
(28) Sun, S.; Murray, C. B. *J. Appl. Phys.* **1999**, *85*, 4325.
(29) Murray, C. B.; Sun, S.; Doyle, H.; Betley, T. *MRS Bull*. **2001**, *26*, 985.
(30) Dinega, D. P.; Bawendi, M. G. *Angew. Chem.* **1999**, *38*, 1788.
(31) Puntes, V. F.; Zanchet, D.; Erdonmez, C. K.; Alivisatos, A. P. *J. Am. Chem. Soc.* **2002**, *124*, 12874.
(32) Puntes, V. F.; Krishnan, K.; Alivisatos, A. P. *Top. Catal*. **2002**, *19*, 145.
(33) Puntes, V. F.; Krishnan, K. M.; Alivisatos, A. P. *Appl. Phys. Lett.* **2001**, *78*, 2187.
(34) Puntes, V. F.; Krishnan, K. M.; Alivisatos, A. P. *Science* **2001**, *291*, 2115.
(35) Sun, S.; Murray, C. B.; Weller, D.; Folks, L.; Moser, A. *Science* **2000**, *287*, 1989.
(36) Sun, S.; Anders, S.; Thomson, T.; Baglin, J. E. E.; Toney, M. F.; Hamann, H. F.; Murray, C. B.; Terris, B. D. *J. Phys. Chem. B* **2003**, *107* (23), 5419.
(37) Zhou, W. L.; He, J.; Fang, J.; Huynh, T.-A.; Kennedy, T. J.; Stokes, K. L.; O'Connor, C. J. *J. Appl. Phys.* **2003**, *93*, 7340.
(38) Shevchenko, E. V.; Talapin, D. V.; Schnablegger, H.; Kornowski, A.; Festin, O.; Svedlindh, P.; Haase, M.; Weller, H. *J. Am. Chem. Soc.* **2003**, *125* (30), 9090.
(39) Shevchenko, E. V.; Talapin, D. V.; Rogach, A. L.; Kornowski, A.; Haase, M.; Weller, H. *J. Am. Chem. Soc.* **2002**, *124* (38), 11480.
(40) Kortan, A. R.; Hull, R.; Opila, R. L.; Bawendi, M. G.; Steigerwald, M. L.; Carroll, P. J.; Brus, Louis, E. *J. Am. Chem. Soc.* **1990**, *112*, 2 (4), 1327.
(41) Hines, M. A.; Guyot-Sionnest, P. *J. Phys. Chem.* **1996**, *100*, 468.
(42) Dabbousi, B. O.; Rodriguez-Viejo, J.; Mikulec, F. V.; Heine, J. R.; Mattoussi, H.; Ober, R.; Jensen, K. F.; Bawendi, M. G. *J. Phys. Chem. B* **1997**, *101*, 9463.
(43) Talapin, D. V.; Rogach, A. L.; Kornowski, A.; Haase, M.; Weller, H. *Nano Lett.* **2001**, *1*, 207.
(44) Danek, M.; Jensen, K. F.; Murray, K. F.; Murray, C. B.; Bawendi, M. G. *Chem. Mater.* **1996**, *8*, 173.
(45) Talapin, D. V.; Koeppe, R.; Goetzinger, S.; Kornowski, A.; Lupton, J. M.; Rogach, A. L.; Benson, O.; Feldmann, J.; Weller, H. *Nano Lett.* **2003**, *3* (12), 1677.
(46) Mekis, I.; Talapin, D. V.; Kornowski, A.; Haase, M.; Weller, H. *J. Phys. Chem. B* **2003**, *107*, 7454.
(47) Peng, X.; Schlamp, M. C.; Kadavanich, A. V.; Alivisatos, A. P. *J. Am. Chem. Soc.* **1997**, *119*, 7019.
(48) Chen, X.; Lou, Y.; Burda, C. *Int. J. Nanotech.* **2004**, *1*, 105.
(49) Chen, X.; Lou, Y.; Samia, A. C.; Burda, C. *Nano Lett.* **2003**, *3*, 799.
(50) Zeng, H.; Li, J.; Wang, Z. L.; Liu, J. P.; Sun, S. *Nano Lett.* **2004**, *4* (1), 187.
(51) Kim, S.; Fisher, B.; Eisler, H.; Bawendi, M. *J. Am. Chem. Soc.* **2003**, *125*, 11466.
(52) Haubold, S.; Haase, M.; Kornowski, A.; Weller, H. *ChemPhysChem* **2001**, *2*, 331.
(53) Sun, S.; Zeng, H. *J. Am. Chem. Soc.* **2002**, *124*, 8204.
(54) Cozzoli, P. D.; Kornowski, A.; Weller, H. *J. Am. Chem. Soc.* **2003**, *125*, 14539.
(55) Yin, M.; O'Brien, S. *J. Am. Chem. Soc.* **2003**, *125*, 10180.
(56) O'Brien, S.; Brus, L.; Murray, C. B. *J. Am. Chem. Soc.* **2001**, *123*, 12085.
(57) McBain, J. W.; Salmon, C. S. *J. Am. Chem. Soc.* **1920**, *43*, 426.
(58) Gutmann, H.; Kertes, A. S. *J. Colloid Interface Sci.* **1973**, *51*, 406.
(59) Liu, J.; Kim, A. Y.; Wang, L. Q.; Palmer, B. J.; Chen, Y. L.; Bruinsma, P.; Bunker, B. C.; Exarhos, G. J.; Graff, G. L.; Rieke, P. C.; Fryxell, G. E.; Virden, J. W.; Tarasevich, B. J.; Chick, L. A. *Adv. Colloid Interface Sci.* **1996**, *69*, 131.
(60) Boutonnet , M.; Kizling, J.; Stenius, P.; Maire, G. *Colloids Surf.* **1983**, *5*, 209.
(61) Boutonnet, M.; Khan-Lodhi A. N.; Towey, T. *Structure and Reactivity in Reversed Micelles*; Pileni, M. P., Ed.; Elsevier: Amsterdam, The Netherlands, 1989; p 198.
(62) Turkevich, J.; Stevenson, P. C.; Hillier, J. *Discuss. Faraday Soc.* **1951**, *11*, 55.
(63) Taleb, A.; Petit, C.; Pileni, M. P. *Chem. Mater.* **1997**, *9*, 950.
(64) Barnickel, P.; Wokaun, A. *Mol. Phys.* **1990**, *69*, 1.
(65) Chen, Z. J.; Qu, X. M.; Fang, F. Q.; Jiang, L. *Colloids Surf. B* **1996**, *7*, 173.
(66) Lisiecki, I.; Pileni, M. P. *J. Am. Chem. Soc.* **1993**, *115*, 3887.
(67) Pileni, M.; Lisiecki, I. *Colloids Surf.* **1993**, *80*, 63.
(68) Pileni, M. P.; Lisiecki, I.; Motte, L.; Petit, C.; Cizeron, J.; Moumen, N.; Lixon, P. *Prog. Colloid Polym. Sci.* **1993**, *93*, 1.
(69) Petit, C.; Lixon, P.; Pileni, M. P. *J. Phys. Chem.* **1993**, *97*, 12974.
(70) Lisiecki, I.; Pileni, M. P. *J. Phys. Chem.* **1995**, *99*, 5077.
(71) Petit, C.; Taleb, A.; Pileni, M. P. *J. Phys. Chem. B* **1999**, *103*, 1805.
(72) Chen, J. P.; Lee, K. M.; Sorensen, C. M.; Klabunde, K. J.; Hadjipanayis. *J. Appl. Phys.* **1994**, *75*, 5876.
(73) Eastoe, J.; Warne, B. *Curr. Opin. Colloid Interface Sci.* **1996**, *1*, 800.
(74) Lopez-Perez J. A.; Lopez-Quintela, M. A.; Mira, J.; Rivas, J.; Charles, S. W. *J. Phys. Chem. B* **1997**, *101*, 8045.
(75) Sangregorio, C.; Galeotti, M.; Bardi, U.; Baglioni, P. *Langmuir* **1996**, *12*, 5800.
(76) Nagy, J. B. *Colloids Surf.* **1989**, *35*, 201.
(77) Tanori, J.; Pileni, M. P. *Langmuir* **1997**, *13*, 639.
(78) Legrand, J.; Petit, C.; Pileni, M. P. *J. Phys. Chem. B* **2001**, *105*, 5643.
(79) Kawai, T.; Fujino, A.; Kon-No, K. *Colloids Surf. A* **1996**, *100*, 245.
(80) Chang, S. Y.; Liu, L.; Asher, S. A. *J. Am. Chem. Soc.* **1994**, *116*, 6739.
(81) Joselevich, E.; Willner, I. *J. Phys. Chem.* **1994**, *98*, 7628.
(82) Chhabra, V.; Pillai, V.; Mishra, B. K.; Morrone, A.; Shah, D. O. *Langmuir* **1995**, *11* (9), 3307.
(83) Osseo-Asare, K.; Arriagada, F. J. *J. Colloids Surf.* **1990**, *50*, 321.
(84) Wang, W.; Fu, X.; Tang, J.; Jiang, L. *Colloids Surf. A* **1993**, *81*, 177.
(85) Arriagada, F. J.; Osseo-Asare, K. *J. Colloid Interface Sci.* **1995**, *170*, 8.
(86) Gan, L. M.; Zhang, K.; Chew, C. H. *Colloids Surf. A* **1996**, *110*, 199.
(87) Chang, C. L.; Fogler, H. S. *Langmuir* **1997**, *13*, 3295.
(88) Esquena, J.; Tadros, T. F.; Kostarelos, K.; Solans, C. *Langmuir* **1997**, *13*, 6400.
(89) Dvolaitzky, M.; Ober, R.; Taupin, C.; Anthore, R.; Auvray, X.; Petipas, C.; Williams, C. *J. Dispersion Sci. Technol.* **1983**, *4* (1), 29.
(90) Chew, C. H.; Gan, L. M.; Shah, D. O. *J. Dispersion Sci. Technol.* **1990**, *11*, 593.
(91) Monnoyer, P.; Fonseca, A.; Nagy, J. B. *Colloid Surf. A.* **1996**, *100*, 233.
(92) Bagwe, R. P.; Khilar, K. C. *Langmuir* **1997**, *13*, 6432.
(93) Motte, L.; Billoudet, F.; Lacaze, E.; Pileni, M. P. *Adv. Mater.* **1996**, *8*, 1018.
(94) Kandori, K.; Kon-No, K.; Kitahara, A. *J. Colloid Interface Sci.* **1987**, *122*, 78.
(95) Kandori, K.; Kon-No, K.; Kitahara, A. *J. Dispersion Sci. Technol.* **1988**, *9*, 61.
(96) Qi, L. M.; Ma, J.; Chen, H.; Zhao, Z. *J. Phys. Chem. B* **1997**, *101*, 3460.
(97) Hopwood, J. D.; Mann, S. *Chem. Mater.* **1997**, *9*, 1819.
(98) Pileni, M. P. *Catal. Today* **2000**, *58*, 151.
(99) Motte, L.; Billoudet, Fl.; Pileni, M. P. *J. Phys. Chem.* **1995**, *99*, 16425.
(100) Lisiecki, I.; Pileni, M. P. *J. Am. Chem. Soc.* **1993**, *115*, 3887.
(101) Cizeron, J.; Pileni, M. P. *J. Phys. Chem.* **1995**, *99*, 17410.
(102) Levy, L.; Hochepied, J. F.; Pileni, M. P. *J. Phys. Chem.* **1996**, *100*, 18322.
(103) Petit, C.; Jain, T. K.; Billoudet, F.; Pileni, M. P. *Langmuir* **1994**, *10*, 4446.

(104) Lisiecki, I.; Billoudet, F.; Pileni, M. P. *J. Phys. Chem.* **1996**, *100*, 4160.
(105) Hao, E.; Bailey, R. C.; Schatz, G. C.; Hupp, J. T.; Li, S. *Nano Lett.* **2004**, *4*, 327.
(106) Maillard, M.; Giorgio, S.; Pileni, M. *Adv. Mater.* **2002**, 1084.
(107) Jana, N. R.; Gearheart, L.; Murphy, C. J. *J. Phys. Chem. B* **2001**, *105*, 4065.
(108) Yu, Y.; Chang, S.; Lee, C.; Wang, C. R. C. *J. Phys. Chem. B* **1997**, *101*, 6661.
(109) Link, S.; Mohamed, M. B.; El-Sayed, M. A. *J. Phys. Chem. A* **1999**, *103*, 1165.
(110) Link, S.; Burda, C.; Nikoobakht, B.; El-Sayed, M. A. *Chem. Phys. Lett.* **1999**, *315*, 12.
(111) Link, S.; El-Sayed, M. A. *J. Phys. Chem. B* **1999**, *103*, 8410−8426.
(112) Callegari, A.; Tonti, D.; Chergui, M. *Nano Lett.* **2003**, *3*, 1565.
(113) Jin, R.; Cao, Y.; Mirkin, C. A.; Kelly, K. L.; Schatz, G. C.; Zheng, J. G. *Science* **2001**, *294*, 1901.
(114) Li, Y.; White, T.; Lim, S. H. *Rev. Adv. Mater. Sci.* **2003**, *5*, 211.
(115) Coln, G.; Hidalgo, M. C.; Navo, J. A. *Catal. Today* **2002**, *76*, 91.
(116) Uekawa, N.; Kajiwara, J.; Kakegawa, K.; Sasaki, Y. J. *Colloid Interface Sci.* **2002**, *250*, 285.
(117) Maira, A. J.; Yeung, K. L.; Soria, J.; Coronado, J. M.; Belver, C.; Lee, C. Y.; Augugliaro, V. *Appl. Catal. B* **2001**, *29* (4), 327.
(118) Li, B.; Wang, X.; Yan, M.; Li, L. *Mater. Chem. Phys.* **2003**, *78*, 184.
(119) Parala, H.; Devi, A.; Bhakta, R.; Fischer, R. A. *J. Mater. Chem.* **2002**, *12*, 1625.
(120) Lackey, W. *J. Nucl. Technol.* **1980**, *49*, 321.
(121) Woodhead, J. L. *Sci. Ceram.* **1983**, *12*, 179.
(122) Chatterjee, A.; Chakravorty, D. *J. Mater. Sci.* **1992**, *27*, 4115.
(123) Gao, J.; Qi, Y.; Yang, W.; Guo, X.; Li, S.; Li, X. *Mater. Chem. Phys.* **2003**, *82* (3), 602.
(124) Kiss, K.; Magder, J.; Vukasovich, M. S.; Lockhart, R. J. *J. Am. Ceram. Soc.* **1966**, *49* (6), 291.
(125) Shen, J.; Zhang, Z.; Wu, G. *J. Chem. Eng. Jpn.* **2003**, *36*, 1270.
(126) Viano, A.; Mishra, S. R.; Lloyd, R.; Losby, J.; Gheyi, T. *J. Non-Cryst. Solids* **2003**, *325* (1−3), 16.
(127) Jitianu, A.; Altindag, Y.; Zaharescu, M.; Wark, M. *J. Sol−Gel Sci. Technol.* **2003**, *26*, 483.
(128) Mondelaers, D.; Vanhoyland, G.; Van den Rul, H.; D'Haen, J.; Van Bael, M. K.; Mullens, J.; Van Poucke, L. C. *Mater. Res. Bull.* **2002**, *37* (5), 901.
(129) Zeng, W. M.; Gao, L.; Guo, J. K. *Nanostruct. Mater.* **1998**, *10*, 543.
(130) Pathak, L. C.; Singh, T. B.; Verma, A. K.; Ramachandrarao, P. *J. Metall. Mater. Sci.* **2000**, *42*, 93.
(131) Grosso, D.; Sermon, P. A. *J. Mater. Chem.* **2000**, *10*, 359.
(132) Chang, Y.-S.; Chang, Y.-H.; Chen, I.-G.; Chen, G.-J.; Chai, Y.-L. *J. Cryst. Growth* **2002**, *243* (2), 319.
(133) Wang, X.; Zhang, Z.; Zhou, S. *Mater. Sci. Eng. B* **2001**, *86*, 29.
(134) Veith, M.; Mathur, S.; Lecerf, N.; Huch, V.; Decker, T.; Beck, H. P.; Eiser, W.; Haberkorn, R. *J. Sol−Gel Sci. Technol.* **2000**, *17*, 145.
(135) Sharma, N.; Shaju, K. M.; Rao, G. V. S.; Chowdari, B. V. R. *Electrochem. Commun.* **2002**, *4*, 947.
(136) Huang, Y. X.; Guo, C. *J. Powder Technol.* **1992**, *72*, 101.
(137) Yamamura, H. *Ceram. Int.* **1985**, *11*, 72.
(138) Potdar, H. S.; Deshpande, S. B.; Date, S. K. *Mater. Chem. Phys.* **1999**, *58*, 121.
(139) Sheen, S. *Mater. Lett.* **1991**, *10*, 489.
(140) Spanhel, L.; Haase, M.; Weller, H.; Henglein, A. *J. Am. Chem. Soc.* **1987**, *109* (19), 5649.
(141) Harrison, M. T.; Kershaw, S. V.; Burt, M. G.; Rogach, A.; Eychmuller, A.; Weller, H. *J. Mater. Chem.* **1999**, *9* (11), 2721.
(142) Rogach, A. L.; Kornowski, A.; Gao, M.; Eychmueller, A.; Weller, H. *J. Phys. Chem. B* **1999**, *103* (16), 3065.
(143) Gao, M.; Richter, B.; Kirstein, S.; Moehwald, H. *J. Phys. Chem. B* **1998**, *102* (21), 8360.
(144) Mews, A.; Eychmueller, A.; Giersig, M.; Schooss, D.; Weller, H. *J. Phys. Chem.* **1994**, *98*, 934.
(145) Mews, A.; Kadavanich, A. V.; Banin, U.; Alivisatos, A. P. *Phys. Rev. B* **1996**, *53*, R13242.
(146) Porteanu, H. E.; Lifshitz, E.; Pflughoefft, M.; Eychmuller, A.; Weller, H. *Phys. Status Solidi B* **2001**, *226* (1), 219.
(147) Kamalov, V. F.; Little, R.; Logunov, S. L.; El-Sayed, M. A. *J. Phys. Chem.* **1996**, *100*, 6381.
(148) Schooss, D.; Mews, A.; Eychmoeller, A.; Weller, H. *Phys. Rev. B* **1994**, *49*, 17072.
(149) Eychmueller, A.; Vossmeyer, T.; Mews, A.; Weller, H. *J. Lumin.* **1994**, *58*, 223.
(150) Braun, M.; Burda, C.; El-Sayed, M. A. *J. Phys. Chem. A* **2001**, *105*, 5548.
(151) Braun, M.; Link, S.; Burda, C.; El-Sayed, M. *Phys. Rev. B* **2002**, *66*, 205312/1.
(152) Braun, M.; Link, S.; Burda, C.; El-Sayed, M. *Chem. Phys. Lett.* **2002**, *361*, 446.
(153) Borchert, H.; Talapin, D. V.; Gaponik, N.; McGinley, C.; Adam, S.; Lobo, A.; Moeller, T.; Weller, H. *J. Phys. Chem. B* **2003**, *107* (36), 7486.
(154) Braun, M.; Burda, C.; Mohamed, M.; El-Sayed, M. *Phys. Rev. B* **2001**, *64*, 035317/1.
(155) Harrison, M. T.; Kershaw, S. V.; Rogach, A. L.; Kornowski, A.; Eychmuller, A.; Weller, H. *Adv. Mater.* **2000**, *12*, 123.
(156) Kershaw, S. V.; Burt, M.; Harrison, M.; Rogach, A.; Weller, H.; Eychmuller, A. *Appl. Phys. Lett.* **1999**, *75*, 1694.
(157) Yang, J.; Mei, S.; Ferreira, J. M. F. *Mater. Sci. Eng. C* **2001**, *15*, 183.
(158) Yoshimura, M.; Somiya, S. *Am. Ceram. Soc. Bull.* **1980**, *59*, 246.
(159) Hirano, S.; Somiya, S. *J. Am. Ceram. Soc.* **1976**, *59*, 534.
(160) Burukhin, A. A.; Churagulov, B. R.; Oleynikov, N. N. *High Press. Res.* **2001**, *20*, 255.
(161) Lu, S. W.; Lee, B. I.; Wang, Z. L.; Guo, J. K. *J. Cryst. Growth* **2000**, *219*, 269.
(162) Chen, C. C.; Jiao, X.; Chen, D.; Zhao, Y. *Mater. Res. Bull.* **2001**, *36*, 2119.
(163) Maclaren, I.; P. A. Trusty, C. B. Ponton *Acta Mater.* **1999**, *47*, 779.
(164) Yu, S.-H.; Shu, L.; Wu, Y.-S.; Qian, Y.-T.; Xie, Y.; Yang, L. *Mater. Res. Bull.* **1998**, *33*, 1207.
(165) Qian, X. F.; Zhang, X. M.; Wang, C.; Tang, K. B.; Xie, Y.; Qian, Y. T. *Mater. Res. Bull.* **1999**, *34*, 433.
(166) Qian, X. F.; Zhang, X. M.; Wang, C.; Wang, W. Z.; Xie, Y.; Qian, Y. T. *J. Phys. Chem. Solids* **1999**, *60*, 415.
(167) Wang, C.; Zhang, W. X.; Qian, X. F.; Zhang, X. M.; Xie, Y.; Qian, Y. T. *Mater. Lett.* **1999**, *40*, 255.
(168) Qian, X. F.; Zhang, X. M.; Wang, C.; Wang, W. Z.; Qian, Y. T. *Mater. Res. Bull.* **1998**, *33*, 669.
(169) Chen, D.; Shen, G. Z.; Tang, K. B.; Liu, Y. K.; Qian, Y. T. *Appl. Phys. A* **2003**, *77*, 747.
(170) Shao, M. W.; Mo, M. S.; Cui, Y.; Chen, G.; Qian Y. T. *J. Cryst. Growth* **2001**, *233*, 799.
(171) Hu, J. Q.; Lu, Q. Y.; Tang, K. B.; Deng, B.; Jiang, R. R.; Qian, Y. T.; Yu, W. C.; Zhou, G. E.; Liu, X. M.; Wu, J. X. *J. Phys. Chem. B* **2000**, *104* (22), 5251.
(172) Ji, M.; Chen, X.; Wai, C. M.; Fulton, J. L. *J. Am. Chem. Soc.* **1999**, *121*, 1, 2631.
(173) Ohde, H.; Hunt, F.; Wai, C. M. *Chem. Mater.* **2001**, *13*, 4130.
(174) McLeod, M. C.; McHenry, R. S.; Beckman, E. J.; Roberts, C. B. *J. Phys. Chem. B* **2003**, *107*, 2693.
(175) Ziegler, K. J.; Doty, R. C.; Johnston, K. P.; Korgel, B. A. *J. Am. Chem. Soc.* **2001**, *123*, 7797.
(176) Cason, J. P.; Roberts, C. B. *J. Phys. Chem. B* **2000**, *104*, 1217.
(177) Cason, J. P.; Miller, M. E.; Thompson, J. B.; Roberts, C. B. *J. Phys. Chem. B* **2001**, *105*, 2297.
(178) Cason, J. P.; Khambaswadkar, K.; Roberts, C. B. *Ind. Eng. Chem. Res.* **2000**, *39*, 4749.
(179) Sun, Y.-P.; Rollins, H. W.; Guduru, R. *Chem. Mater.* **1999**, *11*, 7.
(180) Shah, P. S.; Hanrath, T.; Johnston, K. P.; Korgel, B. A. *J. Phys. Chem. B* **2004**, *108*, 9574.
(181) Lu, X.; Ziegler, K. J.; Ghezelbash, A.; Johnston, K. P.; Korgel, B. A. *Nano Lett.* **2004**, *4*, 969.
(182) Sun, Y.-P.; Guduru, R.; Lin, F.; Whiteside, T. *Ind. Eng. Chem. Res.* **2000**, *39*, 4663.
(183) Shah, P. S.; Novick, B. J.; Hwang, H. S.; Lim, K. T.; Carbonell, R. G.; Johnston, K. P.; Korgel, B. A. *Nano Lett.* **2003**, *3*, 1671.
(184) Ohde, H.; Ohde, M.; Bailey, F.; Kim, H.; Wai, C. M. *Nano Lett.* **2002**, *2*, 721.
(185) Holmes, J. D.; Bhargava, P. A.; Korgel, B. A.; Johnston, K. P. *Langmuir* **1999**, *15*, 6613.
(186) Sun, Y.-P.; Rollins, H. W. *Chem. Phys. Lett.* **1998**, *288*, 585−588.
(187) Hanrath, T.; Korgel, B. A. *J. Am. Chem. Soc.* **2002**, *124*, 1424.
(188) Hanrath, T.; Korgel, B. A. *Adv. Mater.* **2003**, *15*, 437.
(189) Davidson, F. M., III; Schricker, A. D.; Wiacek, R. J.; Korgel, B. A. *Adv. Mater.* **2004**, *16*, 646.
(190) Lee, D. C.; Mikulec, F. V.; Korgel, B. A. *J. Am. Chem. Soc.* **2004**, *126*, 4951.
(191) Larsen, T. H.; Sigman, M.; Ghezelbash, A.; Doty, R. C.; Korgel, B. A. *J. Am. Chem. Soc.* **2003**, *125*, 5638.
(192) Sigman, M.; Ghexelbash, A.; Hanrath, T.; Saunders, A. E.; Lee, F.; Korgel, B. A. *J. Am. Chem. Soc.* **2003**, *125*, 16050.
(193) Ghexelbash, A.; Sigman, M.; Korgel, B. A. *Nano Lett.* **2004**, *4*, 537.
(194) Cai, W.; Zhang, L. *J. Phys. Condensed Matter* **1997**, *9*, 7257.
(195) Maya, L.; Paranthaman, M.; Thundat, T.; Bauer, M. L. *J. Vac. Sci. Technol. B* **1996**, *14*, 15.
(196) Li, W.; Gao, L.; Guo, J. K. *Nanostruct. Mater.* **1998**, *10*, 1043.
(197) Indackers, D.; Janzen, C.; Rellinghaus, B. *Nanostruct. Mater.* **1998**, *10*, 247.
(198) Depero, L. E.; Bonzi, P.; Musci, M.; Casale, C. *J. Solid State Chem.* **1994**, *111*, 247.
(199) Yang, Y.; Leppert, V. J.; Risbud, S. H.; Twamley, B.; Power, P. P.; Lee, H. W. H. *Appl. Phys. Lett.* **1999**, *74*, 2262.

(200) Okuyama, K.; Lenggoro, I. W.; Tagami, N. *J. Mater. Sci.* **1997**, *32*, 1229.
(201) Binder, J. R.; Wedemeyer, H. *Adv. Mater.* **1997**, *9*, 1049.
(202) Valentini, A.; Carreno, N. L. V.; Probst, L. F. D.; Leite, E. R.; Longo, E. *Microporous Mesoporous Mater.* **2004**, *68*, 151.
(203) Jou, S.; Hsu, C. K. *Mater. Science Eng. B* **2004**, *106*, 275.
(204) Dumitrache, F.; Morjan, I.; Alexandrescu, R.; Morjan, R. E.; Voicu, I.; Sandu, I.; Soare, I.; Ploscaru, M.; Fleaca, C.; Ciupina, V.; Prodan, G.; Rand, B.; Brydson, R.; Woodword, A. *Diamond Relat. Mater.* **2004**, *13* (2), 362.
(205) Sen, R.; Govindaraj, A.; Rao, C. N. R. *Chem. Phys. Lett.* **1997**, *267*, 276.
(206) Sen, R.; Govindaraj, A.; Rao, C. N. R. *Chem. Mater.* **1997**, *9*, 2078.
(207) Rao, C. N. R.; Govindaraj, A.; Sen, R.; Satishkumar, B. C. *Mater. Res. Innovations* **1998**, *2*, 128.
(208) Satishkumar, B. C.; Govindaraj, A.; Sen, R.; Rao, C. N. R. *Chem. Phys. Lett.* **1998**, *293*, 47.
(209) Satishkumar, B. C.; Govindaraj, A.; Rao, C. N. R. *Chem. Phys. Lett.* **1999**, *307*, 158.
(210) Rao, C. N. R.; Sen, R.; Satishkumar, B. C.; Govindaraj, A. *Chem. Commun.* **1998**, 1525.
(211) Satishkumar, B. C.; Thomas, P. J.; Govindaraj, A.; Rao, C. N. R. *Appl. Phys. Lett.* **2000**, *77*, 2530.
(212) Deepak, F. L.; Govindaraj, A.; Rao, C. N. R. *Chem. Phys. Lett.* **2001**, *345*, 5.
(213) Rao, C. N. R.; Govindaraj, A. *Acc. Chem. Res.* **2002**, *35*, 998.
(214) Gundiah, G.; Madhav, G. V.; Govindaraj, A.; Rao, C. N. R. *J. Mater. Chem.* **2002**, *12*, 1606.
(215) Deepak, F. L.; Vinod, C. P.; Mukhopadhyay, K.; Govindaraj, A.; Rao, C. N. R. *Chem. Phys. Lett.* **2002**, *353* (5−6), 345.
(216) Fukui, T.; Ando, S.; Tokura, Y.; Toriyama, T. *Appl. Phys. Lett.* **1991**, 58, 2018.
(217) Tanaka, S.; Hirayama, H.; Aoyagi, Y.; Narukawa, Y.; Kawakami, Y.; Fujita, S.; Fujita, S. *Appl. Phys. Lett.* **1997**, *71*, 1299.
(218) Hirayama, H.; Tanaka, A.; Ramvall, P.; Aoyagi, Y. *Appl. Phys. Lett.* **1998**, *72*, 1736.
(219) Ishida, S.; Arakawa, Y.; Wada, K. *Appl. Phys. Lett.* **1998**, *72*, 800.
(220) Tachibana, T.; Someya, T.; Arakawa, Y. *Appl. Phys. Lett.* **1999**, *74*, 383.
(221) Leon, R.; Lobo, C.; Clark, A.; Bozek, R.; Wysmolek, A.; Kurpiewski, A.; Kaminska, M. *J. Appl. Phys.* **1998**, *84* (1), 248.
(222) Huang, Z. P.; Xu, J. W.; Ren, Z. F.; Wang, J. H.; Siegal, M. P.; Provencio, P. N. *Appl. Phys. Lett.* **1998**, *73* (26), 3845.
(223) Han, W.; Fan, S.; Li, Q.; Hu, Y. *Science* **1997**, *277*, 1287.
(224) Liu, Y.; Zhu, W.; Tse, M. S.; Shen, Y. *J. Mater. Sci. Lett.* **1995**, *14*, 1185.
(225) Akhtar, M. K.; Pratsinis, S. E.; Mastrangelo, S. V. R. *J. Mater. Res.* **1994**, *9*, 124.
(226) Zhu, W. Z.; Yan, M. *Mater. Chem. Phys.* **1998**, *53*, 262.
(227) Chen, L.; Goto, T.; Hirai, T. *J. Mater. Sci.* **1989**, *24*, 3824.
(228) Dekker, J. P.; van der Put, P. J.; Veringa, H. J.; Schoonman, J. *J. Am. Ceram. Soc.* **1997**, *80*, 629.
(229) Chang, W.; Skadan, G.; Danforth, S. C.; Kear, B. H.; Hahn, H. *Nanostruct. Mater.* **1994**, *4*, 507.
(230) Chang, W.; Skadan, G.; Hahn, H. Danforth, S. C.; Kear, B. H. *Nanostruct. Mater.* **1994**, *4*, 345.
(231) Iijima, S. *Nature* **1991**, *354*, 56.
(232) Ren, Z. F.; Huang, Z. P.; Xu, J. W.; Wang, J. H.; Bush, P.; Siegel, M. P.; Provencio, P. N. *Science* **1998**, *282* (5391), 1105.
(233) Fan, S. S.; Chapline, M. G.; Franklin, N. R.; Tombler, T. W.; Cassell, A. M.; Dai, H. J. *Science* **1999**, *283*, 512.
(234) Che, G.; Lakshmi, B. B.; Martin, C. R.; Fisher, E. R.; Ruoff, R. S. *Chem. Mater.* **1998**, *10*, 260.
(235) Hiruma, K.; Katsuyama, T.; Ogawa, K.; Koguchi, M.; Kakibayashi, H.; Morgan, G. P. *Appl. Phys. Lett.* **1991**, *59* (4), 431.
(236) Hiruma, K.; Yazawa, M.; Katsuyama, T.; Ogawa, K.; Haraguchi, K.; Koguchi, M. *J. Appl. Phys.* **1995**, *77* (2), 447.
(237) Yazawa, M.; Koguchi, M.; Hiruma, K. *Appl. Phys. Lett.* **1991**, *58*, 1080.
(238) Yazawa, M.; Koguchi, M.; Muto, A.; Ozawa, M.; Hiruma, K. *Appl. Phys. Lett.* **1992**, *61*, 2051.
(239) Kong, Y. C.; Yu, D. P.; Zhang, B.; Fang, W.; Feng, S. Q. *Appl. Phys. Lett.* **2001**, *78* (4), 407.
(240) Bai, Z. G.; Yu, D. P.; Wang, J. J.; Zou, Y. H.; Qian, W.; Fu, J. S.; Feng, S. Q.; Xu, J.; You, L. P. *Mater. Sci. Eng. B* **1999**, *72*, 117.
(241) Dai, H.; Wong, E. W.; Lu, Y. Z.; Fan, S.; Lieber, C. M. *Nature* **1995**, *375* (6534), 769.
(242) Han, W.; Fan, S.; Li, Q.; Liang, W.; Gu, B.; Yu, D. *Chem. Phys. Lett.* **1997**, *265* (3−5), 374.
(243) Han, W. Q.; Fan, S.; Li, Q. Q.; Gu, B. L.; Zhang X. B.; Yu, D. P. *Appl. Phys. Lett.* **1997**, *71*, 2271.
(244) Wu, Y.; Cui, Y.; Huynh, L.; Barrelet, C. J.; Bell, D. C.; Lieber, C. M. *Nano Lett.* **2004**, *4*, 433.
(245) Zhong, Z.; Qian, F.; Wang, D.; Lieber, C. M. *Nano Lett.* **2003**, *3*, 343.
(246) Joselevich, E.; Lieber, C. M. *Nano Lett.* **2002**, *2*, 1137.
(247) Yu, D. P.; Sun, X. S.; Lee, C. S.; Bello, I.; Sun, X. S.; Tang, Y. H.; Zhou, G. W.; Bai, Z. G.; Zhang, Z.; Feng, S. Q. *Solid State Commun.* **1998**, *105*, 403.
(248) Bai, Z. G.; Yu, D. P.; Zhang, H. Z.; Ding, Y.; Wang, Y. P.; Gal, X. Z.; Hang, Q. L.; Xiong, G. C.; Feng, S. Q. *Chem. Phys. Lett.* **1999**, *303*, 311.
(249) Zhang, H. Z.; Yu, D. P. Ding, Y.; Bai, Z. G.; Hang, H. L.; Feng, S. Q. *Appl. Phys. Lett.* **1999**, *73*, 3396.
(250) Gao, P. X.; Ding, Y.; Wang, Z. L. *Nano Lett.* **2003**, *3*, 1315.
(251) Dai, Z. R.; Pan, Z. W.; Wang, Z. L. *J. Phys. Chem. B* **2002**, *106* (5), 902.
(252) Dai, Z. R.; Gole, J. L.; Stout, J. D.; Wang, Z. L. *J. Phys. Chem. B* **2002**, *106* (6), 1274.
(253) Peng, X. *Adv. Mater.* **2003**, *15*, 459.
(254) Peng, Z. A.; Peng, X. *J. Am. Chem. Soc.* **2001**, *123*, 1389.
(255) Link, S.; Burda, C.; Nikoobakht, B.; El-Sayed, M. A. *J. Phys. Chem. B* **2000**, *104*, 6152.
(256) Manna, L.; Milliron Delia, J.; Meisel, A.; Scher Erik, C.; Alivisatos, A. P. *Nat. Mater.* **2003**, *2* (6), 382.
(257) Hu, J.; Odom, T. W.; Lieber, C. M. *Acc. Chem. Res.* **1999**, *32*, 435.
(258) Link, S.; Wang, Z. L.; El-Sayed, M. A. *J. Phys. Chem. B* **2000**, *104*, 7868.
(259) Link, S.; El-Sayed, M. A. *Int. Rev. Phys. Chem.* **2000**, *19*, 409.
(260) Link, S.; El-Sayed, M. A. *Annu. Rev. Phys. Chem.* **2003**, *54*, 331.
(261) Jin, R.; Cao, Y.; Mirkin, C. A.; Kelly, K. L.; Schatz, G. C.; Zheng, J. G. *Science* **2001**, *294* (5548), 1901.
(262) Alivisatos, A. P. *J. Phys. Chem.* **1996**, *100*, 13226.
(263) Steigerwald, M. L.; Alivisatos, A. P.; Gibson, J. M.; Harris, T. D.; Kortan, R.; Muller, A. J.; Thayer, A. M.; Duncan, T. M.; Douglass, D. C.; Brus, L. E. *J. Am. Chem. Soc.* **1988**, *110*, 3046.
(264) Dabbousi, B. O.; Rodriguez-Viejo, J.; Mikulec, F. V.; Bawendi, M. G. *J. Phys. Chem. B* **1997**, *101*, 9463.
(265) Murray, C. B.; Kagan, C. R.; Bawendi, M. G. *Science* **1995**, *270*, 1335.
(266) Berry, C. C.; Curtis, A. S. G. *J. Phys. D* **2003**, *36*, R198.
(267) Kuno, M.; Lee, J. K.; Dabbousi, B. O.; Mikulec, F. V.; Bawendi, M. G. *J. Chem. Phys.* **1997**, *106*, 9869.
(268) Van Blaarderen A.; Ruel, R.; Wiltzius, P. *Nature* **1997**, *385*, 321.
(269) Murray, C. A.; Grier, D. G. *Am. Sci.* **1995**, *83*, 238.
(270) Kagan, C. R.; Murray, C. B.; Bawendi, M. G. *MRS Symp. Proc.* **1995**, *358*, 219.
(271) Kagan, C. R.; Murray, C. B.; Bawendi, M. G. *Phys. Rev. B* **1996**, *54*, 8633.
(272) Vossmeyer, T.; Katsikas, L.; Gersig, M.; Popovic, I. C.; Diesner, K.; Chemseddine, A.; Eychmuller, A.; Weller, H. *J. Phys. Chem.* **1994**, *98*, 7665.
(273) Ptatschek, V.; Schreder, B.; Herz, K.; Hilbert, U.; Ossau, W.; Schottner, G.; Rahauser, O.; Bischof, T.; Lermann, G.; Materny, A.; Kiefer, W.; Bacher, G.; Forchel, A.; Su, D.; Giersig, M.; Muller, G.; Spanhel, L. *J. Phys. Chem. B* **1997**, *101*, 8898.
(274) Gacoin, T.; Malier, L.; Boilot, J. P. *J. Mater. Chem.* **1997**, *7*, 859.
(275) Pusey, P. N.; van Megen, W. *J. Phys. Condens. Matter* **1994**, *6*, A29.
(276) Zhu, P. W.; White, J. W. *J. Chem. Phys.* **1996**, *104*, 9169.
(277) Wang, Z. L.; Harfenist, S. A.; Whetten, R. L.; Bentley, J.; Evans, N. D. *J. Phys. Chem. B* **1998**, *102*, 3068.
(278) Schaaff, T. G.; Shafigullin, M. N.; Khoury, J. T.; Vezmar, I.; Whetten, R. L.; Cullen, W. G.; First, P. N.; Gutierrez-Wing, C.; Ascensio, J.; Jose-Yacaman, M. J. *J. Phys. Chem. B* **1997**, *101*, 7885.
(279) Kiely, C. J.; Fink, J.; Brust, M.; Bethell, D.; Schiffrin, D. J. *Nature* **1998**, *396* (6710), 444.
(280) Burnside, S. D.; Shklover, V.; Barb, C.; Comte, P.; Arendse, F.; Brooks, K.; Gratzel, M. *Chem. Mater.* **1998**, *10*, 2419.
(281) Whetten, R. L.; Shafigullin, M. N.; Khoury, J. T.; Schaaff, T. G.; Vezmar, I.; Alvarez, M. M.; Wilkinson, A. *Acc. Chem. Res.* **1999**, *32*, 397.
(282) Taleb, A.; Petit, C.; Pileni, M. P. *J. Phys. Chem. B* **1998**, *102*, 2214.
(283) Zhang, X. X.; Wen, G. H.; Xiao, G.; Sun, S. *J. Magn. Magn. Mater.* **2003**, *261*, 21.
(284) Dumestre, F.; Chaudret, B.; Amiens, C.; Renaud, P.; Fejes, P. *Science* **2004**, *303* (5659), 821.
(285) Yin, J. S.; Wang, Z. L. *Phys. Rev. Lett.* **1997**, *79*, 2570.
(286) Li, M.; Schnablegger, H.; Mann, S. *Nature* **1999**, *402*, 393.
(287) Zeng, H.; Sun, S.; Sandstrom, R. L.; Murray, C. B. *J. Magn. Magn. Mater.* **2003**, *266*, 227.
(288) Redl, F. X.; Cho, K.-S.; Murray, C. B.; O'Brien, S. *Nature* **2003**, *423*, 968.
(289) Hermanson, K. D.; Lumsdon, S. O.; Williams, J. P.; Kaler, E. W.; Velev, O. D. *Science* **2001**, *294*, 1082.
(290) Collier, C. P.; Saykally, R. J.; Shiang, J. J.; Henrichs, S. E.; Heath, J. R. *Science* **1997**, *277*, 1978.
(291) Kiely, C. J.; Fink, J.; Zheng, J. G.; Brust, M.; Bethell, D.; Schiffrin, D. J. *Adv. Mater.* **2000**, *12*, 640.
(292) Chung, S.-W.; Markovich, G.; Heath, J. R. *J. Phys. Chem. B* **1998**, *102*, 6685.
(293) Li, M.; Schnablegger, H.; Mann, S. *Nature* **1999**, *402*, 393.

(294) Nikoobakht, B.; Wang, Z. L.; El-Sayed, M. A. *J. Phys. Chem. B* **2000**, *104*, 8635.
(295) Kim, F.; Kwan, S.; Akana, J.; Yang, P. *J. Am. Chem. Soc.* **2001**, *123*, 4360.
(296) Yang, P.; Kim, F. *ChemPhysChem* **2002**, *3*, 503.
(297) Kwan, S.; Kim, F.; Akana, J.; Yang, P. *Chem. Commun.* **2001**, 447.
(298) Li, L.-S.; Alivisatos, A. P. *Adv. Mater.* **2003**, *15*, 408.
(299) Jana, N. R.; Gearheart, L. A.; Obare, S. O.; Johnson, C. J.; Edler, K. J.; Mann, S.; Murphy, C. J. *J. Mater. Chem.* **2002**, *12*, 2909.
(300) Dujardin, E.; Hsin, L.-B.; Wang, C. R. C.; Mann, S. *Chem. Commun.* **2001**, 1264.
(301) Caswell, K. K.; Wilson, J. N.; Bunz, U. H. F.; Murphy, C. J. *J. Am. Chem. Soc.* **2003**, *125*, 13914.
(302) Thomas, K. G.; Barazzouk, S.; Ipe, B. I.; Joseph, S. T. S.; Kamat, P. V. *J. Phys. Chem. B* **2004**, *108*, 13066.
(303) Huang, Y.; Duan, X.; Wei, Q.; Lieber, C. M. *Science* **2001**, *291*, 630.
(304) Whang, D.; Jin, S.; Wu, Y.; Lieber, C. M. *Nano Lett.* **2003**, *3*, 1255.
(305) Tao, A.; Kim, F.; Hess, C.; Goldberger, J.; He, R.; Sun, Y.; Xia, Y.; Yang, P. *Nano Lett.* **2003**, *3*, 1229.
(306) Brus, L. E. *Appl. Phys. A* **1991**, *53*, 465.
(307) Alivisatos, A. P. *Science* **1996**, *271*, 933.
(308) Gaponenko. *Optical Properties of Semiconductor Nanocrystals*; Cambridge University Press: Cambridge, U.K., 1998.
(309) Efros, Al. L.; Efros, A. L. *Sov. Phys. Semicond.* **1982**, *16*, 772.
(310) Ekimov, A. I.; Efros, Al. L.; Onushchenko, A. A. *Solid State. Commun.* **1985**, *56*, 921.
(311) Efros, Al. L.; Rosen, M. *Annu. Rev. Mater. Sci.* **2000**, *30*, 475.
(312) Brus, L. E. *J. Chem. Phys.* **1983**, *79*, 5566.
(313) Ekimov, A. I.; Onuschenko, A. A. *JETP Lett.* **1981**, *34*, 345.
(314) Ekimov, A. I.; Onushchenko, A. A. *Sov. Phys. Semicond.* **1982**, *16*, 775.
(315) Ekimov, A. I.; Onushchenko, A. A.; Plukhin, A. G.; Efros, Al. L. *Sov. Phys. JETP* **1985**, *61*, 891.
(316) Itoh, T.; Iwabuchi, Y.; Kirihara, T. *Phys. Status Solidi B* **1988**, *146*, 531.
(317) Ekimov, A. I.; Onushchenco, A. A.; Efros, Al. L. *JETP Lett.* **1986**, *43*, 376.
(318) Ekimov, A. I.; Onushchenko, A. A.; Shumilov, S. K.; Efros, Al. L. *Sov. Technol. Phys. Lett.* **1987**, *13*, 115.
(319) Ekimov, A. I.; Efros, Al. L.; Ivanov, M. G.; Onushchenko, A. A.; Shumilov, S. K. *Solid State Commun.* **1989**, *69*, 565.
(320) Ekimov, A. I.; Onuschenko, A. A. *JETP Lett.* **1984**, *40*, 1136.
(321) Norris, D. J.; Sacra, A.; Murray, C. B.; Bawendi, M. G. *Phys. Rev. Lett.* **1994**, *72*, 2612.
(322) Norris, D. J.; Bawendi, M. G. *J. Chem. Phys.* **1995**, *103*, 5260.
(323) Nirmal, M.; Brus, L. *Acc. Chem. Res.* **1999**, *32*, 407.
(324) Yoffe, A. D. *Adv. Phys.* **2001**, *50*, 1.
(325) Norris, D. J.; Bawendi, M. G. *Phys. Rev. B* **1996**, *53*, 16338.
(326) Banin, U.; Cerullo, G.; Guzelian, A. A.; Alivisatos, A. P.; Shank, C. V. *Phys. Rev. B* **1997**, *55*, 7059.
(327) Efros, Al. L.; Rosen, M.; Kuno, M.; Nirmal, M.; Norris, D. J.; Bawendi, M. *Phys. Rev. B* **1996**, *54*, 4843.
(328) Chen, W. Fluorescence, thermoluminescence, and photostimulated luminescence of nanoparticles. In *Handbook of Nanostructured Materials and Nanotechnology*; Nalwa, H. S., Ed.; Academic Press: New York, 2000; Vol. 4, Chapter 5, p 325.
(329) Klimov, V. I. *J. Phys. Chem. B* **2000**, *104*, 6112.
(330) Richard, D.; Ghanassi, M.; Schanneklein, M. *Opt. Commun.* **1994**, *108*, 311.
(331) Ninomiya, S.; Adachi, A. *J. Appl. Phys.* **1995**, *78*, 4681.
(332) Leatherdale, C. A.; Woo, W. K.; Mikulee, F. V.; Bawendi, M. G. *J. Phys. Chem. B* **2002**, *106*, 7619.
(333) Soloviev, V. N.; Eichhfer, A.; Fenske, D.; Banin, U. *J. Am. Chem. Soc.* **2001**, *123*, 2354.
(334) Soloviev, V. N.; Eichhfer, A.; Fenske, D.; Banin, U. *J. Am. Chem. Soc.* **2000**, *122*, 2673.
(335) Soloviev, V. N.; Eichhfer, A.; Fenske, D.; Banin, U. *Phys. Status Solidi B* **2001**, *224*, 1, 285.
(336) Nirmal, M.; Murray, C. B.; Bawendi, M. G. *Phys. Rev. B* **1994**, *50*, 2293.
(337) Tomasulo, A.; Ramakrishna, M. V. *J. Chem. Phys.* **1996**, *105*, 3612.
(338) Bawendi, M. G.; Carroll, P. J.; Wilson, W. L.; Brus, L. E. *J. Chem. Phys.* **1992**, *96*, 946.
(339) Nirmal, M.; Norris, D. J.; Kuno, M.; Bawendi, M. G. *Phys. Rev. Lett.* **1995**, *75*, 3728.
(340) (a) Chen, W.; Wang, Z.; Lin, Z.; Lin, L.; Efros, A. L.; Rosen, M. *J. Appl. Phys.* **1997**, *82*, 3111. (b) Chen, X.; Lou, Y.; Samia, A. C. S.; Burda, C. *J. Am. Chem. Soc.* 2005, in press.
(341) Kreibig, U.; Vollmer, M. *Optical Properties of Metal Clusters*; Springer: Berlin, Germany, 1995.
(342) Kerker, M. *The Scattering of Light and Other Electromagnetic Rediation*; Academic: New York, 1969.
(343) Bohren, C. F.; Huffman, D. R. *Absorption and Scattering of Light by Small Particles*; Wiley: New York, 1983.
(344) Creighton, J. A.; Eadon, D. G. *J. Chem. Soc., Faraday Trans.* **1991**, *87*, 3881.
(345) Ashcroft, N. W.; Mermin, N. D. *Solid State Physics*; Saunders College: Philadelphia, PA, 1976.
(346) Schmid, G. Metals. In *Nanoscale Materials in Chemistry*; Klabunde, K. J., Ed.; Wiley-Interscience: New York, 2001; Chapter 2, p 15.
(347) Mie, G. *Ann. Phys.* **1908**, *25*, 329.
(348) Alvarez, M. M.; Khoury, J. T.; Schaaff, T. G.; Shafigullin, M. N.; Vezmar, I.; Whetten, R. L. *J. Phys. Chem. B* **1997**, *101*, 3706.
(349) Hostetler, M. J.; Wingate, J. E.; Zhong, C. J.; Harris, J. E.; Vachet, R. W.; Clark, M. R.; Londono, J. D.; Green, S. J.; Stokes, J. J.; Wignall, G. D.; Glish, G. L.; Porter, M. D.; Evans, N. D.; Murray, R. W. *Langmuir* **1998**, *14*, 17.
(350) Kawabata, A.; Kubo, R. *J. Phys. Soc. Jpn.* **1966**, *21*, 1765.
(351) Genzel, L.; Martin, T. P.; Kreibig, U. *Z. Phys. B* **1975**, *21*, 339.
(352) Ruppin, R.; Yatom, H. *Phys. Stat. Solidi B* **1976**, *74*, 647.
(353) Cini, M. *J. Opt. Soc. Am.* **1981**, *71*, 386.
(354) Wood, D. M.; Aschcroft, N. W. *Phys. Rev. B* **1982**, *25*, 6255.
(355) Kraus, W. A.; Schatz, G. C. *J. Chem. Phys.* **1983**, *79*, 6130.
(356) Hache, F.; Richard, D.; Flytzanis, C. *J. Opt. Am. Soc. B* **1986**, *3*, 1647.
(357) Yannouleas, C.; Broglia, R. A. *Ann. Phys.* **1992**, *217*, 105.
(358) Brack, M. *Rev. Mod. Phys.* **1993**, *65*, 677.
(359) Bonacic-Koutecky, V.; Fantucci, P.; Koutecky, J. *Chem. Rev.* **1991**, *91*, 1035.
(360) Persson, N. J. *Surf. Sci.* **1993**, *281*, 153.
(361) Gans, R. *Ann. Phys.* **1915**, *47*, 270.
(362) Papavassiliou, G. C. *Prog. Solid State Chem.* **1980**, *12*, 185.
(363) Link, S.; Mohamed, M. B.; El-Sayed, M. A. *J. Phys. Chem. B* **1999**, *103*, 3073.
(364) van der Zander, B. M. I.; Bohmer, M. R.; Fokkink, L. G. J.; Schonenberger, C. *J. Phys. Chem. B* **1997**, *101*, 852.
(365) Mohamed, M. B.; Ismael, K. Z.; Link, S.; El-Sayed, M. A. *J. Phys. Chem. B* **1998**, *102*, 9370.
(366) Whittle, D. G.; Burstein, E. *Bull. Am. Phys. Soc.* **1981**, *26*, 777.
(367) Boyd, G. T.; Yu, Z. H.; Shen, Y. R. *Phys. Rev. B* **1986**, *33*, 7923.
(368) Moshovists, M. *Rev. Mod. Phys.* **1985**, *57*, 783.
(369) Heritage, J. P.; Bergman, J. G.; Pinczuk, A.; Worlock, J. M. *Chem. Phys. Lett.* **1979**, *67*, 229.
(370) Apell, P.; Monreal, R. *Phys. Scr.* **1988**, *38*, 174.
(371) Plekhanov, V. G.; Siliukova, T. V. *Sov. Phys. Solid State* **1990**, *32*, 1268.
(372) Mooradian, A. *Phys. Rev. Lett.* **1969**, *22*, 185.
(373) Chen, C. K.; Heinz, T. F.; Ricard, D.; Shen, Y. R. *Phys. Rev. B* **1983**, *27*, 1965.
(374) Boyd, G. T.; Rasing, T.; Leite, J. R. R.; Shen, Y. R. *Phys. Rev. B* **1984**, *30*, 519.
(375) Mohamed, M. B.; Volkov, V. V.; Link, S.; El-Sayed, M. A. *Chem. Phys. Lett.* **2000**, *317*, 517.
(376) Soennichsen, C.; Franzl, T.; Wilk, G.; von Plessen, G.; Feldmann, J.; Wilson, O.; Mulvaney, P. *Phys. Rev. Lett.* **2002**, *88*, 77402.
(377) Wilcoxon, J. P.; Martin, J. E.; Parsapour, F.; Wiedenman, B.; Kelley, D. F. *J. Chem. Phys.* **1998**, *108*, 9137.
(378) Hao, E.; Bailey, R. C.; Schatz, G. C.; Hupp, J. T.; Li, S. *Nano Lett.* **2004**, *4*, 327.
(379) Hao, E.; Kelly, K. L.; Hupp, J. T.; Schatz, G. C. *J. Am. Chem. Soc.* **2002**, *124*, 15182.
(380) Sun, Y.; Mayers, B.; Xia, Y. *Nano Lett.* **2003**, *3*, 675.
(381) Alivisatos, A. P. *Endeavour* **1997**, *21*, 56.
(382) Coombes, C. J. *J. Phys.* **1972**, *2*, 441.
(383) Buffat, P.; Borel, J.-P. *Phys. Rev. A* **1976**, *13*, 2287.
(384) Castro, T.; Reifenberger, R.; Choi, E.; Andres, R. P. *Phys. Rev. B* **1990**, *42*, 8548.
(385) Beck, R. D.; St. John, P.; Homer, M. L.; Whetten, R. L. *Science* **1991**, *253*, 879.
(386) Martin, T. P.; Naher, U.; Schaber, H.; Zimmermann, U. *J. Chem. Phys.* **1994**, *100*, 2322.
(387) Couchman, P. R.; Jesser, W. A. *Nature* **1977**, *269*, 481.
(388) Ercolessi, F.; Andreoni, W.; Tosatti, E. *Phys. Rev. Lett.* **1991**, *66*, 911.
(389) Haase, M.; Alivisatos, A. P. *J. Phys. Chem.* **1992**, *96*, 6756.
(390) Tolbert, S. H.; Alivisatos, A. P. *Science* **1994**, *265*, 373.
(391) Klein, D. L.; McEuen, P. L.; Katari, J. E. B.; Roth, R.; Alivisatos, A. P. *Appl. Phys. Lett.* **1996**, *68*, 2574.
(392) Black, C. T.; Ralph, D. C.; Tinkham, M. *Phys. Rev. Lett.* **1996**, *76*, 688.
(393) Ingram, R. S.; Hostetler, M. J.; Murray, R. W.; Schaaff, T. G.; Khoury, J. T.; Whetten, R. L.; Bigioni, T. P.; Guthrie, D. K.; First, P. N. *J. Am. Chem. Soc.* **1997**, *119*, 9279.
(394) Andres, R. P.; Bein, T.; Dorogi, M.; Feng, S.; Henderson, J. I.; Kubiak, C. P.; Mahoney, W.; Osifchin, R. G.; Reifenberger, R. *Science* **1996**, *272*, 1323.
(395) Maltezopoulos, T.; Kubetzka, A.; Morgenstern, M.; Wiesendanger, R.; Lemay, S. G.; Dekker, C. *Appl. Phys. Lett.* **2003**, *83*, 1011.
(396) Janssen, J. W.; Lemay, S. G.; Kouwenhoven, L. P.; Dekker, C. *Phys. Rev. B* **2002**, *65*, 115423/1.
(397) Yao, Z.; Dekker, C.; Avouris, P. *Top. Appl. Phys.* **2001**, *80*, 147.

(398) Venema, L. C.; Meunier, V.; Lambin, Ph.; Dekker, C. *Phys. Rev. B* **2000**, *61*, 2991.
(399) Wildoer, J. W. G.; Venema, L. C.; Rinzier, A. G.; Smalley, R. E.; Dekker, C. *Nature* **1998**, *391*, 59.
(400) Venema, L. C.; Wildoer, J. W. G.; Janssen, J. W.; Tans, S. J.; Tuinstra, H. L. J. T.; Kouwenhoven, L. P.; Dekker, C. *Science* **1999**, *283*, 52.
(401) Dekker, C. *Phys. Today* **1999**, May 22.
(402) Esley, G. L. *Phys. Rev. Lett.* **1983**, *51*, 2140.
(403) Esley, G. L. *Phys. Rev. B* **1986**, *33*, 2144.
(404) Groeneveld, R. H. M.; Sprik, R.; Lagenduk, A. *Phys. Rev. B* **1992**, *45*, 5079.
(405) Groeneveld, R. H. M.; Sprik, R.; Lagenduk, A. *Phys. Rev. B* **1995**, *51*, 11433.
(406) Schoenlein, R. W.; Lin, W. Z.; Fujimoto, J. G.; Esley, G. L. *Phys. Rev. Lett.* **1987**, *58*, 1680.
(407) Brorson, S. D.; Fujimoto, J. G.; Ippen, E. P. *Phys. Rev. Lett.* **1987**, *59*, 1962.
(408) Sun, C. K.; Vallee, F.; Acioli, L. H.; Ippen, E. P.; Fujimoto, J. G. *Phys. Rev. B* **1993**, *48*, 12365.
(409) Sun, C. K.; Vallee, F.; Acioli, L. H.; Ippen, E. P.; Fujimoto, J. G. *Phys. Rev. B* **1994**, *50*, 15337.
(410) del Fatti, N.; Bouffanais, R.; Vallee, F.; Flytzanis, C. *Phys. Rev. Lett.* **1998**, *81*, 922.
(411) Elsayed-Ali, H. E.; Juhasz, T.; Smith, G. O.; Bron, W. E. *Phys. Rev. B* **1991**, *43*, 4488.
(412) Juhasz, T.; Elsayed-Ali, H. E.; Hu, H.; Bron, W. E. *Phys. Rev. B* **1992**, *45*, 13819.
(413) Juhasz, T.; Elsayed-Ali, H. E.; Smith, G. O.; Suarez, C.; Bron, W. E. *Phys. Rev. B* **1993**, *48*, 15488.
(414) Fann, W. S.; Storz, R.; Tom, H. W. K.; Boker, J. *Phys. Rev. B* **1992**, *46*, 13592.
(415) Fann, W. S.; Storz, R.; Tom, H. W. K.; Boker, J. *Phys. Rev. Lett.* **1992**, *68*, 2834.
(416) Schmuttenmaer, C. A.; Aeschlimann, M.; Elsayed-Ali, H. E.; Miller, R. J. D.; Mantell, D. A.; Cao, J.; Gao, Y. *Phys. Rev. B* **1994**, *50*, 8957.
(417) Aeschlimann, M.; Schmuttenmaer, C. A.; Elsayed-Ali, H. E.; Miller, R. J. D.; Cao, J.; Gao, Y.; Mantell, D. A. *J. Chem. Phys.* **1995**, *102*, 8606.
(418) Gao, Y.; Cao, J.; Miller, R. J. D.; Elsayed-Ali, H. E.; Mantell, D. A. *Phys. Rev. B* **1997**, *56*, 1099.
(419) Cao, J.; Gao, Y.; Elsayed-Ali, H. E.; Miller, R. J. D.; Mantell, D. A. *Phys. Rev. B* **1998**, *58*, 10948.
(420) Anisimov, L.; Kapeliovich, B. L.; Perel'sman, T. L. *Soviet Phys. JETP* **1975**, *39*, 375.
(421) Pawlik, S.; Bauer, M.; Aeschlimann, M. *Surf. Sci.* **1997**, *377−379*, 206.
(422) Aeschlimann, M.; Pawlik, S.; Bauer, M. *Ber. Bunsen-Ges., Phys. Chem.* **1995**, *99*, 1504.
(423) Ogawa, S.; Petek, H. *Surf. Sci.* **1996**, *357−358*, 585.
(424) Kreibig, U.; von Fragstein, C. *Z. Phys.* **1969**, *224*, 307.
(425) Kreibig, U. *Z. Phys.* **1970**, *234*, 307.
(426) Perner, M.; Bost, P.; Pauck, T.; von Plessen, G.; Feldmann, J.; Becker, U.; Mennig, M.; Porstendorfer, J.; Schmitt, M.; Schmidt, H. *Ultrafast Phenomena X*; Babara, P. F., Fujimoto, J. G., Knox, W. H., Zinth, W., Eds.; Springer: Berlin, Germany, 1996.
(427) Perner, M.; Bost, P.; Lemmer, U.; von Plessen, G.; Feldmann, J.; Becker, U.; Menning, M.; Schmitt, M.; Schmidt, H. *Phys. Rev. Lett.* **1997**, *78* (11), 2192.
(428) Perner, M.; Klar, T.; Grosse, S.; Lemmer, U.; von Plessen, G.; Spirkl, W.; Feldmann, J. *J. Lumin.* **1998**, *76−77*, 181.
(429) Hodak, J. K.; Martini, I.; Hartland, G. V. *Chem. Phys. Lett.* **1998**, *284*, 135.
(430) Hodak, J. K.; Martini, I.; Hartland, G. V. *J. Phys. Chem.* **1998**, *102*, 6958.
(431) Hodak, J. K.; Martini, I.; Hartland, G. V. *J. Chem. Phys.* **1998**, *108*, 9210.
(432) Hodak, J. K.; Henglein, A.; Hartland, G. V. *J. Chem. Phys.* **1999**, *111*, 8613.
(433) Bigot, J. Y.; Merle, J. C.; Cregut, O.; Daunois, A. *Phys. Rev. Lett.* **1995**, *75*, 4702.
(434) Shahbazyan, T. V.; Perakis, I. E.; Bigot, J. Y. *Phys. Rev. Lett.* **1998**, *81*, 3120.
(435) Roberti, T. W.; Smith, B. A.; Zhang, J. Z. *J. Chem. Phys.* **1995**, *102*, 3860.
(436) Smith, B. A.; Waters, D. M.; Faulhaber, A. E.; Kreger, M. A.; Roberti, T. W.; Zhang, J. Z. *J. Sol−Gel Sci. Technol.* **1997**, *9* (2), 125.
(437) Faulhaber, A. E.; Smith, B. A.; Andersen, J. K.; Zhang, J. Z. *Mol. Cryst. Liq. Cryst.* **1996**, *283*, 25.
(438) Smith, B. A.; Zhang, J. Z.; Giebel, U.; Schmid, G. *Chem. Phys. Lett.* **1997**, *270*, 139.
(439) Hamanaka, Y.; Hayashi, N.; Nakamura, A.; Omi, S. *J. Lumin.* **1998**, *76−77*, 221.
(440) del Fatti, N.; Voisin, C.; Chevy, F.; Vallee, F.; Flytzanis, C. *J. Chem. Phys.* **1999**, *110*, 11484.
(441) del Fatti, N.; Flytzanis, C.; Vallee, F. *Appl. Phys. B* **1999**, *68*, 433.
(442) Feldstein, M. J.; Keating, C. D.; Liau, Y.-H.; Natan, M. J.; Scherer, N. F. *J. Am. Chem. Soc.* **1997**, *119*, 6638.
(443) Inouye, H.; Tanaka, K.; Tanahashi, I.; Hirao, K. *Phys. Rev. B* **1998**, *57*, 11334.
(444) Tokizaki, T.; Nakamura, A.; Kaneko, S.; Uchida, K.; Omi, S.; Tanji, H.; Asahara, Y. *Appl. Phys. Lett.* **1994**, *65* (8), 941.
(445) Averitt, R. D.; Westcott, S. L.; Halas, N. J. *Phys. Rev. B* **1998**, *58*, 10203.
(446) Ahmadi, T. S.; Logunov, S. L.; El-Sayed, M. A. *J. Phys. Chem.* **1996**, *100*, 8053.
(447) Ahmadi, T. S.; Logunov, S. L.; El-Sayed, M. A.; Khoury, J. T.; Whetten, R. L. *J. Phys. Chem.* **1997**, *101*, 3713.
(448) Link, S.; Burda, C.; Wang, Z. L.; El-Sayed, M. A. *J. Chem. Phys.* **1999**, *111*, 1255.
(449) Link, S.; Burda, C.; Mohamed, M. B.; Nikoobakht, B.; El-Sayed, M. A. *Phys. Rev. B* **2000**, *61* (9), 6086.
(450) Rosei, R.; Antongeli, F.; Grassano, U. M. *Surf. Sci.* **1973**, *37*, 689.
(451) Cardona, M. *Modulation Spectroscopy, Solid State Physics, Supplement II*; Seitz, F., Turnball, D., Ehrenreich, H., Eds.; Academic Press: New York, 1969.
(452) Pines, D.; Nozières, P. *The Theory of Quantum Liquids*; Benjamin: New York, 1966.
(453) Stella, A.; Nisoli, M.; De Silvestri, S.; Svelto, O.; Lanzani, G.; Cheyssac, P.; Kofman, R. *Phys. Rev. B* **1996**, *53* (23), 15497.
(454) Stella, A.; Nisoli, M.; de Silvestri, S.; Svelto, O.; Lanzani, G.; Cheyssac, P.; Kofman, R. *Ultrafast Phenomena X*; Barbara, P. F., Fujimoto, J. G., Knox, W. H., Zinth, W., Eds.; Springer: Berlin, Germany, 1996.
(455) Nisoli, M.; Stagira, S.; de Silvestri, S.; Stella, A.; Tognini, P.; Cheyssac, P.; Kofman, R. *Phys. Rev. Lett.* **1997**, *78*, 3575.
(456) Hoda, J. K.; Martini, I.; Hartland, G. V. *J. Chem. Phys.* **2000**, *112*, 5942.
(457) Belotskii, E. D.; Tomchuk, P. M. *Surf. Sci.* **1990**, *239*, 143.
(458) Belotskii, E. D.; Tomchuk, P. M. *Int. J. Electron.* **1992**, *73*, 955.
(459) Shah, J. *Ultrafast Spectroscopy of Semiconductors and Semiconductor Nanostructures*; Springer: New York, 1999.
(460) Tsen, K.-T. *Ultrafast Phenomena in Semiconductors*; Springer: New York, 2001.
(461) Klimov, V. In *Handbook on Nanostructured Materials and Nanotechnology*; Nalwa, H., Ed.; Academic Press: San Diego, CA, 1999; Vol. 4, p 451.
(462) Nozik, A. J. *Annu. Rev. Phys. Chem.* **2001**, *52*, 193.
(463) Zhang, J. Z. *Acc. Chem. Res.* **1997**, *30*, 423.
(464) Zhang, J. Z. *J. Phys. Chem. B* **2000**, *104*, 7239.
(465) Burda, C.; Link, S.; Mohamed, M. B.; El-Sayed, M. *J. Chem. Phys.* **2002**, *116*, 3828.
(466) (a) Burda, C.; Link, S.; Mohamed, M.; El-Sayed, M. *J. Phys. Chem.* **2001**, *105*, 12286. (b) Mohamed, M.; Burda, C.; El-Sayed, M. *Nano Lett.* **2001**, *1*, 589. (c) Mona Mohamed, Ph.D. Thesis, School of Chemistry and Biochemistry, Georgia Institute of Technology, 2002.
(467) Burda, C.; Link, S.; Green, T. C.; El-Sayed, M. A. *J. Phys. Chem.* **1999**, *103*, 10775.
(468) Burda, C.; Green, T. C.; Link, S.; El-Sayed, M. A. *J. Phys. Chem. B* **1999**, *103*, 1783.
(469) Xu, S.; Mikhailovsky, A. A.; Hollingsworth, J. A.; Klimov, V. I. *Phys. Rev. B* **2002**, *65*, 045319/1.
(470) Klimov, V. I.; Mikhailovsky, A. A.; McBranch, D. W.; Leatherdale, C. A.; Bawendi, M. G. *Phys. Rev. B* **2000**, *61*, R13349.
(471) Klimov, V. I.; McBranch, D. W.; Leatherdale, C. A.; Bawendi, M. G. *Phys. Rev. B* **1999**, *60*, 13740.
(472) Klimov, V. I.; Mikhailovsky, A. A.; McBranch, D. W.; Leatherdale, C. A.; Bawendi, M. G. *Science* **2000**, *287*, 1011.
(473) Klimov, V. I.; McBranch, D. W.; Leatherdale, C. A.; Bawendi, M. G. *Phys. Rev. B* **1999**, *60*, 13740.
(474) Klimov, V. I.; Schwarz, Ch. J.; McBranch, D. W.; Leatherdale, C. A.; Bawendi, M. G. *Phys. Rev. B* **1999**, *60*, R2177.
(475) Klimov, V. I.; McBranch, D. W. *Phys. Rev. Lett.* **1998**, *80*, 4028.
(476) Hunsche, S.; Dekorsy, T.; Klimov, V.; Kurz, H. *Appl. Phys. B* **1996**, *62*, 3.
(477) Klimov, V.; Haring Bolivar, P.; Kurz, H. *Phys. Rev. B* **1996**, *53*, 1463.
(478) Klimov, V.; Hunsche, S.; Kurz, H. *Phys. Rev. B* **1994**, *50*, 8110.
(479) Hu, Y.; Koch, S.; Lindberg, M.; Peyghambarian, N.; Pollock, E. L.; Abraham, F. F. *Phys. Rev. Lett.* **1990**, *64*, 1805.
(480) Kang, K.; Kepner, A.; Gaponenko, S.; Koch, S. W.; Hu, Y. Z.; Peyghambarian, N. *Phys. Rev. B* **1993**, *48*, 15449.
(481) Klimov, V.; Haring Bolivar, P.; Kurz, H. *Phys. Rev. B* **1995**, *52*, 4728.
(482) Prabhu, S.; Vengurlekar, A.; Shah, J. *Phys. Rev. B* **1995**, *51*, 14233.
(483) Benisty, H.; Sotomayor-Torres, C.; Weisbuch, C. *Phys. Rev. B* **1991**, *44*, 10945.
(484) Bockelmann, U.; Bastard, G. *Phys. Rev. B* **1999**, *42*, 8947.
(485) Woggon, U.; Giessen, H.; Gindele, F.; Wind, O.; Fluegel, B.; Peyghambarian, N. *Phys. Rev. B* **1996**, *54*, 17681.
(486) Shum, K.; Wang, W. B.; Alfano, R.; Jones, K. *Phys. Rev. Lett.* **1992**, *68*, 3904.

(487) Efros, Al. L.; Kharchenko, V. A.; Rosen, M. *Solid State Commun.* **1995**, *93*, 281.
(488) Guyot-Sionnest, P.; Hines, M. *Appl. Phys. Lett.* **1998**, *72*, 686.
(489) Guyot-Sionnest, P.; Shim, M.; Matranga, C.; Hines, M. *Phys. Rev. B* **1999**, *60*, R2181.
(490) Nirmal, M.; Murray, C. B.; Norris, D. J.; Bawendi, M. G. *Z. Phys. D* **1993**, *26*, 361.
(491) Darugar, Q.; Landes, C.; Link, S.; Schill, A.; El-Sayed, M. A. *Chem. Phy. Lett.* **2003**, *373* (3, 4), 284−291.
(492) Brelle, M.; Zhang, J. Z. *J. Chem. Phys.* **1998**, *108*, 3119.
(493) Zhang, J. Z. Dynamic Properties of Nanoparticles In *Handbook of Nanophase and Nanostructured Materials*; Wang, Z. L., Liu, Y., Zhang, Z., Eds.; Kluwer Academic: New York, 2003; Vol. 2, p 219.
(494) Ellingson, R. J.; Blackburn, J. L.; Yu, P.; Rumbles, G.; Micic, O. I.; Nozik, A. J. *J. Phys. Chem. B* **2002**, *106*, 7758.
(495) Rumbles, G.; Selmarten, D. C.; Ellingson, R. J.; Blackburn, J. L.; Yu, P. R.; Smith, B. B.; Micic, O. I.; Nozik, A. J. *J. Photochem. Photobiol. A* **2001**, *142*, 187.
(496) Blackburn, J. L.; Ellingson, R. J.; Mii, O. I.; Nozik, A. J. *J. Phys. Chem. B* **2003**, *107*, 102.
(497) Ahrenkiel, S. P.; Micic, O. I.; Miedaner, A.; Curtis, C. J.; Nedeljkovic, J. M.; Nozik, A. J. *Nano Lett.* **2003**, *3* (6), 833.
(498) Liu, Z.; Bai, Y.; Cui, D.; Wang, Q. *Solid State Sci.* **2003**, *5*, 1037.
(499) Menoni, C. S.; Miao, L.; Patel, D.; Micic, O. I.; Nozik, A. J. *Phys. Rev. Lett.* **2000**, *84*, 4168.
(500) Sen, P. K.; Andrews, J. T. *Superlatt. Microstruct.* **2001**, *29*, 287.
(501) Klimov, V. I.; Schwarz, Ch. J.; McBranch, D. W.; White, C. W. *Appl. Phys. Lett.* **1998**, *73*, 2603.
(502) Myers, K. E.; Wang, Q.; Dexheimer, S. L. *Phys. Rev. B* **2001**, *64*, R161309.
(503) Franceschetti, A.; Pantelides, S. T. *Phys. Rev. B* **2003**, *68*, 033313.
(504) Jie, Y. X.; Xiong, Y. N.; Wee, A. T. S.; Huan, C. H. A.; Ji, W. *Appl. Phys. Lett.* **2000**, *77*, 3926.
(505) Stagira, S.; Nisoli, M.; De Silvestri, S.; Tognini, P.; Stella, A.; Cheyssac, P.; Kofman, R. *Phys. Rev.* **2000**, *62*, 10318.
(506) Tognini, P.; Stella, A.; De Silvestri, S.; Nisoli, M.; Stagira, S.; Cheyssac, P.; Kofman, R. *Phys. Stat. Sol. A* **2000**, *178*, 355.
(507) Linsebigler, A. L.; Lu, G.; Yates, J. T., Jr. *Chem. Rev.* **1995**, *95*, 735.
(508) Hagfeldt, A.; Grtzel, M. *Chem. Rev.* **1995**, *95*, 49.
(509) Hagfeldt, A.; Grtzel, M. *Acc. Chem. Res.* **2000**, *33*, 269.
(510) Colombo, D. P., Jr.; Roussel, K. A.; Saeh, J.; Skinner, D. E.; Cavaleri, J. J.; Bowman, R. M. *Chem. Phys. Lett.* **1995**, *232*, 207.
(511) Skinner, D. E.; Cholombo, D. P., Jr.; Cavaleri, J. J.; Bowman, R. M. *J. Phys. Chem.* **1995**, *99*, 7853.
(512) Miller, R. J. D.; McLendon, G. L.; Nozik, A. J.; Schmickler, W.; Willig, F. *Surface Electron-Transfer Processes*; VCH: New York, 1995.
(513) Grtzel, M. *Heterogeneous Photochemical Electron Transfer*; CRC Press: Boca Raton, FL, 1989.
(514) Rehm, J. M.; McLendon, G. L.; Nagasawa, Y.; Yoshihara, K.; Moser, J.; Gratzel, M. *J. Phys. Chem.* **1996**, *100*, 9577.
(515) Hannappel, T.; Burfeindt, B.; Storck, W.; Willig, F. *J. Phys. Chem. B* **1997**, *101*, 6799.
(516) Ellingson, R. J.; Asbury, J. B.; Ferrere, S.; Ghosh, H. N.; Sprague, J. R.; Lian, T. Q.; Nozik, A. J. *J. Phys. Chem. B* **1998**, *102*, 6455.
(517) Cherepy, N. J.; Smestad, G. P.; Grtzel, M.; Zhang, J. *J. Phys. Chem. B* **1997**, 9342.
(518) Kamat, P. V. *Prog. Inorg. Chem.* **1997**, *44*, 273.
(519) Martini, I.; Hodak, J. H.; Hartland, G. V. *J. Phys. Chem.* **1998**, *102*, 9508.
(520) Cherepy, N. J.; Liston, D. B.; Lovejoy, J. A.; Deng, H.; Zhang, J. Z. *J. Phys. Chem. B* **1998**, *102* (5), 770.
(521) Patel, A. A.; Wu, F.; Zhang, J. Z.; Torres-Martinez, C. L.; Mehra, R. K.; Yang, Y.; Risbud, S. H. *J. Phys. Chem. B* **2000**, *104*, 11598.
(522) Brelle, M. C.; Torres-Martinez, C. L.; McNulty, J. C.; Mehra, R. K.; Zhang, J. Z. *Pure Appl. Chem.* **2000**, *72* (1−2), 101.
(523) Brelle, M. C.; Zhang, J. Z.; Nguyen, L.; Mehra, R. K. *J. Phys. Chem. A* **1999**, *103*, 10194.
(524) Sengupta, A.; Jiang, B.; Mandal, K. C.; Zhang, J. Z. *J. Phys. Chem. B* **1999**, *103*, 3128.
(525) Sengupta, A.; Mandal, K. C.; Zhang, J. Z. *J. Phys. Chem. B* **2000**, *104*, 9396.
(526) Link, S.; El-Sayed, M. A. *J. Phys. Chem. B* **1999**, *103*, 8410.
(527) Link, S.; Burda, C.; Nikoobakht, B.; El-Sayed, M. A. *J. Phys. Chem. B* **2000**, *104*, 6152.
(528) Sercel, P. C. *Phys. Rev. B* **1995**, *51*, 14532.
(529) Wang, P. D.; Sotomayor-Torres, C. M.; McLelland, H.; Thoms, S.; Holland, M.; Stanley, C. R. *Surf. Sci.* **1994**, *305*, 585.
(530) Mukai, K.; Sugawara, M. *Jpn. J. Appl. Phys.* **1998**, *37*, 5451.
(531) Mukai, K.; Ohtsuka, N.; Shoji, H.; Sugawara, M. *Appl. Phys. Lett.* **1996**, *68*, 3013.
(532) Murdin, B. N.; Hollingworth, A. R.; Kamal-Saadi, M.; Kotitschke, R. T.; Ciesla, C. M.; Pidgeon, C. R.; Findlay, P. C.; Pellemans, H. P. M.; Langerak, C. J. G. M.; Rowe, A. C.; Stradling, R. A.; Gornik, E. *Phys. Rev. B* **1999**, *59*, R7817.
(533) Sugawara, M.; Mukai, K.; Shoji, H. *Appl. Phys. Lett.* **1997**, *71*, 2791.
(534) Heitz, R.; Veit, M.; Ledentsov, N. N.; Hoffmann, A.; Bimberg, D.; Ustinov, V. M.; Kop'ev, P. S.; Alferov, Z. I. *Phys. Rev. B* **1997**, *56* (16), 10435.
(535) Heitz, R.; Kalburge, A.; Xie, Q.; Grundmann, M.; Chen, P.; Hoffmann, A.; Madhukar, A.; Bimberg, D. *Phys. Rev. B* **1998**, *57*, 9050.
(536) Mukai, K.; Ohtsuka, N.; Shoji, H.; Sugawara, M. *Phys. Rev. B* **1996**, *54*, R5243
(537) Yu, H.; Lycett, S.; Roberts, C.; Murray, R. *Appl. Phys. Lett.* **1996**, *69*, 4087.
(538) Adler, F.; Geiger, M.; Bauknecht, A.; Scholz, F.; Schweizer, H.; Pilkuhn, M. H.; Ohnesorge, B.; Forchel, A. *J. Appl. Phys.* **1996**, *80*, 4019.
(539) Adler, F.; Geiger, M.; Bauknecht, A.; Haase, D.; Ernst, P.; Dornen, A.; Scholz, F.; Schweizer, H. *J. Appl. Phys.* **1998**, *83*, 1631.
(540) Brunner, K.; Bockelmann, U.; Abstreiter, G.; Walther, M.; Bohm, G.; Trankle, G.; Weimann, G. *Phys. Rev. Lett.* **1992**, *69*, 3216.
(541) Kamath, K.; Jiang, H.; Klotzkin, D.; Phillips, J.; Sosnowski, T.; Norris, T.; Singh, J.; Bhattacharya, P. *Inst. Phys. Conf. Ser.* **1998**, *156* (*Compound Semicond. Symp*. 1997), 525.
(542) Gfroerer, T. H.; Sturge, M. D.; Kash, K.; Yater, J. A.; Plaut, A. S.; Lin, P. S. D.; Florez, L. T.; Harbison, J. P.; Das, S. R.; Lebrun, L. *Phys. Rev. B* **1996**, *53*, 16474.
(543) Li, X.-Q.; Nakayama, H.; Arakawa, Y. *Proc. Int. Conf. Phys. Semicond. 24th*; Gershoni, D., Ed.; World Science: Singapore, 1998; p 845.
(544) Gershoni, D. *Proc. Int. Conf. Phys. Semicond. 24th*; Gershoni, D., Ed.; World Science: Singapore, 1998; p 763.
(545) Lowisch, M.; Rabe, M.; Kreller, F.; Henneberger, F. *Appl. Phys. Lett.* **1999**, *74*, 2489.
(546) Gontijo, I.; Buller, G. S.; Massa, J. S.; Walker, A. C.; Zaitsev, S. V.; Gordeev, N. Y.; Ustinov, V. M.; Kopev, P. S. *Jpn. J. Appl. Phys.* **1999**, *38*, 674.
(547) Li, X.-Q.; Nakayama, H.; Arakawa, Y. *Jpn. J. Appl. Phys.* **1999**, *38*, 473.
(548) Kral, K.; Khas, Z. *Phys. Status Solidi B* **1998**, *208*, R5.
(549) Bimberg, D.; Ledentsov, N. N.; Grundmann, M.; Heitz, R.; Bohrer, J.; Ustinov, V. M.; Kopev, P. S.; Alferov, Z. I. *J. Lumin.* **1997**, *72*−*74*, 34.
(550) Grundmann, M.; Heitz, R.; Ledentsov, N.; Stier, O.; Bimberg, D.; Ustinov, V. M.; Kopev, P. S.; Alferov, Z. I.; Ruvimov, S. S.; Werner, P.; Gosele, U.; Heydenreich, J. *Superlatt. Microstruct.* **1996**, *19*, 81.
(551) Williams, V. S.; Olbright, G. R.; Fluegel, B. D.; Koch, S. W.; Peyghambarian, N. *J. Mod. Opt.* **1988**, *35*, 1979.
(552) Ohnesorge, B.; Albrecht, M.; Oshinowo, J.; Forchel, A.; Arakawa, Y. *Phys. Rev. B* **1996**, *54*, 11532.
(553) Wang, G.; Fafard, S.; Leonard, D.; Bowers, J. E.; Merz, J. L.; Petroff, P. M. *Appl. Phys. Lett.* **1994**, *64*, 2815.
(554) Sandmann, J. H. H.; Grosse, S.; von Plessen, G.; Feldmann, J.; Hayes, G.; Phillips, R.; Lipsanen, H.; Sopanen, M.; Ahopelto, J. *Phys. Status Solidi B* **1997**, *204*, 251.
(555) Grundmann, M.; Heitz, R.; Bimberg, D. *Physica E* **1998**, *2*, 578.
(556) Li, X.-Q.; Arakawa, Y. *Phys. Rev. B* **1998**, *57*, 12285.
(557) Sosnowski, T. S.; Norris, T. B.; Jiang, H.; Singh, J.; Kamath, K.; Bhattacharya, P. *Phys. Rev. B* **1998**, *57*, R9423.
(558) Meier, A.; Selmarten, D. C.; Siemoneit, K.; Smith, B. B.; Nozik, A. J. *J. Phys. Chem. B* **1999**, *103*, 2122.
(559) Zaban, A.; Meier, A.; Gregg, B. A. *J. Phys. Chem. B* **1997**, *101*, 7985.
(560) Diol, S. J.; Poles, E.; Rosenwaks, Y.; Miller, R. J. D. *J. Phys. Chem. B* **1998**, *102*, 6193.
(561) Chatterji, D. *The Theory of Auger Transitions*; Academic Press: London, U.K., 1976.
(562) Landsberg, P. *Recombination in Semiconductors*; Cambridge University Press: Cambridge, U.K., 1991.
(563) Lou, Y.; Chen, X.; Samia, A. C.; Burda, C. *J. Phys. Chem.* **2003**, *107*, 12431.
(564) Lou, Y.; Samia, A. C. S.; Cowen, J.; Banger, K.; Chen, X.; Lee, H.; Burda, C. *Phys. Chem. Chem. Phys.* **2003**, *5* (6), 1091.
(565) Chikan, V.; Kelley, D. F. *Nano Lett.* **2002**, *2*, 1015.
(566) Yu, D.; Wang, C.; Guyot-Sionnest, P. *Science* **2003**, *300*, 1277.
(567) Ahmadi, T. S.; Wang, Z. L.; Green, T. C.; Henglein, A.; El-Sayed, M. A. *Science* **1996**, *272*, 1924.
(568) Narayanan, R.; El-Sayed, M. A. *Nano Lett.* **2004**, *4* (7), 1343.
(569) Li, Y.; El-Sayed, M. A. *J. Phys. Chem. B* **2001**, *105*, 8938−8943.
(570) Narayanan, R.; El-Sayed, M. A. *J. Phys. Chem. B* **2004**, *108* (18), 5726.
(571) Narayanan, R.; El-Sayed, M. A. *J. Am. Chem. Soc.* **2004**, *126* (23), 7419.
(572) Roucoux, A.; Schulz, J.; Patin, H. *Chem. Rev.* **2002**, *102* (10), 3757.
(573) Moiseev, I. I.; Vargatfik, M. N. *Russ. J. Gen. Chem.* **2002**, *72* (4), 512.
(574) Mayer, A. B. R. *Polym. Adv. Technol.* **2001**, *12* (1−2), 96.

(575) Boennemann, H.; Braun, G.; Brijoux, G.; Brinkman, R.; Tilling, A.; Seevogal, K.; Siepen, K. *J. Organomet. Chem.* **1996**, *520* (1−2), 143.
(576) Toshima, N. *NATO ASI Ser., Ser. 3* **1996**, *12*, 371.
(577) Duff, D. G.; Baiker, A. *Stud. Surf. Sci. Catal.* **1995**, *91*, 505.
(578) Bradley, J. S. In *Clusters and Colloids: From Theory to Application*; Schmid, G., Ed.; VCH: New York, 1994; pp 459−536.
(579) Teranishi, T.; Miyake, M. *Chem. Mater.* **1998**, *10*, 594.
(580) Li, Y.; Hong, X. M.; Collard, D. M.; El-Sayed, M. A. *Org. Lett.* **2000**, *2* (15), 2385.
(581) Li, Y.; Boone, E.; El-Sayed, M. A. *Langmuir* **2002**, *18*, 4921.
(582) Narayanan, R.; El-Sayed, M. A. *J. Am. Chem. Soc.* **2003**, *125* (27), 8340.
(583) Narayanan, R.; El-Sayed, M. A. *J. Phys. Chem. B* **2003**, *107* (45), 12416.
(584) Chen, C. W.; Tano, D.; Akashi, M. *J. Colloid Interface Sci.* **2000**, *225* (2), 349.
(585) Shiraishi, Y.; Nakayama, M.; Takagi, E.; Tominaga, T.; Toshima, M. *Inorg. Chim. Acta* **2000**, *300−302*, 964.
(586) Chen, C. W.; Akashi, M. *Langmuir* **1997**, *13* (24), 6465.
(587) Toshima, N. *NATO ASI Ser.* **1996**, *12*, 371.
(588) Adlim, M.; Abu Bakar, M.; Liew, K. Y.; Ismail, J. *J. Mol. Catal. A: Chem.* **2004**, *212* (1−2), 141.
(589) Yu, W.; Liu, M.; Liu, H.; Zheng, J. *J. Colloid Interface Sci.* **1999**, *210*, 218.
(590) Teranishi, T.; Hosoe, M.; Miyake, M. *Adv. Mater.* **1997**, *9*, 65.
(591) Busser, G. W.; Van Ommen, J. G.; Lercher, J. A. *Adv. Catal. Nanostruct. Mater.* **1996**, 213.
(592) Porta, F.; Ragaini, F.; Cenini, S.; Scari, G. *Gazz. Chim. Ital.* **1992**, *122*, 361.
(593) Bonet, F.; Delmas, V.; Grugeon, S.; Herrera Urbina, R.; Silvert, P.-Y.; Tekaia-Elhsissen, K. *Nanostruct. Mater.* **2000**, *11*, 1277.
(594) Li, Y.; Petroski, J.; El-Sayed, M. A. *J. Phys. Chem. B* **2000**, *104* (47), 10956.
(595) Fu, X.; Wang, Y.; Wu, N.; Gui, L.; Tan, Y. *Langmuir* **2002**, *18* (12), 4619.
(596) Ohde, H.; Wai, C. M.; Kim, H.; Kim, J.; Ohde, M. *J. Am. Chem. Soc.* **2002**, *124* (17), 4540.
(597) Troitski, S. Y.; Serebriakova, M. A.; Fedotov, M. A.; Ignashin, S. V.; Chuvilin, A. L.; Moroz, E. M.; Novgorodov, B. N.; Kochubey, D. I.; Likholobov, V. A.; Blanc, B.; Gallezot, P. *J. Mol. Catal. A: Chem.* **2000**, *158* (1), 461.
(598) Henglein, A. *J. Phys. Chem. B* **2000**, *104* (10), 2201.
(599) Aiken, J. D., III; Finke, R. G. *Chem. Mater.* **1999**, *11* (4), 1035.
(600) Aiken, J. D., III; Finke, R. G. *J. Am. Chem. Soc.* **1999**, *121*, 8803.
(601) Yu, W.; Liu, H. *Chem. Mater.* **1998**, *10*, 1205.
(602) Narayanan, R.; El-Sayed, M. A. *J. Phys. Chem. B* **2004**, *108* (25), 8572.
(603) Tamura, M.; Fujihara, H. *J. Am. Chem. Soc.* **2003**, *125* (51), 15742.
(604) Pittelkov, M.; Moth-Poulsen, K.; Boas, U.; Christensen, J. B. *Langmuir* **2003**, *19* (18), 7682.
(605) Tabuani, D.; Monticelli, O.; Chincarinni, A.; Bianchini, C.; Vizza, F.; Moneti, S.; Russo, S. *Macromol.* **2003**, *36* (12), 4294.
(606) Porta, F.; Prati, L.; Rossi, M.; Scari, G. *J. Catal.* **2002**, *211* (2), 464.
(607) Sau, T. K.; Pal, A.; Pal, T. *J. Phys. Chem. B* **2001**, *105* (38), 9266.
(608) Schulz, J.; Roucoux, A.; Patin, H. *Chem. Eur. J.* **2000**, *6* (4), 618.
(609) Zhao, M.; Sun, L.; Crooks, R. M. *J. Am. Chem. Soc.* **1998**, *120*, 4877.
(610) Zhao, M.; Crooks, R. M. *Angew. Chem., Int. Ed. Engl.* **1999**, *38*, 364.
(611) Zhao, M.; Sun, L.; Crooks, R. M. *Polym. Prepr. (Am. Chem. Soc., Div. Polym. Chem.)* **1999**, *40*, 400.
(612) Chechik, V.; Crooks, R. M. *J. Am. Chem. Soc.* **2000**, *122*, 1243.
(613) Crooks, R. M.; Zhao, M.; Sun, L.; Chechik, V.; Yeung, L. K. *Acc. Chem. Res.* **2001**, *34*, 181.
(614) Zhao, M.; Crooks, R. M. *Adv. Mater.* **1999**, *11*, 217.
(615) Garcia, M. E.; Baker, L. A.; Crooks, R. M. *Anal. Chem.* **1999**, *71*, 256.
(616) Mayer, A. B. R.; Johnson, R. W.; Hausner, S. H.; Mark, J. E. *J. Macromol. Sci., Pure Appl. Chem.* **1999**, *A36*, 1427.
(617) Mayer, A. B. R.; Hausner, S. H.; Mark, J. E. *Polym. J.* **2000**, *32*, 15.
(618) Mayer, A. B. R.; Mark, J. E. *Eur. Polym. J.* **1998**, *34*, 103.
(619) Mayer, A. B. R.; Mark, J. E. *J. Macromol. Sci., Pure Appl. Chem.* **1997**, *A34*, 2151.
(620) Mayer, A. B. R.; Antonietti, M. *Colloid Polym. Sci.* **1998**, *276*, 769.
(621) Wu, S. H.; Chen, D. H. *Chem. Lett.* **2004**, *33* (4), 406.
(622) Demir, M. M.; Gulgun, M. A.; Menceloglu, Y. Z.; Erman, B.; Abramchuk, S. S.; Makhaeva, E. E.; Khokhlov, A. R.; Matveeva, V. G.; Sulman, M. G. *Macromolecules* **2004**, *37* (5), 1787.
(623) Solla-Gullon, J.; Rodes, A.; Montiel, V.; Aldaz, A.; Clavilier, J. *J. Electroanal. Chem.* **2003**, *554−555*, 273.
(624) Wu, S. H.; Chen, D. H. *J. Colloid Interface Sci.* **2003**, *259* (2), 282.
(625) Solla-Gullon, J.; Montiel, V.; Aldaz, A.; Clavilier, J. *J. Electrochem. Soc.* **2003**, *150* (2), E104.
(626) Zhang, X.; Chang, K. Y. *Chem. Mater.* **2003**, *15* (2), 451.
(627) Harriman, A.; Thomas, J. M.; Millward, G. R. *New J. Chem.* **1987**, *11*, 757.
(628) Furlong, D. N.; Launikonis, A.; Sasse, W. H. F.; Sanders, J. V. *J. Chem. Soc., Faraday Trans. 1* **1984**, *80*, 571.
(629) Tano, T.; Esumi, K.; Meguro, K. *J. Colloid Interface Sci.* **1989**, *133*, 530.
(630) Esumi, K.; Suzuki, M.; Tano, T.; Torigoe, K.; Meguro, K. *Colloids Surf.* **1991**, *55*, 9.
(631) Esumi, K.; Tano, T.; Meguro, K. *Langmuir* **1989**, *5*, 268.
(632) Esumi, K.; Sadakane, O.; Torigoe, K.; Meguro, K. *Colloids Surf.* **1992**, *62*, 255.
(633) Son, S. U.; Jang, Y.; Park, J.; Na, H. B.; Park, H. M.; Yun, H. J.; Lee, J.; Hyeon, T. *J. Am. Chem. Soc.* **2004**, *126* (16), 5026.
(634) Son, S. U.; Park, I. K.; Park, J.; Hyeon, T. *Chem. Commun.* **2004**, *7*, 778.
(635) Michaelis, M.; Henglein, A. *J. Phys. Chem.* **1992**, *96*, 4719.
(636) Rafaeloff, R.; Haruvy, Y.; Binenboym, J.; Baruch, G.; Rajbenbach, L. A. *J. Mol. Catal.* **1983**, *22*, 219.
(637) Kurihara, K.; Kizling, J.; Stenius, P.; Fendler, J. H. *J. Am. Chem. Soc.* **1983**, *105*, 2574.
(638) Toshima, N.; Takahashi, T.; Hirai, H. *Chem. Lett.* **1986**, 35.
(639) Toshima, N.; Takahashi, T.; Hirai, H. *Chem. Lett.* **1985**, 1245.
(640) Toshima, N.; Takahashi, T. *Bull. Chem. Soc. Jpn.* **1992**, *65*, 400.
(641) Nagata, Y.; Watanabe, Y.; Fujita, S.; Dohmaru, T.; Taniguchi, S. *J. Chem. Soc., Chem. Commun.* **1992**, 1620.
(642) Fujimoto, T.; Mizukoshi, Y.; Oshima, R.; Nagata, Y.; Maeda, Y. *Trans. Mater. Res. Soc. Jpn.* **2000**, *25*, 95.
(643) Maeda, Y.; Mizukoshi, Y.; Takagi, E.; Fujimoto, T.; Oshima, R.; Nagata, Y. *Trans. Mater. Res. Soc. Jpn.* **2000**, *25*, 99.
(644) Caruso, R. A.; Ashokkumar, M.; Grieser, F. *Colloids Surf., A* **2000**, *169*, 219.
(645) Fujimoto, T.; Terauchi, S.; Umehara, H.; Kojima, I.; Henderson, W. *Chem. Mater.* **2001**, *13*, 1057.
(646) Mizukoshi, Y.; Takagi, E.; Okuno, H.; Oshima, R.; Maeda, Y.; Nagata, Y. *Ultrason. Sonochem.* **2001**, *8*, 1.
(647) Fujimoto, T.; Mizukoshi, Y.; Nagata, Y.; Maeda, Y.; Oshima, R. *Scr. Mater.* **2001**, *44*, 2183.
(648) Takagi, E.; Mizukoshi, Y.; Oshima, R.; Nagata, Y.; Bandow, H.; Maeda, Y. *Stud. Surf. Sci. Catal.* **2001**, *132*, 335.
(649) Bradley, J. S.; Hill, E. W.; Behal, S.; Klein, C.; Chaudret, B.; Duteil, A. *Chem. Mater.* **1992**, *4*, 1234.
(650) De Caro, D.; Bradley, J. S. *New J. Chem.* **1998**, *22*, 1267.
(651) Duteil, A.; Queau, R.; Chaudret, B.; Mazel, R.; Roucau, C.; Bradley, J. S. *Chem. Mater.* **1993**, *5*, 341.
(652) Bradley, J. S.; Millar, J. M.; Hill, E. W.; Behal, S.; Chaudret, B.; Duteil, A. *Faradays Discuss.* **1991**, *92*, 255.
(653) Duteil, A.; Queau, R.; Chaudret, B.; Mazel, R.; Roucau, C.; Bradley, J. S. *Chem. Mater.* **1993**, *5*, 341.
(654) Bradley, J. S.; Millar, J. M.; Hill, E. W.; Behal, S.; Chaudret, B.; Duteil, A. *Faradays Discuss.* **1991**, *92*, 255.
(655) De Caro, D.; Bradley, J. S. *Langmuir* **1997**, *13*, 3067.
(656) Ould Ely, T.; Amiens, C.; Chaudret, B.; Snoeck, E.; Verelst, M.; Respaud, M.; Broto, J. M. *Chem. Mater.* **1999**, *11*, 526.
(657) De Caro, D.; Agelou, V.; Duteil, A.; Chaudret, B.; Mazel, R.; Roucau, C.; Bradley, J. S. *New J. Chem.* **1995**, *19*, 1265.
(658) Osuna, J.; De Caro, D.; Amiens, C.; Chaudret, B.; Snoeck, E.; Respaud, M.; Broto, J. M.; Fert, A. *J. Phys. Chem.* **1996**, *100*, 14571.
(659) Klabunde, K. J.; Cardenas-Trevino, G. In *Active Metals: Preparation, Characterization, Applications*; Furstner, A., Ed.; VCH: New York, 1996; pp 237−278.
(660) Klabunde, K. J. *Platinum Met. Rev.* **1992**, *36*, 80.
(661) Lin, S. T.; Franklin, M. T.; Klabunde, K. J. *Langmuir* **1986**, *2*, 259.
(662) Cardenas-Trivino, G.; Klabunde, K. J.; Brock Dale, E. *Langmuir* **1987**, *3*, 986.
(663) Kilner, M.; Mason, N.; Lambrick, D.; Hooker, P. D.; Timms, P. L. *J. Chem. Soc., Chem. Commun.* **1987**, 356.
(664) Bradley, J. S.; Hill, E.; Leonowicz, M. E.; Witzke, H. *J. Mol. Catal.* **1987**, *41*, 59.
(665) Devenish, R. W.; Goulding, T.; Heaton, B. T.; Whyman, R. *J. Chem. Soc., Dalton Trans.* **1996**, 673.
(666) Collier, P. J.; Iggo, J. A.; Whyman, R. *J. Mol. Catal. A: Chem.* **1999**, *146*, 149.
(667) Cardenas, G. T.; Oliva, R. C. *Mater. Res. Bull.* **2000**, *35*, 2227.
(668) Reetz, M. T.; Helbig, W.; Quaiser, S. A. In *Active Metals: Preparation, Characterization, Applications*; Furstner, A., Ed.; VCH: New York, 1996; pp 279−297.
(669) Reetz, M. T.; Helbig, W. *J. Am. Chem. Soc.* **1994**, *116*, 7401.
(670) Reetz, M. T.; Quaiser, S. A. *Angew. Chem., Int. Ed. Engl.* **1995**, *34*, 2240.
(671) Shiraishi, Y.; Ikenaga, D.; Toshima, N. *Aust. J. Chem.* **2003**, *56* (10), 1025.
(672) Hirai, H.; Yakurat, N. *Polym. Adv. Technol.* **2001**, *12* (11−12), 724.

(673) Pellegatta, J. L.; Blandy, C.; Colliere, V.; Choukroun, R.; Chaudret, B.; Cheng, P.; Philippot, K. *J. Mol. Catal. A: Chem.* **2002**, *178* (1−2), 55.
(674) Borsla, A.; Wilhelm, A. M.; Delmas, H. *Catal. Today* **2001**, *66* (2−4), 389.
(675) Sidorov, S. N.; Volkov, I. V.; Davankov, V. A.; Tsyurupa, M. P.; Valetsky, P. M.; Bronstein, L. M.; Karlinsey, R.; Zwanziger, J. W.; Matveeva, V. G.; Sulman, E. M.; Lakina, N. V.; Wilder, E. A.; Spontak, R. J. *J. Am. Chem. Soc.* **2001**, *123* (43), 10502.
(676) Lakina, N. V.; Sul'man, E. M.; Matveeva, V. G.; Mikhailov, I. A. *Pharm. Chem. J.* **2000**, *34* (3), 138.
(677) Sulman, E.; Lakina, N.; Sulman, M.; Ankudinova, T.; Matveeva, V.; Sidorov, A.; Sidorov, S. *Stud. Surf. Sci. Catal.* **2000**, *130B*, 1787.
(678) Semagina, N. V.; Bykov, A. V.; Sulman, E. M.; Matveeva, V. G.; Sidorov, S. N.; Dubrovina, L. V.; Valetsky, P. M.; Kiselyova, O. I.; Khokhlov, A. R.; Stein, B.; Bronstein, L. M. *J. Mol. Catal. A: Chem.* **2004**, *208* (1−2), 273.
(679) Lu, Z.; Liu, G.; Phillips, H.; Hill, J. M.; Chang, J.; Kydd, R. A. *Nano Lett.* **2001**, *1* (12), 683.
(680) Bronstein, L. M.; Chernyshov, D. M.; Volkov, I. O.; Ezernitskaya, M. G.; Valetsky, P. M.; Matveeva, V. G.; Sulman, E. M. *J. Calal.* **2000**, *196* (2), 302.
(681) Sulman, E.; Bodrova, Y..; Matveeva, V.; Semagina, N.; Cerveny, L.; Kurtc, V.; Bronstein, L.; Platonova, O.; Valetsky, P. *Appl. Catal. A: Gen.* **1999**, *176* (1), 75.
(682) Esumi, K.; Isono, R.; Yoshimura, T. *Langmuir* **2004**, *20* (1), 237.
(683) Pittelkow, M.; Moth-Poulsen, K.; Boas, U.; Christensen, J. B. *Langmuir* **2003**, *19* (18), 7682.
(684) Hayakawa, K.; Yoshimura, T.; Esumi, K. *Langmuir* **2003**, *19* (13), 5517.
(685) Scott, R. W. J.; Datye, A. K.; Crooks, R. M. *J. Am. Chem. Soc.* **2003**, *125* (13), 3708.
(686) Rahim, E. H.; Kamounah, F. S.; Frederiksen, J.; Christensen, J. B. *Nano Lett.* **2001**, *1* (9), 499.
(687) Crooks, R. M.; Lemon, B. I., III; Sun, L.; Yeung, L. K.; Zhao, M. *Topics Curr. Chem.* **2001**, *212*, 81.
(688) Mevellec, V.; Roucoux, A.; Ramirez, E.; Philippot, K.; Chaudret, B. *Adv. Synth. Catal.* **2004**, *346* (1), 72.
(689) Yonezawa, T.; Toshima, N.; Wakai, C.; Nakahara, M.; Nishinaka, M.; Tominaga, T.; Nomura, H. *Colloids Surf. A: Physicochem. Eng. Asp.* **2000**, *169* (1−3), 35.
(690) Schulz, J.; Roucoux, A.; Patin, H. *Chem. Eur. J.* **2000**, *6* (4), 618.
(691) Aiken, J. D., III; Finke, R. G. *J. Mol. Catal. A: Chem.* **1999**, *145*, 1.
(692) Lin, Y.; Finke, R. G. *J. Am. Chem. Soc.* **1994**, *116*, 8335.
(693) Schmid, G.; Pfeil, R.; Boese, R.; Bandermann, F.; Meyers, S.; Calis, G. H. M.; Van Der Velden, J. W. A. *Chem. Ber.* **1981**, *114*, 3634.
(694) Amiens, C.; De Caro, D.; Chaudret, B.; Bradley, J. S.; Mazel, R.; Roucau, C. *J. Am. Chem. Soc.* **1993**, *115*, 11638.
(695) Duteil, A.; Schmid, G.; Meyer-Zaika, W. *J. Chem. Soc., Chem. Commun.* **1995**, 31.
(696) Dassenoy, F.; Philippot, K.; Ould Ely, T.; Amiens, C.; Lecante, P.; Snoeck, E.; Mosset, A.; Casanove, M. J.; Chaudret, B. *New J. Chem.* **1998**, *22*, 703.
(697) Chen, S.; Kimura, K. *J. Phys. Chem. B* **2001**, *105*, 5397.
(698) Schmid, G.; Morun, B.; Malm, J. O. *Angew. Chem., Int. Ed. Engl.* **1989**, *28*, 778.
(699) Schmid, G.; Maihack, V.; Lantermann, F.; Peschel, S. *J. Chem. Soc., Dalton Trans.* **1996**, 589.
(700) Schmid, G.; Emde, S.; Maihack, V.; Meyer-Zaika, W.; Peschel, S. *J. Mol. Catal. A: Chem.* **1996**, *107*, 95.
(701) Moreno-Manas, M.; Pleixats, R.; Villarroya, S. *Organometallics* **2001**, *20* (22), 4524.
(702) Kogan, V.; Aizenshtat, Z.; Popovitz-Biro, R.; Neumann, R. *Org. Lett.* **2002**, *4* (20), 3529.
(703) Liu, Y.; Khemtong, C.; Hu, J. *Chem. Commun.* **2004**, *4*, 398.
(704) Gopidas, K. R.; Whitesell, J. K.; Fox, M. A. *Nano Lett.* **2003**, *3* (12), 1757.
(705) Na, Y.; Park, S.; Han, S. B.; Han, H.; Ko, S.; Chang, S. *J. Am. Chem. Soc.* **2004**, *126* (1), 250.
(706) Thathagar, M. B.; Beckers, J.; Rothenberg, G. *J. Am. Chem. Soc.* **2002** *124* (40), 11858.
(707) Sanji, T.; Ogawa, Y.; Nakatsuka, Y.; Tanaka, M.; Sakurai, H. *Chem. Lett.* **2003**, *32* (10), 980.
(708) Calo, V.; Nacci, A.; Monopoli, A.; Detomaso, A.; Iliade, P. *Organometallics* **2003**, *22* (21), 4193.
(709) Calo, V.; Nacci, A.; Monopoli, A.; Laera, S.; Cioffi, N. *J. Org. Chem.* **2003**, *68* (7), 2929.
(710) Yeung, L. K.; Crooks, R. M. *Nano Lett.* **2001**, *1* (1), 14.
(711) Tsai, S. H.; Liu, Y. H.; Wu, P. L.; Yeh, C. S. *J. Mater. Chem.* **2003**, *13* (5), 978.
(712) Sharma, R. K.; Sharma, P.; Maitra, A. *J. Coll. Interface Sci.* **2003**, *265* (1), 134.
(713) Clint, J. H.; Collins, I. R.; Williams, J. A.; Robinson, B. H.; Towey, T. F.; Cajean, P.; Khan-Lodhi, A. *Faraday Discuss.* **1993**, *95*, 219.
(714) Freund, P. L.; Spiro, M. *J. Phys. Chem.* **1985**, *89*, 1074.
(715) Freund, P. L.; Spiro, M. *J. Chem. Soc., Faraday Trans. 1* **1986**, *82*, 2277.
(716) Ohde, H.; Ohde, M.; Wai, C. M. *Chem. Commun.* **2004**, *8*, 930.
(717) Fonseca, G. S.; Umpierre, A. P.; Fichtner, P. F. P.; Teixeira, S. R.; Dupont, J. *Chem. Eur. J.* **2003**, *9* (14), 3263.
(718) Adlim, M.; Abu Bakar, M.; Liew, K. Y.; Ismail, J. *J. Mol. Catal. A: Chem.* **2004**, *212* (1−2), 141.
(719) Semagina, N. V.; Bykov, A. V.; Sulman, E. M.; Matveeva, V. G.; Sidorov, S. N.; Dubrovina, L. V.; Valetsky, P. M.; Kiselyova, O. I.; Khokhlov, A. R.; Stein, B.; Bronstein, L. M. *J. Mol. Catal. A: Chem.* **2004**, *208* (1−2), 273.
(720) Anderson, K.; Cortinas Fernandez, S.; Hardacre, C.; Marr, P. C. *Inorg. Chem. Commun.* **2003**, *7* (1), 73.
(721) Spiro, M.; De Jesus, D. *Langmuir* **2000**, *16* (6), 2464.
(722) De Jesus, D.; Spiro, M. *Langmuir* **2000**, *16* (11), 4896.
(723) Shiraishi, Y.; Toshima, N. *Colloids Surf. A: Physicochem. Eng. Asp.* **2000**, *169* (1−3), 59.
(724) Shiraishi, Y.; Toshima, N. *J. Mol. Catal. A: Chem.* **1999**, *141*, 187.
(725) Shiraishi, Y.; Toshima, N. *Colloids Surf. A* **2000**, *169*, 59.
(726) Launay, F.; Patin, H. *New J. Chem.* **1997**, *21*, 247.
(727) Launay, F.; Roucoux, A.; Patin, H. *Tetrahedron Lett.* **1998**, *39*, 1353.
(728) Johnson, Brian, F. G. *Top. Catal.* **2003**, *24* (1−4), 147.
(729) Corain, B.; Centomo, P.; Lora, S.; Kralik, M. *J. Mol. Catal. A: Chem.* **2003**, *204−205*, 755.
(730) Wieckowski, A.; Savinova, E. R.; Vayenas, C. G. *Catal. Electrocatal. Nano. Surf.* **2003**, 847.
(731) Santra, A. K.; Goodman, D. W. *Catal. Electrocatal. Nano. Surf.* **2003**, 281.
(732) Haruta, M. *Chem. Rec.* **2003**, *3* (2), 75.
(733) Bell, A. T. *Science* **2003**, *299* (5613), 1688.
(734) Thomas, J. M.; Johnson, B. F. G.; Raja, R.; Sankar, G.; Midgley, P. A. *Acc. Chem. Res.* **2003**, *36* (1), 20.
(735) Somorjai, G. A.; Borodko, Y. G. *Catal. Lett.* **2001**, *76* (1−2), 1.
(736) Rupprechter, G.; Freund, H.-J. *Top. Catal.* **2001**, *14* (1−4), 3.
(737) Eppler, A.; Rupprechter, G.; Guczi, L.; Somorjai, G. A. *J. Phys. Chem. B* **1997**, *101* (48), 9973.
(738) Liu, Z.; Ling, X. Y.; Su, X.; Lee, J. Y. *J. Phys. Chem. B* **2004**, *108*, 8234.
(739) Bulushev, D. A.; Yuranov, I.; Suvorova, E. I.; Buffat, P. A.; Kiwi-Minsker, L. *J. Catal.* **2004**, *224* (1), 8.
(740) Lopez, N.; Janssens, T. V. W.; Clausen, B. S.; Xu, Y.; Mavrikakis, M.; Bligaard, T.; Norskov, J. K. *J. Catal.* **2004**, *223* (1), 232.
(741) Chen, S.; Kucernak, A. *J. Phys. Chem. B*, **2004**, *108* (10), 3262.
(742) Liu, Z.; Lee, J. Y.; Chen, W.; Han, M.; Gan, L. M. *Langmuir* **2004**, *20* (1), 181.
(743) Liu, Z.; Ling, X. Y.; Lee, J. Y.; Su, X.; Gan, L. M. *J. Mater. Chem.* **2003**, *13* (12), 3049.
(744) Nakagawa, K.; Yamagishi, M.; Nishimoto, H.; Ikenaga, N.; Suzuki, T.; Kobayashi, T.; Nishitani-Gamo, M.; Ando, T. *Chem. Mater.* **2003**, *15* (24), 4571.
(745) Fachini, E. R.; Diaz-Ayala, R.; Casado-Rivera, E.; File, S.; Cabrera, C. R. *Langmuir* **2003**, *19* (21), 8986.
(746) Takasu, Y.; Itaya, H.; Kawaguchi, T.; Sugimoto, W.; Murakami, Y. *Stud. Surf. Sci. Catal.* **2003**, *145*, 279.
(747) Li, F.; Zou, J.; Yuan, G. *Catal. Lett.* **2003**, *89* (1−2), 115.
(748) Dubau, L.; Coutanceau, C.; Garnier, E.; Leger, J.-M.; Lamy, C. *J. Appl. Electrochem.* **2003**, *33* (5), 419.
(749) Carrettin, S.; McMorn, P.; Johnston, P.; Griffin, K.; Kiely, C. J.; Hutchings, G. J. *Phys. Chem. Chem. Phys.* **2003**, *5* (6), 1329.
(750) Boudjahem, A. G.; Monteverdi, S.; Mercy, M.; Bettahar, M. M. *J. Catal.* **2004**, *221* (2), 325.
(751) Anderson, K.; Cortinas Fernandez, S.; Hardacre, C.; Marr, P. C. *Inorg. Chem. Commun.* **2003**, *7* (1), 73.
(752) Yang, C.; Kalwei, M.; Schuth, F.; Chao, K. *Appl. Catal. A: Gen.* **2003**, *254* (2), 289.
(753) Khodakov, A. Y.; Bechara, R.; Griboval-Constant, A. *Appl. Catal. A: Gen.* **2003**, *254* (2), 273.
(754) Lang, H.; May, R. A.; Iversen, B. L.; Chandler, B. D. *J. Am. Chem. Soc.* **2003**, *125* (48), 14832.
(755) Komatsu, T.; Inaba, K.; Uezono, T.; Onda, A.; Yashima, T. *Appl. Catal. A: Gen.* **2003**, *251* (2), 315.
(756) Bianchini, C.; Dal Santo, V.; Meli, A.; Moneti, S.; Moreno, M.; Oberhauser, W.; Psaro, R.; Sordelli, L.; Vizza, F. *J. Catal.* **2003**, *213* (1), 47.
(757) Marchetti, S. G.; Cagnoli, M. V.; Alvarez, A. M.; Bengoa, J. F.; Gallegos, N. G.; Yeramian, A. A.; Mercader, R. C. *Hyperfine Interact.* **2002**, *139/140* (1−4/1−4), 33.
(758) Horvath, A.; Beck, A.; Koppany, Z.; Sarkany, A.; Guczi, L. *J. Mol. Catal. A: Chem.* **2002**, *182−183*, 295.
(759) Balint, I.; Miyazaki, A.; Aika, K. *Phys. Chem. Chem. Phys.* **2004**, *6* (9), 2000.
(760) Marconi, G.; Pertici, P.; Evangelisti, C.; Caporusso, A. M.; Vitulli, G.; Capannelli, G.; Hoang, M.; Turney, T. W. *J. Organomet. Chem.* **2004**, *689* (3), 639.
(761) Miyazaki, A.; Balint, I.; Nakano, Y. *J. Nano. Res.* **2003**, *5* (1−2), 69.

(762) Yoo, J. W.; Hathcock, D. J.; El-Sayed, M. A. *J. Catal.* **2003**, *214* (1), 1.
(763) Balint, I.; Miyazaki, A.; Aika, K. *Chem. Commun.* **2002**, *10*, 1044.
(764) Balint, I.; Miyazaki, A.; Aika, K. *J. Catal.* **2002**, *207* (1), 66.
(765) Ingelsten, H. H.; Beziat, J.; Bergkvist, K.; Palmqvist, A.; Skoglundh, M.; Hu, Q.; Falk, L. K. L.; Holmberg, K. *Langmuir* **2002**, *18* (5), 1811.
(766) Miyazaki, A.; Balint, I.; Aika, K.; Nakano, Y. *Chem. Lett.* **2001**, *12*, 1332.
(767) Yoo, J. W.; Hathcock, D.; El-Sayed, M. A. *J. Phys. Chem. A* **2002**, *106* (10), 2049.
(768) Konova, P.; Naydenov, A.; Venkov, Cv.; Mehandjiev, D.; Andreeva, D.; Tabakova, T. *J. Mol. Catal. A: Chem.* **2004**, *213* (2), 235.
(769) Mallick, K.; Scurrell, M. S. *Appl. Catal. A: Gen.* **2003**, *253* (2), 527.
(770) Guczi, L.; Beck, A.; Horvath, A.; Koppany, Zs.; Stefler, G.; Frey, K.; Sajo, I.; Geszti, O.; Bazin, D.; Lynch, J. *J. Mol. Catal. A: Chem.* **2003**, *204*−*205*, 545.
(771) Ishiguro, A.; Nakajima, T.; Iwata, T.; Fujita, M.; Minato, T.; Kiyotaki, F.; Izumi, Y.; Aika, K.; Uchida, M.; Kimoto, K.; Matsui, Y.; Wakatsuki, Y. *Chem. Eur. J.* **2002**, *8* (14), 3260.
(772) Bowker, M.; Stone, P.; Bennett, R.; Perkins, N. *Surf. Sci.* **2002**, *511* (1−3), 435.
(773) Claus, P.; Hofmeister, H. *J. Phys. Chem. B* **1999**, *103* (14), 2766.
(774) Toshima, N.; Ohtaki, M.; Teranishi, T. *React. Polym.* **1991**, *15*, 135.
(775) Hirai, H.; Ohtaki, M.; Komiyama, M. *Chem. Lett.* **1986**, 269.
(776) Hirai, H.; Ohtaki, M.; Komiyama, M. *Chem. Lett.* **1987**, 149.
(777) Ohtaki, M.; Toshima, N.; Komiyama, M.; Hirai, H. *Bull. Chem. Soc. Jpn.* **1990**, *63*, 1433.
(778) Suzuki, K.; Yumura, T.; Mizuguchi, M.; Tanaka, Y.; Chen, C.-W.; Akashi, M. *J. Appl. Polym. Sci.* **2000**, *77*, 2678.
(779) Chen, C.-W.; Chen, M.-Q.; Serizawa, T.; Akashi, M. *Chem. Commun.* **1998**, 831.
(780) Chen, C.-W.; Serizawa, T.; Akashi, M. *Chem. Mater.* **1999**, *11*, 1381.
(781) Greci, M. T.; Pathak, S.; Mercado, K.; Prakash, G. K. S.; Thompson, M. E.; Olah, G. A. *J. Nanosci. Nanotechnol.* **2001**, *1* (1), 3.
(782) Jacobs, P. W.; Wind, S. J.; Ribeiro, F. H.; Somorjai, G. A. *Surf. Sci.* **1997**, *372* (1−3), L249.
(783) Somorjai, G. A. *Appl. Surf. Sci.* **1997**, *121*/*122*, 1.
(784) Eppler, A.; Rupprechter, G.; Guczi, L.; Somorjai, G. A. *J. Phys. Chem. B*, **1997**, *101* (48), 9973.
(785) Yang, M. X.; Gracias, D. H.; Jacobs, P. W.; Somorjai, G. A. *Langmuir* **1998**, *14* (6), 1458.
(786) Avoyan, A.; Rupprechter, G.; Eppler, A. S.; Somorjai, G. A. *Top. Catal.* **2000**, *10* (1, 2), 107.
(787) Eppler, A. S.; Rupprechter, G.; Anderson, E. A.; Somorjai, G. A. *J. Phys. Chem. B* **2000**, *104* (31), 7286.
(788) Eppler, A. S.; Zhu, J.; Anderson, E. A.; Somorjai, G. A. *Top. Catal.* **2000**, *13* (1, 2), 33.
(789) Grunes, J.; Zhu, J.; Anderson, E. A.; Somorjai, G. A. *J. Phys. Chem. B* **2002**, *106* (44), 11463.
(790) Anderson, M. L.; Stroud, R. M.; Rolison, D. R. *Nano Lett.* **2002**, *2* (3), 235.
(791) Pietron, J. J.; Stroud, R. M.; Rolison, D. R. *Nano Lett.* **2002**, *2* (5), 545.
(792) Long, J. W.; Stroud, R. M.; Swider-Lyons, K. E.; Rolison, D. R. *J. Phys. Chem. B* **2000**, *104*, 9772.
(793) Moore, J. T.; Corn, J. D.; Chu, D.; Jiang, R.; Boxall, D. L.; Kenik, E. A.; Lukehart, C. M. *Chem. Mater.* **2003**, *15* (17), 3320.
(794) Moore, J. T.; Chu, D.; Jiang, R.; Deluga, G. A.; Lukehart, C. M. *Chem. Mater.* **2003**, *15* (5), 1119.
(795) Okumura, M.; Nakamura, S.; Tsubota, S.; Nakamura, T.; Azuma, M.; Haruta, M. *Catal. Lett.* **1998**, *51* (1, 2), 53.
(796) Aberdam, D.; Durand, R.; Faure, R.; Gloaguen, F.; Hazemann, J. L.; Herrero, E.; Kabbabi, A.; Ulrich, O. *J. Electroanal. Chem.* **1995**, *398*, (1−2), 43.
(797) Kozlov, A. I.; Kozlova, A. P.; Asakura, K.; Matsui, Y.; Kogure, T.; Shido, T.; Iwasawa, Y. *J. Catal.* **2000**, *196*, (1), 56.
(798) Okumura, M.; Haruta, M. *Chem. Lett.* **2000**, *4*, 396.
(799) Sayo, K.; Deki, S.; Hayashi, S. *J. Mater. Chem.* **1999**, *9*, (4), 937.
(800) Akita, T.; Tanaka, K.; Okuma, K.; Koyanagi, T.; Haruta, M. *J. Electron Microsc.* **2001**, *50*, (6), 473.
(801) Van Craenenbroeck, J.; Andreeva, D.; Tabakova, T.; Van Werde, K.; Mullens, J.; Verpoort, F. *J. Catal.* **2002**, *209*, (2), 515.
(802) Yang, C.-m.; Kalwei, M.; Schuth, F.; Chao, K.-j. *Appl. Catal. A: Gen.* **2003**, *254*, (2), 289.
(803) Biella, S.; Porta, F.; Prati, L.; Rossi, M. *Catal. Lett.* **2003**, *90*, (1−2), 23.
(804) Yadav, O. P.; Palmqvist, A.; Cruise, N.; Holmberg, K. *Colloids Surf. A: Physicochem. Eng. Asp.* **2003**, *221*, (1−3), 131.
(805) Carrettin, S.; McMorn, P.; Johnston, P.; Griffin, K.; Kiely, C. J.; Hutchings, G. J. *Phys. Chem. Chem. Phys.* **2003**, *5*, (6), 1329.
(806) Andreeva, D.; Nedyalkova, R.; Ilieva, L.; Abrashev, M. V. *Appl. Catal.: Gen.* **2003**, *246*, (1), 29.
(807) Johannessen, T.; Koutsopoulos, S. *J. Catal.* **2002**, *205*, (2), 404.
(808) Long, J. W.; Stroud, R. M.; Swider-Lyons, K. E.; Rolison, D. R. *J. Phys. Chem. B* **2000**, *104*, 9772.
(809) Lyman, C. E.; Lakis, R. E.; Stenger, H. G., Jr. *Ultramicroscopy* **1995**, *58* (1), 25.
(810) Lai, S. Y.; Zhang, H.; Ng, C. F. *Catal. Lett.* **2004**, *92* (3−4), 107.
(811) Yin, S.; Xu, B.; Ng, C.; Au, C. *Appl. Catal. B: Environ.* **2004**, *48* (4), 237.
(812) Delpeux, S.; Szostak, K.; Frackowiak, E.; Bonnamy, S.; Beguin, F. *J. Nanosci. Nanotechnol.* **2002**, *2* (5), 481.
(813) Shenhar, R.; Rotello, V. M. *Acc. Chem. Res.* **2003**, *36* (7), 549.
(814) Thomas, K. G.; Kamat, P. V. *Acc. Chem. Res.* **2003**, *36* (12), 888.
(815) Wallraff, G. M.; Hinsberg, W. D. *Chem. Rev.* **1999**, *99* (7), 1801.
(816) Xia, Y.; Rogers, J. A.; Paul, K. E.; Whitesides, G. M. *Chem. Rev.* **1999**, *99* (7), 1823.
(817) Shipway, A. N.; Lahav, M.; Willner, I. *Adv. Mater.* **2000**, *12* (13), 993.
(818) Schrtl, W. *Adv. Mater.* **2000**, *12* (24), 1899.
(819) Haynes, C. L.; Van Duyne, R. P. *J. Phys. Chem. B* **2001**, *105* (24), 5599.
(820) Penner, R. M. *Acc. Chem. Res.* **2000**, *33* (2), 78.
(821) Wise, F. W. *Acc. Chem. Res.* **2000**, *33* (11), 773.
(822) Markovich, G.; Collier, C. P.; Henrichs, S. E.; Remacle, F.; Levine, R. D.; Heath, J. D. *Acc. Chem. Res.* **1999**, *32* (5), 415.
(823) Law, M.; Goldberger, J.; Yang, P. *Annu. Rev. Mater. Res.* **2004**, *34*, 83.
(824) Steigerwald, M. L.; Brus, L. E. *Annu. Rev. Mater. Sci.* **1989**, *19*, 471.
(825) Collier, C. P.; Vossmeyer, T.; Heath, J. R. *Annu. Rev. Phys. Chem.* **1998**, *49*, 371.
(826) Andrews, R.; Jacques, D.; Qian, D.; Rantell, T. *Acc. Chem. Res.* **2002**, *35* (12), 1008.
(827) Ebbesen, T. W. *Acc. Chem. Res.* **1998**, *31* (9), 558.
(828) Khabashesku, V. N.; Billups, W. E.; Margrave, J. L. *Acc. Chem. Res.* **2002**, *35* (12), 1087.
(829) Ebbesen, T. S. *Annu. Rev. Mater. Sci.* **1994**, *24*, 235.
(830) Dresselhaus, M. S.; Dresselhaus, G. *Annu. Rev. Mater. Sci.* **1995**, *25*, 487.
(831) Ajayan, P. M. *Chem. Rev.* **1999**, *99* (7), 1787.
(832) Dai, H.; Kong, J.; Zhou, C.; Franklin, N.; Tombler, T.; Cassell, A.; Fan, S.; Chapline, M. *J. Phys. Chem. B* **1999**, *103* (51), 11246.
(833) Sastry, M.; Rao, M.; Ganesh, K. N. *Acc. Chem. Res.* **2002**, *35* (10), 847.
(834) Daniel, M.-C.; Astruc, D. *Chem. Rev.* **2004**, *104* (1), 293.
(835) Maier, S. A.; Brongersma, M. L.; Kik, P. G.; Meltzer, S.; Requicha, A. A. G.; Atwater, H. A. *Adv. Mater.* **2001**, *13* (19), 1501.
(836) Kamat, P. V. *J. Phys. Chem. B* **2002**, *106* (32), 7729.
(837) Voisin, C.; Fatti, N. D.; Christofilos, D.; Vallee, F. *J. Phys. Chem. B* **2001**, *105* (12), 2264.
(838) Pileni, M. P. *J. Phys. Chem. B* **2001**, *105* (17), 3358.
(839) Xia, Y.; Yang, P.; Sun, Y.; Wu, Y.; Mayers, B.; Gates, B.; Yin, Y.; Kim, F.; Yan, H. *Adv. Mater.* **2003**, *15* (5), 353.
(840) El-Sayed, M. A. *Acc. Chem. Res.* **2004**, *37* (5), 326.
(841) Williams, R. S.; Medeiros-Ribeiro, G.; Kamins, T. I.; Ohlberg, D. A. A. *Acc. Chem. Res.* **1999**, *32* (5), 425.
(842) Empedocles, S.; Bawendi, M. *Acc. Chem. Res.* **1999**, *32* (5), 389.
(843) Roy, D.; Fendler, J. *Adv. Mater.* **2004**, *16* (6), 479.
(844) Skolnick, M. S.; Mowbray, D. J. *Annu. Rev. Mater. Res.* **2004**, *34*, 181.
(845) Banin, U.; Millo, O. *Annu. Rev. Phys. Chem.* **2003**, *54*, 465.
(846) Lifshitz, E.; Fradkin, L.; Glozman, A.; Langof, L. *Annu. Rev. Phys. Chem.* **2004**, *55*, 509.
(847) Empedocles, S. A.; Neuhauser, R.; Shimizu, K.; Bawendi, M. G. *Adv. Mater.* **1999**, *11* (5), 1243.
(848) Pesika, N. S.; Stebe, K. J.; Searson, P. C. *Adv. Mater.* **2003**, *15* (15), 1289.
(849) Eychmller, A. *J. Phys. Chem. B* **2000**, *104* (28), 6514.
(850) Lifshitz, E.; Glozman, A.; Litvin, I. D.; Porteanu, H. *J. Phys. Chem. B* **2000**, *104* (45), 10449.
(851) Sloan, J.; Kirkland, A. I.; Hutchison, J. L.; Green, M. L. H. *Acc. Chem. Res.* **2002**, *35* (12), 1054.
(852) Dai, H. *Acc. Chem. Res.* **2002**, *35* (12), 1035.
(853) Fischer, J. E. *Acc. Chem. Res.* **2002**, *35* (12), 1079.
(854) Avouris, P. *Acc. Chem. Res.* **2002**, *35* (12), 1026.
(855) Charlier, J. C. *Acc. Chem. Res.* **2002**, *35* (12), 1063.
(856) Ouyang, M.; Huang, J.-L.; Lieber, C. M. *Acc. Chem. Res.* **2002**, *35* (12), 1018.
(857) Zhou, O.; Shimoda, H.; Gao, B.; Oh, S.; Fleming, L.; Yue, G. *Acc. Chem. Res.* **2002**, *35* (12), 1045.
(858) Niyogi, S.; Hamon, M. A.; Hu, H.; Zhao, B.; Bhowmik, P.; Sen, R.; Itkis, M. E.; Haddon, R. C. *Acc. Chem. Res.* **2002**, *35* (12), 1105.
(859) Dresselhaus, M. S.; Dresselhaus, G.; Jorio, A.; Filho, A. G. S.; Pimenta, M. A.; Saito, R. *Acc. Chem. Res.* **2002**, *35* (12), 1070.
(860) Bernholc, J.; Brenner, D.; Nardelli, M. B.; Meunier, V.; Roland, C. *Annu. Rev. Mater. Res.* **2002**, *32*, 347.
(861) Terrones, M. *Annu. Rev. Mater. Res.* **2003**, *33*, 419.
(862) Dresselhaus, M. S.; Dresselhaus, G.; Jorio, A. *Annu. Rev. Mater. Res.* **2004**, *34*, 247.

(863) Subramoney, S. *Adv. Mater.* **1998**, *10* (15), 1157.
(864) Odom, T. W.; Huang, J.-L.; Kim, P.; Lieber, C. M. *J. Phys. Chem. B* **2000**, *104* (13), 2794.
(865) Poncharal, P.; Berger, C.; Yi, Y.; Wang, Z. L.; de Heer, W. A. *J. Phys. Chem. B* **2002**, *106* (47), 12104.
(866) Masala, O.; Seshadri, R. *Annu. Rev. Mater. Res.* **2004**, *34*, 41.
(867) Wang, Z. L. *Annu. Rev. Phys. Chem.* **2004**, *55*, 159.
(868) Chakraborty, A. K.; Golumbfskie, A. J. *Annu. Rev. Phys. Chem.* **2001**, *52*, 537.
(869) McCarty, G. S.; Weiss, P. S. *Chem. Rev.* **1999**, *99* (7), 1983.
(870) Wang, Z. L. *Adv. Mater.* **1998**, *10* (1), 13.
(871) Caruso, F. *Adv. Mater.* **2001**, *13* (1), 11.
(872) Herron, N.; Thorn, D. L. *Adv. Mater.* **1998**, *10* (15), 1173.
(873) Cahen, D.; Hodes, G. *Adv. Mater.* **2002**, *14* (11), 789.
(874) Wang, Z. L. *Adv. Mater.* **2003**, *15* (18), 1497.
(875) Wang, Z. L. *J. Phys. Chem. B* **2000**, *104* (6), 1153.
(876) Liz-Marzn, L. M.; Mulvaney, P. *J. Phys. Chem. B* **2003**, *107* (30), 7312.
(877) Feldheim, D. L.; Foss, C. A., Jr. *Metal Nanoparticles: Synthesis, Characterization, and Applications*; Dekker: New York, 2002.
(878) Klimov, V. I. *Semiconductor and Metal Nanocrystals: Synthesis and Electronic and Optical Properties*; Dekker: New York, 2004.
(879) Efros, A. L.; Lockwood, D. J.; Tsybeskov, L. *Semiconductor Nanocrystals: From Basic Principles to Applications*; Kluwer Academic/Plenum Publishers: New York, 2003.
(880) Bandyopadhyay, S.; Nalwa, H. S. *Quantum Dots and Nanowires*; American Scientific Publishers: Stevenson Ranch, CA, 2003.
(881) Borovitskaya, E.; Shur, M. S. *Quantum Dots*; World Scientific: River Edge, NJ, 2002.
(882) Sadowski, M. L.; Potemski, M.; Grynberg, M. *Optical Properties of Semiconductor Nanostructures*; Kluwer Academic: Dordrecht, The Netherlands, 2000.
(883) Chakraborty, T. *Quantum Dots: a Survey of the Properties of Artificial Atoms*; Elsevier: Amsterdam, The Netherlands, 1999.
(884) Bimberg, D.; Grundmann, M.; Ledentsov, N. N. *Quantum Dot Heterostructures*; Wiley: Chichester, U.K., 1999.
(885) Jacak, L.; Hawrylak, P.; Wis, A. *Quantum Dots*; Springer: Berlin, Germany, 1998.
(886) Byai, L.; Koch, S. W. *Semiconductor Quantum Dots*; World Scientific: Singapore, 1993.
(887) Kamat, P. V.; Meisel, D. *Semiconductor Nanoclusters—Physical, Chemical, and Catalytic Aspects*; Elsevier: Amsterdam, The Netherlands, 1997.
(888) Wang, Z. L.; Hui, C. *Electron Microscopy of Nanotubes*: Kluwer Academic Publishers: Boston, MA, 2003.
(889) Harris, P. J. F. *Carbon Nanotubes and Related Structures: New Materials for the Twenty-first Century*; Cambridge University Press: Cambridge, U.K., 2001.
(890) Dresselhaus, M. S.; Dresselhaus, G.; Avouris, P. *Carbon Nanotubes: Synthesis, Structure, Properties, and Applications*: Springer: Berlin, Germany, 2001.
(891) Tomek, D.; Enbody, R. J. *Science and Application of Nanotubes*; Kluwer Academic/Plenum: New York, 2000.
(892) Andreoni, W. *The Physics of Fullerene-Based and Fullerene-related Materials*; Kluwer Academic Publishers: Dordrecht, The Netherlands, 2000.
(893) Saito, R.; Dresselhaus, G.; Dresselhaus, M. S. *Physical Properties of Carbon Nanotubes*; Imperial College Press: London, U.K., 1998.
(894) Endo, M.; Iijima, S.; Dresselhaus, M. S. *Carbon Nanotubes*; Pergamon: Tarrytown, NY, 1996.
(895) Reich, S.; Thomsen, C., Maultzsch, J. *Carbon Nanotubes: Basic Concepts and Physical Properties*; Wiley-VCH: Weinheim, Germany, 2004.
(896) Tomek, D.; Enbody, R. J. *Science and Application of Nanotubes*; Kluwer Academic/Plenum: New York, 2000.
(897) Harris, P. J. F. *Carbon Nanotubes and Related Structures: New Materials for the Twenty-first Century*; Cambridge University Press: Cambridge, U.K., 1999.
(898) Rotello, V. *Nanoparticles: Building Blocks for Nanotechnology*; Kluwer Academic/Plenum Publishers: New York, 2004.
(899) Liz-Marz, L. M.; Kamat, P. V. *Nanoscale Materials*; Kluwer Academic Publishers: Boston, MA, 2003.
(900) Wieckowski, A.; Savinova, E. R.; Vayenas, C. G. *Catalysis and Electrocatalysis at Nanoparticle Surfaces*; Dekker: New York, 2003.
(901) Antonietti, M. *Colloid Chemistry II*; Springer: Berlin, Germany, 2003.
(902) Goddard, W. A., III. *Handbook of Nanoscience, Engineering, and Technology*; CRC Press: Boca Raton, FL, 2003.
(903) Zhang, J. Z. *Self-assembled Nanostructures*; Kluwer Academic/Plenum Publishers: New York, 2003
(904) Schmid, G. *Nanoparticles: From Theory to Application*; Wiley-VCH: Weinheim, Germany, 2003.
(905) Waseda, Y.; Muramatsu, A.; Muramatsu, A. *Morphology Control of Materials and Nanoparticles: Advanced Materials Processing and Characterization*; Springer Series in Materials Science; Springer: Berlin, Germany, 2004.
(906) Wilson, M. *Nanotechnology: Basic science and Emerging Technologies*; Chapman & Hall/CRC: Boca Raton, FL, 2002.
(907) Fendler, J. H. *Nanoparticles and Nanostructured Films: Preparation, Characterization and Applications*; Wiley-VCH: Weinheim, Germany, 1998.
(908) Chow, G.-M.; Noskova, N. I. *Nanostructured Materials: Science & Technology*; Kluwer Academic Publishers: Dordrecht, The Netherlands, 1998.
(909) Chow, G.-M.; Gonsalves, K. E. *Nanotechnology: Molecularly Designed Materials*; American Chemical Society: Washington, DC, 1996.
(910) Yang, S.; Sheng, P. *Physics and Chemistry of Nano-structured Materials*; Taylor & Francis: London, U.K., 2000.
(911) Timp, G. *Nanotechnology*; Springer: New York, 1999.
(912) Goldstein, A. N. *Handbook of Nanophase Materials*; Dekker: New York, 1997.
(913) Tsakalakos, T.; Ovidko, I. A.; Vasudevan, A. K. *Nanostructures: Synthesis, Functional Properties and Applications*: Kluwer Academic: Boston, MA, 2003; published in cooperation with NATO Scientific Affairs Division.
(914) Liz-Marz, L. M.; Giersig, M. *Low-dimensional Systems: Theory, Preparation, and Some Applications*; Kluwer Academic Publishers: Boston, MA, 2003; published in cooperation with NATO Scientific Affairs Division.
(915) Nalwa, H. S. *Nanoclusters and Nanocrystals*; American Scientific Publishers: Stevenson Ranch, CA, 2003.
(916) Edelstein, A. S.; Cammarata, R. C. *Nanomaterials: Synthesis, Properties, and Applications*; Institute of Physics: Bristol, U.K., 1998.
(917) Tang, Z.; Sheng P. *Nano Science and Technology: Novel Structures and Phenomena*; Taylor & Francis: London, U.K., 2003.
(918) Wang, Z. L. *Characterization of Nanophase Materials*; Wiley-VCH: Weinheim, Germany, 2000.
(919) Drexler, K. E. *Nanosystems: Molecular Machinery, Manufacturing, and Computation*; Wiley: New York, 1992.
(920) Rieth, M. *Nano-engineering in Science and Technology: an Introduction to the World of Nano-design*; World Scientific: River Edge, NJ, 2003.
(921) Ying, J. Y. *Nanostructured Materials*; Academic: San Diego, CA, 2001.

CR030063A